MICRO ELECTRONIC MECHANICAL DEVICES COLLECTION

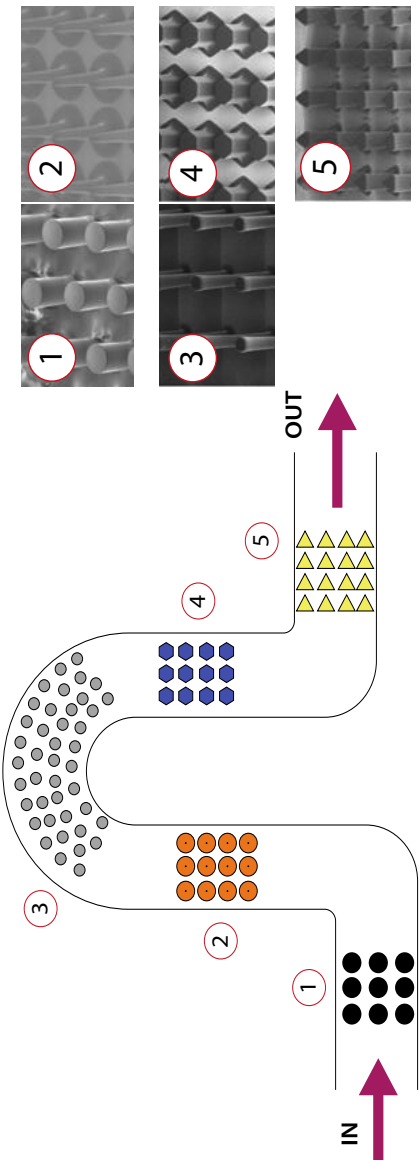

Carbon: The Next Silicon?

Book 1 – Fundamentals

Marc J. Madou
Victor H. Perez-Gonzalez
Bidhan Pramanick

MOMENTUM PRESS
ENGINEERING

CARBON: THE NEXT SILICON?

CARBON: THE NEXT SILICON?

Book 1 – Fundamentals

MARC J. MADOU,
VICTOR H. PEREZ-GONZALEZ, AND
BIDHAN PRAMANICK

MOMENTUM PRESS, LLC, NEW YORK

Carbon: The Next Silicon?: Book 1 – Fundamentals

First published by Momentum Press®, LLC
222 East 46th Street, New York, NY 10017
www.momentumpress.net

ISBN-13: 978-1-60650-723-0 (print)
ISBN-13: 978-1-60650-724-7 (e-book)

Momentum Press Micro Electronic Mechanical Devices Collection

Cover and interior design by Exeter Premedia Services Private Ltd., Chennai, India

10 9 8 7 6 5 4 3 2 1

Printed in the United States of America

Abstract

This book provides an introduction to the state-of-the art in C-MEMS/C-NEMS with an emphasis on lithographically patterned photopolymers, carbonized in an inert atmosphere. It is obvious that we can expand our perspective considerably by learning from the traditional carbon manufacturing community where researchers deal with a much wider variety of carbon feed stocks such as coal, coconut shell, wood, agricultural wastes and industrial wastes to make all types of useful carbons. In addition to their expertise in choosing the right catalysts to end up with the desired carbon nanomaterials from any of these feedstocks, these carbon scientists works with dry and wet pyrolysis processes. Wet pyrolysis process is also known as hydrothermal carbonization, a process new to the C-MEMS/C-NEMS community.

The new concepts are introduced by discussing carbon nanomaterials synthesis aided with catalysts and chemistry and detailing the microstructure of the resulting nanocarbons.

The performance of carbon materials is determined to a large extent by their surface and interfacial properties. The methods to tailor the surface activity of different carbon structures, how to characterize them and the potential applications derived from the modifications achieved are also discussed.

KEYWORDS

Carbon allotropes catalysis electrochemistry surface modification MEMS and NEMS super capacitors energy storage devices CNTs glassy carbon NMR electrospinning redox amplification AC/DC electrokinetics pyrolysis electroanalysis

Contents

List of Figures

List of Tables

About the Contributors

Dr. Marc J. Madou, before joining UCI as the Chancellor's Professor in Mechanical and Aerospace Engineering (MEA), Dr. Madou was Vice President of Advanced Technology at Nanogen in San Diego, California. He specializes in the application of miniaturization technology to chemical and biological problems (BIO-MEMS). He is the author of several books in this burgeoning field he helped pioneer both in Academia and in Industry. He founded several micromachining companies and has been on the board of many more.

Many of his colleagues became well know in their own right in academia and through successful MEMS start-ups. Madou was the founder of the SRI International's Microsensor Department, founder and President of Teknekron Sensor Development Corporation (TSDC), Visiting Miller Professor at UC Berkeley and Endowed Chair at the Ohio State University (Professor in Chemistry and Materials Science and Engineering). The third edition of "Fundamentals of Microfabrication," an introduction to MEMS and NEMS, which has become known as the "bible" of micromachining, was published in July of last year (http://fundamentalsofmicrofabrication.wordpress.com/).

Some of Dr. Madou's current research work involves a compact disc-based fluidic platform and carbon MEMS, the two latter fields were pioneered by Dr. Madou. To find out more about those recent research projects, visit www.biomems.net.

Dr. Victor H. Perez-Gonzalez, received the BS degree in Electronics and Communications Engineering (honors) from *Universidad Autonoma de Nuevo Leon*, Mexico, in 2006; and the MS in Electronics Engineering and PhD in Information Technologies and Communications from *Tecnologico de Monterrey*, Mexico, in 2008 and 2013, respectively. He has held a visiting research position at the University of California Irvine. For the past 2 years he has been a Research Associate at *Tecnologico de Monterrey*,

Mexico. In 2015 he was awarded with the National Researcher Level 1 distinction by the *Sistema Nacional de Investigadores*, Mexico, and became a member of the IEEE *Eta Kappa Nu* Honor Society. His research has been supported by CONACYT and UC-MEXUS.

Dr. Perez-Gonzalez's research interests are focused in the multidisciplinary area of Micro-/Nano- Electro-Mechanical Systems (MEMS/NEMS). From this broad research field, where he has published several papers in international journals and conference proceedings, his efforts are strongly aligned in the development of the sensing or actuating stages of Lab on a Chip devices and their integration with microelectronic elements. For the development of such stages he uses a broad range of materials, including: carbon, metals, electroconductive polymers, PDMS, and glass, among others. His current research projects deal with (1) the application of electrokinetic and mechanical forces for the manipulation, separation, or characterization of particles (e.g., microalgae, proteins, and bacteria) or fluids; (2) the development of highly sensitive amperometric sensors with Carbon-MEMS/NEMS; and (3) the development of novel micro/nano fabrication processes. Research efforts integrate mathematical modeling with experimental work for extending the practical applications of these technologies.

Dr. Bidhan Pramanick, received PhD Degree from Indian Institute of Technology (IIT) Kharagpur, India, in 2012 after completing B. Tech and M. Tech courses in Electronics and Communication Engineering from Kalyani Government Engineering College, India, in 2005 and 2007, respectively. He worked more than 2 years as Assistant Professor in Indian Institute of Space Science and Technology (IIST), an Institute of ISRO (Indian Space Research Organization) family. Dr. Pramanick joined Tecnologico de Monterrey, Mexico as Postdoctoral Research Investigator in January, 2015 in collaboration with University of California Irvine, CA, U.S. He was a recipient of the CSIR SRF Fellowship (India) for his PhD Programme and UGC grant for his Masters Programme.

He has authored or co-authored more than 16 papers in international journals and conference proceedings, two book chapters and one book. He was also one of the editors of two books on C-MEMS. He was a JPO in ISRO-sponsored project and he has successfully developed MEMS-based Microvalve and Micropump for space applications.

His current research interests include Carbon MEMS/NEMS especially Carbon Nanowire based sensors. He is also interested in the area of Micropropulsion and RFMEMS.

Foreword

UC Irvine, Sept 14–16, 2014. Chair: Dr. Marc Madou
Co-Chairs: Dr. Chunlei Wang, Dr. Rodrigo Martinez-Duarte and Mr. Jacob Moebius

Dear reader, two books: Carbon: The Next Silicon? Book 1-Fundamentals and Carbon: The Next Silicon? Book 2-Applications came about as a follow-up to the 1st International Conference on Carbon Micro and Nano Electromechanical Systems (C-MEMS /C-NEMS) held September 14–16, 2014 on the UC Irvine campus (see conference LOGO above). This was an invitation only event with delegates from the US, Italy, Spain, Malaysia, Mexico, Denmark, Germany, Switzerland and India. The group was limited to 60–70 researchers currently working in the field and expected to contribute to breakthroughs in this field and interested in international collaborations. Indeed research funding is weak globally and by leveraging efforts internationally we still have a chance to remain productive scientists regardless of politicians' irresponsibility. The pictures below are from some of the C-MEMS/C-NEMS team at the 2014 conference.

At the conference we had presentations on the latest C-MEMS and C-NEMS results, suggested future directions and discussed what each country is offering in terms of funding for international collaborations and formed several motivated proposal teams. We identified opportunities for students to be part of this international C-MEMS/C-NEMS research

ring and to be able to work in any one laboratory that is part of this ring to faster produce science breakthroughs and in the process become broader-thinking global citizens.

The format of the conference was a new and exciting experiment in itself. Over the last decade we have developed serious doubts about the effectiveness of huge, profit driven conferences so instead we brought together a small group of researchers in an intimate setting and made this an occasion where there was plenty of time to talk and make friends and make plans over drinks and food. Besides the science sessions we had several cultural events, including a class on Ancient Indian History: Aryan Invasion: Myth or Reality? (Prof. A. Ghosh) and a Malay board game: Congkak (Prof. Fatimah Ibrahim). We also had exhibits of paintings and photography and plenty of music [from Persian classical music to sixties rock and roll (UC Irvine Professor Band-Second Law), Russian love ballads (Dr. Lawrence Kulinsky) and Frank Sinatra (Prof. Jan Korvink)] we even had a yoga class (Prof. Regina Ragan) all by and for the invited C-MEMS/C-NEMS researchers. Art and science have a lot in common, in both one must create de-novo, not accept any pre-conceived notion of what the best science/art might be or where it will lead and in both cases, if good enough, one can transcend even the most miserable of times.

Part of the C-MEMS/C-NEMS team at the 1st C-MEMS International Conference. Sept 14–16, 2014. Location: Lobby CalIT2 on the UC Irvine Campus.

Dr. Swati Sharma (Karlsruhe Institute of Technology, Germany) on C-MEMS and EPR (Left panel). Sharifah Bee Binti O.A Abd Hamid on carbon and nano catalysis (Right panel). At the 1st C-MEMS International Conference. UC Irvine, Sept 14–16, 2014

A mixed-media sketch by Ashutosh Sharma (Indian Institute of Technology Kanpur) (Left panel). A Malay board game called Congkak –I kid you not! (Right panel). At the 1st C-MEMS International Conference. UC Irvine, Sept 14–16, 2014.

Prof. Jan Korvink (Karlsruhe Institute of Technology, Germany) singing Frank Sinatra's I did it my way" at the 1st C-MEMS International Conference. UC Irvine, Sept 14–16, 2014.

Quick Overview of Book 1-Fundamentals

In Book 1-Fundamentals, Chapters 1 to 7, we cover the theoretical aspects of carbon and the manufacture of carbon based devices. In Chapter 1, Marc Madou provides an introduction to the state-of-the art in C-MEMS/C-NEMS with an emphasis on lithographically patterned photo-polymers, carbonized in an inert atmosphere. The most prevalent allotrope covered in this first chapter is glassy carbon and we show that by choosing another manufacturing approach – electrospinning (ES) instead of spin-coating the polymer precursor - the material can be rendered more graphitic. It is obvious that we can expand our perspective considerably by learning from the traditional carbon manufacturing community where researchers deal with a much wider variety of carbon feed stocks such as coal, coconut shell, wood, agricultural wastes and industrial wastes to make all types of useful carbons. In addition to their expertise in choosing the right catalysts to end up with the desired carbon nanomaterials from any of these feedstocks, these carbon scientists works with dry and wet pyrolysis processes. Wet pyrolysis process is also known as hydrothermal carbonization, a process new to the C-MEMS/C-NEMS community. In Chapters 2 and 3 Sharifah Bee Abd Hamid and team introduce these new concepts to the C-MEMS/C-NEMS community by discussing carbon nanomaterials synthesis aided with catalysts and chemistry and detail the microstructure of the resulting nanocarbons. The carbon nanowires discussed in Chapter 1 were made by carbonization of electrospun polymer precursors only (either far field electrospinning or electromechanical spinning). Bidhan Pramanick, in Chapter 4, is surveying all the options that are available for the fabrication of carbon nanowires. In Chapter 5 Bidhan Pramanick et al are digging deeper into the theory and application of electrospinning to come up with yet other ways to impact C-MEMS/C-NEMS. We barely touched upon xerogels for C-MEMS/C-NEMS in Chapter 1 but in Chapter 6 Chandra

Sharma and Manohar Kakunuri take on the challenge of integration of organic xerogels more firmly into the C-MEMS/C-NEMS arsenal of tools. In Chapter 7 Salvador Borros et al are turning our attention to the details of C-MEMS/C-NEMS surfaces in terms of their chemical composition and microstructure. They point out that the performance of carbon materials is determined to a large extent by their surface and interfacial properties. This team describes the methods to tailor the surface activity of different carbon structures, how to characterize them and the potential applications derived from the modifications achieved.

Acknowledgments

1. Acknowledgments for “C-MEMS/C-NEMS Introduction”: NSF grant. 1449397
2. Acknowledgments for “The Beautiful World of Carbon”: Financial supports from Malaysian Ministry of Higher Education HIR F00032, TRGS TR002B-2014B, and University of Malaya grant UMRG (RP022-2012A) are acknowledged.
3. Acknowledgments for “Synthesis of Nanocarbons and Tuning of Their Properties”: Financial support from the University Malaya UMRG (RP022-2012A), Ministry of Higher Education (MOHE) Transdisciplinary Research Grant Scheme (TR002A-2014B), Ministry of Science Technology and Innovation (MOSTI) Science Fund (SF-020-2014), and University of Malaya Flagship Grant (FL001-14AET) for the Carbon NEMS research are acknowledged.
4. Acknowledgments for “Historical Overview of Carbon Nanowire Fabrication Methods”: The financial support from UC-Mexus grant UCM-104728 and CONACYT Ciencia Basica CB-2014-01-241458.
5. Acknowledgments for “Carbon Nanowire Fabrication: C-MEMS”: Financial support from CONACYT Ciencia Basica CB-2014-01-241458, Ministry of Higher Education (MOHE) Transdisciplinary Research Grant Scheme (TR002A-2014B), Ministry of Science Technology and Innovation (MOSTI) Science Fund (SF-020-2014), and University of Malaya Flagship Grant (FL001-14AET) for the Carbon NEMS research, University Malaya UMRG (RP022-2012A) are acknowledged.
6. Acknowledgments for “C-MEMS based On-Chip Microsupercapacitors”: This article was supported financially by the National Science Foundation (NSF), (Award number 1506640) and NSF ASSIST center seed funding. Richa Agrawal acknowledges

University Graduate School (UGS) at Florida International University for support through a Doctoral Evidence Acquisition (DEA) Fellowship. The previous works summarized in this chapter were funded by the US Defense Advanced Research Projects Agency (DARPA), Young Faculty Award program (Project No. HR0011-08-1-0036), NSF (MRI program CMMI-0821582) and the American Chemical Society Petroleum Research Fund (49301-0N110).

7. Acknowledgments for "Glassy Carbon Microelectrodes for Neural Signal Sensing and Stimulation": The project described was supported by Award Number EEC-1028725 from the National Science Foundation. The content is solely the responsibility of the authors and does not necessarily represent the official views of the National Science Foundation.
8. Acknowledgments for "Advanced Electroanalysis with C-MEMS": Financial support by MIUR-PRIN 2010AXENJ8 and Veneto Region Project RESMIA is acknowledged.
9. Acknowledgments for "Carbon MEMS for Magnetic Resonance": The financial support from the European Research Council through the senior grant 290586 NMCEL.
10. Acknowledgments for "C-MEMS-Based 3D Interdigitated Electrode Arrays for Redox Amplification": The financial support from UC-Mexus grant UCM-104728 and CONACYT Ciencia Basica CB-2014-01-241458.

CHAPTER 1

C-MEMS AND C-NEMS INTRODUCTION

Marc J. Madou

University of California Irvine, USA

Courtesy of Dr. Samira Hosseini.

1.1 PURPOSE OF CHAPTER 1

The purpose of this chapter is to explain what the most prominent carbon microelectromechanical system (C-MEMS) and carbon nanoelectromechanical system (C-NEMS) fabrication processes are, to illustrate how the

details of the fabrication process enable one to obtain different carbon microstructures, to introduce important current and to discuss anticipated applications.

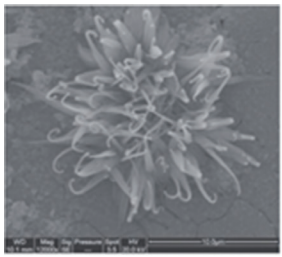

Carbon microflowers. Based on pyrolysis of resorcinol-formaldehyde gels (RF-gels) (Courtesy of Dr. Ashutosh Sharma, IIT Kanpur, India).

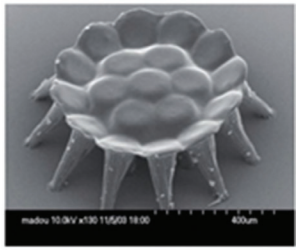

Microtable made with carbon MEMS at UCI. See also Figure 1.3 (Courtesy of Dr. Marc Madou, UC Irvine, CA, USA).

1.2 C-MEMS AND C-NEMS: WHAT IS IT?

Shaping of most carbon allotropes into micro- or nanodevices with mechanical machining techniques is not a straightforward task because the material is usually hard and brittle. Integrated Circuit (IC) processing technologies, such as focused ion beam (FIB) milling [1] and reactive ion etching [2] of carbon, are more up to the task but are often too time consuming and too expensive because of the need for sophisticated equipment involving vacuum systems. Low feature resolution and poor repeatability of the carbon composition limit the application of the less sophisticated and, therefore, less expensive screen-printing technique of carbon inks [3]. As we just noted, carbon, because it is brittle and hard, is a difficult material to machine directly. Polymers, on the other hand, can be machined easily in a wide variety of machine tools and then converted to carbon devices through pyrolysis, resulting in shapes that are often impossible to make in carbon by any other means. Simply stated, the underlying principle of C-MEMS and C-NEMS is to choose an easy to work with polymer precursor, machine, or photopattern this precursor material (in the case of a photoresist) and then convert it to carbon by pyrolysis [4–6]. The words MEMS and NEMS stand for microelectromechanical system and nanoelectromechanical systems, respectively [7]. These used to be made almost exclusively from Si but with C-MEMS and C-NEMS, the 3D (three-dimensional) building materials are any of the many carbon allotropes instead [8, 9].

In one embodiment of the C-MEMS and C-NEMS process, a photoresist is patterned by photolithography and is subsequently pyrolyzed at high temperatures in an oxygen-free environment. By changing the lithography

conditions, soft and hard baking times and temperatures, resist additives (e.g., a catalyst), pyrolysis time, temperature, and environment, C-MEMS and C-NEMS permit a wide variety of interesting new applications that use structures having a wide variety of shapes, resistivities, mechanical properties, and other physicochemical properties.

An example of photolithography process (using SU-8, an epoxy-based negative photoresist) to make C-MEMS and C-NEMS structures is illustrated in Figure 1.1. The process includes spin coating, soft bake (not shown), near-ultraviolet (UV) exposure, postbake (also not shown), and development. After the photolithography steps, C-MEMS and C-NEMS architectures are obtained in a two-step pyrolysis process. The latter may be carried out in an open-ended quartz-tube furnace, where the samples are postbaked in an N_2 atmosphere at 300°C for about 40 minutes first and then heated in an N_2 atmosphere (2,000 sccm) up to 900°C. At this point, the N_2 gas is shut off and forming gas [H_2(5%)/N_2] is introduced (2,000 sccm) for 1 hour and then the heater is turned off and the samples are cooled down again in an N_2 atmosphere to room temperature. The heating rate is about 10°C/min, and the total cooling time is about 10 hours [9].

The resulting microstructure of the carbon material from the process detailed previously was found to be that of glassy carbon (not to be confused with amorphous carbon because it has no dangling bonds and is made up by 2D (two-dimensional) structural elements) [5]. The exact nature of the glassy carbon (also vitreous carbon) microstructure is still a subject of debate, but it is generally agreed to have a fullerene-related microstructure (see also Figure 1.9) that leads to a great variety of unique material properties [10–14]. Glassy carbon is one of the favored electrode materials for electrochemists. Other manufacturing approaches that can lead to other carbon microstructures are discussed in the next section.

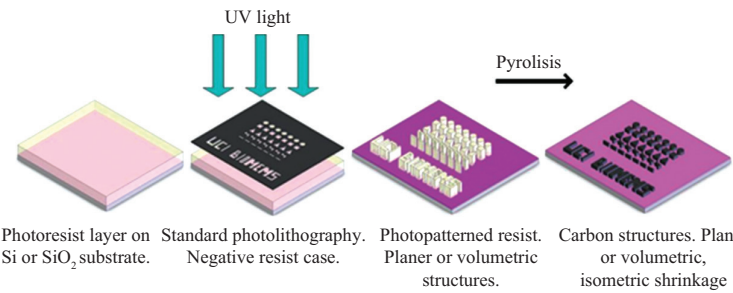

Figure 1.1. An illustration of one type of C-MEMS: photolithographic patterning of a polymer precursor (SU-8 photoresist) and pyrolysis (see text for details) [9].

Initial work that qualifies as C-MEMS and C-NEMS was carried out by Lyons, Wilkins, and Robbins [15]. This team prepared carbon films by the thermal decomposition of photo-defined novolac resist (HPR-206) patterns and observed that the electrical resistivity decreased over 18 orders of magnitude as the pyrolysis temperature was increased to 1050°C. Sometime later, Scheuller et al. used soft lithography to fabricate glassy carbon microstructures [16, 17]. In the latter approach, micromolding of a resin (not a photoresist in this case) such as poly (furfuryl alcohol) in an elastomeric mold yielded polymeric microstructures and the polymeric microstructures were then converted to free-standing carbon by carbonization. In these works, only low aspect ratio (flat) carbon structures were fashioned and involved IC-related applications such as capacitors and masking.

This author and his team optimized the photoresist process from Lyons [18] and Lyons, Wilkins, and Robbins [15]; Lyons, Hale, and Wilkins [19]; Lyons, Wilkins, and Robbins [20] and were the first to make high aspect ratio micro- and nanocarbon microstructures, dope the polymer precursors, create multilevel devices, introduce different carbon microstructures into the arsenal, and explore a wide variety of applications of these novel structures (see Application section) [9].

An example of early work from the UCI C-MEMS and C-NEMS group is shown in Figure 1.2. The average height of the SU-8 posts shown in typical scanning electron microscope (SEM) images (Figure 1.2a and 1.2b, left panel) is around 300 μm. As shown in Figure 1.2c and 1.2d, after pyrolysis, the overall shape of the cylindrical posts is largely retained, and a typical aspect ratio of the carbon post achieved is around 10:1 [9, 21]. To construct yet higher aspect ratio C-MEMS features (up to 40:1), we developed a multilevel C-MEMS process. Here each layer of SU-8

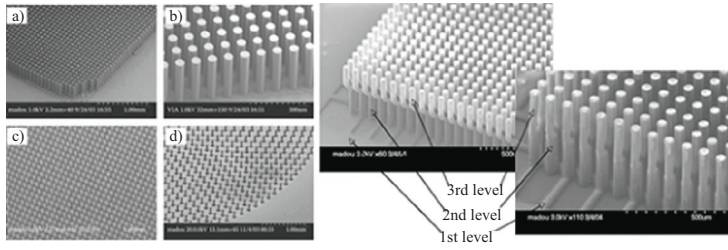

Figure 1.2. SEM images of (a) and (b) SU-8 post arrays before pyrolysis and (c) and (d) carbon post arrays after pyrolysis (left panel) [9]. SEM images of three-level C-MEMS: a three-level C-MEMS structure with two levels in good alignment but with a third-level out of alignment (right panel) [9, 21].

photoresist is exposed and baked separately and then the whole assembly is developed in a last step. SEM images of a three-level C-MEMS device are shown in Figure 1.2 (right panel); in this three-level C-MEMS structure, the first two exposures were in good alignment but the third was out of alignment [9, 21]. This multilevel C-MEMS microfabrication process has its analogy in the multilevel polysilicon surface micromachining process [22].

As alluded to earlier, by tightly controlling the various lithography and carbonization process parameters, a wide range of 3D C-MEMS structures, such as suspended carbon wires (wash cloth lines), bridges, plates (carbon microtable, see also the inset in the heading of this chapter), and self-organized posts (carbon flowers, again see the inset in the heading of this chapter) and ribbons (networks) can be microfabricated. Some examples are shown in Figure 1.3. These intricate 3D structures shown here are fabricated using nontraditional lithography and resist process recipes, such as overexposure, underdevelopment, photoresist additives

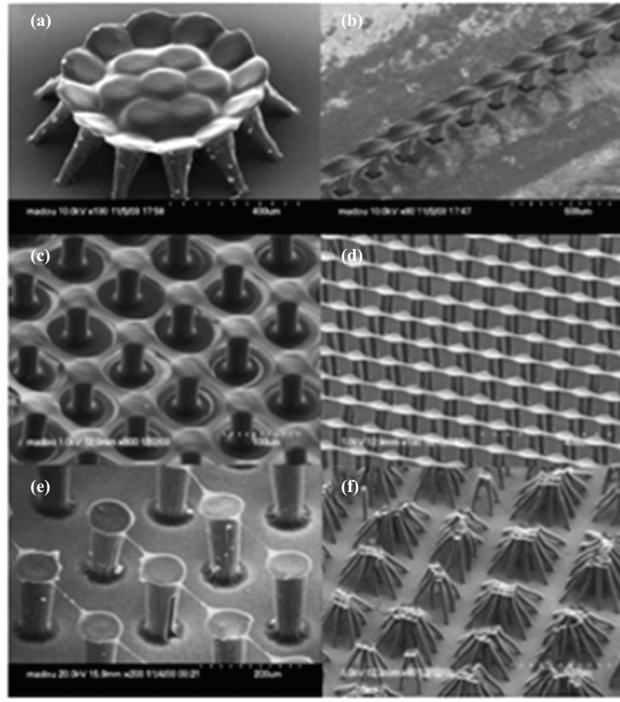

Figure 1.3. Typical SEM images of suspended (a) carbon plates (carbon microtable), (b) carbon bridge, (c) carbon networks, (d) carbon ribbons, (e) carbon fibers (wash cloth lines), and (f) self-assembled C-MEMS (also carbon flowers) [21].

(e.g., catalysts), directed flow of the developer, and exploitation of surface tension in the developing photoresist patterns [21].

It should be noted that upon pyrolysis, the polymer nanofibers with diameters in the several hundreds of nanometer range shrink to fibers with diameters below 100 nm, revealing yet another benefit of this type of nanofabrication approach. In the next section, we return to the controlled manufacture of suspended carbon nanowires (CNWs) (see Figure 1.3e). The suspended wires and other overhanging features illustrated in Figure 1.3 are a result of SU-8 polymer T-topping [23] connecting SU-8 posts, these wires and other overhangs are converted into carbon in the pyrolysis step together with the suspending posts. The T-topping phenomenon is hard to render into a controllable process, however, and we shall see that by electrospinning (ES) of polymer precursor wires onto the SU-8 polymer posts, suspended CNWs can be manufactured in a much more controlled manner.

In Figure 1.4, we show the effect of adding a catalyst to the polymer precursor. Carbon nanofibers (CNFs) (<1 percent weight) with the Fe catalyst nanoparticles still embedded in them were mixed in SU-8 photoresist. In Figure 1.4a, we see an SEM image of a CNF-doped photoresist post before pyrolysis, and in Figure 1.4b and c, we show the same post after pyrolysis. Clearly, the amount of nanofibers on the

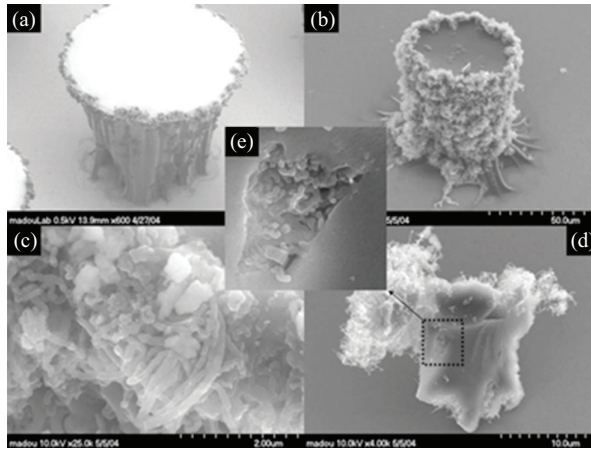

Figure 1.4. Typical SEM images of (a) a photoresist post obtained from modified SU-8 before pyrolysis, (b) a carbon post after pyrolysis, (c) a carbon post surface under high magnification, (d) a broken piece of a carbon post with embedded carbon fibers, and (e) an embedded cavity under high magnification [24, 25].

posts has increased dramatically. Figure 1.4d and e reveals that there are nanofibers in the post too and that the post has some voids also. It is believed that this nanofiber growth during pyrolysis is a chemical vapor deposition (CVD) process with the pyrolyzing polymer matrix providing the hydrocarbon source to redeposit on the original CNWs, which is the reason for the tremendous increase of the amount of CNWs after pyrolysis [24, 25].

As is the case of the lithography process, the carbonization process can be carried out in many different ways as well: changing the heating ramp rate, for example, can produce microporous carbon if carried out fast (say above 10°C/min) [26] and changing the gas composition (e.g., to include some H_2) can lead to a nanoporous carbon amenable to super capacitor manufacturing [27, 28]. In Figure 1.5, we show that when changing the heating ramp rate to reach the final temperature of 900°C from around 15°C/min to 90°C/min the size of the pores is dramatically increased [from a couple of microns (Figure 1.5, left panel) to 10 to 15 μm (Figure 1.5, right panel)]. Sharma, Kamath, and Madou studied the impact on the interfacial capacitance and electrochemical behavior for these types of porous carbons [26]. With a slow ramp rate of 2°C/min, the resulting C-MEMS is non-porous even under Scanning Tunneling Microscopy (STM) observation. During the pyrolysis step, the photoresist transforms into carbon by replacing the carbon chemical bonds with nitrogen, oxygen, and hydrogen with all carbon–carbon bonds. When the pyrolysis rate is very fast, the pyrolysis gaseous products are not yet annealed out and porosity results [29].

Hsia et al. demonstrated that the pyrolysis of SPR-220 photoresist, in an ambient consisting of Ar at 900°C followed by an anneal in an H_2/Ar mixture, results in a high-surface-area porous carbon, applicable to on-Si chip super capacitor fabrication [27]. In this case, a reaction of hydrogen

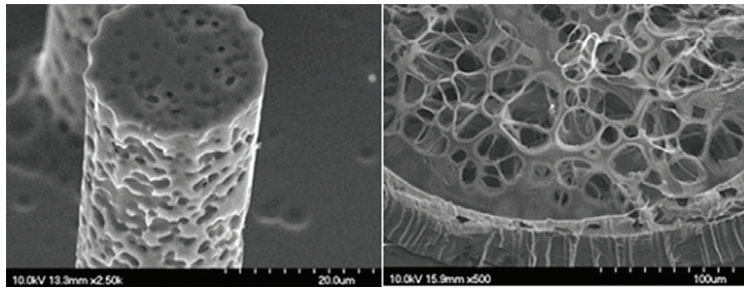

Figure 1.5. Typical SEM images of C-MEMS posts fabricated with a final SU-8 carbonization temperature of 900°C. Temperature ramp rate of 15°C/min (left) to 90°C/min (right) [29].

with the carbon results in nanopores rather than the micropores observed in the case of Figure 1.5 that form because of the escaping pyrolysis gases. Porosity in C-MEMS structures was also studied by Wang et al. who produced porous carbon micropillars using the block copolymer Pluronic F127 composed of (polyethyleneoxide)–(polypropyleneoxide)–(polyethyleneoxide) [(PEO)-(PPO)-(PEO)] as a porogen [30]. Sharma et al. made a variety of carbon structures by the inverse emulsification of resorcinol–formaldehyde sol in cyclohexane with the nonionic surfactant Span-80, followed by pyrolysis at 900°C in nitrogen. Carbon xerogel microspheres and folded fractal-like structures were demonstrated, and by varying the reaction conditions, the porosity could be modulated [31–33]. From the preceding, we recognize that there are at least four different methods to make porous C-MEMS and C-NEMS with different pore size, density, and distribution.

While fast pyrolysis results in microporous high aspect ratio C-MEMS structures (see Figure 1.5), treatment with oxygen plasma can texture the carbon surface on the submicrometer scale. Surface roughening may be achieved by subjecting the pyrolyzed samples to an oxygen plasma environment. Using a moderate power of 300 W and 200 mT of oxygen, 4 minutes is enough to dramatically change the texture of C-MEMS surfaces. Two types of indentations were observed as a result of the plasma treatment: larger indentations around 2 μm in size and smaller ridges around 200 nm in width (see Figure 1.6) [29, 34]. Plasma treatment of

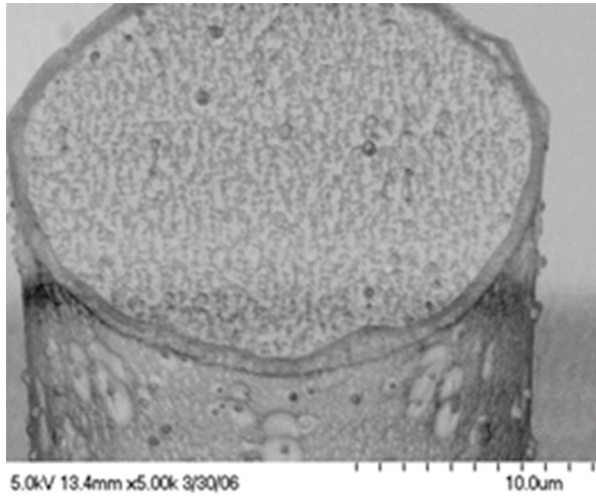

Figure 1.6. SEM of C-MEMS surface after plasma treatment [29].

C-MEMS surfaces has been shown to enhance electrochemical reactivity and interfacial capacitance [16, 26, 35].

It is clear to this author that plenty of opportunities for new C-MEMS and C-NEMS discoveries remain. A prime example with almost untapped potential involves the polymer–carbon intermediates that form during the carbonization of polymer precursors with or without additives (see Figure 1.7 in case of SU-8 carbonization). During pyrolysis, electrically, one goes from an insulating material to a good conductor and mechanically, one transitions from a low Young's modulus polymer to a hard and brittle carbon. Those intermediate materials have hardly been characterized at all. In some initial work along this line, Sharma [36] found that the Young's modulus for a photopatterned SU-8 film as a function of temperature (as shown in Figure 1.8a) features a dip: the material is softest, even softer than the starting SU-8, between 600°C and 700°C, and hardness increases again after 700°C.

This interesting observation can be explained based on the poroelasticity regime of the material between 600°C and 700°C; in this region, mostly gaseous pyrolysis reaction products are generated, and this results in a porous matrix [36].

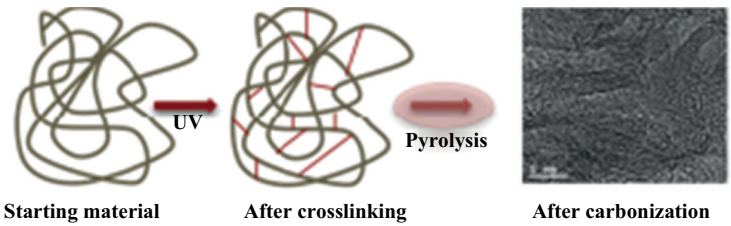

Figure 1.7. Schematic of the SU-8 photoresist pyrolysis process [36].

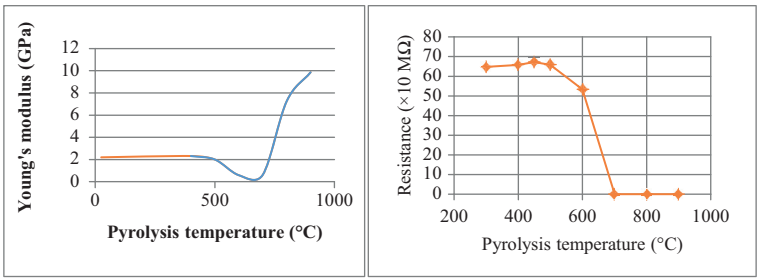

Figure 1.8. (a) Young modulus versus pyrolysis temperature for SU8 carbon intermediate materials [36], (b) electrical properties of polyacrylonitrile (PAN)–carbon intermediates [37].

The pyrolysis temperature regime where most carbonization gases are formed is also the regime where the resistance of the material changes the most dramatically. This is shown in Figure 1.8b for the pyrolysis of PAN [37].

1.3 IN C-MEMS AND C-NEMS THE MANUFACTURING METHOD DETERMINES THE CARBON MICROSTRUCTURE

In all the C-MEMS and C-NEMS examples presented so far, the resulting carbon microstructure obtained is that of glassy carbon [10–12] (see Figure 1.9). But carbon also comes in other allotropes such as diamond, graphite, fullerene, nanotube, amorphous, and diamond like. Based on the details of their microstructure, these allotropes are used in widely differing physical, chemical, mechanical, thermal, and electrical applications (see the Applications section). In this section, we demonstrate how one can obtain a different carbon microstructure by using different manufacturing techniques and how one can even afford the building of hybrid C-MEMS and C-NEMS devices that incorporate components with differing carbon microstructures by combining different manufacturing methods [13, 38, 39].

When the polymer precursor for C-MEMS and C-NEMS is deposited by ES instead of spin coating (as in photolithography), the carbon obtained is much more graphitic. To understand the reason behind this, we have to look somewhat deeper into the physics of the ES process [40]. ES is a simple, versatile, and widely used method for producing all types of polymer fibers, and it comes in three principal flavors, known as

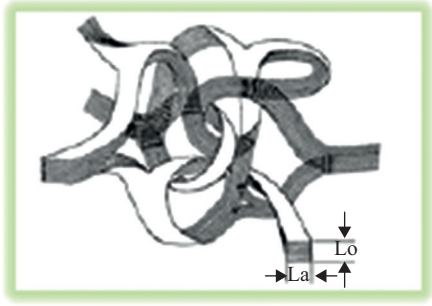

Figure 1.9. Microstructure of glassy carbon proposed by Haris [10], Jenkins and Kawamura [11], and Jenkins [12].

far-field electrospinning (FFES), near-field electrospinning (NFES), and electromechanical spinning (EMS).

FFES involves the application of a high voltage (10–15 kV) to bias a polymer solution in a syringe against a substrate of the opposite polarity with the syringe tip separated 10 to 15 cm from that substrate (also target or collector) (see Figure 1.10a). When the electrostatic field overcomes the surface tension that keeps a droplet of polymer solution at the syringe tip, a Taylor cone forms and if the polymer dissolved in the solution is at a high enough concentration, a fiber is drawn from it. In the air-gap between the nozzle and the collector, the polymer solution jet undergoes a whipping process wherein the solvent evaporates, leaving behind a charged polymer fiber, which lays itself randomly on the grounded collector.

In a C-MEMS and C-NEMS application of FFES, our team electrospun mats of SU-8 [41]. Next, this nanofibrous mat was micropatterned using photolithography, and finally, pyrolysis produced ordered arrays of microdomains containing CNFs. With lithography features in the microdomain and fibers with diameters in the hundreds to tens of nanometers range, this approach enables the fabrication of multiscale hierarchal assemblies such as fractal-like electrodes where a high external surface area is coupled with a minimized internal resistance, which is a feature of great utility, in batteries and fuel cells [42–44]. An example of this combination of lithography with ES to create structured C-MEMS and C-NEMS arrays is shown in Figure 1.11 [41]. Interesting as well is that these arrays of SU-8-derived carbon fibers were found to be very hydrophobic (water contact angle, $\theta \approx 130$) [41]. The biocompatibility of SU-8-derived carbon [45, 46] provides further motivation for the development of multiscale hierarchal scaffolds [47] for tissue engineering and in vivo biosensors [48, 49].

However, FFES is hard to control because of the electric field instabilities that are inherent in the ES process [50]. Despite the whipping of the nanofibers, even with FFES, some alignment along the preferred

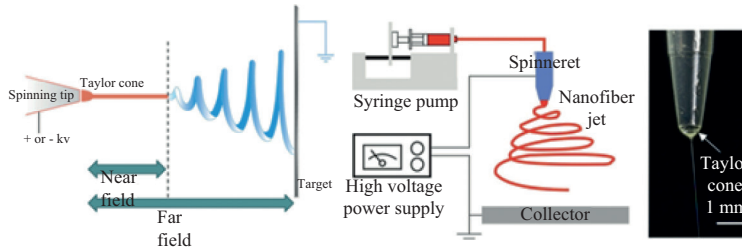

Figure 1.10. (a) Comparison of FFES and NFES and (b) FFES setup.

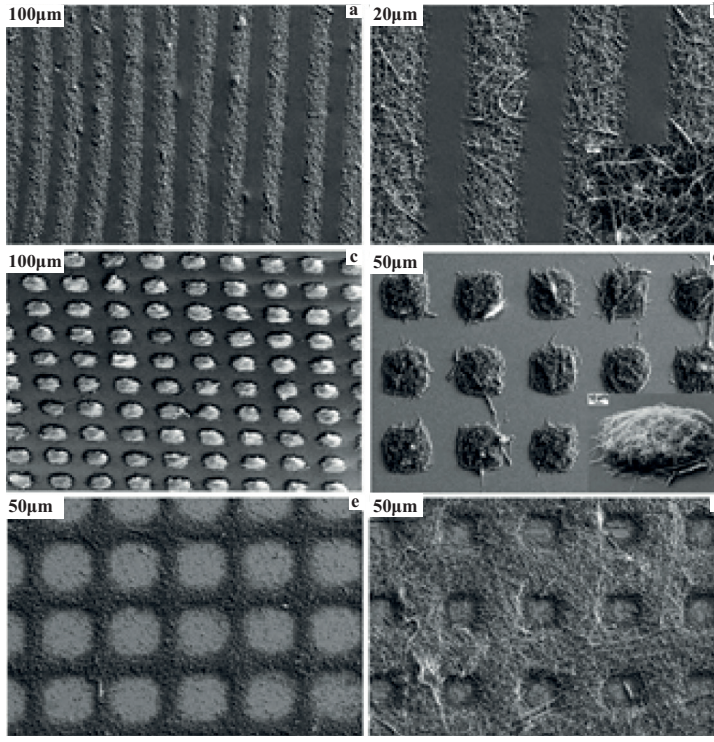

Figure 1.11. SEM images of arrays of patterned fibrous carbon structures: (a, b) lines, (c, d) 3D pillars, and (e, f) connecting squares. Images (b) and (d) are magnified views of images (a) and (c), respectively, and higher-magnification images of (b) and (d) are shown as insets. Images (a)–(d) are on Si wafer substrates, and images (e) and (f) are on a plasma-treated SU-8-derived carbon film on a Si wafer [41].

direction can be achieved by using a rotating drum collector [51] or electrical field manipulation [52]. Using a rotating target drum equipped with Si samples featuring SU-8 contact pads (Figure 1.12), our team deposited polymer nanofibers perpendicular to the suspending SU-8 walls of the contact pad structure [53]. These hybrid contact or nanowire assemblies were then carbonized to yield CNWs suspended between carbon electrodes. A contact pad with CNWs deposited on it is shown in Figure 1.13 (left) and 1.13 (middle). To be able to study single-suspended CNWs, extraneous wires were cut using FIB milling. It was found that these CNWs are better conductors than bulk glassy carbon. The high-resolution transition electron microscope (HR-TEM) images of these electrospun SU-8-derived CNFs revealed high-quality graphitic wire (for the thinnest

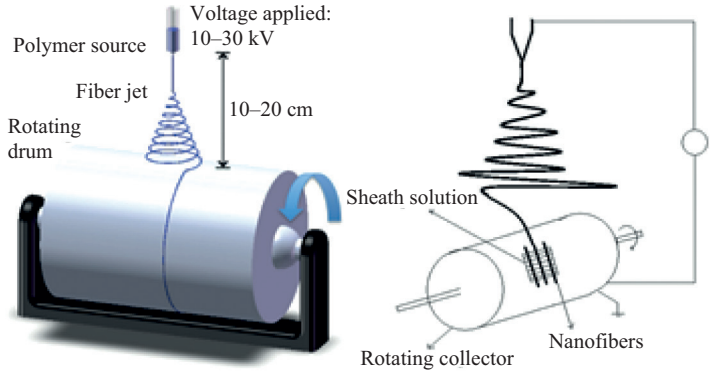

Figure 1.12. FFES with a rotating drum target (left) and Si substrate with SU-8 contact pads perpendicular to the nanowire direction (right) [53].

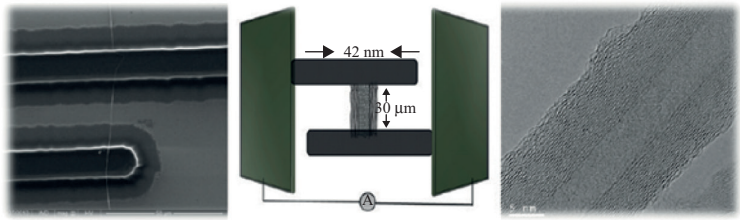

Figure 1.13. Single CNW across suspending carbon walls (left). Schematic of C-MEMS and C-NEMS structure used to collect nanowires (a dense array is shown here) (middle). HR-TEM image of electrospun SU-8-derived CNF: tube-like graphitic CNW with glassy carbon core and graphite shell (right) [53].

ones) and tube-like graphitic CNWs with a glassy carbon core and a graphite shell for the slightly thicker ones (see Figure 1.13 [right], in which we show a tube-like CNW and Figure 1.14 in which we show both types).

These results can be explained with reference to the work by Ji et al. [54] who convincingly demonstrated that the Young's modulus of electrospun polymer fibers increases significantly with a decrease of the fiber's diameter.

This is due to the orientation of the polymer chains in the ES process. The large shear imposed during the ES process orients the chains in the outermost regions of the fiber (see Figure 1.14a).

The smaller the diameter of the fiber, the easier it is for chains to orient themselves along the fiber's length throughout the entire fiber thickness, which results in a larger modulus. Ji et al. speculated and confirmed experimentally

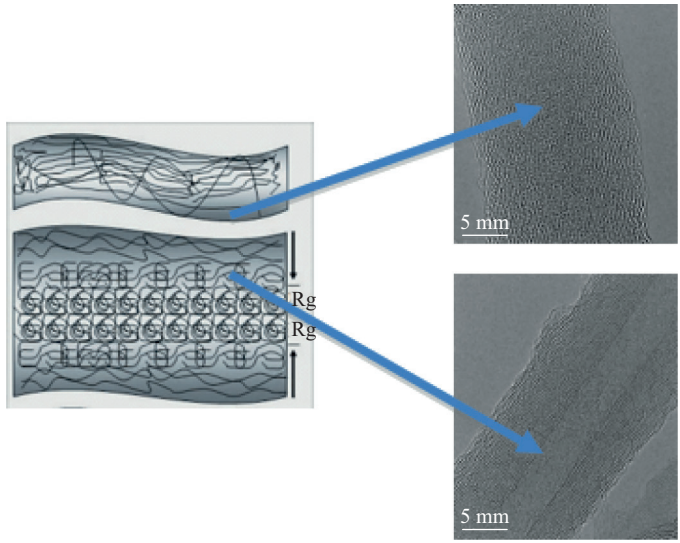

Figure 1.14. (a) Model of the molecular chain orientation according to Ji et al. [54]: (A) thin fiber—polymer chains oriented throughout the entire fiber; (B) thick fiber—polymer chain orientation starts at the surface and propagates into the bulk. R_g is the polymer gyration radius. (b) HR-TEM images of nanowire graphitic all the way to the core (top) and tube-like graphitic CNW with glassy carbon core and graphite shell (bottom) [55].

that the phenomenon scales with R/R_g, where R is the fiber radius and R_g the polymer radius of gyration rather than scaling with the absolute fiber diameter. The effect can propagate radially into the fiber for large distances (~20 R_g) [54]. Our C-MEMS and C-NEMS results depicted in Figure 1.14b nicely validate Ji et al.'s work. Indeed the degree of polymer chain orientation is reflected in the resulting carbon microstructure: carbon fibers are more graphitic when the corresponding polymer region consists of more oriented polymer chains and they are more glassy when corresponding with regions of more random chain orientation. Also in agreement with Ji et al., we found from HR-TEM images that the thinnest CNWs were more graphitic all the way to the core and thicker wires were tubelike with a glassy carbon core and a graphite shell (see Figure 1.14b). The microstructure of the contact pad is mostly glassy carbon, the suspended nanowire, on the other hand, because of the mechanical forces involved in ES, the pulling by the spinning drum, and yet further pulling because of shrinkage during carbonization, all conspire to yield a much more graphitic suspended wire component.

Current voltage (I/V) plots of the suspended carbon wires are linear, clear evidence for the ohmicity of the carbon-to-carbon contacts [53]. For CNWs with diameters in the 42 to 113 nm range, the average value for the electrical conductivity was 6.13×10^4 S/m, which is almost twice that of glassy carbon (2.8×10^4 S/m). The reported electrical conductivity values for graphite range from 2.4×10^4 S/m to 1.02×10^5 S/m parallel and perpendicular to the C-axis, respectively. The experimental conductivity values are lower than that of graphite but higher than that of glassy carbon but not as dramatic a change as we had expected, given the amount of graphitization observed in HR-TEM images. In the following, we demonstrate that the Young's modulus of CNWs fabricated using EMS also increases dramatically as the CNF diameter decreases (Figure 1.17).

Despite the efforts with rotating drums and electrical field manipulation, generally speaking, FFES fails to deliver precise, inexpensive, fast, and continuous nanofiber patterning capability. The problem of random nanofiber whipping was addressed by reducing the distance between the nozzle and the substrate to less than a few millimeters, so that fibers land on the substrate before the onset of whipping (see Figure 1.10a) [56]. In this approach, voltages are as low as 600 V—considerably reducing electric-field-induced instabilities. But with low voltages such as this, the surface of the polymer droplet must be artificially disrupted (e.g., by poking with a sharp glass tip) to create a localized region of a very high electric field on the droplet's surface initiating the ES process [56, 57]. This configuration, known as NFES, was suggested relatively recently [57]. Our group has found that production of yet thinner stable fibers necessitates operation at a yet lower voltage, and the results demonstrate that even nanofibers of sub-20-nm diameter are possible at a bias as low as 300 to 200 V when using superelastic viscoelastic polymers and by moving the stage or working with a rotating drum to mechanically pull and thus thin the wires [58–61]. We call this technique EMS as the moving stage or rotating drum mechanically pull on the viscoelastic fibers to further thin them. The polymers viscoelasticity ensures that the fibers do not break while pulling. The viscoelastic nature of the polymer ink enables continuous ES at a very low voltage of 200 V, considerably lower than that in NFES, thereby reducing bending instabilities and increasing the control of the resulting polymer jet even further. The resulting jet is stable and can be easily and precisely targeted onto a stationary or moving substrate. By controlling the applied voltage and the relative stage speed of the substrate with respect to the nozzle, EMS results in superior nanowire deposition control. In Figure 1.15, we compare FFES with EMS [59].

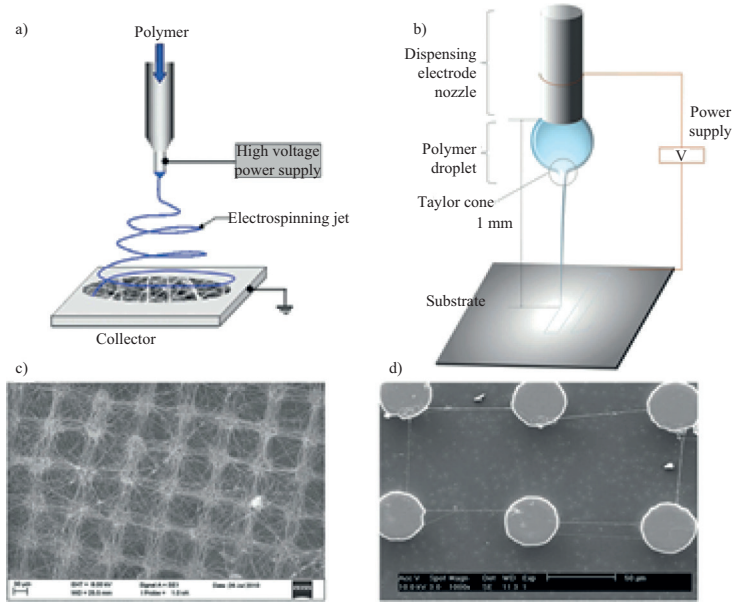

Figure 1.15. FFES (a, c) compared with EMS (b, d). The fibers in Figure 1.15c and 1.15d, when using the correct ink formulation, can subsequently be carbonized, thinning them even further [59].

Now we can combine the photopatterning of SU-8 for making contacts pads with EMS for the suspended nanowires as shown in Figure 1.15d. With the right formulation of the polymer solution, these suspended polymer nanowires can be carbonized, thinning them even further, and glassy carbon contacts can thus be wired together with graphitic EMS electrospun nanofibers.

Such a hybrid microstructure construct is also illustrated in Figure 1.16 in which we show a set of carbonized EMS fibers (graphitic) suspended over a carbon support structure (glassy) that was used to establish the Young's modulus (E) of the CNWs. As shown in the inset of Figure 1.16, these carbon fibers were cut with an FIB to form cantilever beams [62].

A laser Doppler vibrometer was used to measure the natural frequency of the FIB cut nanowires, and using the Euler–Bernoulli beam theory, the Young's modulus as a function of nanowire diameter was derived as shown in Figure 1.17. Just as predicted from the model of Ji et al. [54], the Young's modulus increases very fast as the wire diameter shrinks. At 200 nm, Young's modulus is already up to 400 GPa—this is eight times higher than that for a 1-μm diameter nanowire (carbon nanotubes [CNTs] are between 270 and 950 GPa [1 TPa]). This is a very promising result as

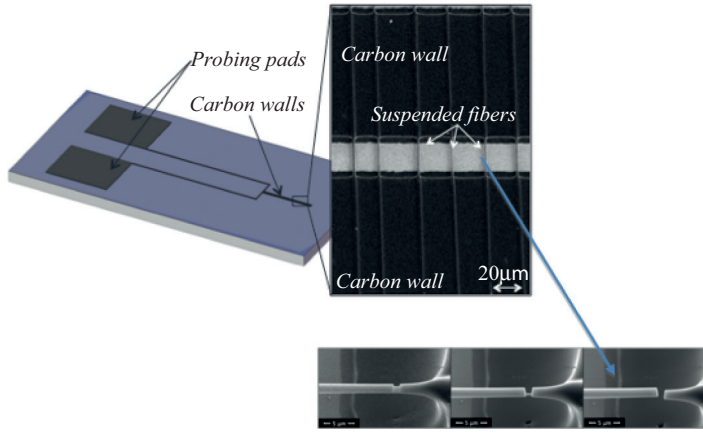

Figure 1.16. Patterned CNWs made by carbonization of nanofiber array of 70 parallel fibers made by continuous EMS. The measured average distance between carbon fibers was 18.6 ± 4.8 µm. Inset: Fibers are cut with a FIB to form cantilever beams [62].

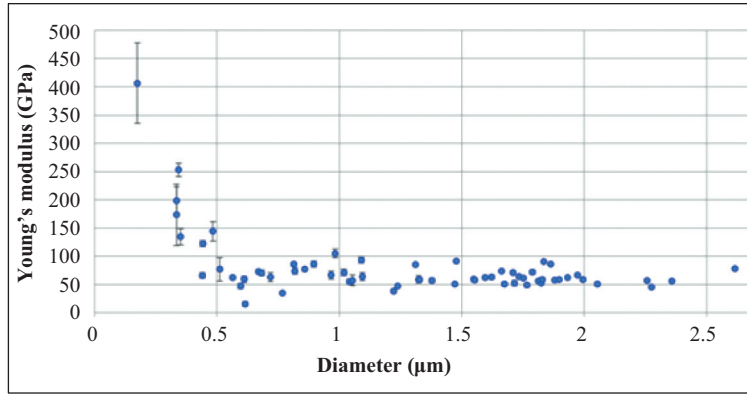

Figure 1.17. Euler–Bernoulli beam theory results for CNWs. At 200 nm, Young's modulus is already up to 400 GPa (CNTs are between 270 and 950 GPa [1 TPa]) [62].

it suggests that CNWs could reach the mechanical performance level of CNTs! As we can make our CNWs very long, this EMS combined with carbonization constitutes a plausible alternative to CNTs that are much harder to make into long *cables*. The maximum conductivity for the same wires is 7×10^4 S/m [62], only a bit more than twice the glassy carbon value (the value of wires obtained with FFES—see earlier information—was very similar at 6.13×10^4 S/m).

1.4 CURRENT AND PROJECTED APPLICATIONS OF C-MEMS AND C-NEMS

Although silicon, human's foremost technological material, is abundant in silicate minerals, carbon is the key to life. It can be argued that carbon, especially with the recent (somewhat frantic) research efforts on CNTs and graphene, is also becoming a more and more important material in human technology. Neither single crystalline nor polycrystalline Si encompasses that wide a range of shapes and microstructures. Some key advantages of carbon compared with Si are summarized in Figure 1.18 [9].

Much has been made of the myriad of applications of just two of the currently most popular carbon allotropes, that is, CNTs [63–69] and graphene [65, 70]. Here we promote the idea that C-MEMS and C-NEMS could eventually, depending on the manufacturing process, incorporate all of the carbon allotropes. In this more holistic view of a world with carbon as the most important technological material, one tailors one allotrope or a combination of allotropes to suit each application.

Some recent examples of C-MEMS and C-NEMS applications include electrochemical sensors [49, 71, 72], substrate for molecular electronics [73–75], batteries [42–44, 76–79], fuel cells [80–83], dielectrophoresis electrodes [84–86], capacitors [27, 35, 87], scaffolds [45, 47], nanoconstrictions [88], hot nanowires for local CVD [36], molds for bulk metallic glasses [89], and gas sensors [90]. Several of these applications

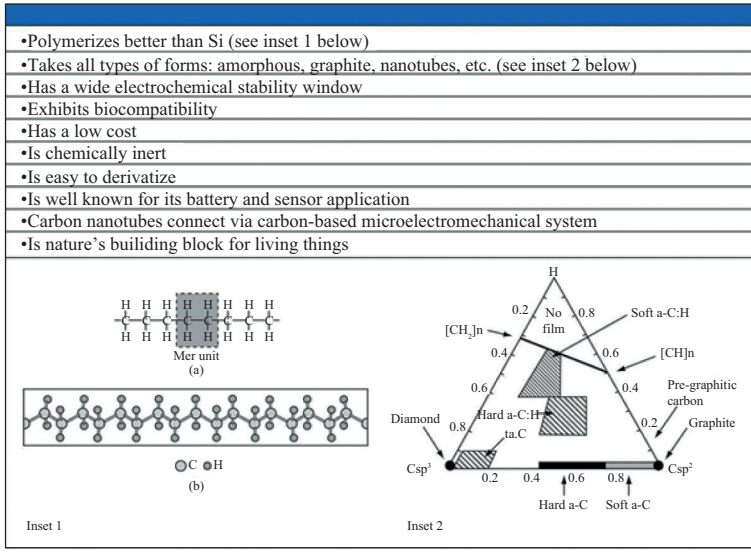

Figure 1.18. Carbon: the next Si? [9].

were also alluded to in the preceding text, and we will single out some of them for more scrutiny in the current section and in subsequent chapters of this book.

Here we limit ourselves to short descriptions of the following three emerging C-MEMS and C-NEMS applications: (i) C-MEMS smart Li-ion batteries, (ii) redox amplifications with carbon interdigitated electrode arrays (IDEAs), and (iii) carbon hot nanowires to make nanogas sensors with local CVD, nanoconstrictions, and nanogaps.

1.4.1 C-MEMS LI-ION BATTERIES

The electrochemical characteristics of carbon produced by pyrolysis of photoresists have been studied to some extent [5]. It is found that electrochemical reactions on pyrolyzed photoresist exhibit kinetics very similar to those on glassy carbon. Glassy carbon electrodes are the gold standard for electrochemists because of their wide electrochemical stability window, low background, and low cost [91]. Also graphite and hard carbons are well known for their utility in Li-ion battery applications because of their Li intercalation or deintercalation capacity [92–95]. Our team established that glassy carbon electrodes produced by carbonization do not only show the same fast kinetics for surface reactions as commercial glassy carbon electrodes [96] but also that they can be intercalated and deintercalated with lithium ions as fast and with as high a capacity as other carbon anodes in commercial Li-ion batteries [31, 78, 97, 98]. The latter observation did set the stage for the introduction of Li-ion batteries based on C-MEMS [99]. The multilevel C-MEMS process described in Figure 1.2 (right panel) was used for making the two-level Li-ion-based C-MEMS battery shown in Figure 1.19 [100]. In the C-MEMS battery depicted here, one layer of carbon constitutes the current collector (20 μm thick) for the rows of anode and cathode posts (250 μm high) made in the second C-MEMS layer. This type of C-MEMS battery holds the promise of changing the battery world in three significant ways [9, 77, 100]:

1. Smarter batteries: C-MEMS batteries contain a multitude of anodes and cathodes (baxels, by analogy to pixels) that are interconnected to provide the optimal current or voltage depending on the application need. This way in-battery smart load leveling is enabled;
2. Faster charging batteries: In charging the C-MEMS battery, Li ions only need to intercalate into the thin individual carbon posts rather than intercalating into one big chunk of carbon;

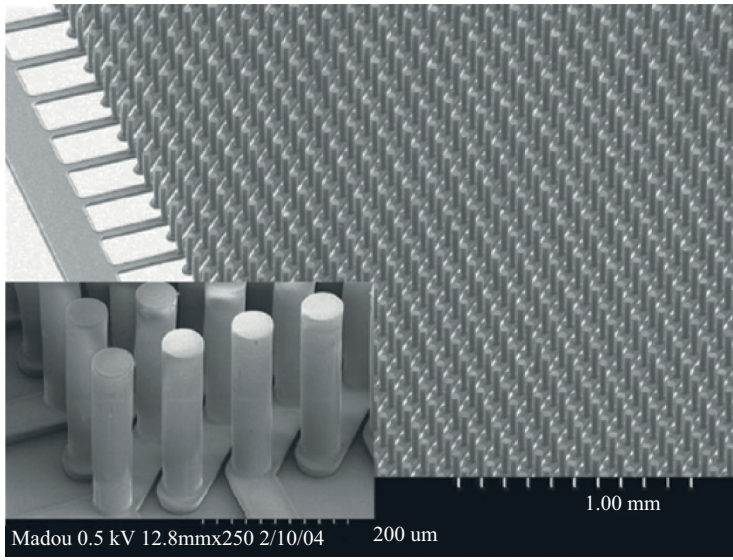

Figure 1.19. Smart Li-ion battery. Typical two-level carbon-based MEMS electrodes with carbon contacts underneath. The inset image shows enlarged SU-8 two-level structure [9].

3. Theoretically, the capacity of the C-MEMS batteries, depending on the aspect ratio of the posts and the thickness of the electrolyte, can be significantly higher than that of current Li-ion batteries [77, 101].

Recently, carbon anodes for Li-ion batteries are combined in clever ways with Si that has yet a higher capacity than carbon but is irreversible [102–104]. By combining these two elements in the correct way, a superior battery that remains reversible can be built, maintaining all the advantages listed earlier and featuring an even higher capacity than when using carbon alone.

1.4.2 REDOX AMPLIFICATION WITH CARBON INTERDIGITATED ELECTRODE ARRAYS

A second recent application of C-MEMS and C-NEMS we are illustrating here is its use in the fabrication of ultramicroelectrodes (UM). UM have become an important tool in electrochemical analysis because the electrochemical signal is determined almost exclusively by diffusion with no or little effect of convection and because the steady-state currents are

achieved very fast owing to the nonlinear diffusion effects that make for more effective mass transport [105]. Most importantly, in UMs, the signal can be amplified through a clever electrode arrangement involving interdigitated working electrodes (generator and collector separated by a narrow gap) (see Figure 1.20). By applying a different potential on the two working electrodes in an IDEA, redox species can be recycled between the electrodes before diffusing away into the bulk of the solution. This recycling results in current amplification. If the electrode gap is small, and especially when the electrodes are high (nonplanar), the redox species may experience multiple redox cycles before diffusing away into the bulk of the solution [106–108]. Better current amplification can be achieved by reducing the electrode gap to the nanometer level by implementing high aspect ratio 3D IDEA electrodes and with a combination of both. To make submicrometer nanogaps, expensive processes such as FIB milling, e-beam lithography, and nanoimprinting are required. However, 3D IDEA electrodes can achieve comparable or better current amplification using more conventional microfabrication technology, which is better for batch fabrication of less expensive commercial sensors. The redox amplification improves the lower limit of detection (LOD) of a simple, inexpensive electrochemical sensor dramatically so much so that it might become competitive with widely used and more expensive and cumbersome optical techniques such as fluorescence sensing.

Today, IDEAs are typically made from noble metals such as thin films of Pt or Au on a Si substrate (see Figure 1.20b [106–108, 114].

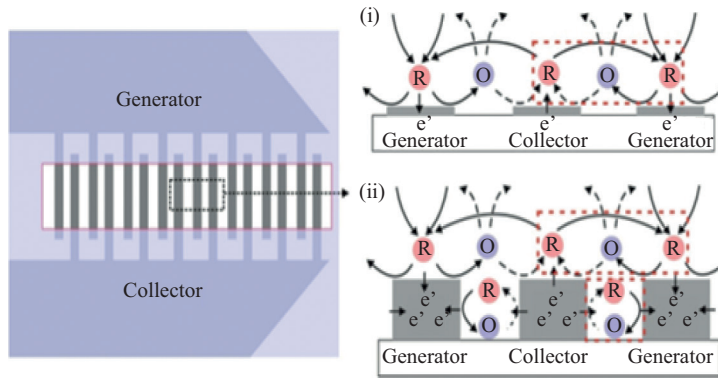

Figure 1.20. IDEAs consist of a pair of comb-shaped electrodes one of which works as a generator and the other as a collector (left panel). Schematic view of redox cycling of oxidized (O) and reduced (R) species in an IDEA: (i) plane electrodes, (ii) 3D electrodes (right panel) [109–113].

These IDEAs require the deposition of a thin layer of a metal adhesion layer (e.g., Cr or Ti) followed by the noble metal layer. The patterning of the noble metal layer requires the use of a cumbersome lift-off process. As two different metals are used, corrosion potentials are hard to avoid. While metal electrodes exhibit a lower electrical resistance than that of carbon, they come with all types of unwanted electrochemical side reactions even at low potentials, while glassy carbon electrodes are stable and come with a wider stability window than any noble metal. C-MEMS and C-NEMS IDEAs are not only much simpler to make (one step process), carbon also is easier to make into a 3D structure (high aspect ratio that benefits redox amplification—see preceding information). As an added benefit, one avoids the corrosion issue by dealing with one material only. Moreover, metal electrodes have lower biocompatibility and a higher fouling propensity compared to carbon electrodes. High aspect ratio metal electrodes, on the other hand, are difficult and expensive to fabricate, especially if nanometer gaps are required. C-MEMS and C-NEMS techniques, on the other hand, excel at reaching both the nanometer dimensions and high—aspect ratios.

Three-dimensional (3D) carbon IDEAs were fabricated in our group by using inexpensive, conventional, UV photolithography of SU-8 with slightly modified exposure and postexposure bake settings followed by pyrolysis in an inert environment (see Figure 1.21) [71]. The redox amplification of sensors made this way was investigated as a function of both the IDEA digit width-to-gap ratio and digit height as a function of potential sweep rate and under flow and no flow conditions. A gradual increase in redox amplification with an increase in the IDEA digit width-to-gap ratio was demonstrated. A maximum amplification of 37 was obtained for a width-to-gap ratio of 1.58 and for an electrode height of 1.1 μm. Redox amplification significantly increased with an increase in the IDEA height, from a factor of 9 at a 0.22 μm digit height to a factor of 37 at a 1.1 μm height. As the sweep rate was decreased from 50 mV/s to 5 mV/s, the collection efficiency increased from 0.92 to 0.97, whereas the amplification increased from 7 to 25. Under flow conditions, the amplification decreases substantially as the cycling of the redox species is impeded by convection. The highest amplification of 37 dropped to 4 at a flow rate of 500 nL/s. Under flow conditions, redox amplification increased with an increase in the IDEA height [71, 115]. This can be understood by the fact that between the electrodes the diffusion paths of cycling redox species are linear and little disturbed by flow, whereas above the electrodes, the diffusion is elliptical and very sensitive to flow (see right panel in Figure 1.20).

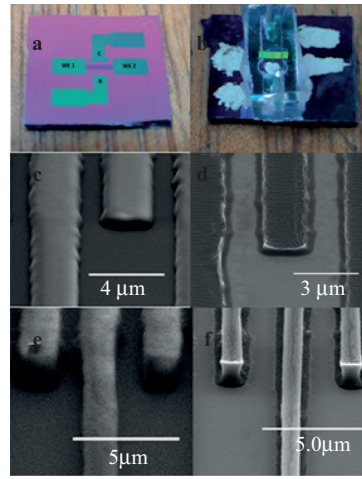

Figure 1.21. (a) Shows the actual 3D carbon IDEA sensor. WE1 and WE2 are contact pads for the generator and the collector, respectively. C and R are counter and reference electrodes, respectively; (b) shows the final device with polydimethylsiloxane flow channels. The reference electrode is coated with Ag or AgCl ink, and contact pads are coated with silver paste for better electrical connection. (c and e) SEM images (tilted view 60°) under 10,000 × magnification of SU-8 IDEA patterning before pyrolysis; height = 0.6 and 2.1 µm, respectively. (d and f) Carbon IDEA after pyrolysis; height = 0.22 and 0.59 µm, respectively [71, 115].

To make the redox amplification even less sensitive to flow, the C-MEMS walls can be made much higher (in the example, walls were only 1.1 µm high).

Voldman et al. experimented with thicker microfabricated nonplanar gold electrode arrays (paired microelectrodes that were 3 µm thick and spaced 10 µm apart) for dielectrophoretic single cell trapping [116, 117]. To fashion the 3D gold electrodes, they used gold electroplating in an SU-8 mold to plate up the thin underlying Au film. These 3D arrangements produce more uniform electrical fields compared to conventional planar microelectrodes and are more efficient at cell trapping just as our 3D IDEAs are more efficient at redox cycling The underlying reason is the same, that is, a higher aspect ratio. But electroplating is cumbersome and expensive compared to the 3D C-MEMS approach, and 3D C-MEMS is now also used in the dielectrophoresis application [86, 118].

1.4.3 CARBON HOT NANOWIRES TO MAKE NANOGAS SENSORS WITH LOCAL CVD, NANOCONSTRICTIONS, AND NANOGAPS

As nanowires are almost all surface and because sensing is usually a surface phenomenon, sensing induced changes on a nanowire has a larger effect on the overall resistivity or impedance of a nanowire than that in the case of a bulk wire and this leads to an improved lower LOD [9]. Suspended CNWs as shown in Figures 1.13 and 1.15 have several further advantages. Suspended nanowires are removed from the supporting substrate, and this leads to significant advantages over other nanowire-based sensors typically embedded on a solid substrate. The suspension arrangement avoids deleterious substrate influences such as contamination and charge shunting. The LOD also further increases because of higher mass transport because of the nonlinear diffusion effects and because the wire can be approached by analyte molecules from all directions. We call this principle wash cloth line sensors, and by derivatizing the CNW surface with a monolayer of sensor molecules (the clothes on the wash line), say protein or DNA molecules, the nanowires can be turned nano-immuno or nano-DNA sensors by monitoring how the binding of the complementary molecules modulates the nanowires's impedance (see Figure 1.22). When coating the CNWs with metal oxide semiconductors (MOS), they can also be turned into nanogas sensors [90, 119–124]. It is the nanogas sensor application we will detail a bit further here, and this brings us to the topic of carbon nano hot wires [36].

Figure 1.22. We compare the suspended nanowire (left) with a wash cloth line (right). By derivatizing the CNW surface with a monolayer of sensor molecules, say proteins or DNA (the clothes on the wash cloth line), these nanowires can be turned into nano-immuno or nano-DNA sensors. The binding of the complementary protein or DNA strands changes the impedance of the nanowire.

In principle, when direct current is applied to a suspended CNW as shown in Figure 1.22 (left panel), the high resistance of the CNW compared to the bulkier supporting C-MEMS contacting electrodes allows for its selective heating, which initiates local CVD on the wires but not on the supporting contact electrodes from any suitable precursor. Local CVD for depositing a metal oxide material for gas sensor applications was first used on CMOS micro hot plates by Semancik et al. [125–128]. However, as the heated area is reduced from the micro to the nano regime, and as one moves from a plate (2D) to a wire (1D), Joule heating becomes much more complicated because of the huge temperature gradient along the wire and the rapid cooling of the nanostructure material [36]. While the suspended CNW remains at a temperature close to that of the contacting electrodes at the contact points (often referred to as *cold points*), its center reaches a much higher temperature and a parabolic temperature profile results [36] (for references discussing Joule heating of metal nanowires consult [129–131]). As an example of MOS deposition that can be used for the fabrication of a NO_x nanogas sensor, we have demonstrated the local CVD on CNWs by depositing a tungsten oxide (WO_3) film from tungsten hexacarbonyl [$W(CO)_6$] as the precursor [36]. WO_3 is a well-known sensitive and selective NO_x sensor material (ammonia and methane are also detected depending on catalyst and temperature used) [132, 133]. SEM images of a 358-nm thick, 30-μm long CNW after WO_3 deposition by local CVD of $W(CO)_6$ are shown in Figure 1.23a and b. The thickness of the deposit follows the temperature profile expected for a heated nanowire with the center being

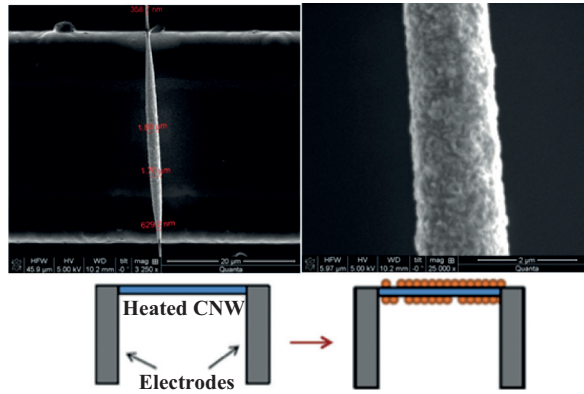

Figure 1.23. (a) SEM images of a 358-nm thick CNW with WO_3 deposited on its surface by selected area CVD, (b) a high-magnification image of the granular surface of WO_3. Inset: schematic of the local CVD process on a suspended nanowire [36].

considerably thicker (diameter of ~1.8 μm) compared to the ends of the CNW (358 nm). The diameter at the center of the wire after deposition as well as the granular nature of the deposited material can be observed in Figure 1.23b, which is a high-magnification micrograph of a central segment of the CNW. The composition of the deposited film was confirmed by Energy Dispersive X-Ray Analysis (EDX) spectroscopy and by evaluating the photoresistive behavior of the deposited material.

The local CVD phenomenon illustrated here is not limited to WO_3 deposition; it can be used to obtain nanowires of any desired material by heating the appropriate precursor gas, volatile liquid, or solid onto a hot CNW. This fabrication technique is compatible with batch manufacturing and offers scalability at low cost that renders it suitable for both research and industrial applications. Joule heating for local CVD on CNWs has the potential to become a useful tool for thermal deposition for the manufacture of all types of nanosensor and nanoelectronics devices.

Controlled Joule heating of suspended nanowires is also intrinsically capable of creating nanoconstrictions and nanogaps. Controlled thinning of CNWs at their center by inducing carbon sublimation might eventually allow one to study the transition from diffusional electron conduction to ballistic conduction as the wire is thinned down to the couple of nanometer range [36, 62, 88]. This way one can manufacture quantum mechanical nanoconstrictions without the need for expensive equipment. The thinning (nanoconstriction) and eventual breakage (nanogaps) of the CNW can be understood as follows. At the beginning of a Joule heating experiment, a central region of the CNW attains the highest temperature, high enough to sublimate some carbon from its surface. If a constant current is imposed, this thinner segment attains the sublimation temperature even faster, as it offers a yet higher resistance, which will lead to yet faster thinning at its center. Finally, when the center cannot withstand further thinning the nanowire breaks. Figure 1.24 shows that the breakage point is not always exactly at the center in the CNW; this is only true for a completely uniform CNW; any imperfection or nick in the carbon wire might have the thinning occur there.

The thinner and shorter the CNW wire, the higher is the temperature gradient and the smaller is the nanogap in its center can be made. Nanogaps (with a dimension of less than 10 nm) in a CNW as described here might have great utility as a building block for molecular electronics, based on molecular interactions in a carbon–molecule–carbon (C-M-C) structure [134–136]. In a C-M-C system, the electronic function will be the property of the molecular structure in the C-M-C chain and can be characterized through I/V measurements. Such a system has the ability to measure and

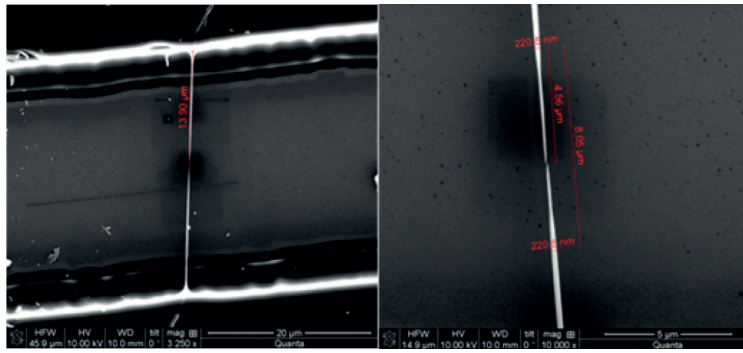

Figure 1.24. SEM images of a 28.3-µm long, 220.5-nm diameter CNW showing breakage due to overheating at its center. The entire CNW with thinning taking place approximately half-way is shown in the panel on the left and the central region of the CNW is illustrated in the panel on the right [36].

to transduce events of specific molecules into useful electrical signals. There are a lot of techniques for obtaining nanogaps, but a process to totally control the gap size has not been found yet.

So far, to use Joule heating of a nanowire to make nanoconstrictions and nanogaps has proven to be difficult; once the thinning process starts, it is difficult to control, and if a constant current is used, the breakage of the CNW takes place very rapidly. Our team is currently developing an electronic control system to control the wire thickness in the center to any desired radius (nanoconstriction) and to make nanogaps of any size. For the fabrication of nanoconstrictions and nanogaps using the nanowire thinning method described here, two requirements must thus be met: (1) exquisite control of the carbon sublimation, which can be achieved by introducing a sophisticated control system in our setup that allows for switching between current and voltage, and (2) creating as short a sublimation zone at the nanowire center as possible, which can be done by tuning the initial CNW length and thickness.

REFERENCES

[1] Youn, S.W., M. Takahashi, H. Goto, and R. Maeda. 2006. "Microstructuring of Glassy Carbon Mold for Glass Embossing–Comparison of Focused Ion Beam, Nano/Femtosecond-Pulsed Laser and Mechanical Machining." *Microelectronic Engineering* 83, no. 11, pp. 2482–92. doi: http://dx.doi.org/10.1016/j.mee.2006.05.007

[2] Hans, L.E., K. Prater, C. Kilchoer, T. Scharf, H.P. Herzig, and A. Hermerschmidt. 2014. *Conference on Advanced Fabrication Technologies for Micro/Nano Optics and Photonics VII*. San Francisco, CA.

[3] Wang, J., B. Tian, V.B. Nascimento, and L. Angnes. 1998. "Performance of Screen-Printed Carbon Electrodes Fabricated from Different Carbon Inks." *Electrochimica Acta* 43, no. 23, pp. 3459–65. doi: http://dx.doi.org/10.1016/s0013-4686(98)00092-9

[4] Madou, M., A. Lai, G. Schmidt, X. Songc, K. Kinoshitac, M. Fendorf, A. Zettl, and R. White. 1997. "Carbon Micromachining (C-Mems)." In *Chemical and Biological Sensors and Analytical Electrochemical Methods: Proceedings of the Symposium on Chemical and Biological Sensors and Analytical Electrochemical Methods*, p. 1961.

[5] Ranganathan, S., R. McCreery, S.M. Majji, and M. Madou. 2000. "Photoresist-Derived Carbon for Microelectromechanical Systems and Electrochemical Applications." *Journal of the Electrochemical Society* 147, no. 1, pp. 277–82. doi: http://dx.doi.org/10.1149/1.1393188

[6] Wang, C.L., G.Y. Jia, L.H. Taherabadi, and M.J. Madou. 2005. "A Novel Method for the Fabrication of High-Aspect Ratio C-MEMS Structures." *Journal of Microelectromechanical Systems* 14, no. 2, pp. 348–58. doi: http://dx.doi.org/10.1109/jmems.2004.839312

[7] Madou, M.J. 2002. *Fundamentals of Microfabrication: The Science of Miniaturization, Second Edition*. Boca Raton, FL: CRC Press.

[8] Madou, M.J. 2011. *Manufacturing Techniques for Microfabrication and Nanotechnology*. Boca Raton, FL: CRC Press.

[9] Madou, M.J. 2011. *From MEMS to Bio-MEMS and Bio-NEMS: Manufacturing Techniques and Applications.* Boca Raton, FL: CRC Press.

[10] Harris†, P.J.F. 2004. "Fullerene-Related Structure of Commercial Glassy Carbons." *Philosophical Magazine* 84, no. 29, pp. 3159–67. doi: http://dx.doi.org/10.1080/14786430410001720363

[11] Jenkins, G.M., and K. Kawamura. 1971. "Structure of Glassy Carbon." *Nature* 231, no. 5299, pp. 175–76. doi: http://dx.doi.org/10.1038/231175a0

[12] Jenkins, G.M. 1976. *Polymeric Carbons—Carbon Fibre, Glass and Char*. Cambridge, New York: Cambridge University Press.

[13] Franklin, R.E. 1951. "The Structure of Graphitic Carbons." *Acta Crystallographica* 4, no. 3, pp. 253–61. doi: http://dx.doi.org/10.1107/s0365110x51000842

[14] Franklin, R.E. 1951. "Crystallite Growth in Graphitizing and Non-Graphitizing Carbons." *Proceedings of the Royal Society A: Mathematical, Physical and Engineering Sciences* 209, no. 1097, pp. 196–218. doi: http://dx.doi.org/10.1098/rspa.1951.0197

[15] Lyons, A.M., C.W. Wilkins, and M. Robbins. 1983. "Thin Pinhole-Free Carbon Films." *Thin Solid Films* 103, no. 4, pp. 333–41. doi: http://dx.doi.org/10.1016/0040-6090(83)90589-8

[16] Schueller, O.J.A., S.T. Brittain, and G.M. Whitesides. 1997. "Fabrication of Glassy Carbon Microstructures by Pyrolysis of Microfabricated Polymeric

Precursors." *Advanced Materials* 9, no. 6, pp. 477–80. doi: http://dx.doi.org/10.1002/adma.19970090604

[17] Schueller, O.J.A., S.T. Brittain, C. Marzolin, and G.M. Whitesides. 1997. "Fabrication and Characterization of Glassy Carbon MEMS." *Chemistry of Materials* 9, no. 6, pp. 1399–406. doi: http://dx.doi.org/10.1021/cm960639v

[18] Lyons, A.M. 1985. "Photodefinable Carbon Films: Electrical Properties." *Journal of Non-Crystalline Solids* 70, no. 1, pp. 99–109. doi: http://dx.doi.org/10.1016/0022-3093(85)90097-3

[19] Lyons, A.M., L.P. Hale, and C.W. Wilkins. 1985. "Photodefinable Carbon Films: Control of Image Quality." *Journal of Vacuum Science & Technology B* 3, no. 1, pp. 447–52. doi: http://dx.doi.org/10.1116/1.583284

[20] Lyons, A.M., C.W. Wilkins, and M. Robbins. 1984. "308. Carbon Films Prepared from a Phenol Formaldehyde Polymer Precursor." *Carbon* 22, no. 2, p. 239. doi: http://dx.doi.org/10.1016/0008-6223(84)90525-6

[21] Wang, C., and M. Madou. 2005. "From MEMS to NEMS with Carbon." *Biosensors and Bioelectronics* 20, no. 10, pp. 2181–187. doi: http://dx.doi.org/10.1016/j.bios.2004.09.034

[22] Ki Bang, L., and L. Liwei. 2003. "Surface Micromachined Glass and Polysilicon Microchannels Using MUMPs." In *Micro Electro Mechanical Systems, 2003.MEMS-03 Kyoto.IEEE The Sixteenth Annual International Conference*, January 19–23, pp. 578–81.

[23] Lee, S.J., W. Shi, P. Maciel, and S.W. Cha. 2003. "University/Government/Industry Microelectronics Symposium, 2003." In *Proceedings of the 15th Biennial*, pp. 389–90.

[24] Wang, C., L. Taherabadi, K. Malladi, and M. Madou. 2005. C, Ni and Si Nanowires Formation by Local CVD and SLS Mechanisms. *Nanotech 2005*, Anaheim, CA.

[25] Wang, C., R. Zaouk, and M. Madou. 2006. "Local Chemical Vapor Deposition of Carbon Nanofibers from Photoresist." *Carbon* 44, no. 14, pp. 3073–77. doi: http://dx.doi.org/10.1016/j.carbon.2006.05.007

[26] Sharma, S., R. Kamath, and M. Madou. 2014. "Porous Glassy Carbon Formed by Rapid Pyrolysis of Phenol-Formaldehyde Resins and Its Performance as Electrode Material for Electrochemical Double Layer Capacitors." *Journal of Analytical and Applied Pyrolysis* 108, pp. 12–18. doi: http://dx.doi.org/10.1016/j.jaap.2014.05.025

[27] Hsia, B., M.S. Kim, M. Vincent, C. Carraro, and R. Maboudian. 2013. "Photoresist-Derived Porous Carbon for On-Chip Micro-Supercapacitors." *Carbon* 57, pp. 395–400. doi: http://dx.doi.org/10.1016/j.carbon.2013.01.089

[28] Wang, S., B. Hsia, C. Carraro, and R. Maboudian. 2014. "High-Performance All Solid-State Micro-Supercapacitor Based on Patterned Photoresist-Derived Porous Carbon Electrodes and an Ionogel Electrolyte." *Journal of Materials Chemistry A* 2, no. 21, pp. 7997–8002. doi: http://dx.doi.org/10.1039/c4ta00570h

[29] Zaouk, R.B. 2008. *Mechanical and Aerospace Engineering*. UC Irvine.

[30] Penmatsa, V., J.H. Yang, Y. Yu, and C. Wang. 2010. "Fabrication of Porous Carbon Micropillars Using a Block Copolymer as Porogen." *Carbon* 48, no. 14, pp. 4109–15. doi: http://dx.doi.org/10.1016/j.carbon.2010.07.019

[31] Sharma, C.S., H. Katepalli, A. Sharma, G.T. Teixidor, and M. Madou. March 25, 2014. "Fabrication of Resorcinol-Formaldehyde Xerogel Based High Aspect Ratio 3-D Hierarchical C-MEMS Structures." *ECS Transactions* 61, no. 7, pp. 45–54. doi: http://dx.doi.org/10.1149/06107.0045ecst.

[32] Sharma, C.S., M.M. Kulkarni, A. Sharma, and M. Madou. 2009. "Synthesis of Carbon Xerogel Particles and Fractal-Like Structures." *Chemical Engineering Science* 64, no. 7, pp. 1536–43. doi: http://dx.doi.org/10.1016/j.ces.2008.12.013

[33] Sharma, C.S., S. Patil, S. Saurabh, A. Sharma, and R. Venkataraghavan. 2009. "Resorcinol-Formaldehyde Based Carbon Nanospheres by Electrospraying." *Bulletin of Materials Science* 32, no. 3, pp. 239–46. doi: http://dx.doi.org/10.1007/s12034-009-0036-6

[34] Teixidor, G.T., R.A. Gorkin, III, P.P. Tripathi, G.S. Bisht, M. Kulkarni, T.K. Maiti, T.K. Battacharyya, J.R. Subramaniam, A. Sharma, B.Y. Park, and M. Madou. 2008. "Carbon Microelectromechanical Systems as a Substratum for Cell Growth." *Biomedical Materials* 3, no. 3, p. 034116. doi: http://dx.doi.org/10.1088/1748-6041/3/3/034116

[35] Kavaliauskas, Z., L. Marcinauskas, and V. Valincius. 2014. "Influence of the Oxygen Plasma Treatment on Carbon Electrode and Capacity of Supercapacitors." *Acta Physica Polonica* A 125, no. 6, pp. 1316–19. doi: http://dx.doi.org/10.12693/aphyspola.125.1316

[36] Sharma, S. 2013. *Microstructural Tuning of Glassy Carbon for Electrical and Electrochemical Sensor Applications* [dissertation]. University of California, Irvine, CA.

[37] Monsur Islam, R.B., S. Sharma, and M.J. Madou. 2013. *Early Career Technical Conference 2013*, pp. 46–52. Birmingham, AL.

[38] Kipling, J.J., J.N. Sherwood, P.V. Shooter, and N.R. Thompson. 1964. "Factors Influencing the Graphitization of Polymer Carbons." *Carbon* 1, no. 3, pp. 315–20. doi: http://dx.doi.org/10.1016/0008-6223(64)90285-4

[39] Oberlin, A. 1984. "Carbonization and Graphitization." *Carbon* 22, no. 6, pp. 521–41. doi: http://dx.doi.org/10.1016/0008-6223(84)90086-1

[40] Wendorff, J.H., S. Agarwal, and A. Greiner. 2012. "Nanofiber Properties." In *Electrospinning*, 69–104. Wiley-VCH Verlag GmbH & Co. KGaA.

[41] Sharma, C.S., A. Sharma, and M. Madou. 2010. "Multiscale Carbon Structures Fabricated by Direct Micropatterning of Electrospun Mats of SU-8 Photoresist Nanofibers." *Langmuir* 26, no. 4, pp. 2218–22. doi: http://dx.doi.org/10.1021/la904078r

[42] Teixidor, G.T., P. Mukherjee, B. Park, and M. Madou. 2009. "Theoretical Evaluation of Fractal-Like Electrode Characteristics for Litium-Ion Batteries." *Meeting Abstracts*, no. 4, pp. 259–59.

[43] Teixidor, G.T., P.P. Mukherjee, and M. Madou. 2008. "Modeling of Fractal Electrodes in Lithium-Ion Batteries." *Meeting Abstracts*, no. 12, pp. 1167–67.

[44] Teixidor, G.T., R.B. Zaouk, B.Y. Park, and M.J. Madou. 2008. "Fabrication and Characterization of Three-Dimensional Carbon Electrodes for Lithium-Ion Batteries." *Journal of Power Sources* 183, no. 2, pp. 730–40. doi: http://dx.doi.org/10.1016/j.jpowsour.2008.05.065

[45] Mitra, J., S. Jain, A. Sharma, and B. Basu. 2013. "Patterned Growth and Differentiation of Neural Cells on Polymer Derived Carbon Substrates with Micro/Nano Structures in Vitro." *Carbon* 65, pp. 140–55. doi: http://dx.doi.org/10.1016/j.carbon.2013.08.008

[46] Teixidor, G.T., R.A. Gorkin, P.P. Tripathi, G.S. Bisht, M. Kulkarni, T.K. Maiti, T. K. Battacharyya, J.R. Subramaniam, A. Sharma, B.Y. Park, and M. Madou. 2008. *Biomedical Materials (Bristol, England)* 3, no. 3, p. 034116. doi: http://dx.doi.org/10.1088/1748-6041/3/3/034116

[47] Amato, L., A. Heiskanen, C. Caviglia, F. Shah, K. Zor, M. Skolimowski, M. Madou, L. Gammelgaard, R. Hansen, E.G. Seiz, M. Ramos, T. Moreno, A. Martínez-Serrano, S.S. Keller, and J. Emnéus. 2014. "Pyrolysed 3D Carbon Scaffolds Induce Spontaneous Differentiation of Human Neural Stem Cells and Facilitate Real-Time Dopamine Detection." *Advanced Functional Materials* 24, no. 44, pp. 7042–52. doi: http://dx.doi.org/10.1002/adfm.201400812

[48] Xu, H., K. Malladi, C. Wang, L. Kulinsky, M. Song, and M. Madou. 2008. "Carbon Post-Microarrays for Glucose Sensors." *Biosensors and Bioelectronics* 23, no. 11, pp. 1637–44. doi: http://dx.doi.org/10.1016/j.bios.2008.01.031

[49] Njagi, J., M.M. Chernov, J.C. Leiter, and S. Andreescu. 2010. "Amperometric Detection of Dopamine in Vivo with an Enzyme Based Carbon Fiber Microbiosensor." *Analytical Chemistry* 82, no. 3, pp. 989–96. doi: http://dx.doi.org/10.1021/ac9022605

[50] Dogan, M., and O. Karatay. 2011. "Modelling of Electrospinning Process at Various Electric Fields." *Micro & Nano Letters* 6, no. 10, pp. 858–62. doi: http://dx.doi.org/10.1049/mnl.2011.0440

[51] Salifu, A.A., B.D. Nury, and C. Lekakou. 2011. "Electrospinning of Nanocomposite Fibrillar Tubular and Flat Scaffolds with Controlled Fiber Orientation." *Annals of Biomedical Engineering* 39, no. 10, pp. 2510–20. doi: http://dx.doi.org/10.1007/s10439-011-0350-1

[52] Viswanadam, G., and G.G. Chase. 2013. "Modified Electric Fields to Control the Direction of Electrospinning Jets." *Polymer* 54, no. 4 pp. 1397–404. doi: http://dx.doi.org/10.1016/j.polymer.2012.12.082

[53] Sharma, S., A. Sharma, Y.K. Cho, and M. Madou. 2012. "Increased Graphitization in Electrospun Single Suspended Carbon Nanowires Integrated with Carbon-MEMS and Carbon-NEMS Platforms." *ACS Applied Materials & Interfaces* 4, no. 1, pp. 34–39. doi: http://dx.doi.org/10.1021/am2014376

[54] Ji, Y., C. Li, G. Wang, J. Koo, S. Ge, B. Li, J. Jiang, B. Herzberg, T. Klein, S. Chen, J.C. Sokolov, and M.H. Rafailovich. 2008. "Confinement-Induced Super Strong PS/MWNT Composite Nanofibers." *EPL (Europhysics Letters)* 84, no. 5, p. 56002. doi: http://dx.doi.org/10.1209/0295-5075/84/56002

[55] Sharma Swati, Y.K.C., and M. Madou. 2010. *Nano-Bio-Tech Montreux*. Montreux 2010.

[56] Chang, C., K. Limkrailassiri, and L. Lin. 2008. "Continuous Near-Field Electrospinning for Large Area Deposition of Orderly Nanofiber Patterns." *Applied Physics Letters* 93, no. 12, p. 123111. doi: http://dx.doi.org/10.1063/1.2975834

[57] Sun, D., C. Chang, S. Li, and L. Lin. 2006. "Near-Field Electrospinning." *Nano Letters* 6, no. 4, pp. 839–42. doi: http://dx.doi.org/10.1021/nl0602701

[58] Bisht, G., G. Canton, A. Mirsepassi, D. Dunn-Rankin, L. Kulinsky, M. Madou. 2011. In *Proceedings of Technologies for Future Micro-Nano Manufacturing*. Napa, CA.

[59] Bisht, G., S. Nesterenko, L. Kulinsky, and M. Madou. 2012. "A Computer-Controlled Near-Field Electrospinning Setup and Its Graphic User Interface for Precision Patterning of Functional Nanofibers on 2D and 3D Substrates." *Journal of Laboratory Automation* 17, no. 4, pp. 302–08. doi: http://dx.doi.org/10.1177/2211068212446372

[60] Bisht, G.S., G. Canton, M. Madou, A. Mirsepassi, and D. Dunn-rankin. 2012. *Low Voltage Near-Field Electrospinning Method and Device*.

[61] Bisht, G.S., G. Canton, A. Mirsepassi, L. Kulinsky, S. Oh, D. Dunn-Rankin, and M.J. Madou. 2011. "Controlled Continuous Patterning of Polymeric Nanofibers on Three-Dimensional Substrates Using Low-Voltage Near-Field Electrospinning." *Nano Letters* 11, no.4, pp. 1831–37. doi: http://dx.doi.org/10.1021/nl2006164

[62] Canton, G. 2014. *Development of Electro-Mechanical Spinning for Controlled Deposition of Carbon Nanofibers* [PhDThesis]. Irvine, CA: Mechanical and Aerospace Engineering, University of California.

[63] Harrison, B.S., and A. Atala. 2007. "Carbon Nanotube Applications for Tissue Engineering." *Biomaterials* 28, no. 2, pp. 344–53. doi: http://dx.doi.org/10.1016/j.biomaterials.2006.07.044

[64] He, H., L.A. Pham-Huy, P. Dramou, D. Xiao, P. Zuo, and C. Pham-Huy. 2013. "Carbon Nanotubes: Applications in Pharmacy and Medicine." *BioMed Research International* 2013, p. 12. doi: http://dx.doi.org/10.1155/2013/578290

[65] Liang, F., and B. Chen. 2010. "A Review on Biomedical Applications of Single-Walled Carbon Nanotubes." *Current Medicinal Chemistry* 17, no. 1, pp. 10–24. doi: http://dx.doi.org/10.2174/092986710789957742

[66] Yang, W., P. Thordarson, J.J. Gooding, S.P. Ringer, and F. Braet. 2007. "Carbon Nanotubes for Biological and Biomedical Applications." *Nanotechnology* 18, no. 41, p. 412001. doi: http://dx.doi.org/10.1088/0957-4484/18/41/412001

[67] Rao, S.S., A. Stesmans, D.V. Kosynkin, A. Higginbotham, and J.M. Tour. 2011. "Paramagnetic Centers in Graphene Nanoribbons Prepared from Longitudinal Unzipping of Carbon Nanotubes." *New Journal of Physics* 13, no. 11, p. 113004. doi: http://dx.doi.org/10.1088/1367-2630/13/11/113004

[68] Sulong, A.B., N. Muhamad, J. Sahari, R. Ramli, M.D. Baba, and J. Park. 2009. "Electrical Conductivity Behaviour of Chemical Functionalized MWCNTs Epoxy Nanocomposites." *European Journal of Scientific Research* 29, no. 1, pp. 13–21.

[69] De Volder, M.F.L., S.H. Tawfick, R.H. Baughman, and A.J. Hart. 2013. "Carbon Nanotubes: Present and Future Commercial Applications." *Science* 339, no. 6119, pp. 535–39. doi: http://dx.doi.org/10.1126/science.1222453

[70] Randviir, E.P., D.A.C. Brownson, and C.E. Banks. 2014. "A Decade of Graphene Research: Production, Applications and Outlook." *Materials Today* 17, no. 9, pp. 426–32. doi: http://dx.doi.org/10.1016/j.mattod.2014.06.001

[71] Kamath, R.R., M.J. Madou. 2014. "Three-Dimensional Carbon Interdigitated Electrode Arrays for Redox-Amplification." *Analytical Chemistry* 86, no. 6, pp. 2963–71. doi: http://dx.doi.org/10.1021/ac4033356

[72] Mardegan, A., R. Kamath, S. Sharma, P. Scopece, P. Ugo, and M. Madou. 2013. "Optimization of Carbon Electrodes Derived from Epoxy-based Photoresist." *Journal of the Electrochemical Society* 160, no. 8, B132–37. doi: http://dx.doi.org/10.1149/2.107308jes

[73] Anariba, F., and R.L. McCreery. 2002. "Electronic Conductance Behavior of Carbon-Based Molecular Junctions with Conjugated Structures." *The Journal of Physical Chemistry B* 106, no. 40, pp. 10355–62. doi: http://dx.doi.org/10.1021/jp026285e

[74] Ranganathan, S., I. Steidel, F. Anariba, and R.L. McCreery. 2001. "Covalently Bonded Organic Monolayers on a Carbon Substrate: A New Paradigm for Molecular Electronics." *Nano Letters* 1, no. 9, pp. 491–94. doi: http://dx.doi.org/10.1021/nl015566f

[75] Solak, A.O., S. Ranganathan, T. Itoh, and R.L. McCreery. 2002. "A Mechanism for Conductance Switching in Carbon-Based Molecular Electronic Junctions." *Electrochemical and Solid-State Letters* 5, no. 8, pp. E43–46. doi: http://dx.doi.org/10.1149/1.1490716

[76] Galobardes, F., C. Wang, and M. Madou. 2006. "Investigation on the Solid Electrolyte Interface Formed on Pyrolyzed Photoresist Carbon Anodes for C-MEMS Lithium-Ion Batteries." *Diamond and Related Materials* 15, no. 11–12, pp. 1930–34. doi: http://dx.doi.org/10.1016/j.diamond.2006.08.015

[77] Long, J.W., B. Dunn, D.R. Rolison, and H.S. White. 2004. "Three-Dimensional Battery Architectures." *Chemical Reviews* 104, no. 10, pp. 4463–92. doi: http://dx.doi.org/10.1021/cr020740l

[78] Sharma, S., A. Khalajhedayati, T.J. Rupert, and M.J. Madou. 2014. "SU8 Derived Glassy Carbon for Lithium Ion Batteries." *ECS Transactions* 61, no.7, pp. 75–84. doi: http://dx.doi.org/10.1149/06107.0075ecst

[79] Turon Teixidor, G., B.Y. Park, P.P. Mukherjee, Q. Kang, and M.J. Madou. 2009. "Modeling Fractal Electrodes for Li-Ion Batteries." *Electrochimica Acta* 54, no. 24, pp. 5928–36. doi: http://dx.doi.org/10.1016/j.electacta.2009.05.060

[80] Wang, Y., K.S. Chen, J. Mishler, S.C. Cho, and X.C. Adroher. 2011. "A Review of Polymer Electrolyte Membrane Fuel Cells: Technology, Applications, and Needs on Fundamental Research." *Applied Energy* 88, no. 4, pp. 981–1007. doi: http://dx.doi.org/10.1016/j.apenergy.2010.09.030

[81] Wang, Y., L. Pham, G.P.S.de. Vasconcellos, and M. Madou. 2010. "Fabrication and Characterization of Micro PEM Fuel Cells Using Pyrolyzed Carbon Current Collector Plates." *Journal of Power Sources* 195, no. 15, pp. 4796–803. doi: http://dx.doi.org/10.1016/j.jpowsour.2010.02.050

[82] Park, B.Y., and M.J. Madou. 2006. "Design, Fabrication, and Initial Testing of a Miniature PEM Fuel Cell with Micro-Scale Pyrolyzed Carbon Fluidic Plates." *Journal of power sources* 162, no. 1, pp. 369–79. doi: http://dx.doi.org/10.1016/j.jpowsour.2006.06.077

[83] Park, B.Y., and M.J. Madou. 2006. *The Sixth International Workshop on Micro and Nanotechnology for Power Generation and Energy Conversion Applications.* University of California, Berkeley, CA.

[84] Rouabah, H. A., B.Y. Park, R.B. Zaouk, M.J. Madou, and N.G. Green. 2008. "Producing Fluid Flow Using 3D Carbon Electrodes." *Journal of Physics: Conference Series* 142, no. 1, p. 012072. doi: http://dx.doi.org/10.1088/1742-6596/142/1/012072

[85] Martinez-Duarte, R., R.A. Gorkin Iii, K. Abi-Samra, and M.J. Madou. 2010. "The Integration of 3D Carbon-Electrode Dielectrophoresis on a CD-Like Centrifugal Microfluidic Platform." *Lab on a Chip* 10, no. 8, pp. 1030–43. doi: http://dx.doi.org/10.1039/b925456k

[86] Martinez-Duarte, R., P. Renaud, and M.J. Madou. 2011. "A Novel Approach to Dielectrophoresis Using Carbon Electrodes." *Electrophoresis* 32, no. 17, pp. 2385–92. doi: http://dx.doi.org/10.1002/elps.201100059

[87] Beidaghi, M., W. Chen, and C. Wang. 2011. "Electrochemically Activated Carbon Micro-Electrode Arrays for Electrochemical Micro-Capacitors." *Journal of Power Sources* 196, no. 4, pp. 2403–09. doi: http://dx.doi.org/10.1016/j.jpowsour.2010.09.050

[88] Mendoza-Buenrostro, C. 2013. *Development and Characterization of Suspended Carbon Fiber Nanoconstriction, Nanogap, Incandescence, and Deformation Effects Induced by Electric Currents* [PhDThesis]. Monterrey, NL, Mexico: Electric and Computer Engineering, Tecnologico de Monterrey.

[89] Schroers, J., G. Kumar, M. Madou, and R. Martinez-Duarte. 2010. *Carbon Molds for Use in the Fabrication of Bulk Metallic Glass Parts and Molds*. Google Patents.

[90] Sharma, S., and M. Madou. "A New Approach to Gas Sensing with Nanotechnology." *Philosophical Transactions of the Royal Society A: Mathematical, Physical and Engineering Sciences* 370, no. 1967, pp. 2448–73. doi: http://dx.doi.org/10.1098/rsta.2011.0506

[91] Pocard, N.L., D.C. Alsmeyer, R.L. McCreery, T.X. Neenan, and M.R., Callstrom. 1992. "Feature Articles. Doped Glassy Carbon: A New Material for Electrocatalysis." *Journal of Materials Chemistry* 2, no. 8, pp. 771–84. doi: http://dx.doi.org/10.1039/jm9920200771

[92] Fong, R., U.von Sacken, and J.R. Dahn. 1990. "Studies of Lithium Intercalation into Carbons Using Nonaqueous Electrochemical Cells." *Journal of The Electrochemical Society* 137, no. 7, pp. 2009–13. doi: http://dx.doi.org/10.1149/1.2086855

[93] Guerard, D., and A. Herold. 1975. "Intercalation of Lithium into Graphite and Other Carbons." *Carbon* 13, no. 4, pp. 337–45. doi: http://dx.doi.org/10.1016/0008-6223(75)90040-8

[94] Kostecki, R., and F. McLarnon. 2003. "Microprobe study of the Effect of Li Intercalation on the Structure of Graphite." *Journal of Power Sources* 119–121, pp. 550–54. doi: http://dx.doi.org/10.1016/s0378-7753(03)00287-8

[95] Shu, Z.X., R.S. McMillan, and J.J. Murray. 1993. "Electrochemical Intercalation of Lithium into Graphite." *Journal of The Electrochemical Society* 140, no. 4, pp. 922–27. doi: http://dx.doi.org/10.1149/1.2056228

[96] Ranganathan, S., R. McCreery, S.M. Majji, and M. Madou. 2000. "Photoresist-Derived Carbon for Microelectromechanical Systems and Electrochemical Applications." *Journal of the Electrochemical Society* 147, no. 1, pp. 277–82. doi: http://dx.doi.org/10.1149/1.1393188

[97] Kinoshita, K., X. Song, J. Kim, and M. Inaba. 1999. "Development of a Carbon-Based Lithium Microbattery." *Journal of Power Sources* 81–82, pp. 170–75. doi: http://dx.doi.org/10.1016/s0378-7753(99)00189-5

[98] Turon-Teixidor, G., C. Wang, and M. Madou. 2006. "Fabrication of 3D Carbon Microelectrodes for Li-Ion Battery Applications." In *Proceedings of the NSTI 2006 Conference*. Boston, MA.

[99] Min, H.-S., B.Y. Park, L. Taherabadi, C. Wang, Y. Yeh, R. Zaouk, M. Madou, and B. Dunn. 2008. "Fabrication and Properties of a Carbon/Polypyrrole Three-Dimensional Microbattery." *Journal of Power Sources* 178, no. 2, pp. 795–800. doi: http://dx.doi.org/10.1016/j.jpowsour.2007.10.003

[100] Wang, C., L. Taherabadi, G. Jia, M. Madou, Y. Yeh, and B. Dunn. 2004. "C-MEMS for the Manufacture of 3D Microbatteries." *Electrochemical and Solid-State Letters* 7, no. 11, p. A435. doi: http://dx.doi.org/10.1149/1.1798151

[101] Wang, C., F.G. Jornet, G.T. Teixidor, R. Zaouk, and M. Madou. June 30, 2006. "C-MEMS for on-Chip Miniaturized Energy Source." *Meeting Abstracts*, vol. MA2006-02, p. 1202.

[102] Yoshio, M., H. Wang, K. Fukuda, T. Umeno, N. Dimov, and Z. Ogumi. 2002. "Carbon-Coated Si as a Lithium-Ion Battery Anode Material." *Journal of The Electrochemical Society* 149, no. 12, pp. A1598–603. doi: http://dx.doi.org/10.1149/1.1518988

[103] Cui, L.F., Y. Yang, C.M. Hsu, and Y. Cui. 2009. "Carbon−Silicon Core−Shell Nanowires as High Capacity Electrode for Lithium Ion Batteries." *Nano Letters* 9, no. 9, pp. 3370–74. doi: http://dx.doi.org/10.1021/nl901670t

[104] Bridel, J.S., T. Azaïs, M. Morcrette, J.M. Tarascon, and D. Larcher. 2010. "Key Parameters Governing the Reversibility of Si/Carbon/CMC Electrodes for Li-Ion Batteries †" *Chemistry of Materials* 22, no. 3, pp. 1229–41. doi: http://dx.doi.org/10.1021/cm902688w

[105] Heinze, J. 1993. "Ultramicroelectrodes in Electrochemistry." *Angewandte Chemie International Edition in English* 32, no. 9, pp. 1268–88. doi: http://dx.doi.org/10.1002/anie.199312681

[106] Lewis, P.M., L.B. Sheridan, R.E. Gawley, I. Fritsch. 2010. "Signal Amplification in a Microchannel from Redox Cycling with Varied Electroactive Configurations of an Individually Addressable Microband Electrode Array." *Analytical Chemistry* 82, no. 5, pp. 1659–68. doi: http://dx.doi.org/10.1021/ac901066p

[107] Takahashi, S., M. Futagawa, M. Ishida, K. Sawada. 2013. "Proposition and Fabrication of Amplified Redox Sensor (ARS) for High Sensitive Chemical Analysis." In Solid-State Sensors, Actuators and Microsystems (TRANSDUCERS & EUROSENSORS XXVII), 2013 Transducers & Eurosensors XXVII: The 17th International Conference.

[108] Takahashi, S., M. Futagawa, M. Ishida, and K. Sawada. 2014. "Directly Amplified Redox Sensor for On-Chip Chemical Analysis." *Japanese Journal of Applied Physics* 53, no. 3, p. 036702. doi: http://dx.doi.org/10.7567/jjap.53.036702

[109] Heo, J.-I., Y. Lim, B. Lee, M. Madou, and H. Shin. 2012. "Development of a Carbon Microchannel Integrated with a Horizontal Carbon Sandwich Electrode Pair for Ultra Sensitive Electrochemical/Bio Sensors." In *16th International Conference on Miniaturized Systems for Chemistry and Life Sciences*, pp. 1240–42. Okinawa, Japan.

[110] Jeong-II, H., L. Yeongjin, M. Madou, and S. Heungjoo. 2012. "Scalable Suspended Carbon Nanowire Meshes as Ultrasensitive Electrochemical Sensing Platforms." In *Micro Electro Mechanical Systems (MEMS), IEEE 25th International Conference*, January 29–February 2, pp. 878–81.

[111] Heo, J.-I., M. Madou, and H. Shin. 2011. "Scalable Monolithic Suspended Carbon Nanowire Array Systems as Ultrasensitive Electrochemical Sensing Platforms." In *15th International Conference on Miniaturized Systems for Chemistry and Life Sciences*, pp. 1971–73. Seattle, Washington, USA.

[112] Heo, J.-I., D.-S. Shim, R. Martinez-Duarte, M. Madou, and H. Shin. 2010. "3-D Carbon Interdigitated Array Nanoelectrodes for Highly Sensitive Sensing of Neurotransmitters." In *14th International Conference on Miniaturized Systems for Chemistry and Life Sciences, MicroTAS 2010*, pp. 1976–78. Groningen, Netherlands.

[113] Heo, J.I., D.S. Shim, G.T. Teixidor, S. Oh, M.J. Madou, and H. Shin. 2011. "Carbon Interdigitated Array Nanoelectrodes for Electrochemical Applications." *Journal of the Electrochemical Society* 158, no. 3, pp. J76–80. doi: http://dx.doi.org/10.1149/1.3531952

[114] Wollenberger, U., M. Paeschke, and R. Hintsche, 1994. "Interdigitated Array Microelectrodes for the Determination of Enzyme Activities." *Analyst* 119, no. 6, pp. 1245–49. doi: http://dx.doi.org/10.1039/an9941901245

[115] Kamath, R.R., and M.J. Madou. 2014. "Selective Detection of Dopamine Against Ascorbic Acid Interference Using 3D Carbon Interdigitated Electrode Arrays." *ECS Transactions* 61, no. 7, pp. 65–73. doi: http://dx.doi.org/10.1149/06107.0065ecst

[116] Voldman, J. 2007. "Dielectrophoretic Traps for Cell Manipulation." In *BioMEMS and Biomedical Nanotechnology*, eds. M. Ferrari, R. Bashir, and S. Wereley, 159–86. Springer US.

[117] Voldman, J., M.L. Gray, M. Toner, and M.A. Schmidt. 2002. "A Microfabrication-Based Dynamic Array Cytometer." *Analytical Chemistry* 74, no. 16, pp. 3984–90.doi: http://dx.doi.org/10.1021/ac0256235

[118] Martinez-Duarte, R., R.A. Gorkin Iii, K. Abi-Samra, and M.J. Madou, 2010. "The Integration of 3D Carbon-Electrode Dielectrophoresis on a CD-Like Centrifugal Microfluidic Platform." *Lab on a Chip* 10, no. 8, p.1030–43. doi: http://dx.doi.org/10.1039/b925456k

[119] Barsan, N., and U. Weimar. 2001. "Conduction Model of Metal Oxide Gas Sensors." *Journal of Electroceramics* 7, no. 3, pp. 143–67. doi: http://dx.doi.org/10.1023/a:1014405811371

[120] Barsan, N., and U. Weimar. 2003. "Understanding the Fundamental Principles of Metal Oxide Based Gas Sensors; the Example of CO Sensing with SnO 2 Sensors in the Presence of Humidity." *Journal of Physics: Condensed Matter* 15, no. 20, pp. R813–39. doi: http://dx.doi.org/10.1088/0953-8984/15/20/201

[121] Basu, S., and P.K. Basu. 2009. "Nanocrystalline Metal Oxides for Methane Sensors: Role of Noble Metals." *Journal of Sensors* 2009, no. 1, pp. 1–20. doi: http://dx.doi.org/10.1155/2009/861968

[122] Simon, I., N. Bârsan, M. Bauer, and U. Weimar. 2001. "Micromachined Metal Oxide Gas Sensors: Opportunities to Improve Sensor Performance." *Sensors and Actuators B: Chemical* 73, no. 1, pp. 1–26. doi: http://dx.doi.org/10.1016/s0925-4005(00)00639-0

[123] Wang, C., L. Yin, L. Zhang, D. Xiang, and R. Gao. 2010. "Metal Oxide Gas Sensors: Sensitivity and Influencing Factors." *Sensors* 10, no. 3, pp. 2088–106. doi: http://dx.doi.org/10.3390/s100302088

[124] Wang, X., W.P. Carey, and S.S. Yee. 1995. "Monolithic Thin-Film Metal-Oxide Gas-Sensor Arrays with Application to Monitoring of Organic Vapors." *Sensors and Actuators B: Chemical* 28, no. 1, pp. 63–70. doi: http://dx.doi.org/10.1016/0925-4005(94)01531-l

[125] Semancik, S., R.E. Cavicchi, K.G. Kreider, J.S. Suehle, and P. Chaparala. 1996. "Selected-Area Deposition of Multiple Active Films for Conductometric Microsensor Arrays." *Sensors and Actuators B: Chemical* 34, no. 1–3, pp. 209–12. doi: http://dx.doi.org/10.1016/s0925-4005(96)01823-0

[126] Semancik, S., R.E. Cavicchi, M.C. Wheeler, J.E. Tiffany, G.E. Poirier, R.M. Walton, J.S. Suehle, B. Panchapakesan, and D.L. DeVoe. 2001. "Microhotplate Platforms for Chemical Sensor Research." *Sensors and Actuators B: Chemical* 77, no. 1–2, pp. 579–91. doi: http://dx.doi.org/10.1016/s0925-4005(01)00695-5

[127] Benkstein, K.D., C.J. Martinez, G. Li, D.C. Meier, C.B. Montgomery, and S. Semancik. 2006. "Integration of Nanostructured Materials with MEMS Microhotplate Platforms to Enhance Chemical Sensor Performance." *Journal of Nanoparticle Research* 8, no. 6, pp. 809–22. doi: http://dx.doi.org/10.1007/s11051-005-9019-8

[128] Cavicchi, R.E., S. Semancik, R.M. Walton, B. Panchapakesan, D.L. DeVoe, M.I. Aquino-Class, J.D. Allen, and J.S. Suehle.1999. "Microhotplate Gas Sensor Arrays." In *Proc. SPIE 3857, Chemical Microsensors and Applications II*, pp. 38–49.

[129] Fangohr, H., D.S. Chernyshenko, M. Franchin, T. Fischbacher, and G. Meier. 2011. "Joule Heating in Nanowires." *Physical Review B* 84, no. 5. doi: http://dx.doi.org/10.1103/physrevb.84.054437

[130] Tohmyoh, H., and S. Fukui. 2012. "Manipulation and Joule Heat Welding of Ag Nanowires Prepared by Atomic Migration." *Journal of Nanoparticle Research* 14, no. 9. doi: http://dx.doi.org/10.1007/s11051-012-1116-x

[131] Léonard, F. 2011. "Reduced Joule Heating in Nanowires." *Applied Physics Letters* 98, no. 10, p. 103101. doi: http://dx.doi.org/10.1063/1.3561772

[132] Ashraf, S., C.S. Blackman, S.C. Naisbitt, and I.P. Parkin. 2008. "The Gas-Sensing Properties of WO 3− x Thin Films Deposited via the Atmospheric Pressure Chemical Vapour Deposition (APCVD) of WCl 6 with Ethanol." *Measurement Science and Technology* 19, no. 2, p. 025203. doi: http://dx.doi.org/10.1088/0957-0233/19/2/025203

[133] Zhao, Y.M., and Y.Q. Zhu. 2009. "Room Temperature Ammonia Sensing Properties of W18O49 Nanowires." *Sensors and Actuators B: Chemical* 137, no. 1, pp. 27–31. doi: http://dx.doi.org/10.1016/j.snb.2009.01.004

[134] Fischbein, M.D., and M. Drndić. 2006. "Nanogaps by Direct Lithography for High-Resolution Imaging and Electronic Characterization of Nanostructures." *Applied Physics Letters* 88, no. 6, p. 193106. doi: http://dx.doi.org/10.1063/1.2172292

[135] Motto, P., A. Dimonte, I. Rattalino, D. Demarchi, G. Piccinini, and P. Civera. 2012. "Nanogap Structures for Molecular Nanoelectronics." *Nanoscale Research Letters* 7, no. 1, pp. 1–9. doi: http://dx.doi.org/10.1186/1556-276x-7-113

[136] Tang, Q., Y. Tong, T. Jain, T. Hassenkam, Q. Wan, K. Moth-Poulsen, and T. Bjørnholm. 2009. "Self-Assembled Nanogaps for Molecular Electronics." *Nanotechnology* 20, no. 24, p. 245205. doi: http://dx.doi.org/10.1088/0957-4484/20/24/245205

CHAPTER 2

THE BEAUTIFUL WORLD OF CARBON

Sharifah Bee Abd Hamid[1], Samira Bagheri[1], Gabriele Centi[2], and Siglinda Perathoner[2]

University of Malaya, Malaysia[1]; University of Messina, Italy[2]

2.1 INTRODUCTION

Carbon is a very versatile material that, depending on its hybridization and assembly in a one-, two-, or three-dimensional network, exhibits important mechanical, optoelectronic, and chemical properties. Because of its versatility, carbon has found numerous applications, for example, it is found in printer inks, pencils, water purification systems, and thermal isolation and antistatic materials. More elaborate carbon materials such as carbon nanotubes (CNTs), graphene, fullerenes, and nanodiamond are used in sensing, electronic, or field emission applications. In addition, carbon materials with tunable microstructure and surface chemical properties are well suited as catalyst supports and the growth of secondary carbon nanofilaments onto a carbon fiber support is of special interest for composites, electronic, and porous macroshaped carbon materials.

2.2 CARBON MATERIALS

Carbon, because of its flexibility of bonding with other elements, forms the basis of organic chemistry and thus life itself, and the flexibility of carbon–carbon bonding in three different geometries gives molecular and solid carbon materials a broad range of properties to be exploited in various

applications [1–9] including microelectromechanical systems (MEMS) and related devices [10–14]. Carbon materials range from nonporous to highly porous, from amorphous to crystalline, from zero dimensional to three dimensional, from insulator to semiconductor and conductor, and from hydrophobic to hydrophilic surfaces. The combination of the three geometries to form carbon–carbon bonds allows for almost unlimited possibilities of carbon materials, each with unique properties. Carbon materials can be tailored further by introduction of controlled defects and heteroatoms such as O, N, and B [15–19]. Not surprisingly, carbon materials have significant economical, industrial, and technological importance today. For example, the global market for CNTs is about $700M to $800M (around 2,500 tons per year of production capacity), and the value is forecast to increase over $1.1B by 2016 at a compound annual growth rate of 10.5 percent. Electrical and electronics industries accounted for 10 percent of the CNTs market share, followed by energy (8 percent), while the largest part of the market (about 70 percent) is accounted for by plastics and composites.

Carbon is the sixth element in the periodic table and its ground electronic state has a $1s^2 2s^2 2p^2$ configuration. The carbon atom hybridized orbitals account for the sp^3, sp^2, and sp^1 configurations of tetrahedral, trigonal, and linear symmetries, respectively. The sp^3 hybridization is the basis for diamond and aliphatic compounds, the sp^2 hybridization for graphite and aromatic compounds, and the sp^1 for carbyne and two-dimensional ordered linear-chain carbon. The combination of these hybridizations in carbon materials is the underlying focus of interest for the synthesis of carbon–MEMS, as it has a profound effect on their properties. For instance, diamond, being sp^3 hybridized and featuring a tetrahedral geometry, is an isotropic material, transparent, super hard, and with negligible electronic conductivity. Graphite, on the other hand, with sp^2 hybridization is an anisotropic and soft material and a semimetal only within the basal plane. In Figure 2.1, we show the unit cell of graphite [20]. The internuclear bond lengths of different hybridizations are different and produce different chemical and physical properties. For example, the basal plane of graphite is inert and as strong as diamond, whereas the interplanar bonds are very weak, making graphite a soft and lubricant material. Chemical reactivity is also profoundly different for the basal and the prismatic edge planes in graphite. So one expects combustion in perfect graphite to start at the prismatic edges. These anisotropies in graphite are the result of its trigonal geometry, and a geometrical change in homonuclear carbon materials (e.g., by introducing vacancies, defects, bending, or the presence of pentagon or heptagon rings within the hexagonal ring network in graphite) alters the graphite properties profoundly. Along

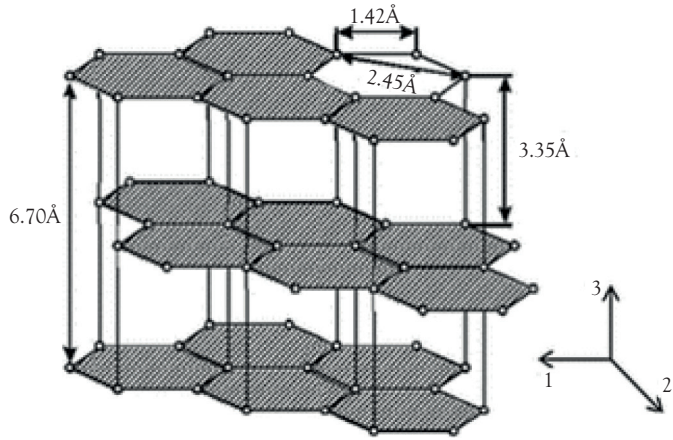

Figure 2.1. The structure of hexagonal graphite with trigonal geometry from sp^2 hybridization [20].

the same line, the broad range of heteroelements that can be incorporated in carbon materials, because of the moderate electronegativity of carbon, is able to modify its electronic properties.

Weak interplanar forces in graphite allow for the swelling and the intercalation of atoms and molecules. Depending on the electronic character of the intercalating elements (donor or acceptor), the electronic properties of the intercalated graphite are modified. Graphite intercalated with SbF_5 and Li are two examples of this type of materials, which have been used as highly conductive materials and in battery applications [21].

As pointed out earlier, three different hybridizations of carbon exist (sp^3, sp^2, and sp^1), resulting in a large variety of nanocarbon structures with diamond, graphene, and carbyne (pure nonmixed materials) as limiting cases, respectively. With the term nanocarbon [9], we capture the broad range of carbon materials having a tailored nanoscale dimension and functional properties that significantly depend on their nanoscale features. CNTs and graphene belong to this class of materials and also nanofibers, nanocoils, nanodiamonds, nanohorns, nanoonions, and fullerenes. We thus make a distinction between nanocarbons and the more *conventional* type of carbon materials, including activated carbon (AC) and other types of porous carbon materials (such as mesoporous carbon materials [22] and carbon aerogels [23]) often utilized as adsorbents and catalysts supports, and the common type of carbon materials utilized in electrodes(such as glassy carbon [GC]) [24], graphite and related materials (pyrolytic and flake graphite and graphitic carbon), and carbon black [25, 26].

Figure 2.2 shows a simplified classification scheme of carbon materials based on the hybridization of the constituent carbon atoms [27]. Although this figure shows only some of the possible carbon materials, it clearly demonstrates that the range of carbon materials is broad, each with different physicochemical properties and functional behavior. As an example, carbyne under tension is about twice as stiff as the previously known stiffest materials (CNTs and graphene, about 4.5×10^8 N·m/kg; almost threefold, over diamond, 3.5×10^8 N·m/kg) with an unrivaled specific strength of up to 7.5×10^7 N·m/kg, requiring a force of ~10 nN to break a single atomic chain [28]. The torsional stiffness of carbyne, on the other hand, is close to zero but can be *switched on* by introducing appropriate functional groups at its ends. With other appropriate termination, carbyne can also be switched into a magnetic-semiconductor state by mechanical twisting [28].

One can distinguish three generations of nanocarbon materials (Figure 2.3):

- The first generation of nanocarbon materials is composed of the three basic types that is, fullerenes, graphene, and CNTs and of the various novel simple morphology carbon materials that may be derived from them such as carbon quantum dots, nanohorns, nanofibers, nanoribbons, nanocapsulates, nanocages, and other

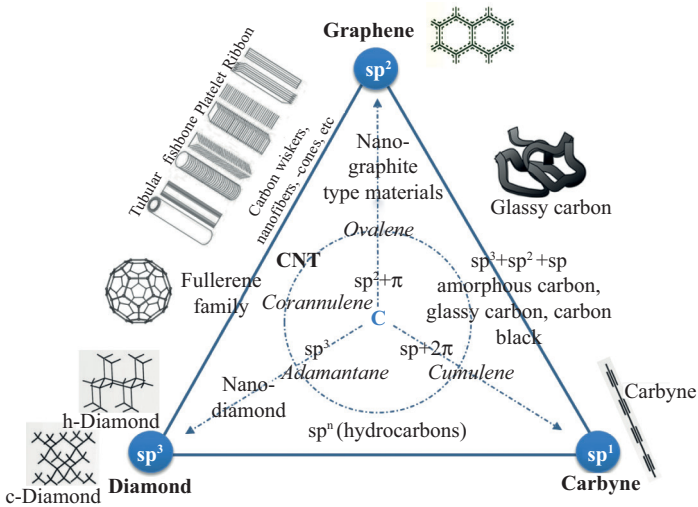

Figure 2.2. Simplified classification of carbon materials based on the hybridization of carbon atoms.

Source: Adapted from Centi and Perathoner [27].

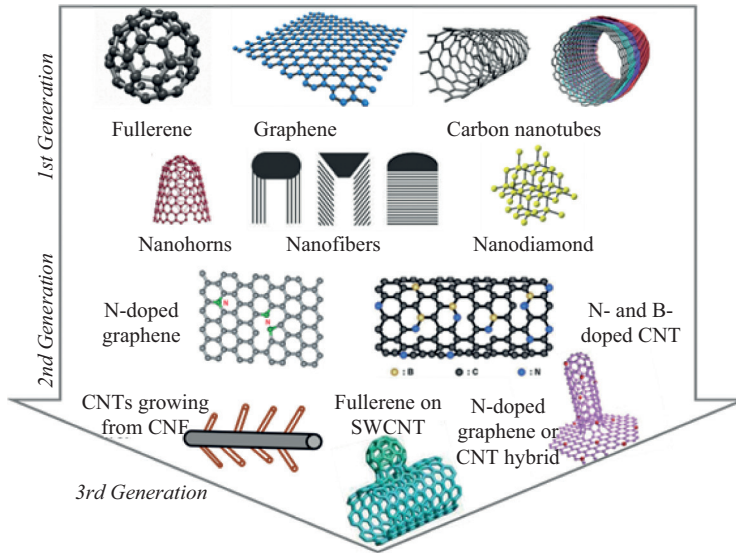

Figure 2.3. Examples of three generation of nanocarbon materials.

Source: Adapted from Centi, Perathoner, and Su [8].

nanomorphologies. These nanocarbons have a low dimensionality and morphology-defined properties.

- The second generation of nanocarbon materials derives from the first generation. However, in this second generation, the electronic structure is tailored by the introduction of heteroatoms (dopants) to tune the properties of the nanocarbon materials. A further level of control in the characteristics of these nanocarbons is introduced during the synthesis or by postsynthesis treatments.
- The third generation of nanocarbon materials, where an additional level of control is achieved through the development of hybrid and hierarchical systems (nanoengineering the architecture of materials at the nanoscale level [29]).

The number of control parameters that can be used to fine-tune the properties of nanocarbon materials increases as we move from the first to the third generation of carbon nanomaterials. Nonetheless, we only have a limited understanding of all the different parameters determining the functional performances of such materials [9, 30, 31]. This is related in part to the difficulty in characterizing the defect state in nanocarbons, which is an intrinsic characteristic of the carbon flexible coordination and hybridization. Fortunately, progress in the characterization of carbon

materials (e.g., by electron microscopy [30]) has improved the understanding in this area. However, there are still problems of homogeneity at the nanoscale and the correlation between the nanocharacteristics and the macroscale behavior. In carbon microelectromechanical systems (C-MEMS) and carbon nanoelectromechanical systems (C-NEMS), the nanoscale characteristics dominate device performance, but the difficulty in achieving full control of the presence and characteristics of defects influences the reproducibility of these devices. A general issue in this regard is that for many of the synthesis reaction paths of nanocarbons, there are competing reactions. This and the presence of (uncontrolled) interfaces may significantly alter the overall resulting nanocarbon properties.

2.2.1 STRUCTURE OF CNTs AND OTHER NANOCARBON MATERIALS

CNTs constitute one of the most widely used types of nanocarbons. A CNT can be viewed as a graphene sheet rolled up with its edges connected in a butt joint. A single rolled sheet forms a single-walled carbon nanotube (SWCNT), while an array of several concentric tubes creates a multiwalled carbon nanotube (MWCNT) [32]. Figure 2.4 shows the ideal structure of an SWCNT (Figure 2.4a) and an MWCNT (Figure 2.4b). Figure 2.4c and d (transmission electron microscopy [TEM] images) shows the examples of the actual structures.

In Figure 2.5, we show the formation of an SWCNT by rolling up a single graphene sheet, and this illustrates how different types of SWCNTs can be obtained depending on the direction along which the sheet is rolled up. The electronic (and other) properties of SWCNTs depend critically on the resulting helicity. A one-dimensional SWCNT is commonly characterized by both a *chiral vector*, $\mathbf{C}_h$, and a *translation vector*, $\mathbf{T}$, evidenced in Figure 2.5. The vector points from the first atom toward the second one in a 2D graphene sheet. Both the vectors ($\mathbf{C}_h$ and $\mathbf{T}$) determine the CNT unit size and are commonly expressed by the Bravais lattice vectors $\mathbf{a}_1$ and $\mathbf{a}_2$ as follows:

$$\mathbf{C}_h = n\mathbf{a}_1 + m\mathbf{a}_2 \tag{2.1}$$

$$\mathbf{T} = t_1\mathbf{a}_1 + t_2\mathbf{a}_2 \tag{2.2}$$

$$t_1 = \frac{2m+n}{d_R}, t_2 = -\frac{2n+m}{d_R}, \tag{2.3}$$

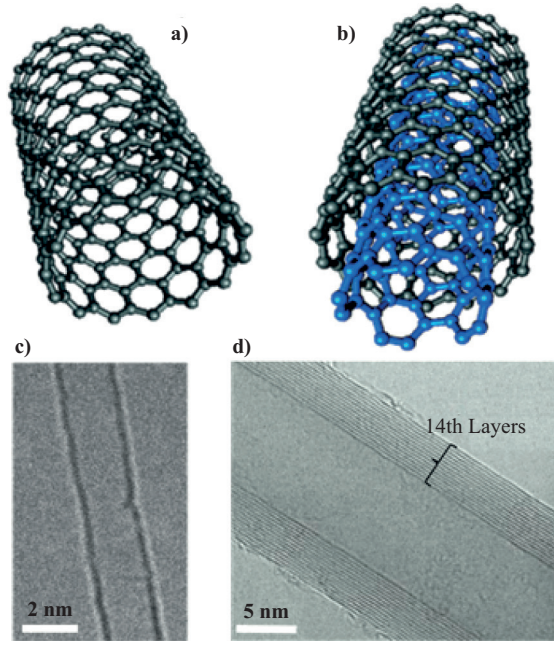

Figure 2.4. (Super) structure representations of (a) SWCNT and (b) MWCNT, with TEM images of the actual structure (c) and (d).

Source: Figure 2.4 (a) and (b) are adapted from Figure 2.1 in Zhao and Stoddart [32].

where $\mathbf{a}_1$ and $\mathbf{a}_2$ are the unit vectors (the primitive axis, e.g., translation vectors, of the hexagonal lattice), n and m are integers, and d_R is the greatest common divisor of $(2n + m, 2m + n)$. Following this methodology, SWCNTs are called (n, m) nanotubes. The magnitude of the $\mathbf{C}_h$ vector is used to calculate the CNT radius as $R = C_h/2\pi$. Based on the integer values, three types of CNTs can form when carbon sheets roll up along a particular single symmetry axis. When $n = m$, it takes on an armchair ($\theta = 0°$) configuration; when $m = 0$, it becomes a zigzag type ($\theta = 30°$) and for $n \neq m$, it forms a chiral tube ($\theta = 0°$ and $30°$) (see Figure 2.6a and b) [33]. The armchair CNT is a mirror image match of the zigzag CNT and vice versa, and therefore, they are considered achiral. Different chiral angles and CNT diameters lead to different properties, for example, the conductive properties, as shown in Figure 2.6. The control of chirality and other aspects of CNTs are necessary in many emerging applications of CNTs, for example, related to their conduction characteristics. Symmetry operations on CNT structures can be expressed as $R = (\Psi/t)$ (see Figure 2.5) and the number

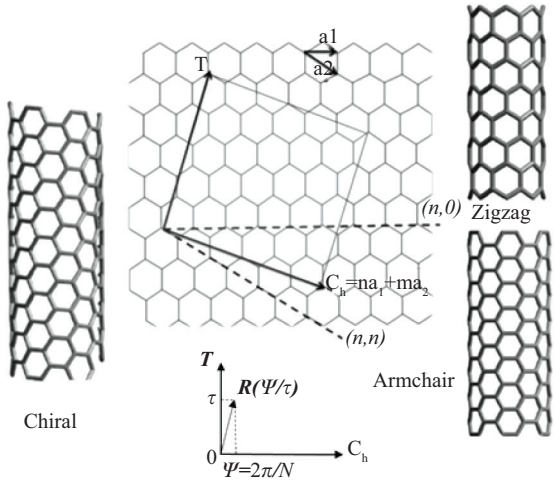

Figure 2.5. A sheet of graphene rolled to show formation of different types of SWCNTs. The space group symmetry operation, R = (ψ/τ), is also shown, in which ψ denotes the angle of rotation around the nanotube axis and τ is the translation in the direction of **T** as specified by the symmetry vector **R**.

of hexagons per unit cell N is obtained as a function of n and m according to Equation (2.4).

$$N = \frac{2(m^2 + n^2 + nm)}{d_R} \tag{2.4}$$

There are thus $2N$ carbon atoms (or $2p_z$ orbitals) in each unit cell of the carbon nanotube. The metallic and semiconducting CNTs defined by the integers (n, m) are illustrated in Figure 2.6.

Caps of growing CNT mouths typically consist of both pentagonal and hexagonal structures, although complying with the pentagonal rule (it is energetically unfavorable for two pentagons to be adjacent to each other). As MWCNTs are formed by joining SWCNTs, the models for SWCNTs can also be used to describe MWCNT structures. According to the *Russian inset doll* model, an MWCNT forms a coaxial cylindrical roll, a coaxial polygonised roll, or a scroll, depending on the interlayer's structural folding, as demonstrated in Figure 2.7 [33–35]. The length of the chiral vector $\mathbf{C}_h$ is the circumference of the CNT and is given by the corresponding relationship:

$$\left|\mathbf{C}_h\right| = a\sqrt{n^2 + nm + m^2}\,, \tag{2.5}$$

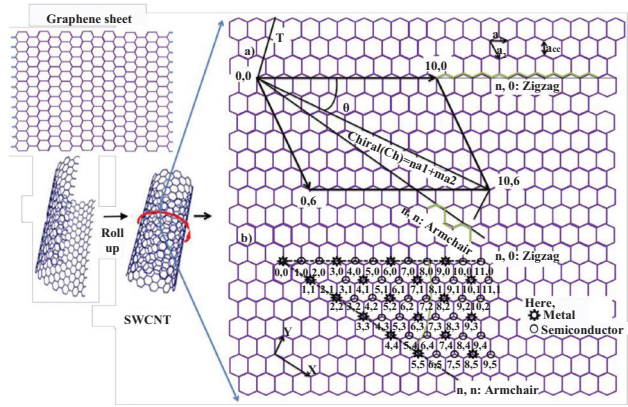

Figure 2.6. The schematic construction of SWCNT from a graphene sheet. (a) $\mathbf{C}_h$, depicts chiral vector, and $\mathbf{a}_1$ and $\mathbf{a}_2$, represent the unit cell vectors of the hexagonal cell. The chiral angle (θ) is the angle between zigzag axis and chiral vector ($\mathbf{C}_h$) and can be represented by $\theta = \tan^{-1}(m\sqrt{3}/m + 2n)$. (b) Representation of the integer values (n, m), which decide among zigzag, armchair, and chiral SWCNTs.

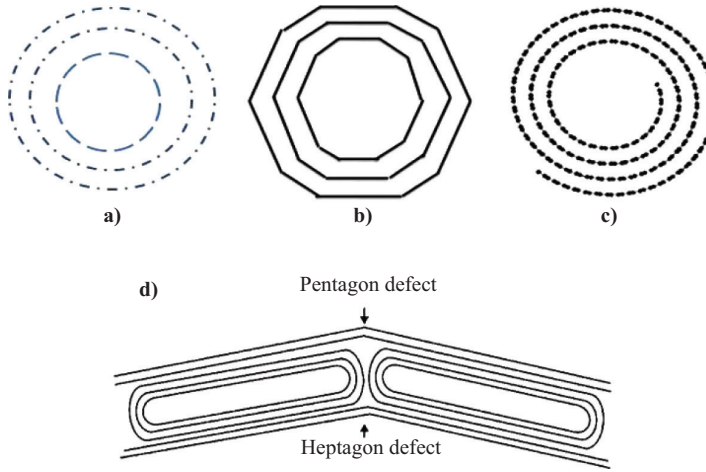

Figure 2.7. Top views of MWCNTs: (a) cylindrically curved Russian inset doll model, (b) coaxial polygon, and (c) graphene sheets scroll (according to Amelinckx et al. [34]). The figure (d) reports instead a scheme representing the structure of an encapsulate kink in an MWCNT.

where a is the length of the unit cell vector $\mathbf{a}_1$ or $\mathbf{a}_2$. This length, a, is related to the carbon–carbon bond length, a_{cc}, by

$$a = |a_1| = |a_2| = a_{cc}\sqrt{3} \tag{2.6}$$

For graphite, a_{cc} is 0.1421. The same value is often used for CNTs, but because of the curvature of the tube, a slightly larger value such as a_{cc} = 0.144 nm should be a better approximation. Using the circumferential length c, the diameter of the CNT is thus given by the relation: $d = c/\pi$.

Ideally, the CNT body structure does not differ from the arrangement of the carbon atoms in graphite, which features only equivalent atoms. Consequently, one might assume that the π electrons are delocalized across the whole cylindrical structure. At the ends of the nanotube, however, the equivalence of the bonds is broken. The cylinder is deformed toward the ends and the degree of π electron delocalization is decreased over the entire system. Several resonance structures are possible, including localized double bonds or six-membered rings without aromatic character. Alternating bonds are most frequent near the ends of the tube, while their number decreases toward the center.

Considering the ends of an open SWCNT, the outermost carbon atoms must be saturated by attaching either functional groups or a cap of carbon atoms. In the latter case, a closed SWCNT is obtained. The range of possible shapes for closed SWCNT caps is broad. Both approximately hemispheric caps and pointed structures have been found, and even concave caps have been observed. Pentagonal defects (with a convex curvature) and seven-membered rings (with inverse curvatures) are responsible for these differently shaped end caps. These defects can lead to beak-shaped caps that exhibit considerably smaller diameters than the tubes themselves. In MWCNTs, five-membered rings are also crucial to the formation of the end cap or open structure (e.g., how the CNTs terminate) of the nanotube, such as the formation of a toroidal ending (the tube does not have a simple double-sheet structure, but rather consists of semitoroidal shells or terminations). Defects in individual tubes may influence the structure of MWCNTs in other ways too. For example, the simultaneous existence of five- and seven-membered rings results in a bent MWCNT. In multiwalled systems, these elbow structures are found between the encapsulated regions (Figure 2.7d). These flexures are confined to a few graphene layers.

Fullerene constitutes another allotrope of carbon. It belongs to a family of molecular carbon cages with all of the carbon atoms in the sp^2 hybridization. In Figure 2.8, we show a large variety of fullerene materials. This includes the best-known C60 fullerene and an example fullerene with partial substitution of carbon with nitrogen [36].

Owing to the strain caused by the curvature (facilitated by pentagons to create a positive curvature in the hexagon network), fullerenes exhibit a profoundly different chemistry from planar graphite. The planarity

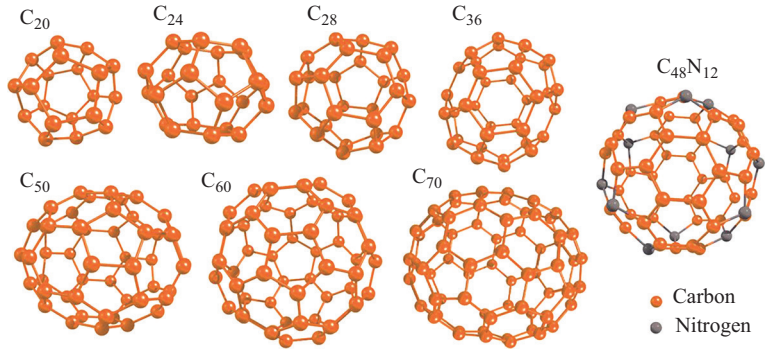

Figure 2.8. Family of fullerene carbon materials.

Source: Adapted from Gusev [36].

of sp^2-hybridized (trigonal) carbon atoms in graphite implies that the pyramidalization angle $\theta_p = 0°$, whereas an sp^3-hybridized (tetragonal) carbon atom feature a $\theta_p = 19.5°$. The deviation from planarity in fullerenes reduces the orbital overlap of the π electrons, resulting in the localization of the double bonds. The curvature effect, present in fullerenes as well as in small diameter CNTs, causes the hybridization of the σ bonds between C–C atoms. Depending on the bending angle, the hybridization of carbon atoms becomes something between that present in sp^3 diamond and sp^2 graphite. As a consequence to this strain, fullerenes are more reactive than graphite. C60, for example, is highly light and air sensitive at room temperature. Owing to the yet high curvature degree, C20 and other smaller carbon atoms structures are highly unstable. The isolated pentagon rule (IPR) commented earlier is obeyed by all pristine fullerenes, and because of the IPR, C60 fullerene is followed by C70 because there are no intermediate structures with isolated pentagons. Beyond C70, there are a set of fullerenes with an even number of carbon atoms, the so-called higher fullerenes. Furthermore, starting with C78, several stable isomers are observed for each carbon skeleton.

C60 is the most available and broadly studied fullerene. It comes in a spherical shape with a distance from the center to the atomic carbon nuclei of about 0.36 nm. C60 forms molecular crystals with the molecules being localized in the nodes of a face-centered cubic lattice.

Other known carbon materials that have been investigated include carbon black, onion carbon, AC, soot, amorphous carbon, carbon nanofibers (CNFs), carbon fibers (CF), vapor grown carbon fibers, and diamond-like carbons (DLCs). These materials are made from various combinations of the basic type of carbon allotropes, as evidenced in Figure 2.2.

Similar to the case of fullerenes, curvature-induced pyramidalization and misalignment of the π orbitals of the carbon atoms in CNTs and soot induce local strain. CNTs and soot materials are thus expected to be more reactive than flat graphene sheets. In the case of CNTs, especially SWCNTs, the end caps resemble a hemispherical fullerene, and this ensures that the end caps will always be more reactive than the perfect SWCNT side wall. Carbon black, fullerene black, and engine soot are produced from the pyrolysis of hydrocarbons or from the incomplete combustion of fuels. In Figure 2.9, we show an example of the morphology of soot from a stationary diesel engine. This high-resolution TEM image reveals the presence of primary particles with sizes varying from 2 to 20 nm featuring multiple fullerene-like shell structures [37] with strongly bent ribbons. The primary particles then agglomerate through interaction between the bent strands of ribbons giving rise to a stable material. The same morphology is observed in the carbon in flame soot showing a fullerene-type nanostructure.

The growth mechanism and microstructure of these soot-derived nanocarbon materials resembles that of the fullerene [38, 39]. They show a reactivity close to that of fullerene-like materials, which originates largely from the modification of the C–C bond characteristics because of the presence of a curved graphene sheet [40, 41].

Graphene, strictly speaking, is formed from a single layer of graphite (Figure 2.10a). However, the term *graphene* is used not only for single layers but also for bilayer and few-layer graphene (up to about 10 layers), which all can be viewed as different types of two-dimensional crystals [42]. The carbon atoms in a graphene layer are sp^2-hybridized forming three in-plane σ bonds per atom, which in turn leads to the formation of a

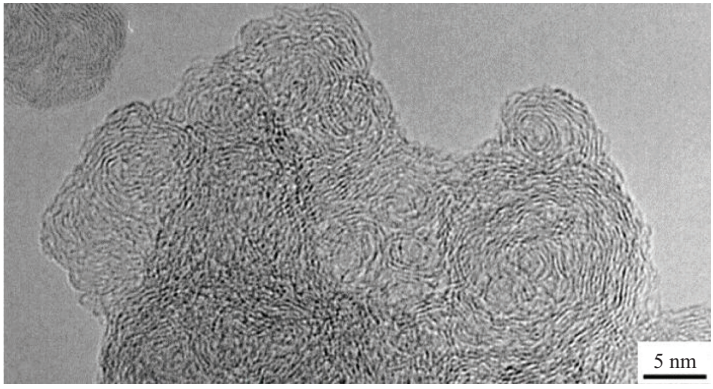

Figure 2.9. Fullerene-like soot deriving from a diesel engine.

Source: Adapted from Su et al. [37].

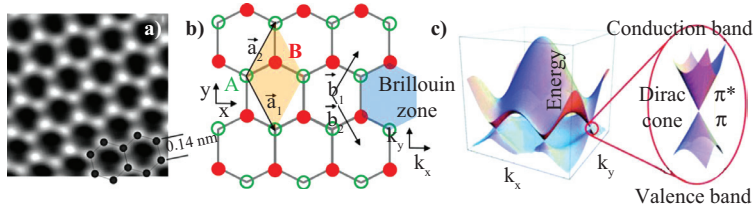

Figure 2.10. (a) Atomic-resolution image of a graphene sheet, with an indication of the carbon–carbon bond length of about 0.142 nm. (b) Honeycomb lattice structure of graphene exhibiting a basis with two carbon atoms, A and B, per unit cell [43]. (c) Idealized Brillouin zone (graphene π-band) with a zoom to the K-point, where the bands cross at the Fermi level forming a Dirac cone.

hexagonal planar layer with a honeycomb-like atomic arrangement. The hexagonal graphene lattice is displayed in a top view model in Figure 2.10b and exhibits a basis with two carbon atoms, A and B, per unit cell. These two atoms form two equivalent sublattices.

The geometry of an sp^2-hybridized carbon atom is responsible for the formation of the hexagonal honeycomb lattice that determines the extraordinary mechanical and electronic properties of graphene. Each of the two equivalent carbon atoms within one unit cell contributes one cosine-shaped band to the electronic structure. These bands cross exactly at the Fermi level, where they form a Dirac cone with a linear electronic dispersion (Figure 2.10c, graphene Brillouin zone) [43]. The remaining fourth electron in the p_z-orbital forms covalent p-bonds with the adjacent carbon atoms. The band structure of graphene (π-bands) is responsible for charge carrier transport. In contrast to semiconductors, which possess a parabolic dispersion relation, graphene exhibits a linear dependence of the electron energy on the wave vector. While monolayer graphene shows a linear dispersion, bilayer graphene exhibits a parabolic spectrum. Both systems are a zero-gap semiconductor or a zero-overlap semimetal.

This idealized electronic structure for extended sheets of graphene changes significantly when dopants or heteroatoms (as well surface metal particles) are present, and this constitutes a way to improve the performance and the electric properties of graphene [44, 45]. Graphene sheets at the edges are saturated with heteroatoms, and doping with various heteroatoms (oxygen, boron, nitrogen, phosphor, sulfur, etc.) is often carried out to improve and tune the performance of graphene, as well as that of all the other nanocarbons [46]. Graphene and graphene nanoribbons, similar to other type of nanocarbons, are characterized from the presence of different types of defects: (a) structural (sp^2-like) defects, (b) topological

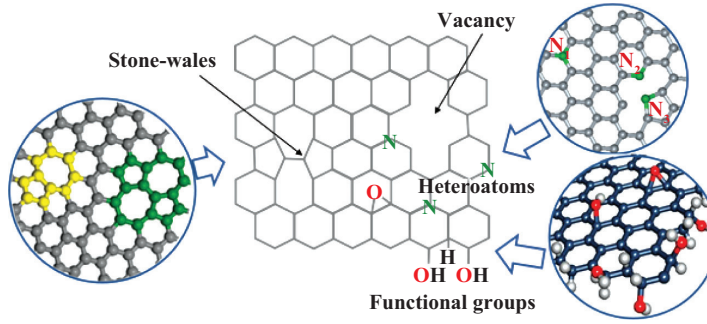

Figure 2.11. Schematic diagram depicting single-layer pristine graphene with various types of defects, functional groups and heteroatoms.

(sp^2-like) defects, (c) defects related to doping or functionalization (sp^2- and sp^3-like), and (d) defects related to vacancies or edge (non-sp^2-like) [47]. Defects, in general, play a key role in physicochemical properties of graphene.

In Figure 2.11, we show an example of the different types of possible defects, functional groups and heteroatoms, which may be present in real graphene and graphene nanoribbons. The effective nature and properties may be thus largely different from those of the idealized single-layer *pristine* graphene. Clearly, the preparation method plays a significant role in the formation of graphene. It may be quite different from another sample, what indicated generically as *graphene* and often large irreproducibility may be present in samples prepared by the same method.

2.2.2 PROPERTIES OF NANOCARBONS

There are various characteristics that make nanocarbons attractive in MEMS and NEMS applications, such as the unique mechanical properties of graphene and CNTs, which include low mass, high Young's modulus, high thermal conductivity, and high surface area-to-volume ratio. However, as mentioned in the previous sections, these properties not only depend on the structure of the nanocarbon but also greatly depend on the specific characteristics, such as the presence of defects and heteroatoms. Therefore, the specific preparation of these materials may greatly influence their final properties. In addition, the integration of the synthesis of these nanomaterials with that of other materials is very important and introduces some additional constraints as processes might not be compatible, for example, in terms of annealing temperature.

Graphene has a Young's modulus of around 2,000 GPa, about 10 times higher than that of steel and about 13 to 15 times higher than that of silicon [10]. SWCNTs have a Young's modulus about half that of graphene, while that of MWCNTs is even lower (the Young's modulus also greatly depends on the CNTs preparation). However, the latter is still two to five times higher than that of silicon. The tensile strength follows the same trend. The band gap of ideal graphene is zero but, as discussed earlier, can be changed by doping or patterning [48]. The band gap of CNTs depends on their characteristics, such as diameter. Zigzag (9,0) SWCNT is metallic, while zigzag (10,0) nanotube is a semiconductor. In MWCNTs, depending on the characteristics (size, number of layers, presence and type of defects, etc.), a behavior from metallic to semiconductor to insulating can be observed. Although the semiconductor characteristics of silicon can also be tuned, carbon nanomaterials offer a much larger degree of flexibility. Another relevant difference regards carrier mobility, which is about two orders of magnitude larger in graphene (about 2×10^5 $cm^2 \cdot V^{-1} \cdot s^{-1}$) than in silicon (about 1×10^3 $cm^2 \cdot V^{-1} \cdot s^{-1}$), although, in this case, the effective carrier mobility depends greatly on the specific sample. The carrier mobility in SWCNTs and MWCNTs is typically lower than that in graphene, but still larger than that in silicon.

In general, various features differentiate nanocarbon materials with respect to the *conventional* carbon ones, such as AC or carbon black, as well as from silicon.

Pore Structure and Surface Area: The AC surface area and porosity can be tuned within some range by controlling the AC preparation procedure, but in large part, the high surface area is due to micropores, which may limit its conductivity and performance for sensing applications. The CNT surface area is mainly associated with the external geometrical area of the CNT (except for SWCNT, where the inner surface contributes significantly, although the situation is different for open or closed nanotubes. In CNTs (particularly in MWCNTs, which are the most widely available and the least expensive type of nanocarbons), mesoporosity is associated with the void space created in the CNT network, when the CNTs do not pack in an ordered way. A typical AC surface area is around 1,000 m^2/g (greatly depending on the type and treatment procedure), while that of a CNT may range from over 1,000 m^2/g for SWCNTs to 700 to 800 m^2/g for DWCNT (double-walled carbon nanotube) and 200 to 300 m^2/g for MWCNT (5 to 10 walls), because the weight of each single nanotube increases with the number of walls. Pore structure and surface area are critical in applications such as sensing and catalysis.

Electron and heat transport: CNTs allow for a faster and more efficient electron and heat transport compared to AC or other type of *conventional*

carbon materials. Although the electron and heat transport properties depend greatly on the specific characteristics of a given carbon material, GC, a common type of carbon widely used in electrode preparation (with much better conductivity than AC), shows a volume resistivity usually higher than 10^1 Ω cm, while CNTs show a volume resistivity in the range 10^{-2} to 10^{-3} Ω cm [49]. These properties are critical in the development of electrochemical devices, such as nanobatteries [49].

The 1D structure of CNTs constrains electron transport in one direction, which endows CNTs with unique electronic properties, that is, near-ballistic transport leading to the outstanding electronic conductivity of CNTs [50]. In commercial CNT materials, the conductivity is much lower because of the defects. Theoretical studies suggest that metallic CNTs can carry an electrical current density of 4×10^9 A/cm^2, which outperforms metals such as copper by three orders of magnitude [51]. For these reasons, CNTs are bound to find applications in a wide range of electronics including room-temperature ballistic transistors, electron field emitters, energy storage devices, supercapacitors, flat panel displays, device coolers, paper batteries, solar cells, light emitting diodes, and nanoradio [52].

Among the many distinctive characteristics of CNTs, one of the main characteristics is the ability of its carbon atoms to rehybridize in response to applied strain or stress, with a certain degree of sp^2 to sp^3 transition. This peculiar behavior may be exploited in piezoresistive strain or stress sensing applications, as the electrical properties (such as resistance) are greatly affected by the deformation of the CNT. The compressive force can easily cause a CNT to bend, flatten, or twist, which gives rise to a very high piezoresistive effect because of the alteration of its electronic transport properties. In addition, absorption of various gases (NO_x, NH_3, etc.) or chemicals onto CNTs also leads to the modification of their electron transport properties. This phenomenon makes CNTs also an excellent choice for chemical sensing [53].

Mechanical and other properties: As introduced earlier, some nanocarbons (e.g., CNTs, graphene, and nanodiamond, the latter formally diamonds of very small size, 4 to 5 nm, but characterized from a diamond core and graphitic-like surfaces) have typically superior mechanical properties over silicon or conventional-type carbon materials, including those used in MEMS applications such as GC [54]. GC is a hard solid prepared by heat treatment at elevated temperatures (1,000–3,000°C) of polymeric precursors such as copolymer resins of phenol–formaldehyde or furfuryl alcohol–phenol. These polymers are used because of their high carbon yield on pyrolysis (the ratio of carbon present after or

before carbonization is ~50 percent). GC is electrically conducting and impermeable to gases and has a low coefficient of thermal expansion. In addition, GC (having a fullerene-related microstructure) has a lower density (1.3 to 1.5 g/cm^3) than that of graphite (2.27 g/cm^3) or diamond (3.52 g/cm^3), because of its porous microstructure (related to bubbles formed during the pyrolysis process). The voids constituting the pores are not connected, and for this reason, GC shows low gas permeability. Moreover, GC has a very high corrosion resistance and inertness under a wide variety of conditions, allowing its use in very corrosive environments. Although some of these properties are better than those of nanocarbon materials, the Young's modulus of GC (10 to 40 GPa) is lower than that of silicon and much lower than that of nanocarbons. On the other hand, this may be useful in some applications, such as in electrostatically driven actuators, where the stiffness of the material is a disadvantage [54].

Diamond and DLC are other types of carbon materials of interest for MEMS applications [55]. Both possess a number of excellent properties that Si and other materials lack, including reduced coefficients of friction and increased resistance to wear, both particularly useful for microsystems that feature sliding interfaces. Both materials also have a very high Young's modulus, tensile, and fracture strength and are suitable for high frequency MEMS devices. They are chemically inert and are stable in air up to 600°C. They feature excellent thermal conductivity and low coefficients of thermal expansion that make them useful for packages with better heat dissipation and bimorph thermal actuators with large displacements. Diamond and DLC are biocompatible, are mechanically strong, and have excellent tribological properties. They are excellent coating materials for medical implants. DLC is hydrophobic with an excellent ability to prevent nonspecific biobinding relevant in biosensor applications.

CNTs usually exhibit an elastic strain of 5 percent, and therefore, they show plastic deformation before fracture. This property is promising for mechanical energy storage. Defect-free CNTs are the stiffest and strongest materials yet discovered in terms of tensile strength (63 GPa) and elastic modulus (~1 TPa). In Table 2.1, we compare mechanical properties of CNTs with stainless steel [56]. CNT fibers have the potential to serve as ultrahigh strength (yet lightweight) fibers, electronic interconnects, power conversion devices, motors, transformers, and electro-storage devices.

The mechanical stiffness in the radial direction of the CNT, however, is much lower, primarily because of its hollow structure and high aspect ratio. The Young's modulus in the radial direction is of the order of several GPa, as shown by nanoindentation experiments on MWCNTs [57]. As the conductivity of a CNT can be greatly altered under stress or strain,

Table 2.1. Comparison of mechanical properties of CNTs with stainless steel

Material	Young's modulus (TPa)	Tensile strength (GPa)	Elongation at break (%)
SWCNT	~1 (from 1 to 5)	13–53	16
MWCNT	0.27–0.95	11–150	-
Stainless Steel	0.186–0.214	0.38–1.55	15–50

this soft characteristic in the radial direction may potentially enhance the performance of CNTs in piezoresistive force or strain sensing.

Stiction: The adhesion between two surfaces depends on van der Waals, electrostatic, and capillary forces. The contribution of capillarity accounts for most of the forces responsible for stiction. Stiction often limits the performance of MEMS: once two surfaces are in contact, only a restoring force can separate them. The density of oxygen-containing, polar surface functional groups is lower on carbon (typically 2 to 10 percent) than on Si or SiO_2. The ability to functionalize the surface of oxidized carbon to introduce hydrocarbon or fluorocarbon groups offers a route to materials with very low surface free energies and low potential for stiction [58]. The relatively rough surface of carbon solids (relative to silicon etched along a crystal face) may also prevent stiction, because the true area of contact between rough surfaces is smaller than that between smoother surfaces.

2.3 APPLICATIONS OF CARBON MATERIALS

2.3.1 USE IN COMPOSITES AND AS CATALYSTS

Carbon fibers, carbon black, CNTs, and CNFs are widely used as reinforcement of certain matrix materials in composites. Carbon fibers, for example, were extensively studied for their optimum graphitic structure and surface functionalities to obtain the best mechanical, electrical, magnetic, and thermal composite properties. Methods such as graphitizations, oxidations of the carbon surface, and whiskerization have been applied to improve the carbon fiber–matrix interaction [59, 60]. The increasing interest of CNFs and CNTs in composites arises from the theorized and proven observations that physical properties of carbon fibers such as surface area, conductivity, and strength improve exponentially as their size becomes nanoscale. Similar to the carbon fibers, the chemical and physical properties of CNFs and CNTs materials depends on their

microstructure. The ratio of prismatic and basal planes and the presence of structural and topological defects in the graphene layers allow for tuning the chemistry and physics of these nanocarbon materials [60, 61].

One way to modify both the macrostructure and microstructure of a final carbon material is by directly growing secondary CNFs or CNTs onto carbon fibers or even inside the CNTs itself, when large diameter CNTs (about 80 to 100 nm inner diameter) are utilized, with mono- or bimetallic catalysts [62–70]. The latter method is somewhat similar to whizkerization of carbon fibers to enhance the carbon–polymer interaction in composites [62]. The secondary CNTs or CNFs provide more surface area and depending on their texture may facilitate further entanglement of the final carbon material resulting in a 3D-like interconnected network. Thus eventually the chemistry can be tuned based on the microstructure of the secondary CNTs or CNFs. The secondary CNFs or CNTs grown on carbon fibers or CNTs supports have found other applications in the field of electronics as the conductivity and electrical capacity of the carbon materials were improved [71, 72].

During the past several years, metal-free catalysts have attracted considerable interest, especially for industrial applications and only graphitic nanocarbons exhibit excellent long-term stability and high catalytic activity [73, 74]. On the other hand, the powdery form of nanocarbons makes them unsuitable for use in fixed-bed reactors on an industrial scale. The compaction of loose nanocarbons to create particles of millimeter size for their use in industrial reactor typically greatly inhibits the access to all the surface. The immobilization of graphitic nanocarbons onto a carbon-based support allows for better reactants diffusion, prevents hot spots and pressure drops, and avoids chemical discontinuities [75]. So, clearly, the mass production of immobilized nanocarbons on a carbon support is the more desirable pathway for industrial applications in chemical reactors. In the current literature on CNTs and CNFs synthesis, the catalytic chemical vapor deposition (CCVD) method appears the most promising method to produce bulk quantities of CNTs and CNFs for composite and other bulk applications. Although of considerable interest, the effect of metal catalysts on carbon supports on the microstructure of the grown CNFs and CNTs has not been covered much at all.

Application of carbon materials as catalyst support has been widely reported with a broad scope of reaction applications [2, 7–9, 76–80]. As a support, AC has attracted much interest because it offers several advantages such as high thermal stability, high surface area, low cost, and easy recovery of the metal catalyst by simple combustion. Carbon–carbon composites represent interesting combinations of carbons featuring

different length scales (from nano to micro) and different crystallinity (graphitic or disordered). Su et al. have successfully synthesized CNFs on an AC support with an Fe catalyst using C_2H_4 as the carbon source [81, 82]. Such composites have found applications both as adsorbents and in catalysis.

Carbon materials cannot be used as catalyst supports at high temperatures and pressures in oxidative or reducing atmospheres. The limits, however, depend on the graphitic nature of the carbon materials and the type of metal catalyst on the supports. Nevertheless, there remains appreciable interest in carbon as a support because of its superiority over traditional catalyst supports for two main reasons:

- Availability in macroscopic shapes suitable for industrial uses [83–85]
- Tunable surface chemistry [86–88]

The possibility of altering the ratio of basal or prismatic planes and controlling the amount of defects present in a carbon material allows for the attachment of heteroatoms (O, N, or H) on the carbon surface. This is done either by the selection of the type of carbon materials or by the selection of synthesis conditions with or without posttreatment. Such flexibility in carbon allows unlimited alternatives to tailor the carbon surface with functional groups.

Different thermal stabilities of surface functional groups allow for the tuning of surface functional groups on carbon materials by controlled heat treatments. As a support, the type and amount of functional groups on the surface have a profound role in the dispersion and stability of catalysts on a carbon surface. In addition, the surface functional groups often provide for the polarity or affinity for the solvent or solutions for maximum surface wetting.

In preparing a catalyst, the choice of a proper precursor is determined, for example, by the surface charge of the carbon to achieve maximum interaction between the precursor and the surface anchoring sites [61]. During calcination, reduction, and catalytic reaction, the functional groups have to be stable to allow for the anchoring of catalyst particles on its surface and to avoid the sintering of the catalyst particles [89]. The nanostructure of carbon filaments also plays a critical role. Carbon fibers have electronic properties that largely depend on the crystallinity and orientation of graphene planes. For example, CNFs having different exposed prismatic edges have a different reactivity in anchoring metal nanoparticles and as a consequence give rise to different catalytic performances [79, 90–91].

2.3.2 USE OF CARBON MATERIALS IN MEMS AND RELATED DEVICES

The superior mechanical, electrical, and structural properties of CNTs have resulted in their utilization in a wide range of fields. For example, implementing these materials into flexible or stretchable systems can lead to flexible microelectronics as well as to pressure monitoring devices inside the human body and energy scavenging from low-frequency motions. The realization of the potential of carbon materials in MEMS and related devices requires the ability to carefully manipulate CNTs, especially on the micro- and nanoscale. The nanodiameter and high surface area of CNTs induce high van der Waals forces between the tubes, resulting in a strong tendency to aggregate with each other in order to minimize the total surface energy. Hence, CNTs have very limited dispersibility in most solvents, but today, it is possible to tune their solvency by controlled functionalization to modify their properties [92, 93].

There are two main categories of procedures for functionalization of CNTs, that is, covalent and noncovalent methods (see also Chapter 7). Covalent functionalization of CNTs is based on the formation of covalent linkages between functional entities and the carbon skeleton of the nanotubes. The covalent methods can be further divided into direct covalent sidewall functionalization and indirect covalent functionalization via carboxylic groups on the surface of CNTs. Direct covalent sidewall functionalization is associated with a change in hybridization from sp^2 to sp^3 and a simultaneous loss of conjugation (e.g., see fluorination of CNTs [94], Figure 2.12, route A). Indirect covalent functionalization takes advantage of chemical transformations of carboxylic groups at the open ends and holes in the CNT sidewalls (Figure 2.12, route B). These carboxylic groups might have been already present on the as-grown CNTs or they might be generated during oxidative purification. In order to increase the reactivity of CNTs, the carboxylic acid groups usually need to be converted into acid chloride and then undergo an esterification or amidation reaction [95, 96]. The drawback of covalent functionalization is that the perfect structure of CNTs is destroyed, resulting in significant changes in the physical properties of CNT.

Noncovalent functionalization is based on supramolecular complexation using various adsorption forces, such as the Van der Waals force, hydrogen bonds, electrostatic force, and π-stacking interactions [97]. Compared to the chemical functionalization, noncovalent functionalization offers two key advantages: it can be accomplished under relatively mild

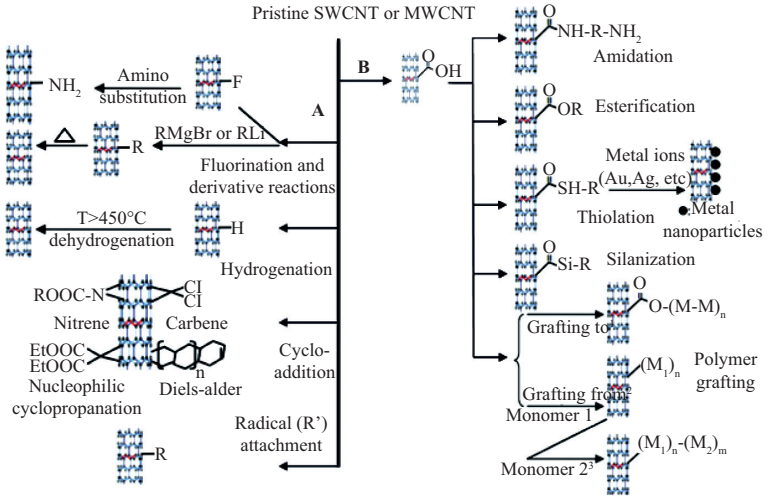

Figure 2.12. Strategies for covalent functionalization of CNTs (A: direct sidewall functionalization; B: defect functionalization).

Source: Adapted from Meng, Fu, and Lu [93].

reaction conditions and the perfect graphitic structure of CNTs is much better maintained.

CNTs, and in general nanofilaments, have been extensively applied in MEMS and NEMS. For example, CNT-based resonators (where CNTs act as the resonating mass detector element) show the highest mass sensing resolution ever established [98]. A single-clamped DWCNT beam was used instead of an SWCNT to avoid issues related to the chirality of CNTs. Owing to the smaller material density compared to other materials, it is possible to obtain a lower natural resonance frequency, resulting in larger sensor responses at lower resonant frequencies. The optimal sensitivity achieved is of the order of 1.3×10^{-25} kg $Hz^{-1/2}$, but depends on the specific characteristics of the DWCNT, which vary within some degree from filament to filament.

Another example of a C-MEMS and C-NEMS application is based on the high carrier mobility of SWCNTs, which can be exploited in CNT-based field effect transistors (FETs) [99]. A modified CNT with a high work function metal (Pd) and posttreatment with hydrogen affords the creation of a CNT–FET with a conductance near the ballistic transportation limit of $4e^2/h$ at room temperature and with an on-to-off ratio as high as 10^6 [100]. However, as indicated earlier, the reproducibility of CNT–FETs is still a major challenge, as it depends on the chirality and band gap

(semiconductor or metallic) of the SWCNTs and as we know by now, this change from CNT to CNT, even if they come from the same batch [101]. The ohmicity of the metal contacts is also still problematic and crucial for the device performance.

CNTs are also interesting for various gas sensing applications [102]. In order to overcome the reproducibility issues associated with single CNTs, an array of patterned CNT is preferred here. Such arrays can be prepared by CVD, as discussed in Chapter 3. In Figure 2.13, we illustrate the basic configuration of such a CNT-based device [102]. A silicon wafer is used as the supporting substrate and thermally grown SiO_2 serves as the insulation layer. The ohmic contact, molybdenum (Mo), constitute both contact pad areas as well as metallic interconnects. The total series resistance of the device comprise three components: the lateral sheet resistance of the CNT forest and the two CNT–metal ohmic contact resistances. The resistances of the Mo contact pads and aluminum bonding wires are small compared to the CNT resistance. When exposed to a gas, the resistance of the CNT-patterned array changes. The sensing threshold is below parts per million for a difficult gas such as NH_3 with a good response time (about 1 minute) [102].

Another concept that may be exploited in C-MEMS and NEMS applications is based on Joule heating when current is applied to a CNT as in a hot-wire sensor. An MWCNT is suspended as the sensing element between MEMS electrodes made of single-crystalline silicon. The device works based on the principle of heat transfer and is sensitive to gas pressure changes, because the pressure influences heat dissipation, modifying the resistance of the CNT. The device may also operate as a gas sensor, because different gases have different heat capacities that changes the heat dissipation. Both sensing mechanisms have been verified [103].

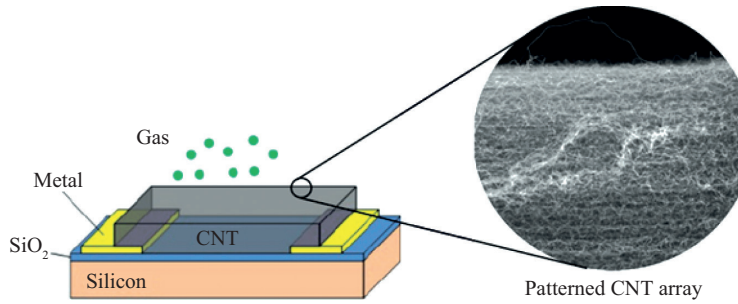

Figure 2.13. Scheme of a CNT-based device for gas sensing.

Source: Adapted from Fam et al. [102].

By combining bottom-up and top-down fabrication methodologies, it is possible to produce 3D CNT structures. First, an array of vertically aligned SWCNTs is grown by CVD on a predefined catalyst pattern on a silicon wafer (Figure 2.14a) and then (after flattening, the CNT array in a liquid densification process to have an uniform thickness) the CNT film is patterned using lithography to further construct devices on the wafer such as SWCNT cantilever (Figure 2.14c) and 3D CNT cantilevers (Figure 2.14d) [10]. By using these parallel and scalable steps, other different structures such as CNT islands, beams, and suspended CNT sheets (Figure 2.14b) can be also constructed onto a single wafer [104].

In Table 2.2, applications of CNT-based C-MEMS and C-NEMS devices from sensors and actuators to energy storage devices are summarized. However, in most cases, these applications are only at the proof-of-concept stage, as the many challenges involved in scaling up production must be resolved first. We also want to note here that in the area of energy storage and electrochemical nanodevices, hybrid CNTs systems, for example, CNTs in conjunction with metal oxides or conductive polymers, can be utilized, although still not systematically explored.

Graphene is another nanocarbon-type material increasingly used in C-MEMS and C-NEMS applications. The low mass and high surface area-to-volume ratio make graphene an excellent candidate for mass

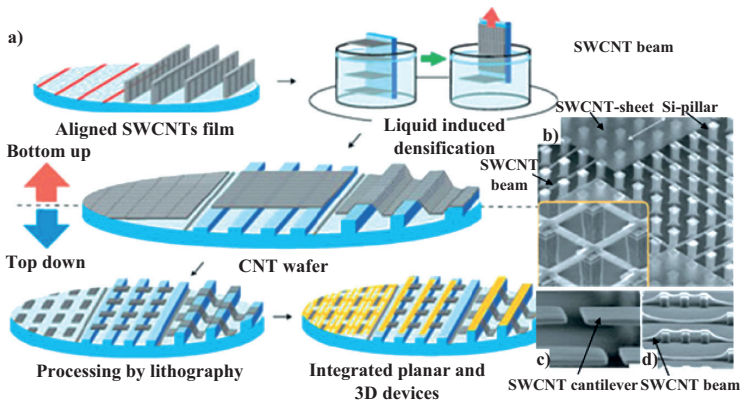

Figure 2.14. (a) Schematics of the bottom-up and top-down hybrid method to fabricate 3D CNT complex structures on a single wafer. (b) SEM image of silicon pillars with CNT sheets and CNT beams suspended on them. Scale bar 1 μm. (c) SEM images of suspended CNT cantilevers on silicon wafer with pre-etched trenches. Scale bar 2 μm. (d) SEM images of 3D CNT cantilevers. Scale bar 10 μm.

Source: Adapted from Zang et al. [10].

Table 2.2. Examples of CNT-based materials in C-MEMS and C-NEMS applications

Application	Type	Materials	Working mode
Sensor	Mass	DWCNT	Resonator frequency
	Strain	MWCNT	AFM
	Flow	SWCNT	Columbic field
	Gas	SWCNT	Capacitance, conductance, or resistance
	Biological	Enzyme or SWCNT	FET conductance (for glucose)
Actuator	Electromechanical	MWCNT	Rotational
		SWCNT or nafion	Displacement
		MWCNT or SWCNT	Nanotweezer
	Electrochemical	SWCNT	Pneumatic
		SWCNT	Bimorph bending
Energy storage		MWCNT	Lithium battery
		SWCNT array	Supercapacitor
		MWCNT or SiNx	Switch capacitor
		GCE, CP, MWCNT, Nf, AOx, and PEI	Biofuel cell

GCE, glassy carbon electrode; CP, carbon powder; Nf, nafion; AOx, alcohol oxidase; PEI, polyethyleneimine.

Source: Adapted from Zang et al. [10].

and gas sensing applications, respectively. Specifically, graphene-based electromechanical resonators have been demonstrated by using suspended graphene structures over silicon dioxide trenches.

The graphene-based device can be utilized as a gas sensor by monitoring the frequency shift because of mass changes related to the absorption of a gas. Sensitivities of 10^{-21} g are possible and in theory even higher sensitivities could be reached [106]. In addition to this type of graphene-based mechanical resonators, graphene-based chemical resistors, and field effect transistors have been utilized for gas sensing applications as well, because the resistance of graphene is sensitive to gas molecules [105]. Table 2.3 summarizes various graphene-based materials in sensing applications.

Graphene-based actuators also have attracted considerable research interest. Examples of laboratory-scale devices include (i) photomechanical actuators based on graphene nanoplatelets, (ii) electrochemical actuators based on surface-modified graphene, and (iii) microactuators based on a graphene-on-organic film hybrid bimorph [107–110].

The latter is a new fabrication method allowing the monolithic integration of a graphene layer as an active component. A photolithographically defined graphene sheet resistor could be used for both actuation and sensing [110]. A multistep fabrication process to produce a graphene and epoxy hybrid cantilever system is necessary. The process begins with the CVD synthesis of centimeter-scale graphene films on a

Table 2.3. Examples of graphene-based materials in C-MEMS and C-NEMS applications

Sensor	Detection	Materials	Detection mode
Physical	Strain	Graphene or PDMS	AFM or resistance
	Pressure	Monolayer graphene	Resistance
Chemical	Gas	Monolayer or few layer graphene	FET resistance change
	Heavy metal ions	Graphene	Electrochemical
Biosensor	DNA or protein	Graphene or Al_2O_3	Conductance
	Protein	GO	Fluorescence
	Dopamine	R-GO	Electrochemical
	H_2O_2	Pt or graphene	Electrochemical

GO, graphene oxide; R-GO, reduced graphene oxide.

Source: Adapted from Zang et al. [10].

Ni(300 nm), SiO_2(300 nm), and Si substrate. A 30-nm gold layer is then deposited on graphene by thermal evaporation to define the four electrodes. Conventional photolithography and reactive ion etching with O_2 plasma is used to pattern the graphene serpentine microheater. Two steps of epoxy photolithography are then used to form the cantilever beam and support body. BOE (buffered oxide etchant) and $FeCl_3$ are finally used to remove the nickel and SiO_2 sacrificial layers followed by rinsing in deionized water to clean the cantilever.

2.4 CHALLENGES AND OPPORTUNITIES IN DESIGNING NANOSTRUCTURED CARBON

The knowledge base on nanostructured carbon materials has increased dramatically over the past decade, in terms of better controlled synthesis methods (for different types of materials, nanoarchitectures, and uniformity of the resulting products), posttreatment procedures to tune the carbon materials' properties and functionalities, and in terms of a more advanced understanding of the microstructure and resulting chemical and mechanical properties. These advances have enabled the development of novel nanostructured carbon materials for a large variety of applications from polymer composites to catalysts and adsorbents, materials for advanced energy applications (from energy storage—Li-ion batteries, supercapacitors—to energy conversion—fuel cells, solar devices) and C-MEMS and C-NEMS.

In the area of energy, the use of CNTs in battery electrodes enables large electrode–electrolyte contact areas for Li-ion batteries, new storage mechanisms that are not possible in bulk materials, and shorter pathways for both electron and ion transport [27, 30]. For applications in supercapacitors, CNTs offer interesting new possibilities when used in composite materials and to develop electrodes [7]. In dye-sensitized solar cells (DSSCs), nanocarbons can improve charge separation and electron transport and offer novel possibilities for a more efficient architecture, for example, to improve electron collection or develop transparent counter electrodes [31]. In PEM (proton exchange membrane) fuel cells, the use of nanocarbons allow to obtain a more efficient metal dispersions (e.g., lower noble metal loading), improve the stability of the electrodes, and lead to optimal hierarchically organized designs for the electrodes to reduce mass transfer limitations [31].

In catalysis, nanocarbons also have a tremendous potential [9], although still it is not exploited commercially. This is mainly because their

nanostructure has not been fully understood yet, especially in terms of defects, surface functionalities, and heteroatoms that affect their catalysis behavior. The rich nanocarbon surface chemistry is starting to be better understood [8], but a better identification of the relationship between the nature of the active sites and their specific catalytic reactivity is necessary. In general, the reactivity of nanocarbons and their functional properties explained for the other applications we introduced here (including C-MEMS and C-NEMS) are to a large extent associated with the presence of defects and edge sites, doping heteroatoms, and the interaction between these sites. The limited capability of controlling these aspects of nanocarbons is the current limitation for scaling up to larger-scale utilizations.

In C-MEMS and C-NEMS, many novel possibilities exist, as shown in the previous sections. In addition, to graphene and CNTs, other types of nanocarbon materials, including hybrid systems, are available today. In general, these materials offer many new opportunities compared to silicon or even than the more conventional types of carbons such as GC. It should also be mentioned that many methods are available for controlling the intrinsic properties of graphene and CNTs, such as doping, introduction of surface functional groups, and creation of hybrid nanocarbon materials with other types of nanocarbons (e.g., fullerene-type molecules grafted to graphene or CNTs) or with metal or metal oxide nanoparticles. There is thus a plethora of possibilities to tune the properties of nanocarbons and enhance their performance in applications such as sensing and actuating systems as presented earlier.

Integration of nanocarbon materials in commercial C-micro and C-nano devices is still a major challenge, especially in terms of large-volume manufacturing of such devices with reproducible performance. There are, in general, two possible approaches to solve this conundrum: (1) integrated processes to fabricate nanocarbons (e.g., graphene or CNTs) together with other components directly onto the same wafer and (2) transfer processes where we prepare first the high-quality nanocarbons (on a different substrate) and then transfer them to a C-MEMS and C-NEMS device. While the first method is preferable in theory, it often lacks the capability to produce high-quality nanocarbons, which are necessary to achieve good performances. On the other hand, the second approach may lack the capability to attain specific nanoarchitecture that are relevant for the properties and functional behavior of the nanocarbon materials. Therefore, an optimal approach is probably a combination of these two pathways.

It should also be mentioned that posttreatment of the obtained carbon materials to tune or modify their properties has been scarcely utilized in

C-MEMS, but as shortly introduced before, it is a great opportunity to improve their performance.

As a general concluding remark, and as outlined in the previous sections, not only the nanostructure itself is relevant but also the specific characteristics of the nanocarbons (type of defects, surface functional groups, heteroatoms, nanoarchitecture, etc.) that determine their performances. A single CNT can go from metallic to insulating behavior, passing through a semiconductor behavior, even if, formally, the nanostructure is the same. The method of preparation should account for these aspects but a detailed characterization of the carbon nanomaterials remains mandatory. These considerations are valid in general for all types of carbon nanomaterial applications, including the emerging area of energy storage and conversion [7] as well as catalysis [8, 9]. Knowledge in these scientific areas is growing rapidly, with special emphasis on controlled synthesis of nanocarbons, their posttreatment, and understanding of the nature of defects and surface functional groups. This has been achieved by combining novel characterization methodologies with theoretical modeling. This knowledge can now be used for setting a quantum leap forward in C-MEMS and C-NEMS and achieving superior device performance.

REFERENCES

[1] Messina, G., and S. Santangelo. 2006. *Carbon Topics in Applied Physics*. Vol. 100. Berlin, Germany: Springer.

[2] Serp, P., and B. Machado. 2015. *Nanostructured Carbon Materials for Catalysis*. RSC Catalysis Series.

[3] Gogotsi, Y., and V. Presser. 2014. *Carbon Nanomaterials*. 2nd ed. Boca Raton, FL: CRC Press.

[4] Da, L. 2006. *Carbon Nanotechnology*. Amsterdam, Netherlands: Elsevier.

[5] Tanaka, K., and S. Iijima. 2014. *Carbon Nanotubes and Graphene*. 2nd ed. Amsterdam, Netherlands: Elsevier.

[6] Lu, W., J.-B. Baek, and L. Dai. 2015. *Carbon Nanomaterials for Advanced Energy Systems: Advances in Materials Synthesis and Device Applications*. Hoboken, NJ: Wiley.

[7] Su, D.S., and G. Centi. 2013. "A Perspective on Carbon Materials for Future Energy Application." *Journal of Energy Chemistry* 22, no. 2, pp. 151–73. doi: http://dx.doi.org/10.1016/s2095-4956(13)60022-4

[8] Centi, G., S. Perathoner, and D.S. Su. 2014. "Nanocarbons: Opening New Possibilities for Nano-Engineered Novel Catalysts and Catalytic Electrodes." *Catalysis Surveys from Asia* 18, no. 4, pp. 149–63. doi: http://dx.doi.org/10.1007/s10563-014-9172-0

[9] Su, D.S., S. Perathoner, and G. Centi. 2013. "Nanocarbons for the Development of Advanced Catalysts." *Chemical Reviews* 113, no. 8, pp. 5782–16. doi: http://dx.doi.org/10.1021/cr300367d

[10] Zang, X., Q. Zhou, J. Chang, Y. Liu, and L. Lin. 2015. "Graphene and Carbon Nanotube (CNT) in MEMS/NEMS Applications." *Microelectronic Engineering* 132, pp. 192–206. doi: http://dx.doi.org/10.1016/j.mee.2014.10.023

[11] Hummelgen, I.A., N.J. Coville, I. Cruz-Cruz, and R. Rodrigues. 2014. "Carbon Nanostructures in Organic WORM Memory Devices." *Journal of Material Chemistry C: Materials for Optical and Electronic Devices* 2, no. 37, pp. 7708–14. doi: http://dx.doi.org/10.1039/c4tc00816b

[12] Sharma, S., and M. Madou. 2012. "Micro and Nano Patterning of Carbon Electrodes for Biomems." *Bioinspired, Biomimetic and Nanobiomaterials* 1, no. 4, pp. 252–65. doi: http://dx.doi.org/10.1680/bbn.12.00010

[13] Liao, M., and Y. Koide. 2011. "Carbon-Based Materials: Growth, Properties, MEMS/NEMS Technologies, and MEM/NEM Switches." *Critical Reviews in Solid State and Materials Sciences* 36, no. 2, pp. 66–101. doi: http://dx.doi.org/10.1080/10408436.2011.572748

[14] Hanein, Y. 2010. "Carbon Nanotube Integration into MEMS Devices." *Physica Status Solidi B: Basic Solid State Physics* 247, no. 11–12, pp. 2635–40. doi: http://dx.doi.org/10.1002/pssb.201000109

[15] Podyacheva, O.Yu., and Z.R. Ismagilov. 2015. "Nitrogen-Doped Carbon Nanomaterials: To the Mechanism of Growth, Electrical Conductivity and Application in Catalysis." *Catalysis Today* 249, pp. 12–22. doi: http://dx.doi.org/10.1016/j.cattod.2014.10.033

[16] Gebhardt, P., and D. Eder. 2014. *Nanocarbon-Inorganic Hybrids*, eds. D. Eder and R. Schlögl, 3–23. Berlin, Germany: De Gruyter Pub.

[17] Shi, H., Y. Shen, F. He, Y. Li, A. Liu, S. Liu, and Y. Zhang. 2014. "Recent Advances of Doped Carbon as Non-Precious Catalysts for Oxygen Reduction Reaction." *Journal of Material Chemistry A: Material for Energy and Sustainability* 2, no. 38, pp. 15704–16. doi: http://dx.doi.org/10.1039/c4ta02790f

[18] Chen, Y., and X. Sun. 2013. *Applications of Carbon Nanotubes*, ed. A.K. Mishra, 195–210. New York, NY: Nova Pub.

[19] Jana, D., C.-L. Sun, L.-C. Chen, and K.-H. Chen. 2013. "Effect of Chemical Doping of Boron and Nitrogen on the Electronic, Optical, and Electrochemical Properties of Carbon Nanotubes." *Progress in Materials Science* 58, no. 5, pp. 565–635. doi: http://dx.doi.org/10.1016/j.pmatsci.2013.01.003

[20] Rinaldi, A. 2010. *Synthesis of Carbon Nanotubes on Carbon supports and the Purification of Carbon Nanotubes*. Jakarta.

[21] Vogel, F.L., G.M.T. Foley, C. Zeller, E.R. Falardeau, and J. Gan. 1977. "High Electrical Conductivity in Graphite Intercalated with Acid Fluorides." *Materials Science and Engineering* 31, pp. 261–65. doi: http://dx.doi.org/10.1016/0025-5416(77)90043-x

[22] Liang, C., Z. Li, and S. Dai. 2008. "Mesoporous Carbon Materials: Synthesis and Modification." *Angewandte Chemie International Edition* 47, no. 20, pp. 3696–717. doi: http://dx.doi.org/10.1002/anie.200702046

[23] Wu, X.-L., and A.-W. Xu. 2014. "Carbonaceous Hydrogels and Aerogels for Supercapacitors." *Journal of Materials Chemistry A: Materials for Energy and Sustainability* 2, no. 14, pp. 4852–64. doi: http://dx.doi.org/10.1039/c3ta13929h

[24] Desimoni, E., and B. Brunetti. 2012. "Glassy Carbon Electrodes Film-Modified with Acidic Functionalities. A Review." *Electroanalysis* 24, no. 7, pp. 1481–500. doi: http://dx.doi.org/10.1002/elan.201200125

[25] Frackowiak, E., and F. Beguin. 2001. "Carbon Materials for the Electrochemical Storage of Energy in Capacitors." *Carbon* 39, no. 6, pp. 937–50. doi: http://dx.doi.org/10.1016/s0008-6223(00)00183-4

[26] McCreery, R.L. 2008. "Advanced Carbon Electrode Materials for Molecular Electrochemistry." *Chemical Reviews* 108, no. 7, pp. 2646–87. doi: http://dx.doi.org/10.1021/cr068076m

[27] Centi, G., and S. Perathoner. 2011. *ChemSusChem* 4, 913.

[28] Liu, M., V.I. Artyukhov, H. Lee, F. Xu, and B.I. Yakobson. 2013. "Carbyne from First Principles: Chain of C Atoms, a Nanorod or a Nanorope." *ACS Nano* 7, no. 11, pp. 10075–82. doi: http://dx.doi.org/10.1021/nn404177r

[29] Centi, G., and S. Perathoner. 2011. "Creating and Mastering Nano-Objects to Design Advanced Catalytic Materials." *Coordination Chemistry Reviews* 255, no. 13–14, pp. 1480–98. doi: http://dx.doi.org/10.1016/j.ccr.2011.01.021

[30] Su, D.S., G. Centi, and S. Perathoner. 2012. "Catalysis on Nano-Carbon Materials: Going Where to?" *Catalysis Today* 186, no. 1, pp. 1–6. doi: http://dx.doi.org/10.1016/j.cattod.2012.04.002

[31] Centi, G., and S. Perathoner. 2009. "The Role of Nanostructure in Improving the Performance of Electrodes for Energy Storage and Conversion." *European Journal Inorganic Chemistry* 26, pp. 3851–78. doi: http://dx.doi.org/10.1002/ejic.200900275

[32] Zhao, Y,-L., and J.F. Stoddart. 2009. "Noncovalent Functionalization of Single-Walled Carbon Nanotubes." *Accounts of Chemical Research* 42, no. 8, pp. 1161–71. doi: http://dx.doi.org/10.1021/ar900056z

[33] Reznik, D., C.H. Olk, D.A. Neumann, and J.R.D. Copley. 1995. "X-Ray Powder Diffraction from Carbon Nanotubes and Nanoparticles." Physical Review B 52, no. 1, pp. 116–25. http://dx.doi.org/10.1103/physrevb.52.116

[34] Amelinckx, S., and D. Bernaerts. 1998. "Supercarbon, Synthesis, Properties and Application." In *Springer Series in Materials Science*, eds. Y. Yoshimura and R.P.H. Chang, 51–80. Berlin, Germany: Springer.

[35] Belin, T., and F. Epron. 2005. "Characterization Methods of Carbon Nanotubes: A Review." *Materials Science Engineering B* 119, no. 2, pp. 105–18. doi: http://dx.doi.org/10.1016/j.mseb.2005.02.046

[36] Gusev, A.I. 2007. *Nanomaterials, Nanostructures, and Nanotechnologies*. Moscow, Russia: Fizmatlit.

[37] Su, D.S., J.-O. Müller, R.E. Jentoft, D. Rothe, E. Jacob, and R. Schlögl. 2004. "Fullerene-Like Soot from EuroIV Diesel Engine: Consequences for Catalytic Automotive Pollution Control." *Topics in Catalysis* 30–31, pp. 241–45. doi: http://dx.doi.org/10.1023/b:toca.0000029756.50941.02

[38] Homann, K. 1998. "Fullerenes and Soot Formation—New Pathways to Large Particles in Flames." *Angewandte Chemie International Edition* 37, no. 18, pp. 2434–51. doi: http://dx.doi.org/10.1002/(sici)1521-3773(19981002)37:18%3C2434::aid-anie2434%3E3.0.co;2-l

[39] Kroto, H.W. 1988. "Space, Stars, C60, and Soot." *Science* 242, no. 4882, p. 1139–45. doi: http://dx.doi.org/10.1126/science.242.4882.1139

[40] Müller, J., D. Su, R. Jentoft, J. Kröhnert, F. Jentoft, and R. Schlögl. 2005. "Morphology-Controlled Reactivity of Carbonaceous Materials Towards Oxidation." *Catalysis Today* 102–103, pp. 259–265. doi: http://dx.doi.org/10.1016/j.cattod.2005.02.025

[41] Cataldo, F. 2002. "The Impact of a Fullerene-Like Concept in Carbon Black Science." *Carbon* 40, no. 2, pp. 157–62. doi: http://dx.doi.org/10.1016/s0008-6223(01)00167-1

[42] Geim, A.K., and K.S. Novoselov. 2007. "The Rise of Graphene." *Nature Materials* 6, no. 3, pp. 183–91. doi: http://dx.doi.org/10.1038/nmat1849

[43] Riedl, C., C. Coletti, and U. Starke. 2010. "Structural and Electronic Properties of Epitaxial Graphene on SiC(0 0 0 1): A Review of Growth, Characterization, Transfer Doping and Hydrogen Intercalation." *Journal of Physics D: Applied Physics* 43, no. 37, pp. 374009–26. doi: http://dx.doi.org/10.1088/0022-3727/43/37/374009

[44] Liu, H., Y. Liu, and D. Zhua. 2011. "Chemical Doping of Graphene." *Journal of Matererials Chemistry* 21, no. 10, pp. 3335–45. doi: http://dx.doi.org/10.1039/c0jm02922j

[45] Ivanovskii, A.L. 2012. "Graphene-Based and Graphene-Like Materials." *Russian Chemical Review* 81, no. 7, pp. 571–605. doi: http://dx.doi.org/10.1070/rc2012v081n07abeh004302

[46] Wang, X., G. Sun, P. Routh, D.-H. Kim, W. Huang, and P. Chen. 2014. "Heteroatom-Doped Graphene Materials: Syntheses, Properties and Applications." *Chemical Society Reviews* 43, no. 20, pp. 7067–98. doi: http://dx.doi.org/10.1039/c4cs00141a

[47] Terrones, H., R. Lv, M. Terrones, and M.S. Dresselhaus. 2012. "The Role of Defects and Doping in 2D Graphene Sheets and 1D Nanoribbons." *Reports on Progress Physics* 75, no. 6, pp. 062501–31. doi: http://dx.doi.org/10.1088/0034-4885/75/6/062501

[48] Hopcroft, M.A., W.D. Nix, and T.W. Kenny. 2010. "What Is the Young's Modulus of Silicon?" *Journal of Microelectromechanical Systems* 19, no. 2, pp. 229–38. doi: http://dx.doi.org/10.1109/jmems.2009.2039697

[49] Wen, M., X. Sun, L. Su, J. Shen, J. Li, and S. Guo. 2012. "The Electrical Conductivity of Carbon Nanotube/Carbon Black/Polypropylene Composites Prepared Through Multistage Stretching Extrusión." *Polymer* 53, no. 7, pp. 1602–10. doi: http://dx.doi.org/10.1016/j.polymer.2012.02.003

[50] Baughman, R.H., A.A. Zakhidov, and W.A. de Heer. 2002. "Carbon Nanotubes—the Route Toward Applications." *Science* 297, no. 5582, pp. 787–92. doi: http://dx.doi.org/10.1126/science.1060928

[51] Lu, X., and Z. Chen. 2005. "Curved Pi-Conjugation, Aromaticity, and the Related Chemistry of Small Fullerenes." *Chemical Reviews* 105, no. 10, pp. 3643–96. doi: http://dx.doi.org/10.1021/cr030093d

[52] Avouris, P., and R. Martel. 2010. "Progress in Carbon Nanotube Electronics and Photonics." *MRS Bulletin* 35, no. 4, pp. 306–13. doi: http://dx.doi.org/10.1557/mrs2010.553

[53] Liu, S., Q. Shen, Y. Cao, L. Gan, Z.X. Wang, M.L. Steigerwald, and X.F. Guo. 2010. "Chemical Functionalization of Single-Walled Carbon Nanotube Field-Effect Transistors as Switches and Sensors." *Coordination Chemistry Reviews* 254, no. 9–10, pp. 1101–16. doi: http://dx.doi.org/10.1016/j.ccr.2009.11.007

[54] Schueller, O.J.A., S.T. Brittain, C. Marzolin, and G.M. Whitesides. 1997. "Fabrication and Characterization of Glassy Carbon MEMS." *Chemistry of Materials* 9, no. 6, pp. 1399–1406. doi: http://dx.doi.org/10.1021/cm960639v

[55] Luo, J.K.Y., Q. Fu, H.R. Le, J.A. Williams, S.M. Spearing, and W.I. Milne. 2007. "Diamond and Diamond-Like Carbon MEMS." *Journal of Micromechanics and Microengineering* 17, no. 7, pp. S147–63. doi: http://dx.doi.org/10.1088/0960-1317/17/7/s12

[56] Hoekstra, K.J., and T. Bein. 1996. "Adsorption of Zirconium−Phosphonate Multilayers onto Phosphate-Derivatized Glassy Carbon Substrates." *Chemistry of Materials* 8, no. 8, pp. 1865–70. doi: http://dx.doi.org/10.1021/cm960147i

[57] Yu, M.F., O. Lourie, M.J. Dyer, K. Moloni, T.F. Kelly, and R.S. Ruoff. 2000. "Strength and Breaking Mechanism of Multiwalled Carbon Nanotubes Under Tensile Load." *Science* 287, no. 5453, pp. 637–40. doi: http://dx.doi.org/10.1126/science.287.5453.637

[58] Palaci, I., S. Fedrigo, H. Brune, C. Klinke, M. Chen, and E. Riedo. 2005. "Radial Elasticity of Multiwalled Carbon Nanotubes." *Physical Review Letters* 94, no. 17, pp. 175502–06. doi: http://dx.doi.org/10.1103/physrevlett.94.175502

[59] Mallick, P.K. 1993. *Fibre-Reinforced Composites*. New York, NY: Marcel Dekkar, Inc.

[60] Zhang, H., Z. Zhang, and C. Breidt. 2004. "Comparison of Short Carbon Fibre Surface Treatments on Epoxy Composites." *Composites Science and Technology* 64, no. 13–14, pp. 2021–29. doi: http://dx.doi.org/10.1016/j.compscitech.2004.02.009

[61] Schlögl, R. 2008. *Handbook of Heterogeneous Catalysis*, eds. G. Ertl, H. Knözinger, F. Schüth, and J. Weitkamp, 357–427. Weinheim, Germany: Wiley-VCH.

[62] Downs, W., and R. Baker. 1991. "Novel Carbon Fiber-Carbon Filament Structures." *Carbon* 29, no. 8, pp. 1173–79. doi: http://dx.doi.org/10.1016/0008-6223(91)90035-h

[63] Xia, W., X. Chen, S. Kundu, X. Wang, G. Grundmeier, Y. Wang, M. Bron, W. Schuhmann, and M. Muhler. 2007. "Chemical Vapor Synthesis of Secondary Carbon Nanotubes Catalyzed by Iron Nanoparticles Electrodeposited on Primary Carbon Nanotubes." *Surface and Coatings*

Technology 201, no. 22–23, pp. 9232–37. doi: http://dx.doi.org/10.1016/j.surfcoat.2007.05.031

[64] Bron, M., W. Xia, X. Chen, C. Jin, S. Kundu, T. Nagaiah, R. Chetty, T.Schilling, N. Li, W. Schuhmann, and M. Muhler. 2009. "Elektrokatalyse in Brennstoffzellen Und Elektrolyseuren: Kohlenstoff-Nanoröhren-Basierte Katalysatoren Und Neuartige Untersuchungsmethoden." *Chemie Ingenieur Technik* 81, no. 5, pp. 581–89. doi: http://dx.doi.org/10.1002/cite.200900013

[65] Duan, H., J. Liang, and Z. Xia. 2010. "Synthetic Hierarchical Nanostructures: Growth of Carbon Nanofibers on Microfibers by Chemical Vapor Deposition." *Materials Science and Engineering B* 166, no. 3, pp. 190–95. doi: http://dx.doi.org/10.1016/j.mseb.2009.11.019

[66] Handuja, S., P. Srivastava, and V. Vankar. 2009. "Utilization of Catalyst Deactivation for the Growth of Aligned and Random Carbon Nanotubes by a Single-Step Process." *Physica E: Low-Dimensional Systems and Nanostructures* 41, no. 7, pp. 1210–16. doi: http://dx.doi.org/10.1016/j.physe.2009.02.006

[67] Thostenson, E.T., W.Z. Li, D.Z. Wang, Z.F. Ren, and T.W. Chou. 2002. "Carbon Nanotube/Carbon Fiber Hybrid Multiscale Composites." *Journal of Applied Physics* 91, no. 9, p. 6034. doi: http://dx.doi.org/10.1063/1.1466880

[68] Lim, S., S. Yoon, Y. Shimizu, H. Jung, and I. Mochida. 2004. "Surface Control of Activated Carbon Fiber by Growth of Carbon Nanofiber." *Langmuir* 20, no. 13, pp. 5559–63. doi: http://dx.doi.org/10.1021/la036077t

[69] Down, W., and R. Baker. 1995. "Modification of the Surface Properties of Carbon Fibers via the Catalytic Growth of Carbon Nanofibers." *Journal of Materials Research* 10, no. 3, pp. 625–33. doi: http://dx.doi.org/10.1557/jmr.1995.0625

[70] Kurachi, H., S. Uemura, J. Yotani, T. Nagasako, H. Yamada, T. Ezaki, T. Maesoba, T. Nakao, M. Ito, A. Sakurai, H. Shimoda, Y. Saito, and H. Shinohara. 2006. "Formation of Secondary Thin Carbon Nanotubes on Thick Ones and Improvement in Field-Emission Uniformity." *Japanese Journal of Applied Physics* 45, no. 6A, pp. 5307–10. doi: http://dx.doi.org/10.1143/jjap.45.5307

[71] Li, N., X. Chen, L. Stoica, W. Xia, J. Qian, J. Aßmann, W. Schuhmann, and M. Muhler. 2007. "The Catalytic Synthesis of Three-Dimensional Hierarchical Carbon Nanotube Composites with High Electrical Conductivity Based on Electrochemical Iron Deposition." *Advanced Materials* 19, no. 19, pp. 2957–60. doi: http://dx.doi.org/10.1002/adma.200602625

[72] Zhang, J., Y. Hu, J. Tessonnier, G. Weinberg, J. Maier, R. Schlögl, and D.S. Su. 2008. "CNFs@CNTs: Superior Carbon for Electrochemical Energy Storage." *Advanced Materials* 20, no. 8, pp. 1450–55. doi: http://dx.doi.org/10.1002/adma.200701685

[73] Mestl, G., N.I. Maksimova, N. Keller, V.V. Roddatis, and R. Schlögl. 2001. "Carbon Nanofilaments in Heterogeneous Catalysis: An Industrial Application for New Carbon Materials?" *Angew Chemie International Edition* 40, no. 11, pp. 2066–68. doi: http://dx.doi.org/10.1002/1521-3773(20010601)40:11%3C2066::aid-anie2066%3E3.3.co;2-9

[74] Su, D., N. Maksimova, J. Delgado, N. Keller, G. Mestl, M. Ledoux, and R. Schlögl. 2005. "Nanocarbons in Selective Oxidative Dehydrogenation Reaction." *Catalysis Today* 102–103, pp. 110–14. doi: http://dx.doi.org/10.1016/j.cattod.2005.02.012

[75] Delgado, J., D. Su, G. Rebmann, N. Keller, A. Gajovic, and R. Schlögl. 2006. "Immobilized Carbon Nanofibers as Industrial Catalyst for ODH Reactions." *Journal of Catalysis* 244, no. 1, pp. 126–29. doi: http://dx.doi.org/10.1016/j.jcat.2006.08.007

[76] Furimsky, E. 2008. *Carbons and Carbon-Supported Catalysts in Hydroprocessing*. Royal Society of Chemistry.

[77] Rodríguez-reinoso, F. 1998. "The Role of Carbon Materials in Heterogeneous Catalysis." *Carbon* 36, no. 3, pp. 159–75. doi: http://dx.doi.org/10.1016/s0008-6223(97)00173-5

[78] Rodriguez, N.M., M. Kim, and R.T.K. Baker. 1994. "Carbon Nanofibers: A Unique Catalyst Support Medium." *Journal of Physical Chemistry* 98, no. 50, pp. 13108–11. doi: http://dx.doi.org/10.1021/j100101a003

[79] Baker, R.T.K., K. Laubernds, A. Wootsch, and Z. Paál. 2000. "Pt/Graphite Nanofiber Catalyst in n-Hexane Test Reaction." *Journal of Catalysis* 193, no. 1, pp. 165–67. doi: http://dx.doi.org/10.1006/jcat.2000.2886

[80] Wu, G., Y. Chen, and B. Xu. 2005. "Remarkable Support Effect of SWNTs in Pt Catalyst for Methanol Electrooxidation." *Electrochemistry Communications* 7, no. 12, pp. 1237–43. doi: http://dx.doi.org/10.1016/j.elecom.2005.07.015

[81] Su, D.S., X. Chen, G. Weinberg, A. Klein-Hofmann, O. Timpe, S.B.A. Hamid, and R. Schlögl. 2005. "Hierarchically Structured Carbon: Synthesis of Carbon Nanofibers Nested Inside or Immobilized onto Modified Activated Carbon." *Angewandte Chemie International Edition* 44, no. 34, pp. 5488–92. doi: http://dx.doi.org/10.1002/anie.200500685

[82] Chen, X., D.S. Su, S.B. Hamid, and R. Schlögl. 2007. "The Morphology, Porosity and Productivity Control of Carbon Nanofibers or Nanotubes on Modified Activated Carbón." *Carbon* 45, no. 4, pp. 895–98. doi: http://dx.doi.org/10.1016/j.carbon.2006.12.005

[83] Ledoux, M., and C. Pham-Huu. 2005. "Carbon Nanostructures with Macroscopic Shaping for Catalytic Applications." *Catalysis Today* 102–03, pp. 2–14. doi: http://dx.doi.org/10.1016/j.cattod.2005.02.036

[84] Louis, B., R. Vieira, A. Carvalho, J. Amadou, M. Ledoux, and C. Pham-Huu. 2007. "Carbon Nanofibers Grown Over Graphite Supported Ni Catalyst: Relationship Between Octopus-Like Growth Mechanism and Macro-shaping." *Topics in Catalysis* 45, no. 1–4, pp. 75–80. doi: http://dx.doi.org/10.1007/s11244-007-0243-6

[85] Pham-Huu, C., and M. Ledoux. 2006. "Carbon Nanomaterials with Controlled Macroscopic Shapes as New Catalytic Materials." *Topics in Catalysis* 40, no. 1–4, pp. 49–63. doi: http://dx.doi.org/10.1007/s11244-006-0104-8

[86] Serp, P., and J.L. Figueiredo. 2008. *Carbon Materials for Catalysis*. Hoboken, NJ: John Wiley and Sons.

[87] Derbyshire, F., V. de Beer, G. Abotsi, A. Scaroni, J. Solar, and D. Skrovanek. 1986. "The Influence of Surface Functionality on the Activity of Carbon-supported Catalysts." *Applied Catalysis* 27, no. 1, pp. 117–31. doi: http://dx.doi.org/10.1016/s0166-9834(00)81051-9

[88] Tessonnier, J., D. Rosenthal, F. Girgsdies, J. Amadou, D. Begin, C. Pham-Huu, D.S. Su, and R. Schlögl. 2009. "Influence of the Graphitisation of Hollow Carbon Nanofibers on Their Functionalisation and Subsequent Filling with Metal Nanoparticles." *Chemical Communications*, no. 46, pp. 7158–60. doi: http://dx.doi.org/10.1039/b916150c

[89] Toebes, M.L., F.F. Prinsloo, J.H. Bitter, A.J. van Dillen, and K.P. de Jong. 2003. "Influence of Oxygen-Containing Surface Groups on the Activity and Selectivity of Carbon Nanofiber-Supported Ruthenium Catalysts in the Hydrogenation of Cinnamaldehyde." *Journal of Catalysis* 214, no. 1, pp. 78–87. doi: http://dx.doi.org/10.1016/s0021-9517(02)00081-7

[90] Baker, R.T.K., and J.J. Chludzinski. 1986. "In-Situ Electron Microscopy Studies of the Behavior of Supported Ruthenium Particles. 2. Carbon Deposition from Catalyzed Decomposition of Acetylene." *Journal of Physical Chemistry* 90, no. 20, pp. 4734–38. doi: http://dx.doi.org/10.1021/j100411a005

[91] Zhang, Y., M.L. Toebes, A. van der Eerden, W.E. O'Grady, K.P. de Jong

[92] Koningsberger, D.C. 2004. *Journal of Physical Chemistry B* 108, pp. 18509–19.

[93] Meng, L., C. Fu, and Q. Lu. 2009. *Progress in Natural Science* 19, pp. 801–81.

[94] Ma, P.-C., N.A. Siddiqui, G. Marom, and J.-K. Kim. 2010. "Dispersion and Functionalization of Carbon Nanotubes for Polymer-based Nanocomposites: A Review." *Composites: Part A* 41, no. 10, pp. 1345–67. doi: http://dx.doi.org/10.1016/j.compositesa.2010.07.003

[95] Qian, D., G.J. Wagner, W.K. Liu, M.F. Yu, and R.S. Ruoff. 2002. "Mechanics of Carbon Nanotubes." *Applied Mechanics Reviews* 55, no. 6, pp. 495–533. doi: http://dx.doi.org/10.1115/1.1490129

[96] Reich, S., C. Thomsen, and J. Maultzsch. 2004. *Carbon Nanotubes: Basic Concepts and Physical Properties*, 31–40. Wiley-VCH.

[97] Koo, J.H. 2006. *Polymer Nanocomposites: Processing, Characterization, and Applications*, 1–8. New York, NY: McGraw-Hill.

[98] Xie, X.L., Y.W. Mai, and X.P. Zhou. 2005. "Dispersion and Alignment of Carbon Nanotubes in Polymer Matrix: A Review." *Materials Science Engineering R* 49, no. 4, pp. 89–112. doi: http://dx.doi.org/10.1016/j.mser.2005.04.002

[99] Jensen, K., K. Kim, and A. Zettl. 2008. "An Atomic-Resolution Nanomechanical Mass Sensor." *Nature Nanotechnology* 3, no. 9, pp. 533–37. doi: http://dx.doi.org/10.1038/nnano.2008.200

[100] Biswas, C., and Y.H. Lee. 2011. "Graphene Versus Carbon Nanotubes in Electronic Devices." *Advanced Functional Materials* 21, no. 20, pp. 3806–26. doi: http://dx.doi.org/10.1002/adfm.201101241

[101] Javey, A., J. Guo, Q. Wang, M. Lundstrom, and H. Dai. 2003. "Ballistic Carbon Nanotube Field-Effect Transistors." *Nature* 424, no. 6949, pp. 654–57. doi: http://dx.doi.org/10.1038/nature01797

[102] Fam, D.W.H., A. Palaniappan, A.I.Y. Tok, B. Liedberg, and S.M. Moochhala. 2011. "A Review on Technological Aspects Influencing Commercialization of Carbon Nanotube Sensors." *Sensors and Actuators B* 157, no. 1, pp. 1–7. doi: http://dx.doi.org/10.1016/j.snb.2011.03.040

[103] Jiang, Y.Q., P.B. Wang, and L.W. Lin. 2011. "Characterizations of Contact and Sheet Resistances of Vertically Aligned Carbon Nanotube Forests with Intrinsic Bottom Contacts." *Nanotechnology* 22, no. 36, pp. 365704–12. doi: http://dx.doi.org/10.1088/0957-4484/22/36/365704

[104] Kawano, T., H.C. Chiamori, M. Suter, Q. Zhou, B.D. Sosnowchik, and L.W. Lin. 2007. "An Electrothermal Carbon Nanotube Gas Sensor." *Nano Letters* 7, no. 12, pp. 3686–90. doi: http://dx.doi.org/10.1021/nl071964s

[105] Hayamizu, Y., T. Yamada, K. Mizuno, R.C. Davis, D.N. Futaba, M. Yumura, and K. Hata. 2008. "Integrated Three-Dimensional Microelectromechanical Devices from Processable Carbon Nanotube Wafers." *Nature Nanotechnology* 3, no. 5, pp. 289–94. doi: http://dx.doi.org/10.1038/nnano.2008.98

[106] Cheng, Z.G., Q.Y. Zhou, C.X. Wang, Q.A. Li, C. Wang, and Y. Fang. 2011. "Toward Intrinsic Graphene Surfaces: A Systematic Study on Thermal Annealing and Wet-Chemical Treatment of SiO 2 -Supported Graphene Devices." *Nano Letters* 11, no. 2, pp. 767–71. doi: http://dx.doi.org/10.1021/nl103977d

[107] Eichler, A., J. Moser, J. Chaste, M. Zdrojek, I. Wilson-Rae, and A. Bachtold. 2011. "Nonlinear Damping in Mechanical Resonators Made from Carbon Nanotubes and Graphene." *Nature Nanotechnology* 6, no. 6, pp. 339–42. doi: http://dx.doi.org/10.1038/nnano.2011.71

[108] Loomis, J., B. King, T. Burkhead, P. Xu, N. Bessler, E. Terentjev, and B. Panchapakesan. 2012. "Graphene-Nanoplatelet-Based Photomechanical Actuators." *Nanotechnology* 23, no. 4, pp. 045501–12. doi: http://dx.doi.org/10.1088/0957-4484/23/4/045501

[109] Xie, X., L. Qu, C. Zhou, Y. Li, J. Zhu, H. Bai, G. Shi, and L. Dai. 2010. "An Asymmetrically Surface-Modified Graphene Film Electrochemical Actuator." *ACS Nano* 4, no. 10, pp. 6050–54. doi: http://dx.doi.org/10.1021/nn101563x

[110] Zhu, S.E., R. Shabani, J. Rho, Y. Kim, B.H. Hong, J.H. Ahn, and H.J. Cho. 2011. "Graphene-Based Bimorph Microactuators." *Nano Letters* 11, no. 3, pp. 977–81. doi: http://dx.doi.org/10.1021/nl103618e

CHAPTER 3

SYNTHESIS OF NANOCARBONS AND TUNING OF THEIR PROPERTIES

Sharifah Bee Abd Hamid[1], Gabriele Centi[2], and Siglinda Perathoner[2]

University of Malaya, Malaysia[1]; University of Messina, Italy[2]

3.1 INTRODUCTION

Carbon, because of the various microstructures (with quite different properties) in which it can be found, offers many possibilities for the development of a whole new range of applications in the area of microelectromechanical systems (MEMS) and nanoelectromechanical systems (NEMS). Also, as widely discussed in the rest of this book, such peculiar characteristics allow one to improve the performance of carbon-based devices used in many applications. The behavior of these carbon materials is also governed by their particular dimensionality type, for example, 1D (carbon nanotube [CNT] or other type of nanofilaments) or 2D (graphene), and depends to a large extent on their specific physical and chemical characteristics, such as structural defects, presence of functional groups, and heteroatoms. Therefore, a broad range of properties and characteristics may be reported for what is apparently the same type of nanocarbon utilized in say an NEMS and NEMS device.

The catalysis research field has witnessed ample growth over the past decade, developing new protocols and improving readily available ones, specifically for the preparation and modification of nanocarbon materials. This wide background of carbon catalysis knowledge is of great relevance for the preparation of novel or improved carbon-based

microelectromechanical systems (C-MEMS) and carbon-based nanoelectromechanical systems (C-NEMS) devices.

In this chapter, we present a short overview of the synthesis of nanocarbons and the tuning of their properties. Writing a full review on this topic is outside the scope of this book, so only selected aspects will be presented to reveal the complexity of the research field, the possibilities offered by it, and the relevance of these topics for C-MEMS and C-NEMS devices.

Among the wide class of nanomaterials currently available, CNTs or more general nanofilaments (which include various types of nanofibers and related systems) and graphene or graphene-like materials are those mostly used in C-MEMS and C-NEMS devices. Thus, our attention is mainly focused on those nanomaterials.

3.2 CARBON MATERIALS

3.2.1 NANOTUBE GROWTH METHODS

Figure 3.1 summarizes currently used CNTs synthesis methods. Three methods are commonly used for the production of CNTs. These are the arc discharge (AD), laser ablation (LA), and chemical vapor deposition (CVD) methods. Many new techniques are under continuous development, although their large-scale production capability or their effective advantages are not often verified or even revealed. Interestingly, most of the preparation methods rely on common experimental materials and parameters such as carbon feedstock, metal catalysts, and temperature control. Some methods such as LA and template or bottom-up are dedicated to the synthesis of single-walled carbon nanotubes (SWCNTs),

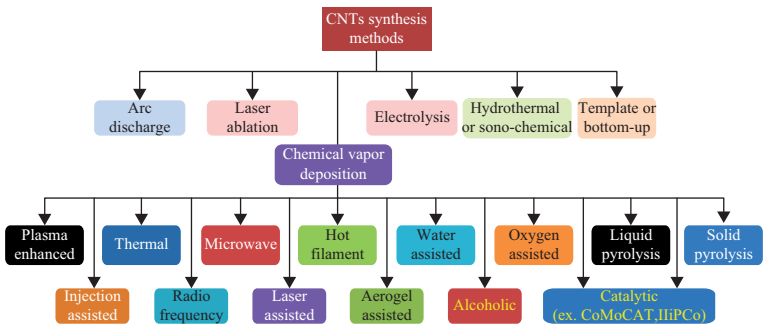

Figure 3.1. Currently available CNT synthesis methods.

whereas others such as CVD, electrolysis, and hydrothermal methods are more suitable for multiwalled carbon nanotubes (MWCNTs). AD is an old method that has been applied for the synthesis of both SWCNTs and MWCNTs. Furthermore, some interesting literature articles demonstrated the use of rapid and cheap domestic microwave oven techniques such as the metal complex method [1], the mixture method [2], the nanofiber method [3], and the nickel nanoparticle method [4] for producing MWCNTs. In addition, Kumar Singh and Pandey [5] used a simple autoclave and obtained CNTs with diameters in the range of 3 to 14 nm by decomposing acetone at 650°C without any metal catalyst.

Because of the many attractive features it provides, catalytic chemical vapor deposition (CCVD) is currently the most common technique to synthesize CNTs [6–11]. For instance, CCVD is (i) easy to implement on a large industrial scale, either in a fixed or in a, preferably, fluid-bed reactor, and using different types of carbon sources (in the gas phase) ranging from CO to hydrocarbons; (ii) a flexible process (although not easy to control) that enables one to finetune the characteristics of the produced CNTs within some range through a large number of process parameters; and (iii) quite effective, with mass production up to over 400 percent wt with respect to the catalyst weight, where the active catalytic element is typically a small percentage of the catalyst total mass.

The reaction leading to solid carbon formation must be thermodynamically stable under the chosen temperature and pressure conditions. In the case of the decomposition of hydrocarbons, the Gibbs free energy may become negative depending on the type of hydrocarbon. Methane decomposition, for example, is only thermodynamically favored at a temperature above 600°C, while temperatures above 200°C are enough for ethylene, acetylene, or benzene. However, the growth of CNTs also requires sufficient fast kinetics. Typically, for growth of CNTs from methane, temperatures above 850°C are necessary, while from acetylene and ethylene, temperatures of about 500°C to 750°C and 650°C to 850°C, respectively, are necessary. However, the temperature range required to produce *good-quality* CNTs (e.g., without amorphous carbon) is typically quite narrow (10°C to 20°C) and depends not only on the type of carbon source used but also on many other aspects (e.g., specific reactor configuration, flow conditions, composition, presence of H_2, and specific catalyst characteristics).

The early interpretation of the mechanism of growth of CNTs proposed by Baker and coworkers [12, 13] was based on the vapor–liquid–solid (VLS) model adapted to explain the mechanism of carbon filament growth. This model was developed by Wagner and Ellis to explain the growth of

Si whiskers [14] and is based on the three successive steps depicted in Figure 3.2a to c [12]. A hydrocarbon (or another carbon source) adsorbs and dissociates on the surface of the catalyst particle to form elementary carbon atoms. These are dissolved in the bulk of the catalyst nanoparticles to form a liquid metastable carbide and diffuse within the rest of the particle. Above a threshold (which depends on the solubility characteristics of carbon in the metal particle and thus on the type of metal and size of the nanoparticles), the solid carbon precipitates at the rear side of the nanoparticles to form carbon nanofilaments.

The VLS growth mechanism received large attention, as it explained that the apparent activation energy, measured for the growth of CNTs, fits the apparent activation energy for carbon dissolution in the metal (Fe, Co). The kinetic analysis of CNTs grown on iron was also in agreement with this mechanism [15]. However, more recent studies have questioned the validity of the VLS model [16]. At present, the main problem faced by this model is the uncertainty on the driving force that pushes carbon atoms to diffuse through the whole catalyst particle. With the dissociation of several hydrocarbons being an exothermic process and the precipitation of solid carbons an endothermic one, a driving force could be the temperature gradient within the catalyst nanoparticle [12]. However, this hypothesis fails to explain the growth when the dissociation of the carbon precursor is endothermic, such as in the case of alkanes [17].

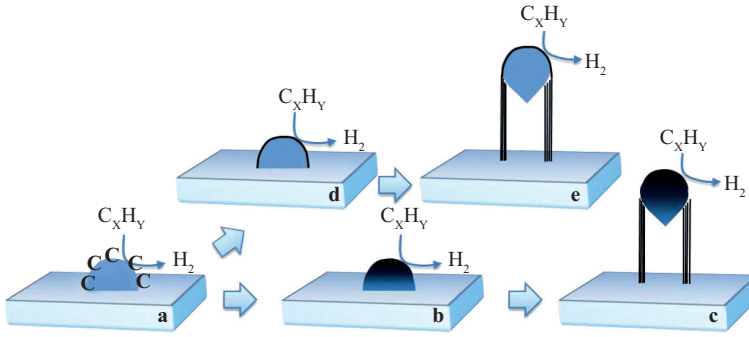

Figure 3.2. The three steps involved in the VLS mechanism: (a) decomposition of the carbon-containing precursor on the surface of the catalyst particle; (b) diffusion of carbon atoms through the particle as a solid solution; and (c) precipitation of carbon at the metal–support interface and formation of a nanofiber or a nanotube. In an alternative mechanism, carbon species diffuse only on the surface of the catalyst particle (d–e).

Source: Adapted from Tessonnier and Su [6].

A variation of the VLS mechanism presents the idea that carbon diffusion is confined to regions near the surface [18], which may explain why CNTs are hollow (see Figure 3.2d and e; the CNT grows below the metal nanoparticle, which is transported far from the surface of the support, leaving thus a hollow fiber). Furthermore, Audier et al. showed that there exists a strong correlation between the orientation of the carbon plane and the crystallography of the catalyst particle [19]. Many other studies support this hypothesis [20], as well as some theoretical calculations [21]. High-resolution transmission electron microscopy (HRTEM) showed that during the growth phase, the particle exhibits a pear-like morphology, similar to a melted metal droplet. For metals with a body-centered cubic (bcc) structure, the (100) axis of the particle coincides with the carbon tube axis [19]. The metal–gas interface is always on the (100) surface. For metals with a face-centered cubic (fcc) structure, the (110) axis is parallel to the tube axis. The metal–gas interface is always on the (111) plane in this case. This crystallographic relation between carbon walls and the metal particle supports the idea of a surface diffusion, rather than bulk diffusion, mechanism.

Time-resolved *in situ* HRTEM images of an MWCNT growing from a nickel particle [22] proved unambiguously that MWCNTs can grow from solid nickel particles through a mechanism involving the surface diffusion of carbon species. It should be remembered, however, that depending on the reaction temperature, type of metal and its interaction with the support, feed composition, and other parameters, the reaction mechanism may switch from surface to bulk. In general, the metal nanoparticle plays a crucial role in the growth of MWCNTs by CCVD, affecting structural parameters, such as the diameter of the CNTs and the orientation of the graphene sheets in the CNTs (see Figure 3.3).

The quality of the obtained CNTs is also greatly dependent on the metal nanoparticles used, in addition to the reaction conditions present during CCVD. An interesting example of this is provided in [11], with FeCo metal nanoparticles confined within the ordered mesopores of a (SBA-15) or located on the external surface of the SBA-15 matrix. The confinement of nanoparticles silica matrix within the mesoporous channels of SBA-15 determines that the nanoparticles have a size similar to that of the mesoporous channels, that is, around 6.5 nm. On the contrary, the nanoparticles located on the external surface of SBA-15 crystals have a larger diameter, around 23 nm (Figure 3.3a and b). The CNTs, which grow from these nanoparticles (with CCVD using propane as reactant), have a diameter similar to that of the nanoparticles. Interestingly, CNTs exhibit a very different nanostructure depending on their length. Large CNTs show

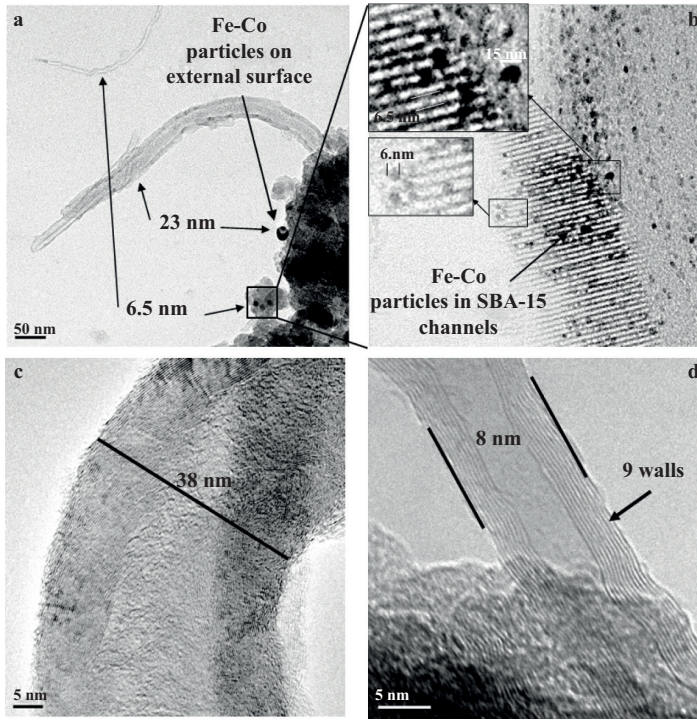

CNT walls are ordered at 45° respect to the growing axes

Graphene sheets are well ordered parallel to the growing direction

Figure 3.3. Top: HRTEM images of FeCo and SBA-15 catalyst, with HRTEM images of the larger (c) and smaller (d) CNTs obtained from FeCo nanoparticles located outside and inside the SBA-15 mesoporous channel, respectively.

Source: Adapted from Centi and Perathoner [11].

walls oriented at 45° with respect to the growing axes (Figure 3.3c). On the other hand, small MWCNTs have graphene sheets well ordered and parallel to the growing direction (Figure 3.3d). Moreover, large CNTs display a much more defective structure than that observed in small ones [11]. The presence of the metal nanoparticles within the mesoporous channels of SBA-15 induces thus an ordered growing of MWCNTs in reaction conditions when otherwise a less-ordered growing may occur. This example presents evidence that even if under strictly the same experimental conditions, the characteristics of the metal nanoparticles acting as catalyst may greatly influence the type and quality of the thus obtained CNTs, which have different functional properties. Therefore, when a dispersion

of metal nanoparticles is present, as typically occurs, different types of CNTs (with different properties) result.

The growth mechanism of SWCNTs is slightly different from that of MWCNTs [2, 23,]. Fe_xC_y and Ni_xC_y clusters quickly expel the carbon that dissolved in the bulk to the surface and subsurface of metal nanoparticles, after which a cap forms on the metal nanoparticles and the SWCNT starts growing. The chirality of SWCNTs, for example, the number of C5, C6, and C7 rings created during growth, strongly depends on the carbon precursor decomposition rate. A fast decomposition rate leads to a fast growth of SWCNTs. However, these SWCNTs contain many structural defects (high number of C5 and C7 rings), which can lead to a change of the chirality along the tube, thus resulting in intramolecular junctions of SWCNT sections with different electronic properties [24]. A slow decomposition rate gives the catalyst particle enough time to *heal* its structure, with mainly the formation of C6 rings and the chirality of the SWCNT defined by the nucleation of its cap. Some control of the SWCNT chirality can also be obtained from the composition of the catalyst particles [25]. Depending on the relative amount of Ni and Fe in the clusters, the crystallographic structure of the particles changes progressively from fcc (as for pure Ni) to bcc (as for pure Fe), which influences the metal–carbon binding as well as the cap structure. Semiconducting SWCNTs can be prepared with a 90 percent selectivity using $Ni_{0.27}Fe_{0.73}$ clusters [26], but in general, selectivity is lower. Therefore, also for SWCNTs, it is quite difficult to prepare strictly uniform samples. In general, to decrease the diameter of SWCNTs and the distribution of chiralities, the following aspects are relevant:

- Synthesize small catalyst particles, with a narrow size distribution.
- Modify the work of adhesion of carbon on the catalyst particle, for example, by modifying its elemental composition, in order to grow SWCNTs exclusively from the smallest particles.

Reactive molecular dynamics simulations allowed to analyze how the catalyst particle size and the strength of adhesion between the surface and nascent carbon structures may affect the growth process of SWCNTs [27], in particular whether the process leads to cap lift-off or if it causes graphitic encapsulation and, therefore, poisoning of the catalyst. The work of adhesion must be weak enough so the curvature energy of a spherical fullerene is less favorable than that of a SWCNT with the same diameter, thus allowing the cap-lifting process to take place. A simple model combining curvature energy and kinetic effects may help to

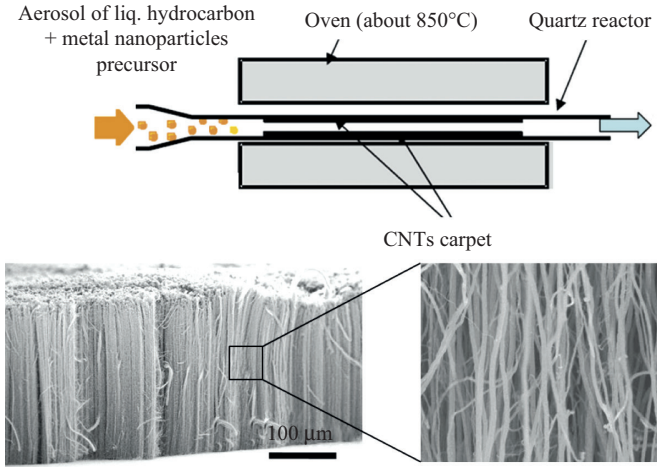

Figure 3.4. Simplified scheme of the synthesis of aligned CNT (CNTs carpet) by CCVD with scanning electron microscopy (SEM) images of the samples obtained.

identify regions of SWCNT growth in the phase space defined by work of adhesion, temperature, and catalyst size [27].

CNTs arrays may be also prepared via CCVD. This is normally carried out by flowing a solution of a hydrocarbon and a metal–organic complex, such as Ferrocene or Nickelocene, through a furnace (Figure 3.4). An array of vertically aligned CNTs (indicated also as a CNT carpet) can be obtained by this methodology [28]. Growing individually aligned CNTs on various substrates by plasma-enhanced CVD is also possible [29]. Their applications range from field emission, optical antennas, subwavelength light transmission to nanocoax arrays for novel solar cell structures.

3.2.2 CARBON NANOFIBERS

Filamentous carbons were first investigated in the 1960s, as side products in the petroleum and nuclear industries. Various forms and microstructures of filamentous carbon were reported to deposit on metal surfaces after exposure to carbon-containing gases within a broad range of temperatures from 323°C to 1,000°C. The formation of carbon nanofibers (CNFs) in various high-temperature catalytic reactions such as hydrocarbon reforming is known for long time, but they were considered as a form of *coke* formed over the catalyst surface leading to deactivation. Attention was thus not given in the past to understand their mechanism of formation

and how to control their characteristics. The characterization of the carbon filaments and the quantification of both, the solid and gaseous, products under various reaction conditions were carried out in the pioneering work of Alstrup and Baker in the 1970s for the study of steam reforming catalysis and *in situ* TEM works, respectively [12, 13, 30].

The investigation of CNFs further attracted researchers with the advent of the HRTEM, followed by the discovery of CNTs by Iijima in 1991 [31]. Thus numerous papers arose with respect to the synthesis and applications of filamentous carbon materials. A filamentous carbon material can have various microstructures; the graphene layer can stack in a perpendicular or parallel manner, or even come with a certain inclination angle relative to the filament's axis with and without a hollow channel (the latter case is that of CNTs discussed in the previous section). Platelets, herringbone CNFs, and CNTs are terms used in the literature to describe filamentous carbons of different microstructure. Figure 3.5 reports some examples, with HRTEM images at the bottom, of different types of carbon nanofilaments [32]. We have included here CNTs, although already discussed in the previous section, to evidence the common aspects with CNFs.

There are several chemical and physical ways to synthesize CNFs, very similar to the methods used for CNTs commented on in the previous section. In the AD technique, CNFs or CNTs are grown on graphite electrodes during the direct current AD evaporation of carbon in the

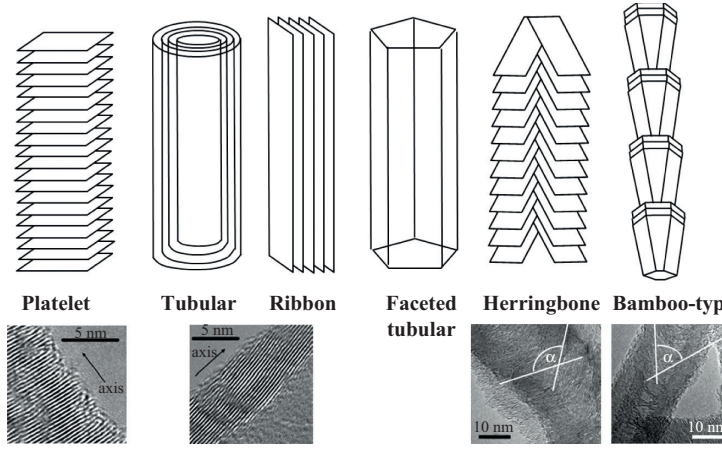

Figure 3.5. Possible structures of carbon nanofilaments, with HRTEM images on the bottom of the different nanostructure, in particular of the terminating graphitic planes on the surface.

presence of an inert atmosphere such as He or Ar. The crystallinity of nanofilaments produced from this method is high; however, control of the diameter and length are extremely difficult. Moreover, the AD process is expensive as the synthesis of CNFs requires high-purity graphite electrodes and He or Ar gasses.

LA is another well-known method used to synthesize nanofilaments. In this method, nanofilaments are grown by vaporization of a target composed of graphite and a mixture of transition metals using a laser in an inert He or Ar atmosphere inside a furnace at high temperatures (about 1,000°C). This technique is costly requiring high-purity graphite starting materials and high laser power.

The preferable method to date for the synthesis of nanofilaments is CCVD. This method involves the catalytic decomposition of hydrocarbons or CO onto metal nanoparticle surfaces at temperatures ranging from 450°C to 1,000°C. Depending on the metal characteristics and the metal–support interaction, as well as the reaction conditions, a base growth or tip growth mechanism may occur, leading to the formation of CNFs or CNTs, respectively. Silicon, silica, alumina, and graphite are substrates used in the literature to support the metal catalyst. For a given catalyst system, the quality and quantity of the grown carbon nanofilament depends on the reaction parameters such as temperature, pressure, carbon source, and growth time [6, 33]. Calcination–reduction and annealing treatments of the catalyst have been shown to play an important role in the carbon filament synthesis.

Two types of CNFs can be prepared by CCVD [34]: cup-stacked CNFs (also called conical CNFs) and platelet CNFs. The cup-stacked CNFs were first found by Ge and Sattler. For the preparation of CNFs by CCVD, several types of metals or alloys, which are able to dissolve carbon to form a metal carbide, have been used as catalysts, including iron, cobalt, nickel, chromium, and vanadium. Additionally, methane, carbon monoxide, synthesis gas (H_2/CO), ethyne, or ethene are used to provide carbon sources in the temperature range from 500°C to 800°C [35]. Generally, the shape of a catalytic nanosized metal particle will define the type of CNF synthesized from it with CCVD. Figure 3.6 reports the schematic drawing of the growth mechanism of the cup-stacked and platelet CNFs [36, 37].

The dynamics of metal nanoparticles during the nucleation and growth of CNFs has been studied by a controlled atmosphere HRTEM [38]. During the steady growth, occasional interruptions such as the formation of graphene layers perpendicular to the growth axis (bamboolike structure) and bending were observed. Such interruptions

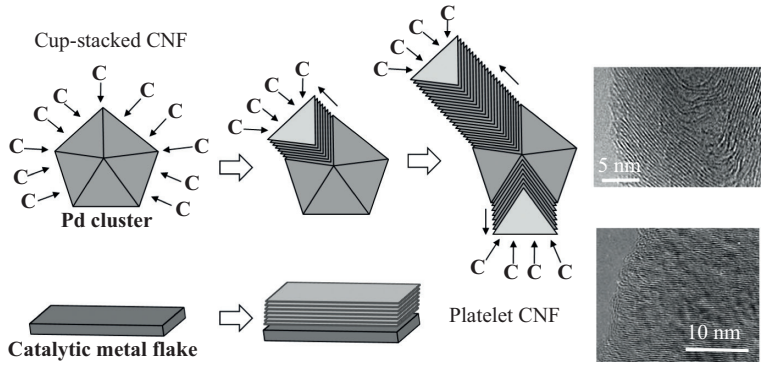

Figure 3.6. Schematic drawing of the CCVD growth mechanism of cup-stacked and platelet CNFs with relative HRTEM, images.

Source: Adapted from Zheng et al. [37].

are preceded by changes in the shape of nanoparticles, leading to interruption in the carbon diffusion and creation of discontinuities in the graphitic network.

The involvement of a metal carbide phase in the growth mechanism of carbon nanofilaments is an aspect still open [39]. Baker and colleagues [12, 13] showed that the carbide phase is not active to grow carbon nanofilament, because Ru is quite an active metal to grow carbon filaments but do not form bulk carbide. On the other hand, it has been demonstrated by an *in situ* TEM study that the iron catalyst forms a stable carbide phase during the course of the growth [40]. The discrepancies in the role of carbide may have originated from the variation of conditions reported in the literature. Other ex situ investigations with Ni and Fe catalysts have suggested the role of carbide as an intermediate step and active site for CNF growth [41–44]. The issue of carbon diffusion, its pathways, and energy as the origin or consequence of the catalyst structure are thus of crucial importance to the growth process. A recent study [39] showed that different growth modes occur on hydrocarbon exposure, depending on the as-formed phase composition in iron catalyst nanoparticles. For γ-rich Fe nanoparticle distributions, metallic Fe is the active catalyst phase, implying that carbide formation is not a prerequisite for nanofilament growth. For α-rich catalyst mixtures, Fe_3C formation more readily occurs and constitutes part of the growth process. The behavior can be rationalized in terms of kinetically accessible pathways, which may be related to the bulk iron−carbon phase diagram with the inclusion of phase equilibrium lines for metastable Fe_3C [39].

In addition to direct mechanisms of synthesis of CNFs, indirect mechanisms, via other type of nanocarbon species, to prepare CNFs may be possible. Kanzow et al. [45] reported the formation of graphitic filaments by heating fullerene blacks covered with thin Ni films at 1,000°C. This indicates the possibility of a solid-state mechanism model [46]. Gorbunov et al. [47] and Kataura et al. [48] demonstrated the production of nanofilaments after heating soot obtained from LA of an Ni–Co graphite target in an inert atmosphere at temperatures <1,000°C. Their reports clearly demonstrated the conversion of disordered carbons into ordered nanofilaments promoted by metal particles. Owing to the high temperature applied for the previous experiments, it is believed that the metal nanoparticles are in the molten state.

An interesting work by Ichihashi et al. [49] of amorphous carbon nanofilament conversion into graphitic nanofilaments by Fe catalyst suggested the solid–quasi-liquid–solid mechanism. They demonstrated the conversion process by annealing experiments inside a TEM instrument. The TEM resolution, however, was not high enough to notice the arrangements of Fe atoms during the movement of nanoparticles in the amorphous filament. Similar to the observation by Helveg et al. [23], the Fe nanoparticles undergo changes in shape during the course of the conversion reaction. The changes in shape are also shown to be in accordance with the presence of bamboolike structures. It may be indicated that growth of carbon nanofilaments and carbon graphitization follow likely the same general mechanism of carbon–carbon bond breaking, carbon atom dissolution and diffusion, and finally, graphitic carbon precipitation. For this reason, secondary posttreatments after the synthesis of CNFs or CNTs may lead to either ordering of residual amorphous carbon areas present on them (a common aspect, but requiring HRTEM studies to be evidenced) or formation of amorphous areas, especially when some fragments of metal nanoparticles are present.

3.2.3 IMPURITIES PRESENT IN CARBON NANOFILAMENTS

The CCVD technique, although requiring a careful control of the reaction conditions to prepare reproducible materials, is the preparation method that is economically more feasible in comparison to the other synthesis techniques for carbon nanofilaments. For this reason, CCVD is the preparation method used industrially for mass production. However, an issue (although common to other techniques) is that the nanofilaments contain impurities such as pyrolytic carbon and the metal catalyst. With

very active catalysts, the final concentration of the metal catalyst in a batch of CNTs can be very low (<0.1% wt), but still may influence the CNTs performance. Various purification procedures are available, even for mass production [50, 51]. Although the residual metal after these purification procedures is very small (at the limit of detection), little amounts may still be present.

Filamentous carbon contains pyrolytic carbon, for example, a disorganized form of carbon that mostly coats the outer walls. The extent of the coating can vary from one filament to another within the agglomerate. Some filaments show random coatings and some exhibit more homogeneous coatings. The pyrolytic carbon can be easily noticed in TEM images. Figure 3.7 shows an example of commercial samples indicated as CNTs but characterized instead from pyrolytic carbon (turbographic structure) on the external surface and well-aligned graphitic layers along the main axis are present in the inner structure (Figure 3.7a) [52, 53]. The analysis of the sample by SEM (Figure 3.7b) indicates an apparent CNT structure, but the sample should be instead described as a hollow fishbone fiber core wrapped with pyrolitically grown carbon. Without an in-depth analysis of even commercial CNT materials [52], the wrong conclusions may be reached. Other commercial CNTs (from Bayer Material Science and Nanocyl) appeared to be more homogeneous in size and morphology and also exhibit some amorphous carbon and debris on their surface [52]. CNTs from Nanocyl had well-aligned walls, parallel to the main axis, thus being relatively close to the perfect MWCNT structure.

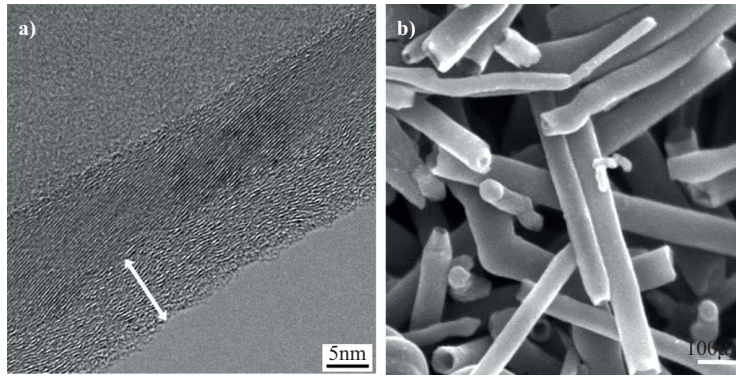

Figure 3.7. (a) HRTEM and (b) SEM images of commercial Pyrograf Products PR24.

Source: Adapted from Tessonnier et al. [52] and Genovese et al. [53].

In contrast, Baytubes presented many structural defects leading to tube wall terminations.

Different experimental techniques should be combined to obtain a good understanding of the nanostructure of these materials. For example, X-ray diffraction, TEM, electron energy loss spectrum, Raman spectroscopy, and X-ray photoelectron spectroscopy measurements were combined in [52] to obtain detailed insights on the nanostructure of the CNTs, including structural defects, which may significantly alter the physicochemical properties of these carbon nanostructures.

So far there is only limited knowledge about the nanostructure of the pyrolytic carbon present as impurities on carbon nanofilaments [52]. However, from the extensive studies concerning soot, carbon black, and noncrystalline carbons, it can be deduced that the microstructure strongly depends on the conditions applied during the CCVD process. For instance, different hydrocarbons used as carbon source may pyrolyze into fragments with different morphologies and dimensions attached to the CNTs surface. Thus a broad range of hydrogen content and sp^2-to-sp^3 hybridization ratios can be expected for the pyrolytic carbon impurities. This variance in graphitic content can be expected to bring out particular chemical and physical properties. In comparison with a pure graphitic structure, pyrolytic carbon exposes more defects per unit volume and allows for additional reactivity at these defects. The pyrolytic impurities tend to enhance functionalization and thereby can induce the combustion of the graphitic CNTs by creating hotspots during their exothermic oxidations [54, 55]. However, such defective carbon coatings can also be exploited to produce carbon materials with tunable properties, for example, vapor-grown CNT [56]. In this case, disorganized carbons are deliberately allowed to coat homogeneously and develop long-range order to a certain extent onto the parent carbon nanofilaments (Figure 3.8) [57].

Pyrolytic carbon is usually classified based on its hybridization compositions. Broad ranges of sp^2–sp^3 carbon mixtures are known to exist within the carbon materials with only short-range order [58]. The hydrogen content can vary broadly within their C–C network. Earlier studies dealing with the mechanism of soot formation have pointed out the polyacetylene and polyaromatics routes for the conversion of hydrocarbon into solid carbons [59]. Despite the ongoing debate on what is the dominant route in the soot formation, there seems to be a general agreement that carbon molecule condensation involves radicals and ions [60].

A general question regards the type of interaction (physical and chemical) between pyrolytic carbon and the underlying CNT surface. The interaction is considered physical, based on the argument that the

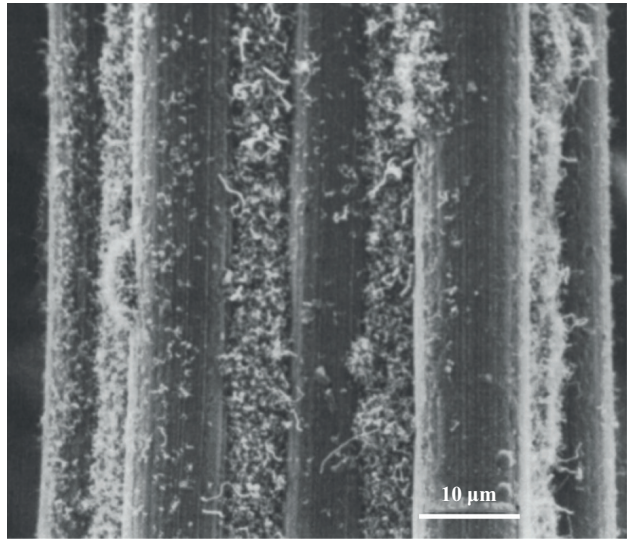

Figure 3.8. Carbon nanofilaments grown on the surface of carbon fibers.

Source: Adapted from Downs and Baker [57].

CNTs merely provide a surface for the carbon clusters to nucleate. The irregular texture of the pyrolytic carbon provides some kind of a wrapping mechanism over the CNT body. However, π–π interaction between the polyene and polyaromatics (present in pyrolytic carbon) with the graphitic surface of CNT may be possible [61, 62] and may lead to chemical interactions, which cause a decrease of the pyrolytic carbon nucleation energy when forms over the CNT surface. The fact that the pyrolytic carbon is randomly dispersed onto the CNT surface (not limited to defects sites), however, provides an argument for a physical type of interaction.

The support for the chemical interaction argument comes from the radical scavenging activity of CNTs and the possible generation of radicals under pyrolytic conditions [63, 64]. The high electrophilicity of CNTs is attributed to high strain sites, which are very likely to be reactive toward the additions of free radicals. Envisaging the CNTs' radical scavenging reactivity, radical-containing soot nuclei and developed networks of solid carbons can terminate at the high-energy sites on the CNTs. In addition, the graphitic prismatic edges and structural defects in CNTs under CCVD conditions (nonoxidative atmosphere at high temperatures) could be the initiation sites to catalyze carbon polymerization via a free radical

mechanism [65]. Finally, in all these cases, there would be a resulting covalent C–C bond between the graphitic surface and the pyrolytic carbon.

The complexity of pyrolytic carbon is reflected in the broad variation of encountered textures (including flat, curvy, fullerene-like, and soot-like structures) observed in TEM images. Such structural variation often also represents a variation in different chemical properties, thus making it rather difficult to generalize a purification method in a specific optimized treatment for a particular CNT sample. Especially with the well-known selective oxidation approach, the reactivity difference between pyrolytic carbon and the parent CNTs can vary widely. Hence, the optimization of a particular method for different samples can also vary broadly.

Numerous studies have been devoted to the purification of CNT samples with the aim of removing single layer or multilayers of pyrolytic carbons. The abundant curvature present in pyrolytic carbons allows for their removal with a selective oxidation [66] approach using a variety of oxidants such as CO_2 [67], air [68], HNO_3 [69], and H_2O_2 [70]. The chosen purification method influences the chemical and physical properties of the purified CNTs, that is, they may open CNT caps, induce CNT fragmentation, and functionalize inner and outer walls. Of all the purification methods, treatment with HNO_3 has drawn the most attention because of its simplicity and also the advantage that it simultaneously removes residual catalyst particles impurities.

Moderate synthetic conditions and more active catalysts lead eventually to a minimum amount of pyrolytic carbon and catalyst impurities. However, mono- or multilayer coatings of pyrolytic carbon and oxidation debris are still frequently observed on as-received and oxidized CNTs, respectively. Such conditions are enough to cause problems, especially in applications under an oxidative environment and applications that exploit the contact between a substrate and the graphitic surface of the CNTs. Such situations are of crucial importance in catalysis, electrochemistry, and composite sciences.

3.2.4 GRAPHENE SYNTHESIS

Various synthesis methods have been reported for graphene or graphene-like materials [71], but only some of them may be applied on a large scale. In general, graphene characteristics depend on the synthesis method.

Graphene was first exfoliated mechanically from graphite in 2004 [72] to produce graphene flakes, which raised the possibility for the production of low-cost graphene materials. However, these materials are usually

available at a size of several micrometers only (or tens of micrometers at best), have irregular shapes, and their azimuthal orientation is not controlled. Most of the technological applications of graphene require very controlled properties, such as electronic transport properties on a large scale (e.g. wafer-scale). In Table 3.1, we give an overview of graphene synthesis processes [73].

By mechanical cleavage, high-quality graphene can be produced with high electronic mobility, but the process is not suitable for large-scale production. High-quality graphene can also be grown epitaxially by decomposing SiC [74], but the process is expensive and a high processing temperature is necessary. One of the most used methods starts with graphite oxide (produced with various methods, the most common being the Hummers method using sodium nitrate in sulfuric acid), which is ultrasonically separated as flakes and dispersed or deposited onto a substrate before reduction to graphene [75–79]. Unfortunately, for microelectronics applications, the boundaries between the graphene flakes reduce the carrier mobility. Graphene has also been grown by carbon precipitation from metals (including Ni, Co, and Ga) [80]. The low atomic percentage of carbon dissolved into a metal precipitates onto the surface during the annealing process. Graphene has been grown on diamond using this method and patterned on electrodes [80]. Garcia et al. [80] prepared a thin nickel film deposited by e-beam evaporation on a single crystal diamond (001)-oriented substrate. After annealing at 800°C, few-layer graphene (FLG) precipitates upon cooling on the surface.

The preferred method to synthesize graphene is probably by CVD, but it requires a very strict control of the precursor, catalyst, pressure, and temperature to produce high-quality graphene [81]. Graphene has been synthesized on different metal materials including Cu, Ni, Au, Ag, and so on. However, copper and nickel give the best results [82].

Graphene and FLG have been grown by CVD from C-containing gases on catalytic metal surfaces and by surface segregation of C dissolved in the bulk of such metals. Depending on the solubility of C in the metal, the former or the latter can be the dominant growth process, or they can coexist. Quite intensive studies have been devoted to the formation of single- or few-layer graphite by surface segregation of C during annealing of various C-doped metals such as Ni, Fe, Pt, Pd, and Co.

In single-crystal Ni (111), the atomically smooth surface and the absence of grain boundaries produce uniform and thinner FLG, while in polycrystalline Ni, grain boundaries serve as graphene nucleation sites favoring multilayer growth. Different cooling rates lead to different C segregation behaviors, affecting the thickness and quality of the resulting

Table 3.1. Overview of graphene synthesis processes

	Quality	Size (μm²)	Mobility (cm²/V·s)	Temperature, °C	Layer	Cost
Cleavage	High	1,000	$2 \cdot 10^5$	r.t	Single	High
Epitaxial (SiC)	Medium	~100	$\sim 10^4$	>1,000	Controllable	Medium
Exfoliation	Poor	~100	~1	r.t	Stacked	Medium
CVD	High	Wafer	$\sim 10^4$	~1,000	Single	Low
Precipitation	High	1,000	$\sim 10^3$	~1,000	Single	High

Source: Adapted from Zang et al. [73].

graphene films. Annealing the Ni surface in H_2 before graphene formation is beneficial to the thickness uniformity of the graphene layer [83]. The presence of H_2 eliminates impurities such as S and P that cause local variations of carbon solubility, affecting the local graphene thickness. Reina et al. [84] used ambient-pressure CVD to synthesize 1-to-12-layer graphene films on polycrystalline Ni films, while ethylene decomposition on Pt(111) surfaces, resulted in the formation of a single layer of epitaxial graphite.

The deposition of graphene on Cu surfaces provides a good example of a purely surface-mediated CVD process [81]. The solubility of C in Cu is minimal (less than 0.001 atom% at 1,000°C versus 1.3 atom% at 1,000°C in pure Ni), thus graphene can form on Cu only by direct decomposition of the C-containing gas on the catalytic Cu surface. The graphene growth process is self-limiting, effectively stopping at one monolayer (ML). Such control is very difficult in the case of graphene grown on Ni, because of the considerable solubility of C in Ni. Graphene has also been grown epitaxially on Ru(0001) by surface segregation and on Ir(111) by low-pressure CVD [77].

Although graphene grows epitaxially on most metals, on polycrystalline metal substrates, it has a polycrystalline structure in 2D, that is, within the same graphene layer, there are single-crystal domains of graphene azimuthally rotated relative to neighboring domains and stitched together with defective domain boundaries, such as alternating pentagon–heptagon structures [85]. CVD graphene grown on Cu constitute ML growth, but even on single-crystal Cu, a multidomain structure is present because of the rotational disorder between domains and the many grain boundaries. A strict epitaxial relation between the graphene and Cu lattices has yet to be proven. However, under the appropriate conditions, large single crystals of graphene can be grown.

CVD graphene exhibits electrical transport properties similar to those of exfoliated graphene flakes (e.g., high mobility) but only when a single graphene domain is studied. In typical samples, the grain boundaries may drastically reduce the performances. For this reason, techniques that allow uniformity at the wafer scale, such as based on SiC, are used, notwithstanding the other cited drawbacks.

During annealing, the top layers of SiC crystals undergo thermal decomposition, with Si atoms desorbing and the carbon atoms remaining on the surface, following rearrangement and rebonding to form epitaxial graphene layers [86]. The kinetics of graphene formation as well as the resulting graphene structure and properties depend on the reactor pressure and the type of gas atmosphere. The best results are obtained with the Si-face of hexagonal SiC wafers, that is, h-SiC(0001). Graphene

formation starts at the top surface layers of SiC and proceeds inwards. Approximately three Si–C bilayers decompose (ca. 0.75 nm) to form one graphene layer (ca. 0.34 nm).

3.3 FUNCTIONALIZATION OF NANOCARBONS

Functionalization of nanocarbons by posttreatment may considerably change their properties. Therefore, it constitutes a convenient approach to tune and control nanocarbons properties. This approach has been only exploited limitedly up to now in C-MEMS and C-NEMS. But on the contrary, it is widely used in other sectors such as catalysis [87–89]. According to the interaction of the functional groups with the nanocarbon, the methodologies of functionalization can be categorized as covalent attachment of chemical groups, through reactions with the conjugated sp^2 carbon skeleton and noncovalent supramolecular adsorption (wrapping) of various functional molecules on the nanocarbon. Noncovalent functionalization mostly involves decoration of nanocarbons with (large and in many cases organic) molecules.

Noncovalent functionalizations do not disturb the characteristic π electron system and are widely used in the preparation of both aqueous and organic solutions to obtain highly stable suspensions of individually dispersed nanotubes or graphenes. Between the most common covalent functionalizations, the oxidation and amination of nanocarbons are the most important and well-studied methods to introduce O- or N-containing groups on the surface [90–92] (Figure 3.9).

Liquid-phase oxidation of CNTs is the most common method and involves mainly acidic etching by hot nitric acid or sulfuric acid and nitric acid mixtures. This is a simple and well-established method to purify and functionalize nanocarbons simultaneously. The functionalization is not selective, and various O-containing groups can be anchored on the defect sites of sidewalls and open caps of CNTs or on the defect sites and edges of graphene, respectively. Hydrogen peroxide may also be used as an oxidant. Liquid-phase purification and functionalization cause the loss of SWCNT metallic character and change the physicochemical properties of MWCNTs, although the nature of the latter changes depend significantly on the specific characteristics of the MWCNTs. In Figure 3.10, we display an example of oxygen functionalities that can be created on a graphene sheet at (a) the edges or (b) defect sites [88]. Similar type of oxygen functionalities are also created in CNTs and CNFs.

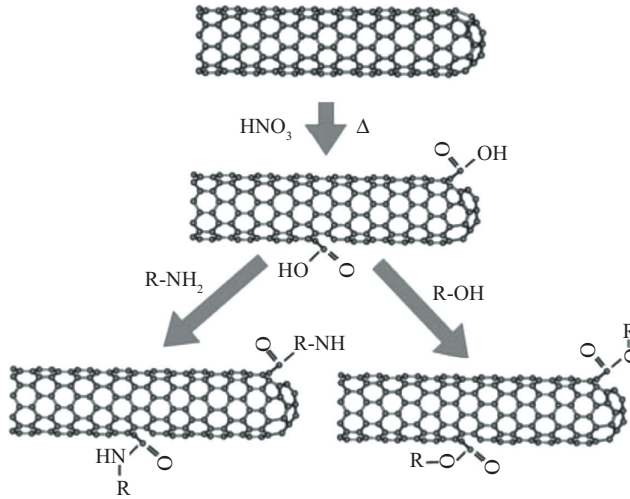

Figure 3.9. Chemical modification of nanotubes through thermal oxidation, followed by subsequent esterification or amidization of the carboxyl group.

Source: Adapted from Balasubramanian and Burghard [92].

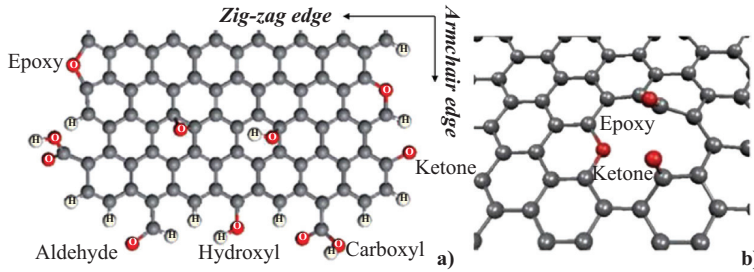

Figure 3.10. Oxygen functionalities created by oxidation treatment with HNO_3 (or other oxidants) in a graphene sheet at the edges (a) or at defect sites (b).

Source: Adapted from Centi, Perathoner, and Su [88].

After oxidation treatment, part of the oxygen functional groups can be converted to nitrogen by gaseous nitrogen-precursor species (e.g., NH_3 and acetonitrile). Depending on the temperature of treatment and post-treatment annealing, different amounts and types of functional species can be created in the nanocarbon materials. For more details on nanocarbon functionalization, see also Chapter 7.

3.3.1 HYBRID MATERIALS

Another characteristic of nanocarbon materials exploited in other areas such as catalysis, but not much explored yet in C-MEMS and C-NEMS, concerns the possibility to develop devices that incorporate hybrid materials [93], for example, nanocarbons and metal-oxide nanoparticles (e.g., TiO_2) [94]. TiO_2 nanoparticles interact with the nanocarbon acting as electron acceptors or donors, depending on the characteristics of the nanocarbons and the type of interaction with the metal-oxide nanoparticles. This could be exploited in solar cells where illumination causes charge separation and photocurrent in the semiconductor particles and changes in the properties of the nanocarbon can be used to modulate and finetune the photo effect.

There are other interesting possible applications in the area of C-MEMS and C-NEMS, which can be exploited using these hybrid materials. For example, hybridizing metal-oxide nanostructures (e.g., CoO, Fe_2O_3, and V_2O_5) with carbon nanostructures (e.g., graphene or reduced graphene oxide and CNTs) can be an effective route to achieve better Li storage properties in lithium-ion batteries by improving the kinetics of charge transfer and alleviating the structural strain during the charge or discharge process [95, 96].

Individual metal atoms, cations, clusters, or even nanoparticles coupled to carbon nanostructures introduce new properties either through covalent metal–carbon bonds or coordination bonds via a ligand group, charge transfer, electrostatic, or van der Waals interactions. Many of these properties are not present in all-carbon materials. For example, fullerenes and nanotubes are able to bind metals either directly through M–C bonds or via functional groups containing nitrogen or oxygen donor atoms or can entrap metal atoms in the internal cavities of the fullerene cages. Metals can bring magnetic, optical, and redox activities into the carbon nanostructures, thus broadening the spectrum of their practical applications.

Yet another opportunity is in carbon–carbon hybrid materials, for example, composed of different types of nanocarbons. A large range of possibilities exists here, for example, by linking porphyrin–fullerene-linked dyads (electron-donating conjugated molecules) to CNTs or graphene, eventually via spacers to separate the donor (porphyrin) and the acceptor (fullerenes). Endohedral and exohedral hybrids involving fullerenes and CNTs [97] enable the development of third generation nanocarbon materials combining the properties of both carbon allotropes, for example, the electronic and optical properties of CNTs with the excellent electron

acceptor characteristic of fullerenes. In these hybrids, the fullerene can be located inside (endohedral) or outside (exohedral) the CNT and both types of hybrid contribute their own specific features. CNT–fullerene hybrids have been studied for various applications, including photovoltaics, nonlinear optical materials, and flame retardancy, among others.

Hybrid structures composed of covalently interconnected CNTs with graphene sheets, where CNTs act as *reinforcing bars*, enable the improvement of the mechanical strength of polycrystalline graphene sheets and bridge different crystalline domains so as to enhance the electrical conductivity [98]. These 3D graphene networks could be used in many fields, including flexible conductors, supercapacitors, solar cells, microbial fuel cells, and so on.

3.4 CONCLUSIONS

The synthesis of carbon nanomaterials and the tuning of their properties (by posttreatment, functionalization, control of the defective state, preparation of hybrid materials, etc.) is a scientific area of fast-growing interest. This chapter has outlined the main aspects in the synthesis of CNTs, CNFs, graphene, and graphene-like materials, with also some elements regarding other types of carbon nanomaterials (carbon onion, turbographitic carbon, etc.). The focus was on the preparation by CCVD, being the technique largest used in mass production of these materials. The aim was not to provide a full review on this topic but to evidence some of the aspects that may be relevant for the preparation of C-MEMS and similar devices.

For this reason, attention was focused at clarifying how the specific properties of the carbon materials prepared depend on many aspects, between which the specific nanostructure, and the presence of defects and impurities (because of the presence of other types of nanocarbon materials and residual catalysts used in their synthesis). The properties of the produced nanocarbons depend critically on these aspects, and often materials labeled in the same way (e.g., CNTs) possess completely different characteristics, going, for example, from insulating to metallic character. It was also mentioned in a concise way how the properties can be tuned, from simple posttreatment purification or thermal annealing to more complex procedures of functionalization or development of hybrid materials. This offers further possibilities to tailor the properties of carbon materials for C-MEMS or similar applications and in turn develop improved devices.

REFERENCES

[1] Takagaki, Y., H.D. Nguyen-Tran, and K. Ohta. 2010. "Development of Facile Synthetic Methods of Carbon Nanotubes Using a Domestic Microwave Oven." *Bulletin Chemical Society Japan*. 83, no. 9, pp. 1100–06. doi: http://dx.doi.org/10.1246/bcsj.20100008

[2] Page, A.J., Y. Ohta, S. Irle, and K. Morokuma. 2010. "Mechanisms of Single-Walled Carbon Nanotube Nucleation, Growth, and Healing Determined Using QM/MD Methods." *Accounts of Chemical Research* 43, no. 10, pp. 1375–85. doi: http://dx.doi.org/10.1021/ar100064g

[3] Takagi, Y., L. Tauchi, H.D. Nguyen-Tran, T. Ohta, M. Shimizu, and K. Ohta. 2011. "Development of a Novel Method to Synthesize Carbon Nanotubes from Granulated Polystyrene and Nickel Nanoparticles by Microwave Heating." *Journal of Materials Chemistry* 21, no. 38, pp. 14569–74. doi: http://dx.doi.org/10.1039/c1jm12069g

[4] Ohta, K., T. Nishizawa, T. Nishiguchi, R. Shimizu, Y. Hattori, S. Inoue, M. Katayama, K. Mizu-uchi, and T. Kono. 2014. "Synthesis of Carbon Nanotubes by Microwave Heating: Influence of Diameter of Catalytic Ni Nanoparticles on Diameter of CNTs." *Journal of Materials Chemistry A: Materials for Energy and Sustainability* 2, no. 8, pp. 2773–80. doi: http://dx.doi.org/10.1039/c3ta13297h

[5] Kumar, A., K. Singh, and O.P. Pandey. 2014. "One Step Synthesis and Growth Mechanism of Carbon Nanotubes." *Journal of Materials Science & Technology* 30, no. 2, pp. 112–16. doi: http://dx.doi.org/10.1016/j.jmst.2013.09.005

[6] Tessonnier, J.P., and D.S. Su. 2011. "Recent Progress on the Growth Mechanism of Carbon Nanotubes: A Review." *ChemSusChem* 4, no. 7, pp. 824–47. doi: http://dx.doi.org/10.1002/cssc.201100175

[7] MacKenzie, K.J., O.M. Dunens, and A.T. Harris. 2010. "An Updated Review of Synthesis Parameters and Growth Mechanisms for Carbon Nanotubes in Fluidized Beds." *Industrial and Engineering Chemistry Research* 49, no. 1, pp. 5323–38. doi: http://dx.doi.org/10.1021/ie9019787

[8] Moisala, A., A.G. Nasibulin, and E.I. Kauppinen. 2003. "The Role of Metal Nanoparticles in the Catalytic Production of Single-Walled Carbon Nanotubes—A Review." *Journal of Physics Condensed Matter* 15, no. 42, pp. S3011–35. doi: http://dx.doi.org/10.1088/0953-8984/15/42/003

[9] Zhang, Q., J.Q. Huang, W.Z. Qian, Y.Y. Zhang, and F. Wei. 2013 "The Road for Nanomaterials Industry: A Review of Carbon Nanotube Production, Post-Treatment, and Bulk Applications for Composites and Energy Storage." *Small* 9, no. 8, pp. 1237–65. doi: http://dx.doi.org/10.1002/smll.201203252

[10] Zhang, Q., J.Q. Huang, M.Q. Zhao, W.Z. Qian, and F. Wei. 2011. "Carbon Nanotube Mass Production: Principles and Processes." *ChemSusChem* 4, no. 7, pp. 864–89. doi: http://dx.doi.org/10.1002/cssc.201100177

[11] Centi, G., and S. Perathoner. 2011. "Carbon Nanotubes for Sustainable Energy Applications." *ChemSusChem* 4, no. 7, pp. 913–25. doi: http://dx.doi.org/10.1002/cssc.201100084

[12] Baker, R.T.K., M.A. Barber, P.S. Harris, F.S. Feates, and R.J. Waite. 1972. "Nucleation and Growth of Carbon Deposits from the Nickel Catalyzed Decomposition of Acetylene." *Journal of Catalysis* 26, no. 1, pp. 51–62. doi: http://dx.doi.org/10.1016/0021-9517(72)90032-2

[13] Baker, R.T.K., J.R. Alonzo, J.A. Dumesic, and D.J.C. Yates. 1982. "Effect of the Surface State of Iron on Filamentous Carbon Formation." *Journal of Catalysis* 77, no. 1, pp. 74–84. doi: http://dx.doi.org/10.1016/0021-9517(82)90148-8

[14] Wagner, R.S., and W.C. Ellis. 1964. "Vapor-Liquid-Solid Mechanism of Single Crystal Growth." *Applied Physics Letters* 4, no. 5, pp. 89–90. doi: http://dx.doi.org/10.1063/1.1753975

[15] Pirard, S.L., S. Douven, C. Bossuot, G. Heyen, and J.P. Pirard. 2007. "A Kinetic Study of Multi-Walled Carbon Nanotube Synthesis by Catalytic Chemical Vapor Deposition Using a Fe–Co/Al2O3 Catalyst." *Carbon* 45, no. 6, pp. 1167–75. doi: http://dx.doi.org/10.1016/j.carbon.2007.02.021

[16] Prasek, J., J. Drbohlavova, J. Chomoucka, J. Hubalek, O. Jasek, V. Adamc, and R. Kizek. 2014. "Methods for Carbon Nanotubes Synthesis—Review." *Journal of Materials Chemistry* 21, no. 40, pp. 15872–884. doi: http://dx.doi.org/10.1039/c1jm12254a

[17] Baird, T., J.R. Fryer, and B. Grant. 1971. "Structure of Fibrous Carbon." *Nature* 233, no. 5318, pp. 329–30. doi: http://dx.doi.org/10.1038/233329b0

[18] Philippe, R., B. Caussat, A. Falqui, Y. Kihn, P. Kalck, S.Bordre, D. Plee, P. Gaillard, D. Bernard, and P. Serp. 2009. "An Original Growth Mode of MWCNTs on Alumina Supported Iron Catalysts." *Journal of Catalysis* 263, no. 2, pp. 345–58. doi: http://dx.doi.org/10.1016/j.jcat.2009.02.027

[19] Oberlin, A., M. Endo, and T. Koyama. 1976. "Filamentous Growth of Carbon Through Benzene Decomposition." *Journal of Crystal Growth* 32, no. 3, pp. 335–49. doi: http://dx.doi.org/10.1016/0022-0248(76)90115-9

[20] Audier, M., A. Oberlin, and M. Coulon. 1981. "Crystallographic Orientations of Catalytic Particles in Filamentous Carbon; Case of Simple Conical Particles." *Journal of Crystal Growth* 55, no. 3, pp. 549–56. doi: http://dx.doi.org/10.1016/0022-0248(81)90114-7

[21] Hofmann, S., G. Csànyi, A.C. Ferrari, M.C. Payne, and J. Robertson. 2005. "Surface Diffusion: The Low Activation Energy Path for Nanotube Growth." *Physical Review Letters* 95, no. 3, p. 036101. doi: http://dx.doi.org/10.1103/physrevlett.95.036101

[22] Raty, J.-Y., F. Gygi, and G. Galli. 2005. "Growth of Carbon Nanotubes on Metal Nanoparticles: A Microscopic Mechanism from Ab Initio Molecular Dynamics Simulations." *Physical Review Letters* 95, no. 9, p. 096103. doi: http://dx.doi.org/10.1103/physrevlett.95.096103

[23] Helveg, S., C. Lopez-Cartes, J. Sehested, P.L. Hansen, B.S. Clausen, J.R. Rostrup-Nielsen, F. Abild-Pedersen, and J.K. Norskov. 2004. "Atomic-Scale Imaging of Carbon Nanofibre Growth." *Nature* 427, no. 6973, pp. 426–29. doi: http://dx.doi.org/10.1038/nature02278

[24] Page, A.J., H. Yamane, Y. Ohta, S. Irle, and K. Morokuma. 2010. "QM/MD Simulation of SWNT Nucleation on Transition-Metal Carbide Nanoparticles." *Journal of the American Chemical Society* 132, no. 44, pp. 15699–707. doi: http://dx.doi.org/10.1021/ja106264q

[25] Wei, D., and Y. Liu. 2008. "The Intramolecular Junctions of Carbon Nanotubes." *Advanced Materials* 20, no. 15, pp. 2815–41. doi: http://dx.doi.org/10.1002/adma.200800589

[26] Chiang, W.-H., and R.M. Sankaran. 2009. "Linking Catalyst Composition to Chirality Distributions of As-Grown Single-Walled Carbon Nanotubes by Tuning NixFe1−x Nanoparticles." *Nature Materials* 8, no. 11, pp. 882–86. doi: http://dx.doi.org/10.1038/nmat2531

[27] Burgos, J.C., H. Reyna, B.I. Yakobson, and P.B. Balbuena. 2010. "Interplay of Catalyst Size and Metal−Carbon Interactions on the Growth of Single-Walled Carbon Nanotubes." *Journal of Physical Chemistry C* 114, no. 15, pp. 6952–58. doi: http://dx.doi.org/10.1021/jp911905p

[28] Rinaldi, A., N. Abdullah, M. Ali, A. Furche, S.B. Abd Hamid, D.S. Su, and R. Schlögl. 2009. "Controlling the Yield and Structure of Carbon Nanofibers Grown on a Nickel/Activated Carbon Catalyst." *Carbon* 47, no. 13, pp. 3023–33. doi: http://dx.doi.org/10.1016/j.carbon.2009.06.056

[29] Lan, Y., Y. Wang, and Z.F. Ren. 2011. "Physics and Applications of Aligned Carbon Nanotubes." *Advances in Physics* 60, no. 4, pp. 553–678. doi: http://dx.doi.org/10.1080/00018732.2011.599963

[30] Alstrup, I. 1988. "A New Model Explaining Carbon Filament Growth on Nickel, Iron, and Ni$z.sbnd; Cu Alloy Catalysts." *Journal of Catalysis* 109, no. 2, pp. 241–51. doi: http://dx.doi.org/10.1016/0021-9517(88)90207-2

[31] Iijima, S. 1991. "Helical Microtubules of Graphitic Carbón." *Nature* 354, no. 6348, pp. 56–58. doi: http://dx.doi.org/10.1038/354056a0

[32] Monthioux, M., L. Noé, L. Dussault, J.-C. Dupin, N. Latorre, T. Ubieto, E. Romeo, C. Royo, A. Monzón, and C. Guimon. 2007. "Texturising and Structurising Mechanisms of Carbon Nanofilaments During Growth." *Journal of Materials Chemistry* 17, no. 43, pp. 4611–18. doi: http://dx.doi.org/10.1039/b707742d

[33] Yoon, S.-H., S. Lim, S.-H. Hong, W. Qiao, D.D. Whitehurst, I. Mochida, B. An, and K. Yokogawa. 2005. "A Conceptual Model for the Structure of Catalytically Grown Carbon Nano-Fibers." *Carbon* 43, no. 9, pp. 1828–38. doi: http://dx.doi.org/10.1016/j.carbon.2005.02.031

[34] Tanaka, A., S.-H. Yoon, and I. Mochida. 2004. "Preparation of Highly Crystalline Nanofibers on Fe and Fe–Ni Catalysts with a Variety of Graphene Plane Alignments." *Carbon* 42, no. 3, pp. 591–97. doi: http://dx.doi.org/10.1016/j.carbon.2003.12.067

[35] Ge, M., and K. Sattler. 1994. "Observation of Fullerene Cones." *Chemical Physics Letters* 220, no. 3–5, pp. 192–96. doi: http://dx.doi.org/10.1016/0009-2614(94)00167-7

[36] De Jong, K.P., and J.W. Geus. 2000. "Carbon Nanofibers: Catalytic Synthesis and Applications." *Catalysis Reviews* 42, no. 4, pp. 481–510. doi: http://dx.doi.org/10.1081/cr-100101954

[37] Zheng, R., Y. Zhao, H. Liu, C. Liang, and G. Cheng. 2006. "Preparation, Characterization and Growth Mechanism of Platelet Carbon Nanofibers." *Carbon* 44, no. 4, pp. 742–46. doi: http://dx.doi.org/10.1016/j.carbon.2005.09.015

[38] Hofmann, S., R. Sharma, C. Ducati, G. Du, C. Mattevi, C. Cepek, M.Cantoro, S. Pisana, A. Parvez, F. Cervantes-Sodi, A.C. Ferrari, R. Dunin-Borkowski, S. Lizzit, L. Petaccia, A. Goldoni, and J. Robertson. 2007. "In Situ Observations of Catalyst Dynamics During Surface-Bound Carbon Nanotube Nucleation." *Nano Letters* 7, no. 3, pp. 602–08. doi: http://dx.doi.org/10.1021/nl0624824

[39] Wirth, C.T., B.C. Bayer, A.D. Gamalski, S. Esconjauregui, R.S. Weatherup, C. Ducati, C. Baehtz, J. Robertson, and S. Hofmann. 2012. "The Phase of Iron Catalyst Nanoparticles During Carbon Nanotube Growth." *Chemistry of Materials* 24, no. 24, pp. 4633–40. doi: http://dx.doi.org/10.1021/cm301402g

[40] Feng, L., N. Xie, and J. Zhong. 2014. "Carbon Nanofibers and Their Composites: A Review of Synthesizing, Properties and Applications." *Materials* 7, no. 5, pp. 3919–45. doi: http://dx.doi.org/10.3390/ma7053919

[41] Yoshida, H., S. Takeda, T. Uchiyama, H. Kohno, and Y. Homma. 2008. "Atomic-Scale In-Situ Observation of Carbon Nanotube Growth from Solid State Iron Carbide Nanoparticles." *Nano Letters* 8, no. 7, pp. 2082–86. doi: http://dx.doi.org/10.1021/nl080452q

[42] de Bokx, P.K., A.J.H.M. Kock, E. Boellaard, W. Klop, and J.W. Geus. 1985. "The Formation of Filamentous Carbon on Iron and Nickel Catalysts I. Thermodynamics." *Journal of Catalysis* 96, no. 2, pp. 454–67. doi: http://dx.doi.org/10.1016/0021-9517(85)90314-8

[43] Schaper, A.K., H. Hou, A. Greiner, and F. Phillipp. 2004. "The Role of Iron Carbide in Multiwalled Carbon Nanotube Growth." *Journal of Catalysis* 222, no. 1, pp. 250–54. doi: http://dx.doi.org/10.1016/j.jcat.2003.11.011

[44] Ni, L., K. Kuroda, L. Zhou, K. Ohta, K. Matsuishi, and J. Nakamura. 2009. "Decomposition of Metal Carbides as an Elementary Step of Carbon Nanotube Synthesis." *Carbon* 47, no. 13, pp. 3054–62. doi: http://dx.doi.org/10.1016/j.carbon.2009.07.009

[45] Kanzow, H., A. Ding, J. Nissen, H. Sauer, T. Belz, and R. Schlögl. 2000. "Formation of Chains of Graphitic Nanoparticles by Heating Fullerene Blacks Covered with Thin Metal Films." *Physical Chemistry Chemical Physics* 2, no. 12, pp. 2765–71. doi: http://dx.doi.org/10.1039/b002735i

[46] Harris, P.J. 2007. "Solid State Growth Mechanisms for Carbon Nanotubes." *Carbon* 45, no. 2, pp. 229–39. doi: http://dx.doi.org/10.1016/j.carbon.2006.09.023

[47] Gorbunov, A., O. Jost, W. Pompe, and A. Graff. 2002. "Solid–Liquid–Solid Growth Mechanism of Single-Wall Carbon Nanotubes." *Carbon* 40, no. 1, pp. 113–18. doi: http://dx.doi.org/10.1016/s0008-6223(01)00080-x

[48] Sen, R., S. Suzuki, H. Kataura, and Y. Achiba. 2001. "Growth of Single-Walled Carbon Nanotubes from the Condensed Phase." *Chemical Physics Lett*ers 349, no. 5–6, pp. 383–88. doi: http://dx.doi.org/10.1016/s0009-2614(01)01208-8

[49] Ichihashi, T., J. Fujita, M. Ishida, and Y. Ochiai. 2004. "In Situ Observation of Carbon-Nanopillar Tubulization Caused by Liquidlike Iron Particles." *Physical Review Letters* 92, no. 21, pp. 215702. doi: http://dx.doi.org/10.1103/physrevlett.92.215702

[50] Yong, P.Y. 2012. "Preparation, Purification and Properties of Carbon Nanotubes." *Advanced Materials Research* 557–559, pp. 472–77. doi: http://dx.doi.org/10.4028/www.scientific.net/amr.557-559.472

[51] Ying, L.S., M.A. bin Mohd Salleh, H.B.M. Yusoff, S.B.A. Rashid, and J.A. Razak. 2011. "Continuous Production of Carbon Nanotubes—A Review." *Journal of Industrial Engineering Chemistry* 17, no. 3, pp. 367–76. doi: http://dx.doi.org/10.1016/j.jiec.2011.05.007

[52] Tessonnier, J.-P., D. Rosenthal, T.W, Hansen, C. Hess, M.E. Schuster, R. Blume, F. Girgsdies, N. Pfänder, O. Timpe, D.S. Su, and R. Schlögl. 2009. "Analysis of the Structure and Chemical Properties of Some Commercial Carbon Nanostructures." *Carbon* 47, no. 7, pp. 1779–98. doi: http://dx.doi.org/10.1016/j.carbon.2009.02.032

[53] Genovese, C., C. Ampelli, S. Perathoner, and G. Centi. 2013. "Electrocatalytic Conversion of CO2 to Liquid Fuels Using Nanocarbon-Based Electrodes." *Journal of Energy Chemistry* 22, no. 2, pp. 202–13. doi: http://dx.doi.org/10.1016/s2095-4956(13)60026-1

[54] Verdejo, R., S. Lamoriniere, B. Cottam, A. Bismarck, and M. Shaffer. 2007. "Removal of Oxidation Debris from Multi-Walled Carbon Nanotubes." *Chemical Communications* no. 5, pp. 513–15. doi: http://dx.doi.org/10.1039/b611930a

[55] Shimada, T., H. Yanase, K. Morishita, J. Hayashi, and T. Chiba. 2004. "Points of Onset of Gasification in a Multi-Walled Carbon Nanotube Having an Imperfect Structure." *Carbon* 42, no. 8–9, pp. 1635–39. doi: http://dx.doi.org/10.1016/j.carbon.2004.02.019

[56] Allouche, H., and M. Monthioux. 2005. "Chemical Vapor Deposition of Pyrolytic carbon on Carbon Nanotubes. Part 2. Texture and Structure." *Carbon* 43, no. 6, pp. 1265–78. doi: http://dx.doi.org/10.1016/j.carbon.2004.12.023

[57] Downs, W.B., and R.T.K. Baker. 1991. "Novel Carbon Fiber-Carbon Filament Structures." *Carbon* 29, no. 8, pp. 1173–79. doi: http://dx.doi.org/10.1016/0008-6223(91)90035-h

[58] Robertson, J. 1996. "Amorphous Carbón." *Current Opinion in Solid State and Materials Scienc*e 1, no. 4, pp. 557–61. doi: http://dx.doi.org/10.1016/s1359-0286(96)80072-6

[59] Lahaye, J., and G. Prado. 1976. *Petroleum Derived Carbons.* Vol. 21. ACS Symposium Series, 335–47. American Chemical Society.

[60] Fenoglio, I., M. Tomatis, D. Lison, J. Muller, A. Fonseca, J.B. Nagy, and B. Fubini. 2006. "Reactivity of Carbon Nanotubes: Free Radical Generation or Scavenging Activity?" *Free Radical Biology and Medicine* 40, no. 7, pp. 1227–33. doi: http://dx.doi.org/10.1016/j.freeradbiomed.2005.11.010

[61] Wang, C., Z. Guo, S. Fu, W. Wu, and D. Zhu. 2004. "Polymers Containing Fullerene or Carbon Nanotube Structures." *Progress in Polymer Science* 29, no. 11, pp. 1079–41. doi: http://dx.doi.org/10.1016/j.progpolymsci.2004.08.001

[62] Curran, S.A., P.M. Ajayan, W.J. Blau, D.L. Carroll, J.N. Coleman, A.B. Dalton, A.P. Davey, A. Drury, B. McCarthy, S. Maier, and A. Strevens. 1998. "A Composite from Poly(m-Phenylenevinylene-co-2,5-Dioctoxy-p-Phenylenevinylene) and Carbon Nanotubes: A Novel Material for Molecular Optoelectronics." *Advanced Materials* 10, no. 14, pp. 1091–93. doi: http://dx.doi.org/10.1002/(sici)1521-4095(199810)10:14%3C1091::aid-adma1091%3E3.3.co;2-c

[63] Krusic, P.J., E. Wasserman, P.N. Keizer, J.R. Morton, and K.F. Preston. 1991. "Radical Reactions of C60." *Science* 254, no. 5035, pp. 1183–85. doi: http://dx.doi.org/10.1126/science.254.5035.1183

[64] Fenoglio, I., G. Greco, M. Tomatis, J. Muller, E. Raymundo-Piñero, F. Béguin, A. Fonseca, J.B. Nagy, D. Lison, and B. Fubini. 2008. "Structural Defects Play a Major Role in the Acute Lung Toxicity of Multiwall Carbon Nanotubes: Physicochemical Aspects." *Chemical Research Toxicology* 21, no. 9, pp. 1690–97. doi: http://dx.doi.org/10.1021/tx800100s

[65] Bandosz, T. 2008. *Carbon Material for Catalysis*, eds. P. Serp and J.L. Figueiredo, 68–69. Hoboken, NJ: John Wiley and Sons.

[66] Brukh, R., and S. Mitra. 2007. "Kinetics of Carbon Nanotubeoxidation." *Journal of Materials Chemistry* 17, no. 7, pp. 619–23. doi: http://dx.doi.org/10.1039/b609218g

[67] Smith, M.R., S.W. Hedges, R. LaCount, D. Kern, N. Shah, G.P. Huffman, and B. Bockrath. 2003. "Selective Oxidation of Single-Walled Carbon Nanotubes Using Carbon Dioxide." *Carbon* 41, no. 6, pp. 1221–30. doi: http://dx.doi.org/10.1016/s0008-6223(03)00054-x

[68] Park, Y.S., Y.C. Choi, K.S. Kim, D. Chung, D.J. Bae, K.H. An, S.C. Lim, X.Y. Zhu, and Y.H. Lee. 2001. "High Yield Purification of Multiwalled Carbon Nanotubes by Selective Oxidation During Thermal Annealing." *Carbon* 39, no. 5, pp. 655–61. doi: http://dx.doi.org/10.1016/s0008-6223(00)00152-4

[69] Hu, H., B. Zhao, M.E. Itkis, and R.C. Haddon. 2003. "Nitric Acid Purification of Single-Walled Carbon Nanotubes." *Journals of Physical Chemistry B* 107, no. 50, pp. 13838–42. doi: http://dx.doi.org/10.1021/jp035719i

[70] Hernadi, K., A. Siska, L. Thiên-Nga, L. Forró, and I. Kiricsi. 2001. "Reactivity of Different Kinds of Carbon During Oxidative Purification of Catalytically Prepared Carbon Nanotubes." *Solid State Ionics* 141–142, pp. 203–09. doi: http://dx.doi.org/10.1016/s0167-2738(01)00789-5

[71] Avouris, P., and C. Dimitrakopoulos. 2012. "Graphene: Synthesis and Applications." *Materials Today* 15, no. 3, pp. 86–97. doi: http://dx.doi.org/10.1016/s1369-7021(12)70044-5

[72] Novoselov, K.S., A.K. Geim, S.V. Morozov, D. Jiang, Y. Zhang, S.V. Dubonos, I.V. Grigorieva, and A.A. Firsov. 2004. "Electric Field Effect in Atomically Thin Carbon Films." *Science* 306, no. 5696, pp. 666–69. doi: http://dx.doi.org/10.1126/science.1102896

[73] Zang, X., Q. Zhou, J. Chang, Y. Liu, and L. Lin. 2015. "Graphene and Carbon Nanotube (CNT) in MEMS/NEMS Applications." *Microelectronic Engineering* 132, pp. 192–206. doi: http://dx.doi.org/10.1016/j.mee.2014.10.023

[74] Virojanadara, C., M. Syvajarvi, R. Yakimova, L.I. Johansson, A.A. Zakharov, and T. Balasubramanian. 2008. "Homogeneous Large-Area Graphene Layer Growth on 6 H -SiC(0001)." *Physical Review B* 78, no. 24, pp. 245403. doi: http://dx.doi.org/10.1103/physrevb.78.245403

[75] Zhu, Y., D.K. James, and J.M. Tour. 2012. "New Routes to Graphene, Graphene Oxide and Their Related Applications." *Advanced Materials* 24, no. 36, pp. 4924–55. doi: http://dx.doi.org/10.1002/adma.201202321

[76] Compton, O.C., and S.T. Nguyen. 2010. "Graphene Oxide, Highly Reduced Graphene Oxide, and Graphene: Versatile Building Blocks for Carbon-Based Materials." *Small* 6, no. 6, pp. 711–23. doi: http://dx.doi.org/10.1002/smll.200901934

[77] Zhong, Y.L., Z. Tian, G.P. Simon, and D. Li. 2015. "Scalable Production of Graphene Via Wet Chemistry: Progress and Challenges." *Materials Today* 18, no. 2, pp. 73–78. doi: http://dx.doi.org/10.1016/j.mattod.2014.08.019

[78] Eigler, S., and A. Hirsch. 2014. "Chemistry with Graphene and Graphene Oxide-Challenges for Synthetic Chemists." *Angewandte Chemie, International Edition* 53, no. 30, pp. 7720–38. doi: http://dx.doi.org/10.1002/anie.201402780

[79] Chua, C.K., and M. Pumera. 2014. "Chemical Reduction of Graphene Oxide: A Synthetic Chemistry Viewpoint." *Chemical Society Review* 43, no. 1, pp. 291–312. doi: http://dx.doi.org/10.1039/c3cs60303b

[80] García, J.M., R. He, M.P. Jiang, P. Kim, L.N. Pfeiffer, and A. Pinczuk. 2011. "Multilayer Graphene Grown by Precipitation Upon Cooling of Nickel on Diamond." *Carbon* 49, no. 3, pp. 1006–12. doi: http://dx.doi.org/10.1016/j.carbon.2010.11.008

[81] Li, X.S., W.W. Cai, J.H. An, S. Kim, J. Nah, D.X. Yang, R. Piner, A. Velamakanni, I. Jung, E. Tutuc, S.K. Banerjee, L. Colombo, and R.S. Ruoff. 2009. "Large-Area Synthesis of High-Quality and Uniform Graphene Films on Copper Foils." *Science* 324, no. 5932, pp. 1312–14. doi: http://dx.doi.org/10.1126/science.1171245

[82] Zhang, Y., L.Y. Zhang, and C.W. Zhou. 2013. "Review of Chemical Vapor Deposition of Graphene and Related Applications." *Accounts of Chemical Research* 46, no. 10, pp. 2329–39. doi: http://dx.doi.org/10.1021/ar300203n

[83] Yu, Q., J. Lian, S. Siriponglert, H. Li, Y.P. Chen, and S.-S. Pei. 2008. "Graphene Segregated on Ni Surfaces and Transferred to Insulators." *Applied Physics Letters* 93, no. 11, pp. 113103–06. doi: http://dx.doi.org/10.1063/1.2982585

[84] Reina, A., X. Jia, J. Ho, D. Nezich, H. Son, V. Bulovic, M.S. Dresselhaus, and J. Kong. 2009. "Large Area, Few-Layer Graphene Films on Arbitrary Substrates by Chemical Vapor Deposition." *Nano Letters* 9, no. 1, pp. 30–35. doi: http://dx.doi.org/10.1021/nl801827v

[85] Huang, P.Y., C.S. Ruiz-Vargas, A.M. van der Zande, W.S. Whitney, M.P. Levendorf, J.W. Kevek, S. Garg, J.S. Alden, C.J. Hustedt, Y. Zhu, J.Park, P.L. McEuen, and D.A. Muller. 2011. "Grains and Grain Boundaries in Single-Layer Graphene Atomic Patchwork Quilts." *Nature* 469, no. 7330, pp. 389–92. doi: http://dx.doi.org/10.1038/nature09718

[86] Berger, C., Z. Song, T. Li, X. Li, A.Y. Ogbazghi, R. Feng, Z. Dai, A.N. Marchenkov, E.H. Conrad, P.N. First, and W.A. de Heer. 2004. "Ultrathin Epitaxial Graphite: 2D Electron Gas Properties and a Route Toward Graphene-Based Nanoelectronics." *Journal of Physical Chemistry B* 108, no. 52, pp. 19912–16. doi: http://dx.doi.org/10.1021/jp040650f

[87] Su, D.S., and G. Centi. 2013. "A Perspective on Carbon Materials for Future Energy Application." *Journal of Energy Chemistry* 22, no. 2, pp. 151–73. doi: http://dx.doi.org/10.1016/s2095-4956(13)60022-4

[88] Centi, G., S. Perathoner, and D.S. Su. 2014. "Nanocarbons: Opening New Possibilities for Nano-Engineered Novel Catalysts and Catalytic Electrodes." *Catalysis Surveys from Asia* 18, no. 4, pp. 149–63. doi: http://dx.doi.org/10.1007/s10563-014-9172-0

[89] Su, D.S., S. Perathoner, and G. Centi. 2013. "Nanocarbons for the Development of Advanced Catalysts." *Chemical Reviews* 113, no. 8, pp. 5782–816. doi: http://dx.doi.org/10.1021/cr300367d

[90] Toebes, M.L., M.K. van der Lee, L.M. Tang, M.H. Huis in 't Veld, J.H. Bitter, A.J. van Dillen, and K.P. de Jong. 2004. "Preparation of Carbon Nanofiber Supported Platinum and Ruthenium Catalysts: Comparison of Ion Adsorption and Homogeneous Deposition Precipitation." *Journal of Physical Chemistry B* 108, no. 31, p. 11611. doi: http://dx.doi.org/10.1021/jp0313472

[91] Plomp, A.J., D.S. Su, K.P. de Jong, and J.H. Bitter. 2009. "On the Nature of Oxygen-Containing Surface Groups on Carbon Nanofibers and Their Role for Platinum Deposition—An XPS and Titration Study." *Journal of Physical Chemistry C* 113, no. 22, p. 9865. doi: http://dx.doi.org/10.1021/jp900637q

[92] Balasubramanian, K., and M. Burghard. 2005. "Chemically Functionalized Carbon Nanotubes." *Small* 1, no. 2, pp. 180–92. doi: http://dx.doi.org/10.1002/smll.200400118

[93] Vilatela, J.J., and D. Eder. 2012. "Nanocarbon Composites and Hybrids in Sustainability: A Review." *ChemSusChem* 5, no. 3, pp. 456–78. doi: http://dx.doi.org/10.1002/cssc.201100536

[94] Centi, G., and S. Perathoner. 2014. *Nanocarbon-Inorganic Hybrids*, eds. D. Eder and R. Schlögl, 429–54. Berlin, Germany: De Gruyter Pub.

[95] Shi, W., X. Rui, J. Zhu, and Q. Yan. 2012. "Design of Nanostructured Hybrid Materials Based on Carbon and Metal Oxides for Li Ion Batteries." *Journal of Physical Chemistry C* 116, no. 51, pp. 26685–93. doi: http://dx.doi.org/10.1021/jp309000r

[96] Lowy, D.A., and A. Patrut. 2008. "Nonobatteries: Decreasing Size Power Sources for Growing Technologies." *Recent Patents on Nanotechnology* 2, no. 3, pp. 208–19. doi: http://dx.doi.org/10.2174/187221008786369642

[97] Vizuete, M., M. Barrejon, M.J. Gomez-Escalonilla, and F. Langa. 2012. "Endohedral and Exohedral Hybrids Involving Fullerenes and Carbon Nanotubes." *Nanoscale* 4, no. 15, pp. 4370–81. doi: http://dx.doi.org/10.1039/c2nr30376k

[98] Lv, R., E. Cruz-Silva, and M. Terrones. 2014. "Building Complex Hybrid Carbon Architectures by Covalent Interconnections: Graphene–Nanotube Hybrids and More." *ACS Nano* 8, no. 5, pp. 4061–69. doi: http://dx.doi.org/10.1021/nn502426c

CHAPTER 4

HISTORICAL OVERVIEW OF CARBON NANOWIRE FABRICATION METHODS

Bidhan Pramanick

Tecnologico de Monterrey, Mexico and UC Irvine, CA, USA

4.1 OBJECTIVE

Carbon as a material is becoming a tough competitor to silicon and is getting more and more scientific and industrial attention for the construction of miniaturized devices like ICs and microelectromechanical systems (MEMS) or nanoelectromechanical systems (NEMS). Carbon-based micro- or nanostructures are the strongest in nature because of the strength of the carbon–carbon chemical bond and crystallinity that is maintained even down to the molecular scale of a benzene ring. Carbon is available in many allotropes such as diamond, graphite, nanotubes, glassy carbon, buckyballs, and amorphous [1]. Carbon nanotubes (CNTs), graphene, and carbon nanowires (CNWs) with the highest conductivity are the more obvious choices for fundamental research as well as nanoelectronics applications. This property makes them, for example, potential candidates for interconnects in all types of nanodevices. Large-surface-to-volume ratios of one-dimensional structures such as CNTs and CNWs make them also unique to solve problems such as the high power waste in modern computer systems. There are many other applications of CNTs and CNWs such as catalysis, energy storage, active filters, and nanowire sensors [2–5]. As

explained in Section 4.2, CNWs have several advantages over CNTs, and therefore, in contrast with Chapters 2 and 3, this chapter focuses on CNWs only.

This chapter deals with the various fabrication methods of CNWs including template methods, ion and electron beam processes, catalytic growth, Langmuir–Blodgett (LB), chemical liquid deposition (CLD) and chemical vapor deposition (CVD), DC arc discharge, and carbon-based microelectromechanical systems (C-MEMS). The work of different researchers is reported here with the aim of identifying the most suitable CNW and C-MEMS fabrication process for a given application. We will learn that certain C-MEMS approaches offer several advantages such as good ohmic contact, precise CNW positioning, and low cost. The making of CNWs with C-MEMS is discussed in yet more detail in Chapter 5, where the main objective is to discuss the most unique and suitable techniques for the fabrication, positioning, and integration of single or arrays of CNWs with the underlying platforms.

4.2 CNWs COMPARED WITH CNTs

CNT research started as early as 1950, and although it is a quite mature field, it continues to be plagued by several major problems: (1) the difficulty in making ohmic contact, (2) selecting for a precise tube diameter, (3) selecting for a precise tube length, and (4) positioning accuracy. With respect to making ohmic contacts to CNTs, postprocessing metallization steps on precisely positioned wires is required. Nonetheless, the variability of contact resistance from CNT sample to sample remains a major problem. In the case of CNWs, ohmic contacts are automatically established during carbon–carbon bond formation in the carbonization process (see the following). We will also discover that some special CNW processes enable the fine-tuning of wire thickness, length, and position. In contrast, CNTs after synthesis often come with a distribution in lengths and diameters, so they must be isolated and then carefully nanopositioned for integration. This constitutes a low-throughput technique and is unacceptable for mass manufacturing of solid-state devices [2–5]. Finally, CNTs are typically fabricated on a flat substrate, and the interference of the substrate with the CNT proper functioning is unavoidable. In the case of CNWs, it is quite simple to suspend them between carbon electrodes, solving the surface interference problem, and making for better sensor and electronic component performance.

4.3 BACKGROUND OF CARBON NANOWIRE FABRICATION PROCESSES

CNWs were first processed by thermal evaporation as reported by Tang et al. [6]. This group synthesized and characterized amorphous CNWs using Ni catalysts. For the experiments, they used graphite powder (mean particle size: 30 μm, purity: 99.85 percent, most prevalent impurity: O) mixed with 0.1 wt% Ni powder that was pressed into a tablet with a hydraulic press at room temperature. Then, the tablet was placed into a quartz tube mounted in a high-temperature furnace. At a pressure of 4×10^{-2} Torr, high purity Ar was passed through the quartz tube that was heated up to 1,200°C. Smooth and curvy amorphous CNWs with an average diameter of 40 nm were collected from the quartz tube inner wall. Figure 4.1a shows the bright-field transmission electron microscope (TEM) image of nanowires, and in the inset, a selected-area electron diffraction (SAED) pattern from an individual nanowire is presented. This diffuse fraction ring reveals the nanowire to be amorphous.

The concentration of Ni catalyst was found to determine the diameter of the thus obtained CNWs. In Figure 4.1b, we can see the metal catalysts on the tips of the nanowires for a Ni, concentration of 1 wt%. This team also observed that the nanowires with smaller diameters had no catalysts balls on the tips (these are pointed out by arrows in the Figure 4.1b). For the explanation of the disappearance of the metal particles, they speculated that initially the small-diameter nanowires also had metallic particles on their tips but that the metallic balls gradually shrink as the nanowire grows in length.

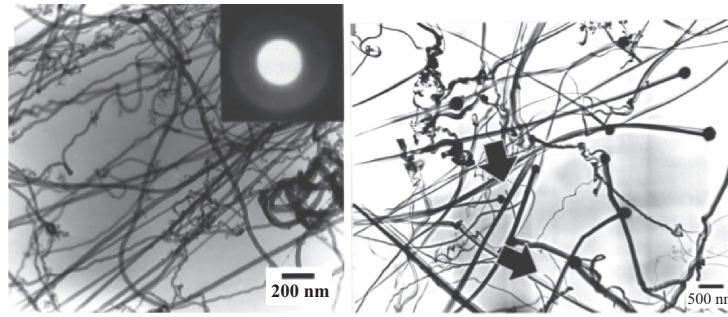

Figure 4.1. (a) Bright-field TEM image of CNWs and SAED pattern of a single nanowire (inset), and (b) TEM image of metallic catalysts on the tips of the nanowires [6].

In a nanowire review paper, Yogeswaran, and Chen listed several biosensors and electrochemical sensors in which nanowires were used as the sensing element [7]. Among others, the application of ZnO nanowires as hydrogen sensors and ethanol sensors is described. Other materials used for nanowire sensing include Pd, Cd, Mo, Au, Ag, and Cu [7–9]. For instance, gold nanowires coated with chitosan to sense H_2O_2 and coated with glucose oxidase (GOx) to sense glucose are discussed. Furthermore, interesting biomedical applications of nanowire-based technology, such as cholesterol and DNA sensing, are explored.

Several methods have been developed for the fabrication of nanowires and nanowire arrays, including template methods, ion and electron beam processes, catalytic growth, LB, CLD and CVD, DC arc discharge, and C-MEMS. These are the methods that we discuss next.

4.3.1 PEDAL PROCESS

The first technique we review here was applied to the fabrication of Pd wires, but it is a generic process that can be extended to CNW fabrication. In [10], Sonkusale and Franzon described a very well-controlled IC wafer-scale process for the fabrication of sub-25 nm arrays of aligned nanowires and nanowire templates, which they call planar edge defined alternate layer (or PEDAL). In the PEDAL process, instead of writing one nanowire at a time (such as in e-beam serial writing lithography) or making one die at a time (such as in step-and-repeat photolithography), nanowires are fabricated all across the wafer simultaneously. In Figure 4.2a to f, we illustrate the PEDAL process that involves defining the path and location of nanowires by making a trench in the substrate (silicon wafer) or in a layer deposited on the silicon wafer. The trench is made using anisotropic dry etching (Figure 4.2a) and after defining the trench, a buffer layer of a-silicon is deposited on it (Figure 4.2b) followed by the conformal deposition of alternate layers of silicon nitride and amorphous silicon (Figure 4.2c). A thick layer of a-silicon is deposited for filling the trench and then a polymer layer using spin coating to planarize the topography of the trench (Figure 4.2d). The stack of polymer, a-silicon, and silicon nitride is planarized down to the required depth (Figure 4.2e) using a single-etch process that is nonselective to silicon nitride, amorphous silicon, and polymer or using a combination of etch processes (Figure 4.2e). The lines and spaces are then revealed using selective etching of the a-silicon material (Figure 4.2f). The width of lines and spaces is dictated by the thickness of the deposited thin films, and the number of depositions controls the number of lines and

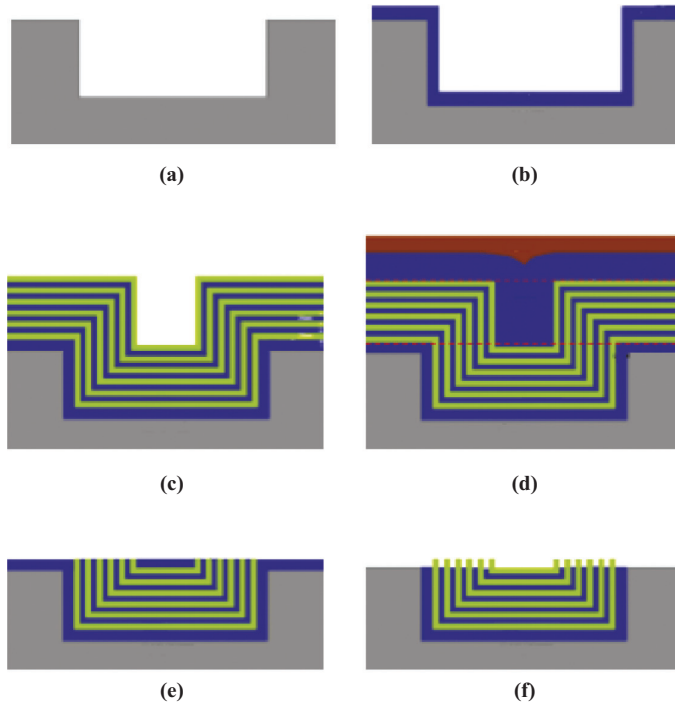

Figure 4.2. (a)–(f) PEDAL process flow [10].

spaces in an array. The PEDAL process has the potential to result in sub-5 nm nanowire structures when using atomic layer deposition (a technique capable of depositing conformal monolayers of a wide range of materials with nanometer accuracy and control) for the deposition of the alternating layers. The PEDAL process fits in with existing IC fabrication infrastructure, and it does not require costly lithography tools that are required in most nanofabrication techniques to make masks, molds, or templates. Sonkusale and Franzon used the PEDAL process for the fabrication of Pd nanowires and observed that the standard deviation of the width of the lines and spaces in an array, across a 4 inch wafer for the case of a 43 nm pitch template was less than 2 nm, and for the case of a 23 nm pitch template, it was less than 1 nm. This PEDAL process is an effective fabrication method for wafer-scale nanowire imprint templates, and it has the capability of making various nanowire routing (Figure 4.3). The CNWs can be directly patterned by this PEDAL process on the template using the commonly used polymer films such as amorphous carbon (a-Carbon) film and fullerene thin-films.

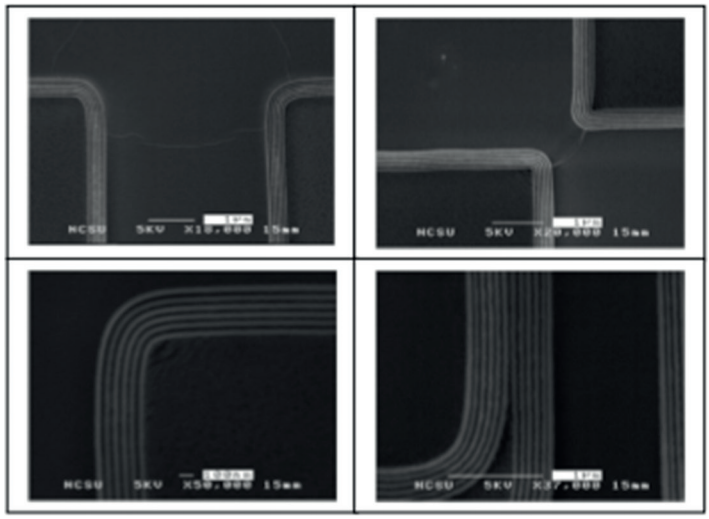

Figure 4.3. Various nanowire routing of PEDAL process [10].

4.3.2 CNW GROWTH THROUGH ION AND ELECTRON BEAM PROCESSES

Avasthi et al. used fullerene thin films to fabricate arrays of CNWs perpendicular to the substrate and perfectly parallel to each other [11]. The conducting CNWs are made using heavy ion irradiation of fullerene thin films. The as-deposited fullerene films exhibit poor field emission characteristics with breakdown fields of up to 51 V/μm. Even a low dose of ion irradiation lowers the threshold field to 9 V/μm. When passing through a material, a swift heavy ion (i.e., a heavy Au ion with energy >1 MeV/nucleon) induces a continuous trail of damage, several nanometers wide, and typically several tens of micrometers long. This results in ion tracks with properties dissimilar to those of the surrounding virgin material. To start the fabrication process, 500 nm thick fullerene films were deposited on a 50 nm thick Au layer on a silicon substrate. The Au layer was deposited using thermal evaporation and provides ohmic contact to the vertically aligned nanowires. Fullerene films were then deposited by sublimation from a C60 pellet and were used as the structural material. In Figure 4.4a and b, we show a schematic of the conducting nanowire formation in fullerene thin films by energetic ion irradiation and atomic force microscopy (AFM) measurements of the resulting CNWs, respectively. A typical resulting AFM image of an irradiated fullerene thin film is presented in Figure 4.4c. The vertical bars in Figure 4.4c represent the

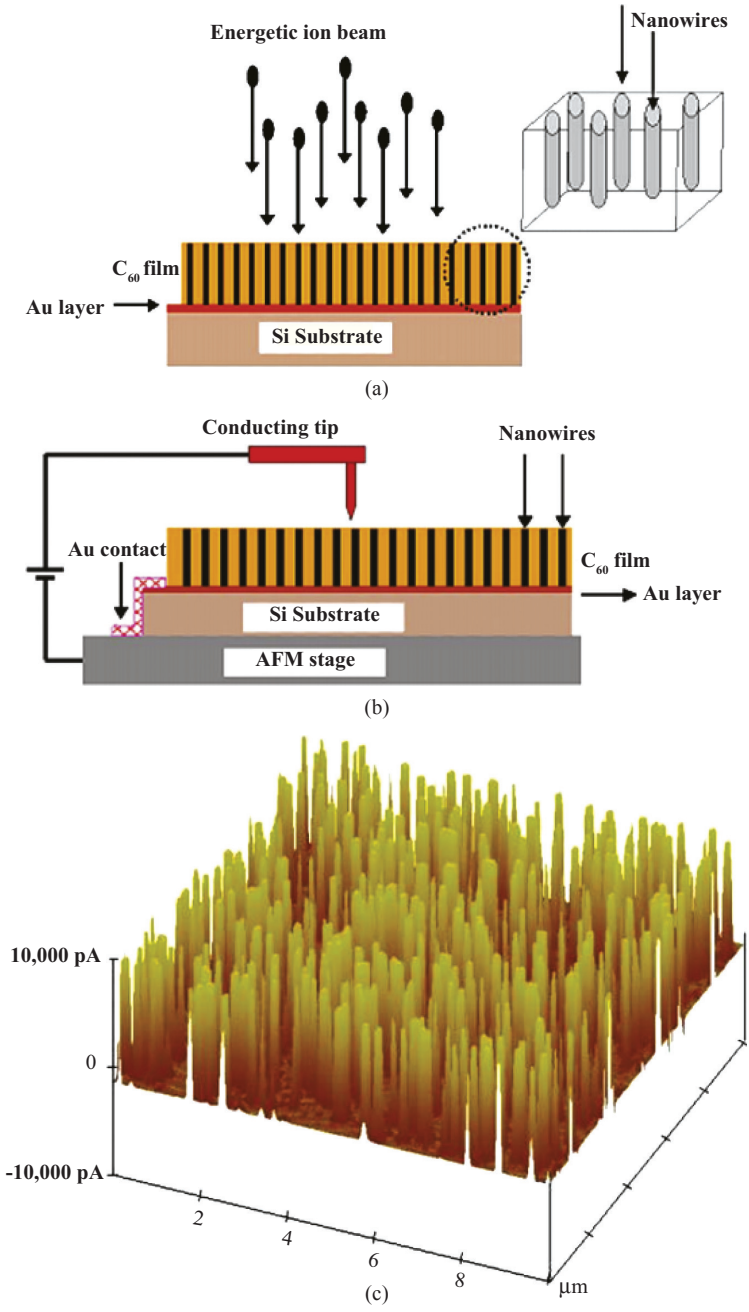

Figure 4.4. (a) Generation of conducting nanowires. (b) Conducting AFM measurement of nanowires. (c) Conducting AFM image of irradiated fullerene thin film. The vertical bars represent the current flowing through individual nanowires [11].

current flowing through the individual nanowires, and it can be observed from the figure that the current in the ion tracks is significantly higher than that in regions not hit by the ions. Sometimes the observed tracks show some mismatch between incident ions doses and the ion track areal density, from random ion impacts, resulting in overlapping tracks and lateral conduction with the neighboring tracks.

Characterization of the nanowire array revealed an average separation between nanowires of 710 nm and an average nanowire length of 500 nm. The process is quite promising for large-scale production of CNWs without a catalyst; ion irradiation treatment for even a few seconds produces CNWs with controlled length and orientation, defined by the thickness of the fullerene films and the ion-beam angle of incidence, respectively. Further optimization of the CNWs fabrication process by (reducing the mismatch between incident ions and ion track areal density) energetic ion irradiation led to the development of individual and continuous nanowires with an average diameter of 4 nm [12].

CNWs fabricated on diamond surfaces using focused ion beam (FIB) either feature high ohmic electrical conductivity, and therefore may serve as electrical nanoconnectors, or may exhibit very nonlinear electronic properties and, as such, serve as active elements in nanoelectronics. Typically, diamond is a perfect insulator with the highest thermal conductivity and hardness and it is very chemically inert, making diamond-based sensors robust and stable. But diamond can also be easily converted into a semiconductor (semiconducting diamond) by doping with boron (for p-type) or phosphorous (for n-type) or into a metal-like conductor by radiation-induced graphitization. So one can envision the possibility here to use the high contrast in electrical conductivity and electronic properties of differently processed areas of a diamond substrate to build a complete electronic circuit. Semiconducting diamond has been used, for example, as a temperature sensor. However, semiconducting diamond also has some drawbacks because of its light sensitivity. CNWs made on diamond surfaces are a viable alternative to those made on semiconducting diamond, as they may exhibit superior temperature sensitivity, exhibit perfect light blindness (no response to light), are easier to fabricate, and allow for nanostructuring at the 10 nm scale. Using FIB irradiation, one can purposely make CNWs and nanodots of a predetermined geometry and in predetermined configurations on a diamond substrate. The same FIB irradiation can also be used to make interconnects between the nanowire–nanodot structures, as well as to fabricate contact pads to connect the nanostructures to the outside world. Ion irradiation at doses exceeding a certain amorphization threshold converts many carbonaceous materials

into a-Carbon that possess relatively high electrical conductivity (compared to insulators). In Figure 4.5, we show the conductivity of several single CNWs versus the annealing temperature curve. The nanowire conductance is increased fast with the annealing temperature, and a-Carbon is eventually completely converted to graphite above a certain temperature (800°C). After the annealing step, the CNWs become several orders of magnitude more conductive than they are in the as-irradiated state. In their work [13], Zaitsev, Levine, and Zaidi used a focused 30 keV Ga^+ ion beam with a radiation dose of 10^{16} ions/cm^2, which exceeds the amorphitization threshold of diamond (may range from 5×10^{14} to 3×10^{15} ions/cm^2) and used the thus produced CNWs as temperature and chemical sensors. Specifically, the CNWs were fabricated using a Micrion 2500 FIB System with a 30 keV Ga^+ ion beam in a vacuum of about 8×10^{-8} mbar. The ion beam current irradiation was controlled in the range from 10 pA to 1 nA during irradiation. A polycrystalline CVD diamond film (optical grade) was used as the substrate. The CNW sensors exhibited a high-temperature sensitivity, rapid and selective response to chemical analytes, and blindness to white light. The same research group noticed that these sensors responded to human breathing at a distance of up to 1 m. They brought tiny droplets of different liquids to the sensor at a distance of 1 cm to verify that observation and found that the sensor exhibited an immediate response, revealing a maximum sensitivity to water. It reacts in seconds to

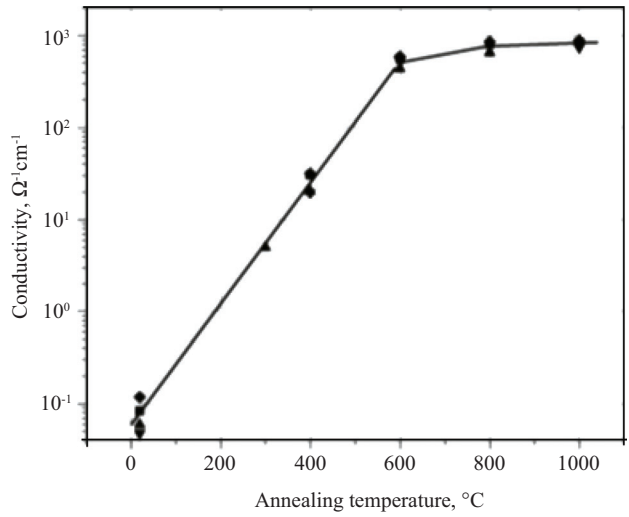

Figure 4.5. The conductivity versus annealing temperature graph [13].

the appearance of a droplet and to its removal. Furthermore, CNW sensors revealed a positive response (increase in current) to water and alcohol, but a negative one to toluene (decrease in current). In Figure 4.6, we show the polycrystalline CVD diamond film substrate with CNWs, and the response of the sensor to droplets of different liquids is shown in Figure 4.7.

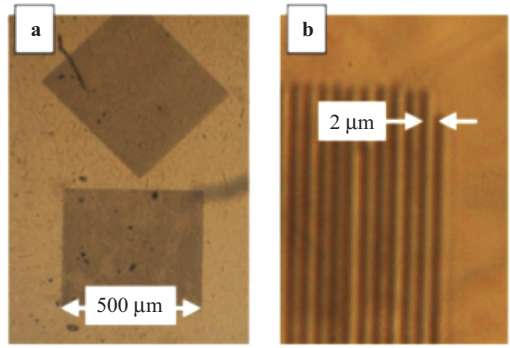

Figure 4.6. (a) Polycrystalline CVD diamond film substrate with two 500 µm CNW structures. (b) A fragment of one of the 500 µm structures showing individual nanowires [13].

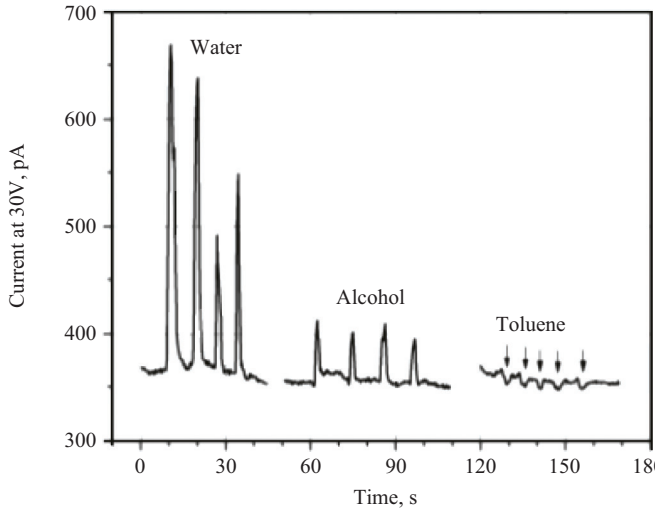

Figure 4.7. Response of the sensor to the droplets of the different liquids rapidly brought to a distance of 1 cm to the sensor and then rapidly retracted [13].

An ion-beam-based method for nanowire fabrication was also reported by Ni et al. in which amorphous carbon nanowire (ACN) networks were fabricated by Si ion beam irradiation of multiwalled carbon nanotubes (MWCNTs) [14]. The MWCNTs, synthesized by thermal CVD, were dispersed on Si substrates and irradiated by a 40 keV Si ion beam. Experiments were performed using different ion doses at room temperature in a 100 keV electromagnetic isotope separator. The morphological evolution and structural changes of the specimens were observed. The energetic particle bombardment results in structural changes in CNTs because of the continuous collisions of Si ions with carbon atoms, which then evolve into solid ACNs at high irradiation doses. It was observed that 2 percent of Si atoms were incorporated into the ACNs. In the method of Ni et al., the formation of CNWs is a three-step process: (1) ion irradiation resulting in gradual amorphitization of the nanotube atomic network, (2) formation of bonds as bridges between nanowires because of irradiation of two crossing nanotubes at certain doses, and finally, (3) formation of networks through further connection of different junctions between adjacent ACNs when large quantities of junctions are generated with a further increase in irradiation dose. This processing technique can be treated as a general approach for the construction of random ACNs for interconnection in nanoelectronic and optical devices. In Figure 4.8a and b, we show the scanning electron microscope (SEM) images of the CNTs before and after ion irradiation, respectively.

Electron beam-induced deposition was used by Peng et al. to fabricate individual a-CNWs [15]. Both fabrication and characterization of the a-CNWs were carried out inside a TEM. In the TEM, an electron beam was focused on a W tip on which organic molecules were adsorbed. The organic molecules are mainly hydrocarbons that are always present in a conventional TEM anyways. As a result of complex beam-induced surface

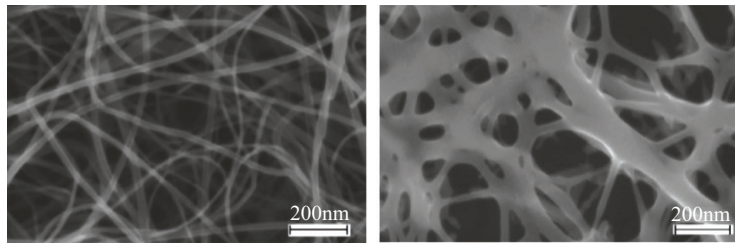

Figure 4.8. SEM images of CNTs (a) before and (b) after ion beam irradiation [14].

reactions, the adsorbed organic molecules were converted into a-Carbon and volatile fragments that were pumped away. The geometry of the fabricated a-CNWs was manually controlled by the movement of the electron beam. The resulting a-CNWS had a diameter of about 29 nm and a length of about 711 nm. The same team also worked on the graphitization of a-CNWs by introducing Fe particles into the fibers and controlling the movement of Fe particles inside the CNWs. A microscopically flat platinum wire was used as a counter electrode to form an electrical loop with W-tip, and MWCNTs with embedded Fe particles were preassembled onto the platinum wire for the study of how current affected the subsequent graphitization of the a-CNWs. Results revealed that current-induced movement of Fe particles plays a significant role in purifying a-CNWs and transforming them into graphitized carbon nanowires (g-CNWs). g-CNWs exhibited very good electrical conductivity of approximately 5.3×10^{-4} Ω·cm. In addition, a current carrying capacity of at least 4.35 mA was calculated, with a current density of 4.6×10^8 A/cm^2. In Figure 4.9a, we show a low-magnification TEM image of a single a-CNW deposited on a W tip. A high-resolution transmission electron microscopy (HRTEM) image of an a-CNW revealing its amorphous nature is shown in Figure 4.9b (inset is an SAED pattern). In Figure 4.10, we display the TEM images of Fe particles in an a-CNW and the resulting structural modification of the a-CNW by the Fe particles. An MWCNT filled with Fe particles was considered to modify the structure and electrical property of the a-CNW and made a contact with the a-CNW. Upon exceeding the applied current threshold value, the encapsulated Fe particles in the MWCNT were started to move toward the a-CNW (Figure 4.10a) and almost all Fe particles were moved to the a-CNW (Figure 4.10b).

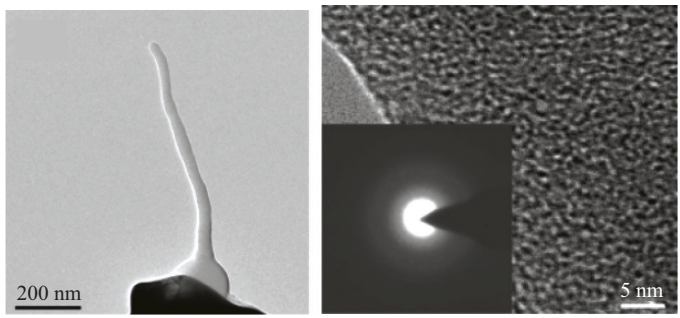

Figure 4.9. (a) TEM image of a single a-CNW deposited on W tip. (b) HRTEM image showing amorphous nature [15].

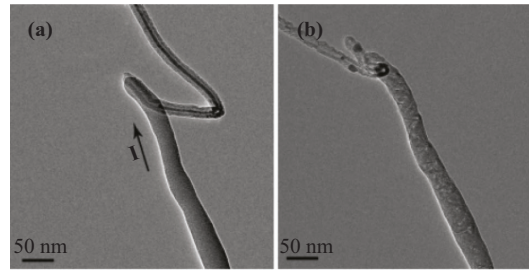

Figure 4.10. TEM images. (a) The a-CNW (the lower part) was controlled to make contact with a Fe filled MWCNT (the upper part), with the arrow indicating the direction of the current, (b) Almost all Fe particles had been introduced into the a-CNW [15].

4.3.3 CATALYTIC CNWS GROWTH

Sellam et al. reported on the catalytic growth of CNWs on a composite diamond–silicon substrate [16]. The CNWs are grown at low temperature on a silicon substrate partially covered by a thin film of polycrystalline diamond. The process flow of the growth of CNWs in this case includes four steps: (1) deposition of diamond film to prepare the diamond or silicon composite substrate, (2) plasma cleaning of the composite substrate to prepare for the metal deposition, (3) metallic thin film deposition to use as catalyst, and (4) metal dewetting (explained in the following) and nanowires growth. In step 1, CVD diamond–silicon composite substrates are prepared through bias-enhanced nucleation (BEN). In BEN, CVD diamond nucleation on pristine single crystal silicon is obtained by in situ cathodic biasing of the substrate under a high CH_4-to-H_2 ratio. The bias voltage and the duration of the voltage application determine the nucleation density of diamond over the silicon surface. The diamond–silicon composite obtained in step 1 was then systematically treated in a microwave plasma to reduce surface impurities and contaminants in step 2. In step 3, the substrate was placed in a magnetron sputter-deposition chamber with a nickel target. The sputtering deposition rate was set to obtain a 5 nm thick nickel film. In step 4, the Ni thin film on the composite was dewetted in a microwave plasma CVD reactor under a hydrogen flow. Upon annealing, thin metal films can degrade into islands in a process that is known as dewetting or sometimes also called agglomeration. The dewetting mechanism is well known to be associated with surface energy minimization. Before the thermal treatment (annealing), pure hydrogen

was introduced into the chamber at a pressure of 60 hPa (hectopascal). The chamber was heated inductively, increasing the temperature progressively up to 580°C. Then the samples were cooled down to room temperature under hydrogen flow. The formation and growth of filamentary structures of nanometric size was observed with filaments with a length of 150 nm and few nanometers in diameter. Normally, a carbon source is necessary for CNWs growth, so carbonaceous species C_xH_y must be present in the gas phase for CNWs to form. However, only pure hydrogen was used in the reaction chamber in this case. The research group predicted that the formation of C_xH_y species could be due to contamination or to diamond etching by atomic hydrogen that is locally generated by H_2 dissociation on the surface of the nickel droplets (formed because of dewetting) and by carbon desorption from the droplet surface with the assistance of hydrogen atmosphere when these droplets etch the diamond surface. Sellam's work stands out in that it uses diamond crystals as the unique carbon source rather than any hydrocarbon species. It can be observed that dewetting results in Ni-based nanodroplets of different sizes and shapes. Also, nanowires systematically include an Ni droplet at their tip as one expects based on the *tip-growth model*. More details on the latter model are presented in Chapter 3. It was also concluded that nanowire growth depends on the metal droplet size and the nature of droplet–substrate interactions. In Figure 4.11, we show TEM images of the obtained filamentary structures.

4.3.4 CNWS FROM LANGMUIR–BLODGETT FILMS AND REACTIVE ION ETCHING

Chong Wei Tan and Beng Kang Tay used the LB method to fabricate CNWs from a-Carbon films that were 500 nm to 1 μm thick [17]. Reactive ion etching (RIE) was used for the anisotropic etching of those carbon films covered with a monolayer of polystyrene (PS) balls deposited using LB technology. In Figure 4.12, we illustrate this fabrication process.

A P-type silicon wafer was chosen for the substrate material and is plasma treated using a CF_4: O_2 gas to remove the native oxide, a process that increases the adhesion between the deposited carbon and silicon. Double-bend filtered cathodic vacuum arc system was used for the deposition of a 1 μm thick a-Carbon layer (step 1). A thin layer of SiO_2 is then deposited using plasma-enhanced CVD at low temperature (50°C) to provide a hard mask layer (step 2). The SiO_2 surface is treated in an oxygen plasma to make the surface hydrophilic and to ensure the adhesion of a monolayer of PS balls that is deposited using the LB method. The initial

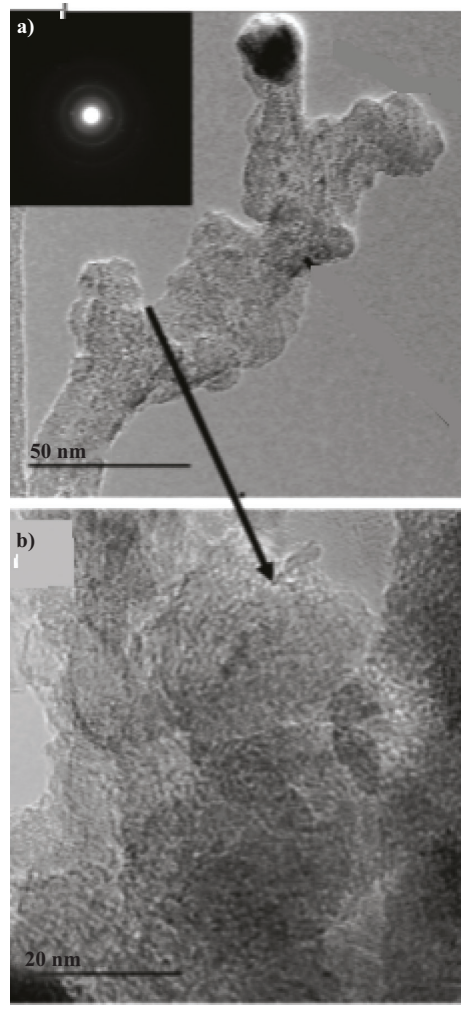

Figure 4.11. (a) TEM images of filamentary structures. Inset, SAED pattern showing three rings corresponding to 002, 111, and 200 graphite diffraction reflections. (b) HRTEM image of selected area of filamentary structure [16].

diameter of the LB-deposited PS balls was 450 nm (step 3), and these shrunk to 150 nm after the RIE (step 4). An RIE process with calibrated parameters is used to etch SiO_2 (step 5) and subsequently the a-Carbon layer (step 6) to produce CNWs. In Figure 4.13, we show the SEM images of the fabricated CNWs.

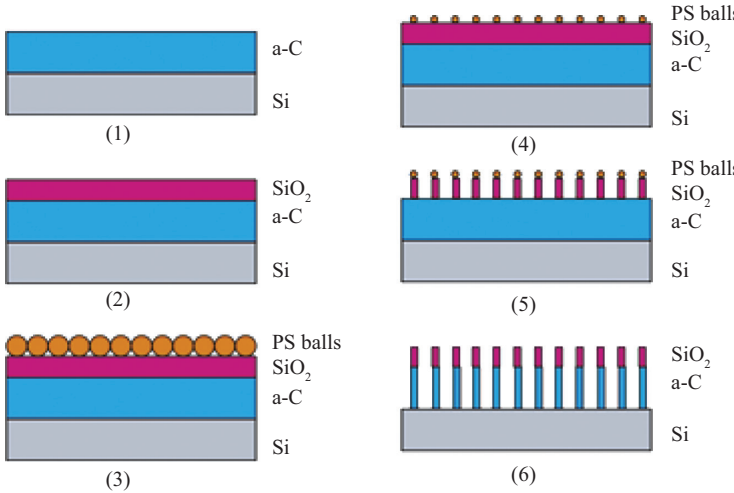

Figure 4.12. Schematic of CNWs fabrication process [17].

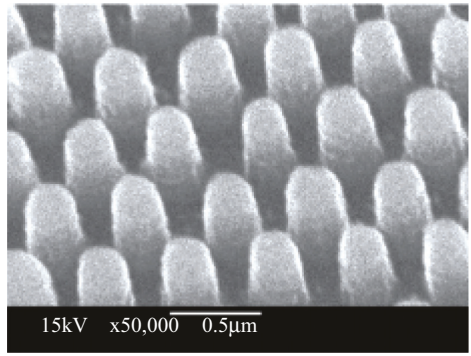

Figure 4.13. SEM images of CNWs [17].

4.3.5 CNWS FABRICATED WITH CATALYTIC CHEMICAL LIQUID DEPOSITION AND CVD METHODS

Cao et al. reported on the fabrication of CNWs, CNTs, and graphene by catalytic chemical liquid deposition (CCLD) of ethanol [18]. In Figure 4.14, we show a schematic of their experimental setup. First, a monocrystalline silicon (111) substrate was ultrasonically cleaned in ethanol and hydrofluoric acid (HF). Then it was dried with Ar at room temperature and coated with a Fe film by electron beam evaporation. The CCLD system shown in Figure 4.14 consists of a main reaction chamber, a recycling-cooling

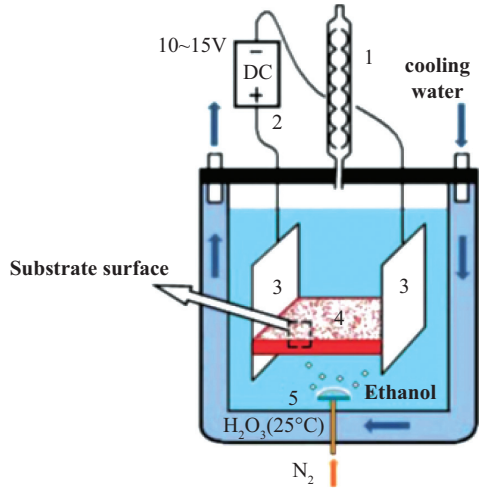

Figure 4.14. Schematic setup of the experimental process: (1) cooling-regurgitated pipe, (2) DC electric power supply, (3) graphite electrodes, (4) silicon chip coated with Fe film, and (5) gas diffuser [18].

system for the ethanol, and a gas purging system. The Fe-film-coated silicon chip was placed transversely (see Figure 4.14) at the center of the reaction chamber and was anchored between two graphite electrodes connected to a DC power supply to heat up the silicon substrate.

Finally, N_2 was pumped into the reaction chamber. Growth parameters such as voltage, organic liquid used, organic liquid-to-water ratio, reaction time, and sweep gas flow rate determine the production of CNTs, CNWs, and graphene. Initially, using pure ethanol, only CNTs were produced on the Fe-coated silicon substrate in this setup. The CNT diameters ranged from 20 to 30 nm and were only a few micrometers long. It was observed that the as-fabricated CNTs had very little a-Carbon on their surfaces (thus, improved purity and structural quality). The presence of H_2O in the ethanol helps in the removal of a-Carbon contamination and plays an indirect role in the growth of single-walled carbon nanotubes (SWCNTs) (more details are provided in Chapter 3). The same research group found that increasing the amount of H_2O in the ethanol gradually decreased the inner diameter of the CNTs. Large quantities of CNWs with lengths of approximately 25.5 μm were densely formed on the silicon surface when 5 percent H_2O was added to the ethanol, thereby providing a method for mass production of CNWs. In Figure 4.15, we present TEM images of

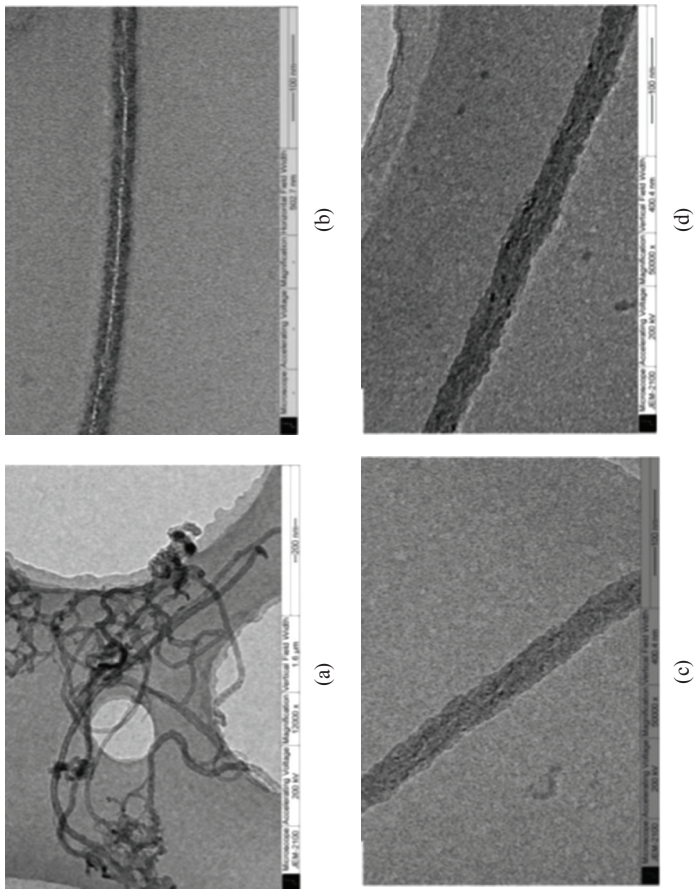

Figure 4.15. TEM images of CNTs and CNWs synthesized with different H_2O contents (a) in pure ethanol, (b) in ethanol with 2 percent H_2O, (c) in ethanol with 5 percent H_2O, and (d) in ethanol with 8 percent H_2O [18].

CNTs grown in pure ethanol and in ethanol with 2, 5, and 8-percent H_2O. The inherent cleanliness of the procedure allows for a perfect contamination-free synthetic process without the use of expensive equipment. When the ratio of H_2O was further increased to 8 percent, a-Carbon forms on the silicon chip instead of CNTs or CNWs.

Generally, the catalytic growth of CNT, CNW, or graphene is considered to occur in two steps: the decomposition of the carbon source at the catalytic surface and vapor–liquid–solid (VLS) mechanisms. Although the research group observed the end of the tube was capped by a cone-shaped catalytic particle (Fe), which suggests the *tip*-like growth model as observed in VLS method discussed in Chapter 3, all the results observed are not explained properly by the existing models.

As the bulk of the liquid in CCLD remains at room temperature, carbon diffusion through the particles and atomic carbon surface transport and carbon precipitation forming CNWs is impossible once the growth leaves the substrate surface. The experimental results support the idea that in CCLD, graphene bubbles play a key role in the nucleation and growth of CNTs. In Figure 4.16, we illustrate the growth steps of CNTs, CNWs, and graphene in CCLD in three steps. In step 1, the catalyst is coated on the silicon substrate. In step 2, the graphene layer forms on the silicon substrate at the same time that the Fe catalysts melts to produce droplets. As we show in step 3, the nanostructure (CNT or CNW) grows vertically into the organic liquid with the simultaneous crystallization of the graphene.

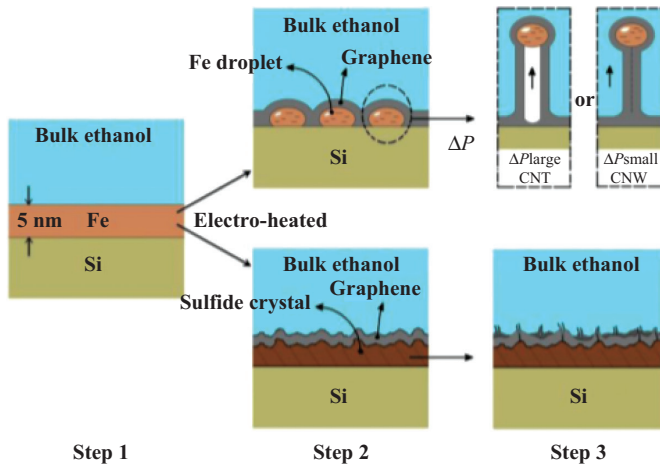

Figure 4.16. Schematic growth steps of CNWs, CNTs, or graphene [18].

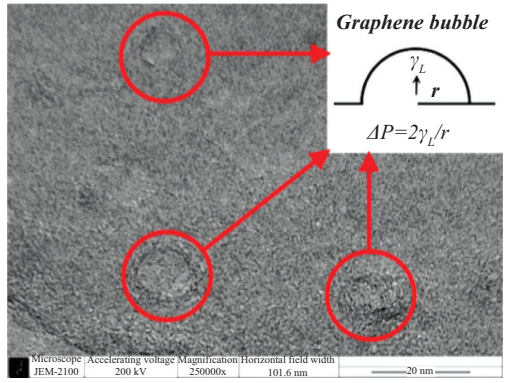

Figure 4.17. TEM images of silicon chip surface during the experiments [18].

In Figure 4.17, we show a TEM image of the silicon surface from process step 2, which indicates the presence of distinguishable graphene layers.

When the silicon chip is electroheated, the internal pressure P_1 (pressure inside ethanol) of the silicon chip surface is changed to P_2, and the formation of graphene bubbles is thus a result of the pressure difference, ΔP, between P_1 and P_2, and this pressure difference is expected to follow the Young–Laplace law of surface tension and is given as

$$\Delta P = \frac{2\gamma_L}{r} \tag{4.1}$$

where r is the radius of curvature and γ_L is the surface tension of graphene film. This surface tension is also known as Laplace pressure and L stands for that in the equation.

Depending on the curvature, ΔP and γ_L, the final reaction products are CNWs, CNTs, or graphene. In Figure 4.18, we show CNWs synthesized in pure ethanol with the top capped by a Fe particle.

CVD is the most popular method for the production of nanocarbon in the form of CNTs and CNWs. However, it requires changing the experimental setup for each desired nanocarbon form and has very stringent growth conditions. A CVD-based method for processing CNWs on a large scale was presented, for example, by Zhao et al. in [19]. In a typical experiment, this group used 10 mL of tetrachloride (CCl_4) and 10 mL of ethylenediamine ($(CH_2NH_2)_2$) to be mixed together in a test tube. The mixture was heated at 100°C for 10 min. A polymerized brown liquid with C–N

bonds resulted and was used as the carbon precursor material for the CVD process. In Figure 4.19, we show a schematic drawing of the CVD reactor used by this team. A 0.5 mL of the brown liquid precursor was mixed with 0.2 mL of $Ni(NO_3)_2 \cdot 6H_2O$ solution in a Al_2O_3 crucible and the crucible was

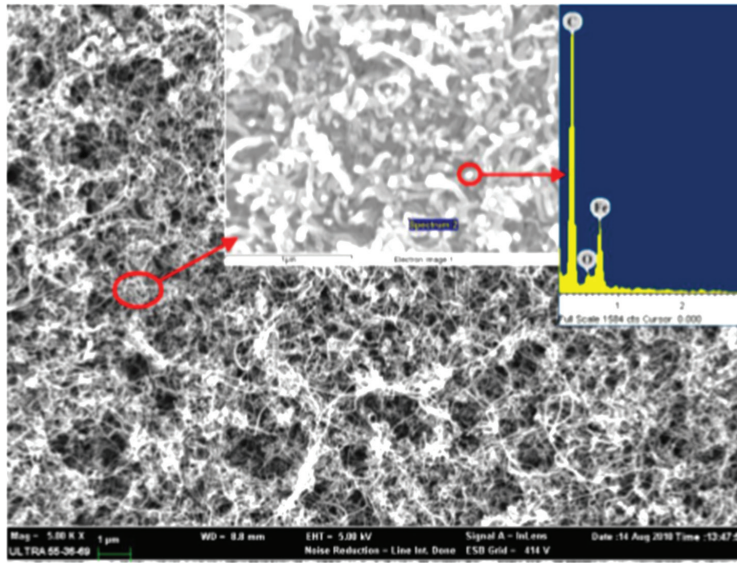

Figure 4.18. CNWs synthesized in pure ethanol with the top capped by a Fe particle. The top right corner image is the energy dispersive X-ray spectroscopy image of the synthesized CNWs [18].

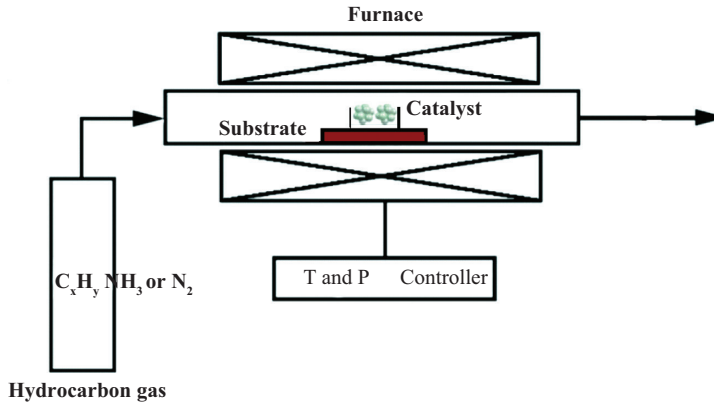

Figure 4.19. Schematic drawing of the experimental settings [19].

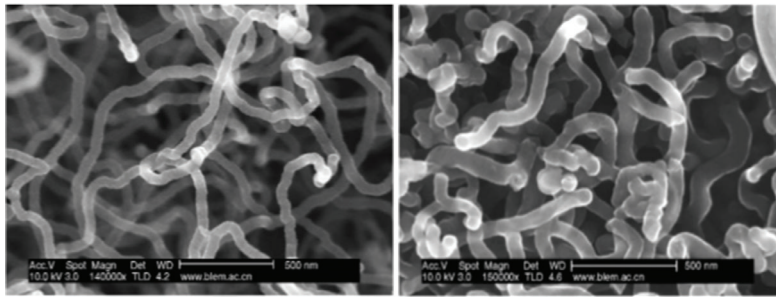

(a) (b)

Figure 4.20. SEM images of the CNWs grown on the Si (100) in (a) NH_3/C_2H_2 ambient and (b) N_2/C_2H_2 ambient [19].

put on a cleaned silicon substrate that was then placed in a quartz tube. At a pressure of 4×10^{-2} Torr, high purity NH_3 (or N_2), C_2H_2 was introduced in the system. The quartz tube was then heated and maintained at 600°C for 4 h and then cooled naturally to room temperature. The crucible and substrate were taken out from the quartz tube furnace and were found to be covered with black carbon layers. In Figure 4.20a and b, we show the SEM images of the CNWs grown on a Si (100) substrate in NH_3–C_2H_2 and N_2–C_2H_2 ambience, respectively. They obtained CNWs with diameters in the range of 50 to 60 nm and with length in the tens of micrometers in an NH_3–C_2H_2 ambient, while in N_2–C_2H_2, the diameter of the nanowires was ~80 nm with lengths shorter than those obtained with NH_3–C_2H_2.

4.3.6 CNWS BY DC ARC DISCHARGE

Su et al. fabricated a novel type of nanowires with an SWCNT core and an amorphous carbon shell (abbreviated as SWCNT–αCNWs) [20]. DC arc discharge method was used to grow a-Carbon directly on the surfaces of SWCNTs. In Figure 4.21, we show the TEM and HRTEM images of SWCNT–αCNWs. A graphite rod with a 40 mm diameter and a 70 mm length and an Ni or Y were mixed by ball milling, which was followed by extrusion molding to form graphite rods with a coal tar as the binder. The catalyst mixed in graphite rod was used as the anode, the mole ratio being (94.8):(4.2):(1.0). A pure graphite rod with an 8 mm diameter and a 300 mm length was used as the cathode. The anode–cathode gap was set between 2 and 3 mm, and the DC arc discharge was run at a current of 90 A, a voltage of 60 V, and a helium pressure of 30 kPa. It was found that

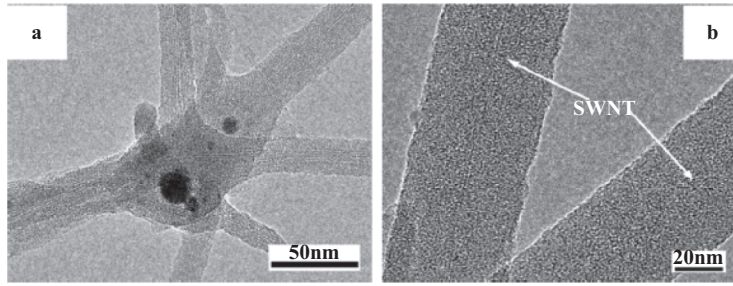

Figure 4.21. (a) TEM and (b) HRTEM images of SWCNT–αCNWs [20].

under these conditions, branched SWCNT–αCNWs with clean and smooth surfaces are formed. The diameters of the branched SWCNT–αCNWs are in the range of 40 to 60 nm and their lengths varied from 20 nm to several micrometers. The distance between the anode and cathode was adjusted to produce different time intervals in the arc discharge process, producing different average diameters. The a-Carbon shell thickness in the coaxial direction increases as a function of that time interval.

Combining electric fields with thermal CVD enables aligned CNW growth directly on a substrate. Kim et al., for example, performed experiments in which CNWs were grown by corona-discharge-assisted thermal chemical vapor deposition (TCVD) in a microgap between electrodes [21]. The corona discharge phenomenon is produced by using an electrode at a very high potential in air, creating a plasma around the electrode. The high energy of the corona around the electrode increases the local temperature around it. In Figure 4.22a, we show the experimental setup for corona-discharge-assisted TCVD, and in Figure 4.21b, we show the schematic of the device that Kim et al. used in their experiments. Silicon wafers with a thick thermally grown layer of SiO_2 were used as the substrates. Bilayers of chrome and nickel were used for electrodes to establish the corona discharge in the device shown in Figure 4.21b. The nickel acts as catalyst to initiate the carbon growth between the electrodes, and the chrome layer is the adhesion layer between SiO_2 and the nickel film. The gap of 1 to 3 μm between the sharp-tipped electrodes and the electrodes themselves were patterned using lift-off photolithography. Aligned CNWs across the microgap between the electrodes were grown in a CVD system. The experiment was carried out at three different temperatures 500°C, 600°C, and 700°C, and in Figure 4.23a to c, we show the respective SEM images. At 500°C, a single CNW was found to be grown between the electrodes whereas at 600°C, a large number of nanowires was grown. The

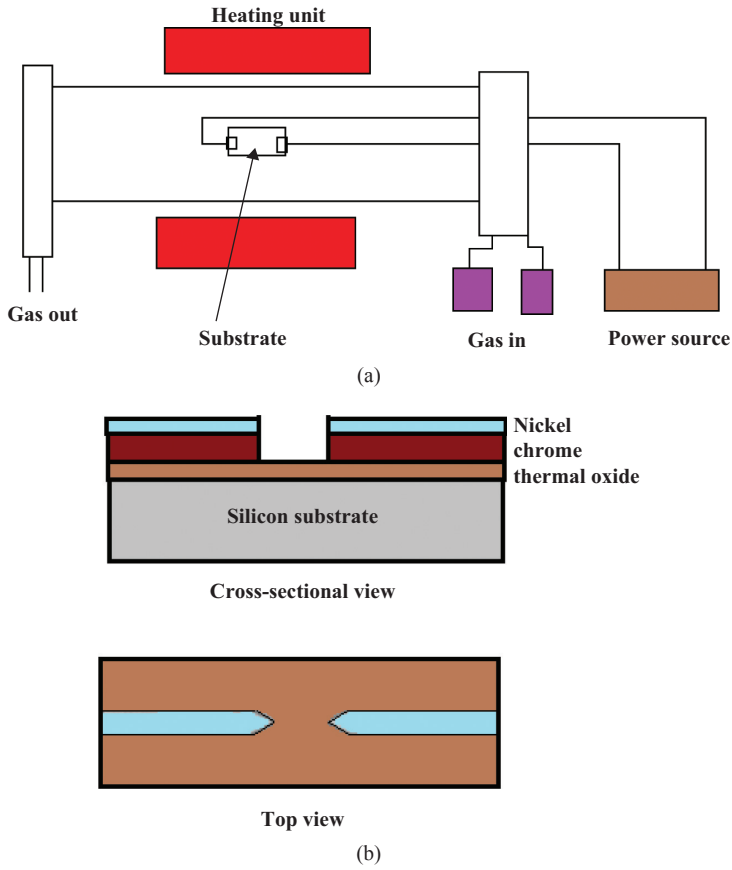

Figure 4.22. (a) Experimental setup for corona-discharge-assisted TCVD. (b) Schematic of the device (cross-sectional and top view) [21].

electrodes were damaged at 700°C because of the high local temperature and CNWs were grown very densely at this temperature.

4.3.7 CNWS MADE BY C-MEMS

C-MEMS defines the fabrication methods used to derive glassy carbon microstructures or nanostructures from a prepatterned organic polymer precursor. The most common manufacturing methodology for C-MEMS realization begins with conventional photolithography of a carbon-precursor-based photosensitive polymer, which is then followed by a carbonization step of the fabricated patterns via pyrolysis. In Figure 4.24, we show some of the first reported C-MEMS structures.

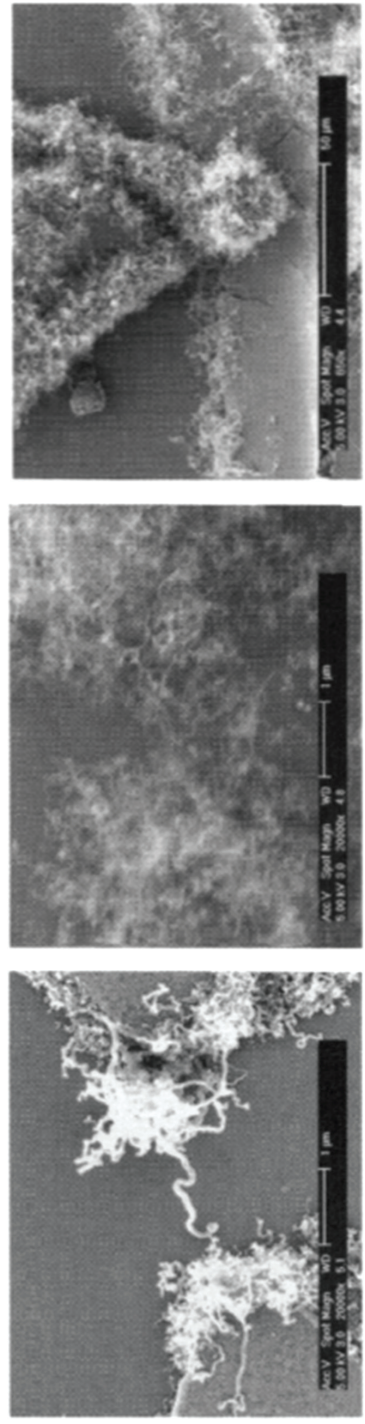

(a) (b) (c)

Figure 4.23. SEM images of corona-discharge-assisted TCVD growth of CNW at (a) 500°C, (b) 600°C, and (c) 700°C [21].

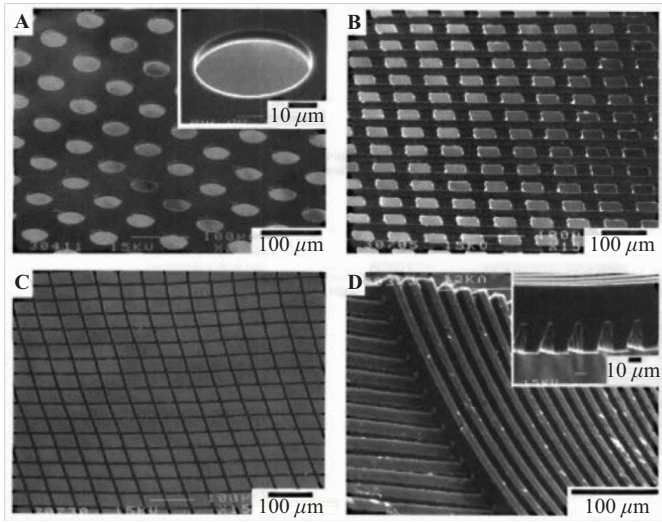

Figure 4.24. First reported C-MEMS structures [22].

In 2005, Madou et al. reported a technique for the patterning of carbon structures from SU8 photoresist [23]. Electron beam lithography (EBL) was used to pattern an SU8 thin film on an Si wafer. The resulting SU8 pattern was then pyrolyzed. CNWs were thus fabricated following a top-down methodology, which allowed for controlling the dimensions and location of the nanofeatures. A very simple schematic illustration of the process steps is presented in Figure 4.25.

Madou et al. also demonstrated a method to fabricate arrays of suspended CNWs by carbonization (also pyrolysis) of polymeric nanowires made from polyacrylonitrile (PAN) and SU8 [24]. The polymer nanowires in this case were fabricated using far-field electrospinning and were suspended between specially designed three-dimensional electrodes (posts), which were made of an organic resorcinol-formaldehyde-based xerogel by using the microreplica molding technique. The details of the electrospinning process are explained in Chapter 5. The processing of PAN-based and SU8 photoresist suspended nanowires before pyrolysis is different. Before pyrolysis of PAN nanowires, a thermal stabilization at 250°C in an oxygen atmosphere is needed. Stabilization is an important step and key to the CNW fabrication, which is performed under heat treatment in air or oxygen-containing atmosphere. Cyclization, dehydrogenation, and oxidation are three major chemical reactions that occur in the production of PAN-based CNWs [25]. The SU8 nanowires, on the other hand, must be exposed to UV light for cross-linking. However, the pyrolysis is carried

out in a nitrogen inert environment at 900°C in both the cases. In Figure 4.26, we show an SEM image of suspended CNWs.

An average diameter of 180 ± 24 nm was achieved for SU8 nanowires, while one of 340 ± 19 nm was observed for PAN nanowires. In Figure 4.27, we show SEM images of a single suspended nanowire made from (a) SU8 and (b) PAN, suspended between two photographically patterned C-MEMS electrodes. The I–V curves for both are presented in Figure 4.27c.

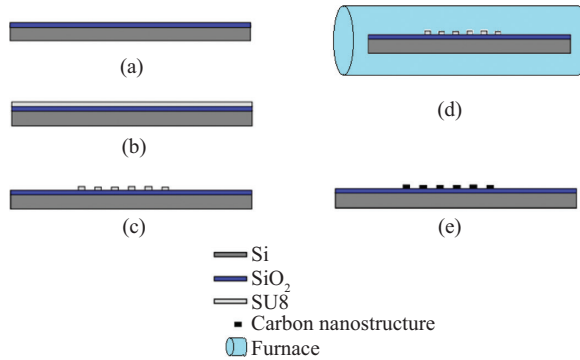

Figure 4.25. Fabrication process steps of carbon nanostructures: (a) SU8 spin coating, (b) patterning by EBL, (c) PR development, (d) pyrolysis process, and (e) carbon nanostructure [23].

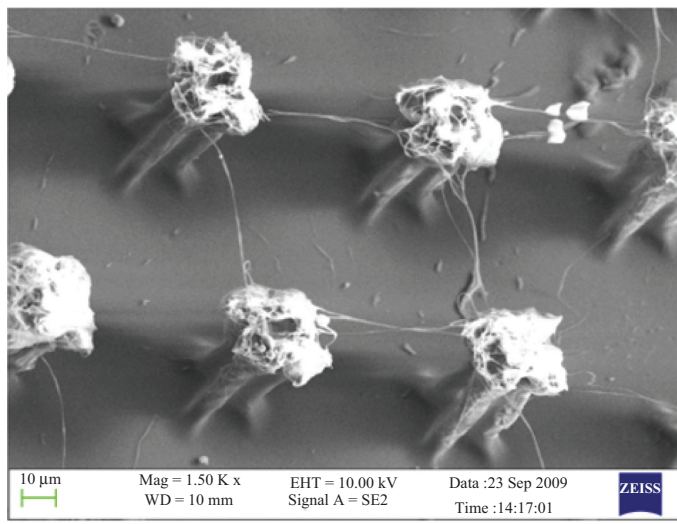

Figure 4.26. SEM image of suspended CNW on 3D carbon post [24].

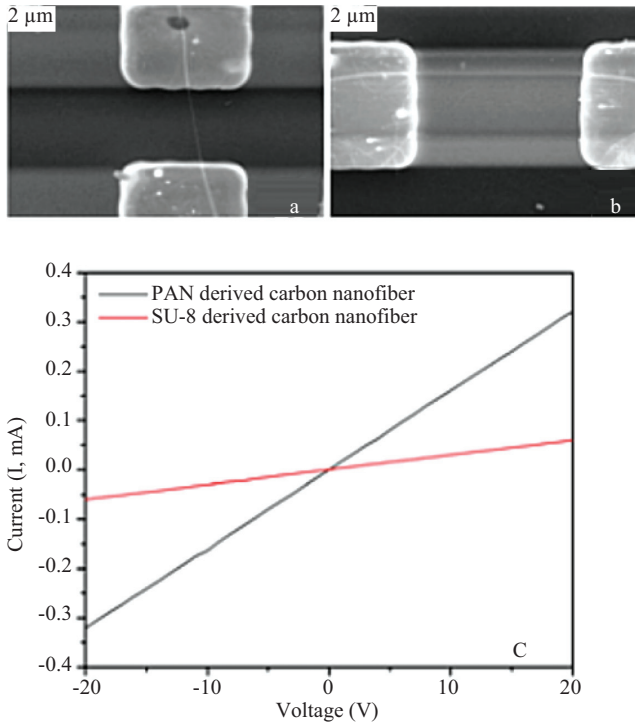

Figure 4.27. SEM images of single suspended nanowire: (a) Su8 derived and (b) PAN derived. (c) I–V curve for the both cases [24].

The linear behavior of the I–V curves in both the cases implies an ohmic contact between the electrodes and the suspended nanowires. This is facilitated by the close integration of the nanowire with its support structures during pyrolysis producing a carbon monolith. The conductance was calculated by measuring the slope of the I–V curves for both the cases, and it was revealed that PAN-derived CNFs are more graphitic than SU8-derived CNF and, therefore, exhibit higher conductivities.

Madou and a collaborator group in South Korea reported the fabrication of scalable suspended CNW meshes using the C-MEMS process [26]. The fabricated CNW meshes were used as electrochemical sensing platforms. A 6-inch silicon wafer with a thermally grown SiO_2 layer was used as the substrate material. The following three photolithography steps were carried out using SU8 as the resist: (1) define the 4-µm thick planar polymer pads (step 4), (2) define the tall contact pads to support the suspended photoresist microwire meshes (step 7), and (3) pattern the suspended photoresist microwire meshes bridging the prepatterned photoresist contact pads (step 8).

Planar electrodes and suspended microwire meshes were released in a single-process step. The completed photoresist structures were converted into carbon by pyrolysis. For the electrochemical application (redox amplification measurements), a polydimethylsiloxane (PDMS) microchannel was fashioned over the carbon nanoelectrodes. Using the previously described process, nanowire mesh structures of various geometries were developed by changing the photomask pattern in the third UV exposure step. In Figure 4.28, we show the fabrication steps of a group

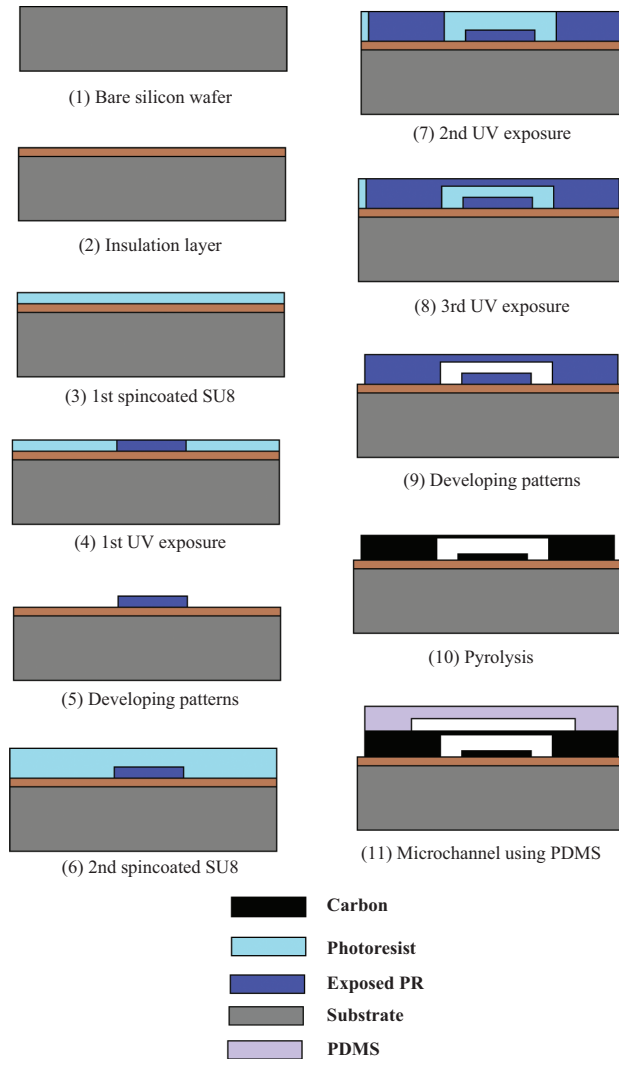

Figure 4.28. Fabrication steps of a group of nanoelectrode set in a microchannel [26].

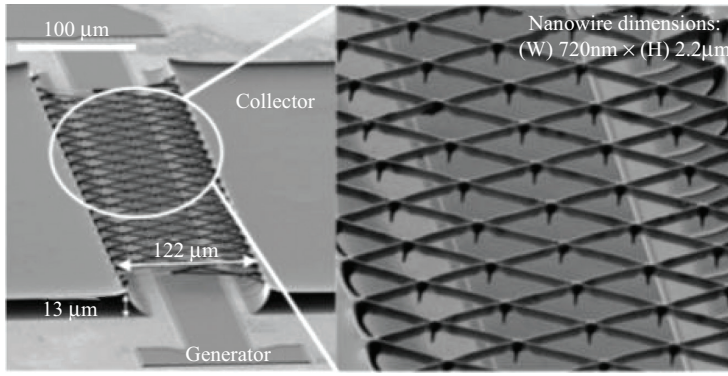

Figure 4.29. SEM images of nanoelectrode set [26].

of nanoelectrode set in a microchannel, and in Figure 4.29, we show two SEM images of a group of nanoelectrode set.

Shin et al. reported on the processing of monolithic suspended glassy carbon nanostructures using two batch processes: UV lithography and polymer pyrolysis [27]. The fabricated carbon structures included two tall carbon pads and a suspended nanowire bridging the pads. The carbonization step causes a dramatic volume reduction of up to 90 percent, converting microscale photoresist structures into nanoscale carbon structures. The resultant suspended CNWs were characterized with SEM, revealing a width, thickness, and length of 300 nm, 600 nm, and 100 μm, respectively. The wire was suspended 7.3 μm above the substrate. In Figure 4.30, we illustrate the fabrication process. SEM images of the single CNW are shown in Figure 4.31. A hydrogen sensor based on the preceding fabricated nanowire was reported by the same research group [28]. For the detection of hydrogen, a thin palladium layer was deposited on the suspended carbon wire. The selective permeability of hydrogen into palladium induces a change in the resistance of the palladium film. This resistance change of the metal layer can be monitored directly by measuring the resistance change between the two suspending carbon posts. The ohmic contact through the monolithic carbon structure ensured a stable and linear sensor response to changes in hydrogen gas concentration. The hydrogen concentration could be resolved down to 20 ppm in atmospheric conditions.

Madou et al. described a simple and scalable fabrication technique for the positioning and integration of suspended CNWs with good ohmic contact to C-MEMS support structures [29]. A combination of photolithography for the C-MEMS suspending structures and electrospinning (electrospinning is detailed in Chapter 5) for the CNWs was used. The

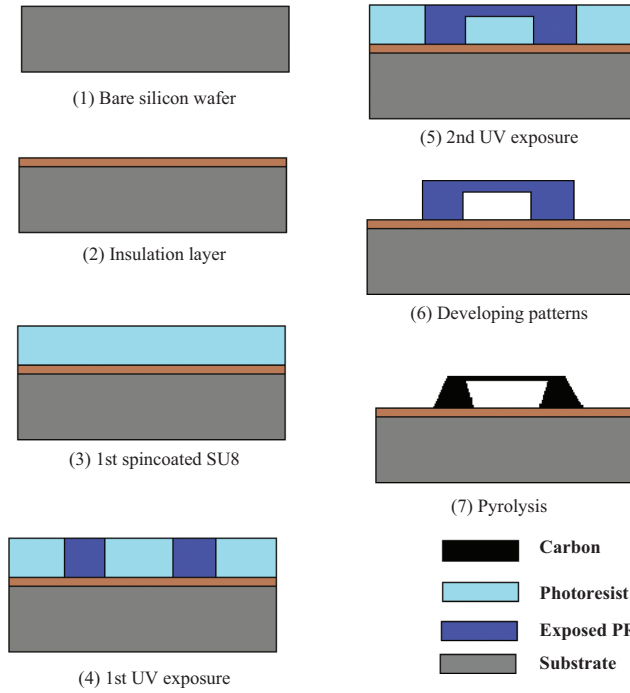

Figure 4.30. Fabrication steps of a suspended nanowire structure [27].

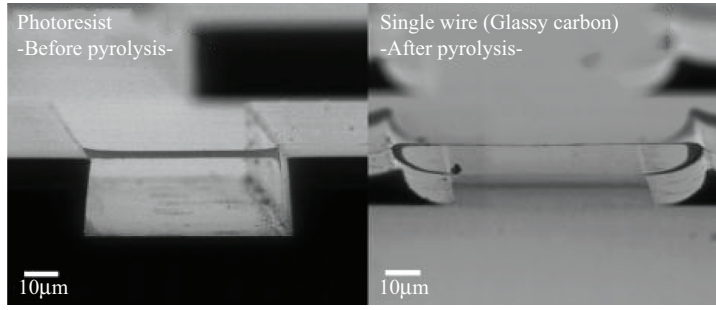

Figure 4.31. SEM images of photoresist and suspended nanowire structure [27].

aim of this team is to ultimately fabricate perfect graphitic wires from contact to contact [29]. The microstructure of the suspended nanowires is very different from the glassy C-MEMS support structures. Most of the CNWs were found to feature a core–shell geometry, with a glassy core

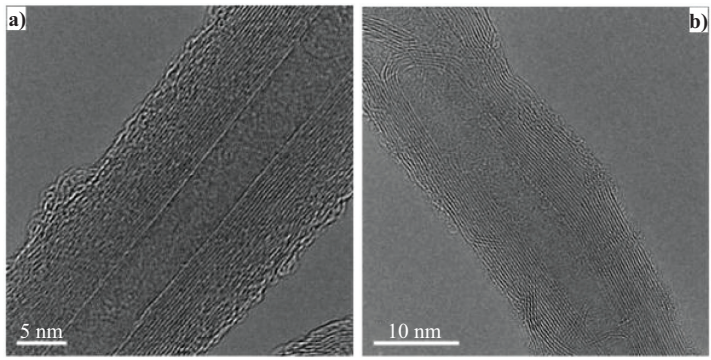

Figure 4.32. HRTEM images of Su8-derived CNWs: (a) tubelike graphitic CNW with glassy carbon core and graphite shell and (b) glassy carbon trapped between graphite walls in a CNW [29].

and a graphitic shell as shown in Figure 4.32. During electrospinning, the polymer precursors molecules in the ink are aligned because of the shear forces in the flow of the jet emanating from the electrospinning nozzle. This forms a template, and the chain configuration is maintained in the pyrolysis process resulting in a graphitic material in which the polymer chains were aligned the best (outside part of the jet) and a glassy carbon (in which chains remained entangled: inside of the jet). Summarizing a polymer with a large chain disentanglement leads to more graphitic CNWs after pyrolysis. The polymer chain, once converted to carbon, cannot be unwound. So the tangled polymer chains that yield glassy carbon, even at high temperature, cannot be reverted back to produce graphitic carbon [30–32].

Some important controlling parameters that influence the wires graphitization are (a) physical properties of the precursor polymer such as chemical composition and viscosity [33], (b) polymer wire thickness [34], (c) carbonization temperature [35], (d) the flow pattern of polymer and nozzle size for the alignment of polymer molecules [36, 37], (e) alignment of polymer chains caused by high electric field [38], (f) catalysts in the precursor polymer [39], and (g) templating [40–43] (as illustrated and shown in Figure 4.32).

The alignment of polymer chains in electrospinning is due to the shear forces generated because of the ink jet being forced through the nozzle during the spinning process itself, but other factors come into play as well. For example, in electrospinning, a high voltage is applied. As the SU8 polymer has a very low electrical conductivity, that high voltage exerts a mechanical force on the SU8 nanowires during their formation, stretching

and disentangling the polymer chains. More details on the process will be discussed in Chapter 5.

Additional mechanical pulling on the polymer can improve the graphitization during carbonization even further. One approach to exert additional mechanical stress on the wires is to suspend them between tall polymer walls. Then, during pyrolysis, the gap between the walls increases (especially at the top, at the bottom, where they are anchored, that gap does increase less), stretching the fiber and at the same time, it carbonizes.

The use of a rotating drum in electrospinning was also found to introduce additional mechanical pull on the nanowires, enhancing graphitization during pyrolysis by molecular combing [29]. The rotating drum acts as a collector for electrospinning nanowires and forces the nanowires to follow a straight pattern, and because of drum's rotation, the nanowires remain taut without touching the substrate (more details are in chapter 5). In the far-field electrospinning experiments on a rotating drum a Si chip was mounted and the precursor polymer, nanowires were jetted out perpendicularly to a set of C-MEMS wall fabricated on the Si substrate using SU8 photolithography. The two 10 μm tall SU8 wall structures on the Si substrate served as underlying electrodes with a 20 μm gap between them. After pyrolysis, the wall height shrunk to 2 μm and the gap increased to ~29 μm. CNWs, ~29 μm long and 42.2 nm thick, were successfully fabricated by this way. Electrical measurements revealed excellent ohmic contact, and therefore, no postprocessing steps were required to mitigate ohmic loses. In Figure 4.33a, we depict an SEM image of two suspended CNWs. One fiber was cut using FIB to ensure that only one CNW was remained on the carbon electrodes. Then the carbon electrode pads were connected to Cu wires with silver paste that then were connected to an

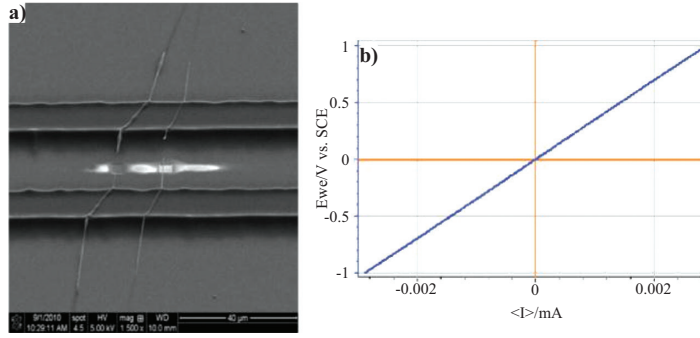

Figure 4.33. (a) FIB cutting for extra CNWs and (b) I–V curve for a single suspended CNW [29].

impedance analyzer to find out the I–V characteristic. A typical I–V curve demonstrating the ohmicity of the CNW contact to the supporting electrodes is shown in Figure 4.33b.

The diameter of the fibers exhibited a significant reduction of 30 percent after pyrolysis. The electrical conductivity of CNWs was found to be in the range of 42 to 113 nm with an average value of 6.13×10^4 S/m, which is almost twice as high as that reported for glassy carbon [29].

4.3.8 OTHER CNWS FABRICATION TECHNIQUES

In addition to the previously described CNWs fabrication processes, many more have been developed by different research groups. Some of the most interesting additional approaches for fabricating CNWs are listed as follows.

1. Lee, Lee, and Lee used a neat one-step photolithography technique to fabricate high aspect ratio SU8 tips on a fused silica substrate [44]. SU8 100 photoresist was used as a carbon precursor material. A UV backside exposure was optimized for producing tip-shaped SU8 structures after development. Pyrolysis transformed the thus obtained SU8 structures into carbon tips. In Figure 4.34,

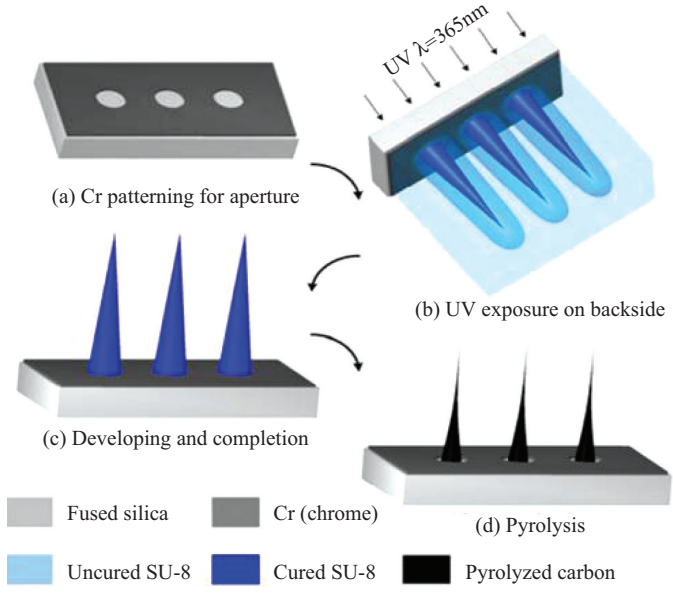

Figure 4.34. Fabrication process steps [44].

the fabrication process is illustrated. The average length (the height above the quartz surface) and diameter of the vertically aligned CNWs were found to be 3.2 μm and 450 nm, respectively, where the diameter at the tip is much smaller. The research group occasionally found the average diameters of CNWs using this technique were less than 100 nm. SEM images, before and after pyrolysis, are shown in Figure 4.35.

2. Wang et al. reported on the nucleation of CNWs at the tip of CNTs under strong electric fields [45]. MWCNTs, 1 to 20 μm long with diameters in the range of 5 to 30 nm, were fabricated following a conventional direct current discharge method (as described in Section 4.3.6). These MWCNTs were glued to a nanomanipulator probe made of tungsten using silver paste for electrical contact. The probe and ground plate counter electrode were set at a distance of 20 μm using a microscope. This specially constructed manipulation holder was inserted into a TEM and the potential difference between the probe and the grounded plate counter electrode was raised to 150 V. Then the distance was readjusted carefully to 500 nm using a

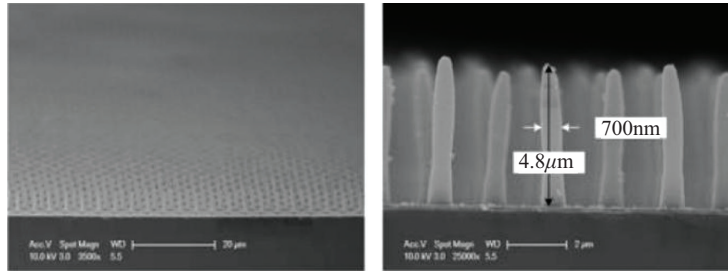

(a)

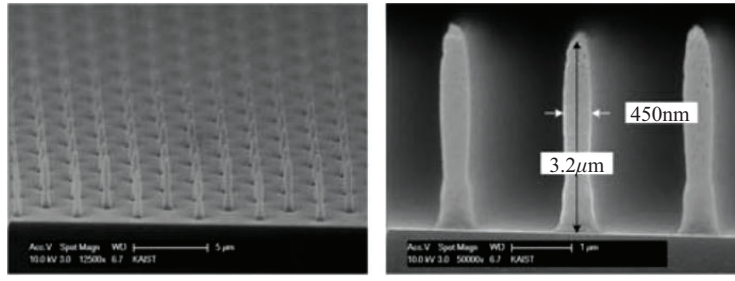

(b)

Figure 4.35. SEM images of fabricated results (a) before and (b) after pyrolysis [44].

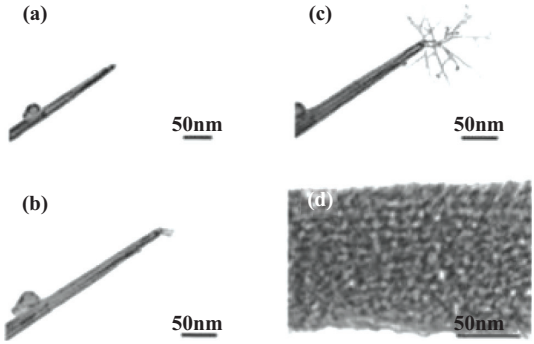

Figure 4.36. TEM images of the formation of CNT–CNW junction under strong electric field, (a) capped CNT, (b) nucleation of the CNW at the tube tip, (c) the growth of nanowire, and (d) high-resolution image of the CNW depicts amorphous nature [45].

piezoelectric actuator. Owing to the negative potential applied to the nanomanipulator probe, the protruding CNTs became electrically charged and were attracted toward the counter electrode. In Figure 4.36, we show two TEM images of the formation of CNT–CNW junctions. The CNWs nucleated at the CNT tip under the strong electric field, similar to what is reported in various other works [46–48]. The CNWs roughly grew along the electric field gradients near the tip. Fractal growth of CNWs resulted in a treelike morphology. The growth rate can be controlled by changing the applied voltage and it was found to decrease when the field strength is decreased. It was demonstrated that the thus produced CNWs had diameters in the range of 5 to 10 nm and lengths of more than 100 nm.

4.4 CONCLUSIONS

CNWs fabrication is still a growing field of research. Many different processes have been attempted by various research groups. The details of the fabrication procedures control the characteristics of the resulting CNWs and a process choice must be based on those desired CNW characteristics as well as reproducibility, the nature of the intended application, production costs, postprocessing requirements, ohmic contact with the supported structure, alignment, and so on. The PEDAL template method appears promising as it constitutes a very controlled IC-like process for nanowire fabrication. However, it has not yet been applied to CNWs, and it also

uses costly fabrication equipment and will be even more expensive when reaching in to the sub-5 nm regime by using ALD. The ion and electron beam processes are also very expensive. Catalytic growth of CNWs is a cost effective process; however, the CNWs made this way are difficult to align. The LB process provides the simplest way of producing out-of-plane CNWs for limited applications. The chemical liquid and vapor deposition methods again use costly equipment. DC arc discharge is a suitable method; however, it does not easily lend itself to aligning and controlling the CNW growth. Among all the many fabrication methods discussed in this chapter, we believe that C-MEMS is the most promising for providing low cost, precise aligned CNWs which are capable of making ohmic contact with the supporting structures with no extra postprocessing steps needed. The details of this process are discussed in Chapter 5.

REFERENCES

[1] Wanekaya, A.K., W. Chen, N.V. Myung, and A. Mulchandani. 2006. "Nanowire-Based Electrochemical Biosensors." *Electroanalysis* 18, no. 6, pp. 533–50. doi: http://dx.doi.org/10.1002/elan.200503449

[2] Walter, E.C., K. Ng, M.P. Zach, R.M. Penner, and F. Favier. 2002. "Electronic Devices from Electrodeposited Metal Nanowires." *Microelectronic Engineering* 61–62, pp. 555–61. doi: http://dx.doi.org/10.1016/s0167-9317(02)00582-8

[3] Chai, Y., Y. Wu, K. Takei, H.Y. Chen, S. Yu, P.C.H. Chan, A. Javey, and H.S.P. Wong. December 6−8, 2010. In *2010 IEEE International Electron Devices Meeting (IEDM*), pp. 214−17. San Francisco, CA: IEEE.

[4] Huang, J., and Q. Wan. 2009. "Gas Sensors Based on Semiconducting Metal Oxide One-Dimensional Nanostructures." *Sensors* 9, no. 12, pp. 9903−24. doi: http://dx.doi.org/10.3390/s91209903

[5] Bibekananda, S., V.J. Babu, V. Subramanian, and T.S.J. Natarajan. 2008. "Preparation and Characterization of Electrospun Fibers of Poly (methyl methacrylate)-Single Walled Carbon Nanotube Nanocomposites." *Journal of Engineered Fibers Fabrics*. 3, no. 4, pp. 39−45. http://journaldatabase.info/articles/preparation_characterization_electrospun.html

[6] Tang, Y.H., N. Wang, Y.F. Zhang, C.S. Lee, I. Bello, and S.T. Lee. 1999. "Synthesis and Characterization of Amorphous Carbon Nanowires." *Applied Physics Letters* 75, no. 19, pp. 2921–23. doi: http://dx.doi.org/10.1063/1.125190

[7] Yogeswaran, U., and S.M. Chen.2008. "A Review on the Electrochemical Sensors and Biosensors Composed of Nanowires as Sensing Material." *Sensors* 8, no. 1, pp. 290–313. doi: http://dx.doi.org/10.3390/s8010290

[8] Kiuchi, M., Y. Isono, S. Sugiyama, T. Morita, and S. Matsui. 2005. In *Proceedings of 5th IEEE Conference on Nanotechnology*. Japan.

[9] Sharma, C.S., A. Verma, M.M. Kulkarni, D.K. Upadhyay, and A. Sharma. 2010. "Microfabrication of Carbon Structures by Pattern Miniaturization in Resorcinol-Formaldehyde Gel." *Applied Materials and Interfaces* 2, no. 8, pp. 2193–97. doi: http://dx.doi.org/10.1021/am100512c

[10] Sonkusale, S., and P. Franzon. 2006. In *1st International Conference on Nano-Networks and Workshops*. NanoNet '06.

[11] Kumar, A., D.K. Avasthi, A. Tripathi, L.D. Filip, J.D. Carey, and J.C. Pivin. 2007. "Formation and Characterization of Carbon Nanowires." *Journal of Applied Physics* 102, no. 4, 044305. doi: http://dx.doi.org/10.1063/1.2767227

[12] Kumar, A., F. Singh, J.C. Pivin, and D.K. Avasthi. 2007. "Fabrication of Carbon Nanostructures (Nanodots, Nanowires) by Energetic Ion Irradiation." *Journal of Physics D: Applied Physics* 40, no. 7, pp. 2083–88. doi: http://dx.doi.org/10.1088/0022-3727/40/7/033

[13] Zaitsev, A.M., A.M. Levine, and S.H. Zaidi. 2008. "Temperature and Chemical Sensors Based on FIB-Written Carbon Nanowires." *IEEE Sensors Journal* 8, no. 6, pp. 849–56. doi: http://dx.doi.org/10.1109/jsen.2008.923252

[14] Ni, Z., Q. Li, D. Zhu, and J. Gong. 2006. "Fabrication of Carbon Nanowire Networks by Si Ion Beam Irradiation." *Applied Physics Letters* 89, no. 5, p. 053107. doi: http://dx.doi.org/10.1063/1.2245372

[15] Jin, C.H., J.Y. Wang, Q. Chen, and L.M. Peng. 2006. "In Situ Fabrication and Graphitization of Amorphous Carbon Nanowires and Their Electrical Properties." *Journals of Physics Chemistry B* 110, no. 11, pp. 5423–28. doi: http://dx.doi.org/10.1021/jp057240r

[16] Sellam, A., P. Miska, J. Ghanbaja, and S. Barrat. 2014. "Catalytic Growth of Carbon Nanowires on Composite Diamond/Silicon Substrates." *Applied Surface Science* 288, pp. 702–09. doi: http://dx.doi.org/10.1016/j.apsusc.2013.10.108

[17] Tan, C.W., and B.K. Tay. 2012. "Carbon Nanowires Fabrications via Top Down Approach." *Journals of Nanoscience and Nanotechnology* 12, no. 1, pp. 707–13. doi: http://dx.doi.org/10.1166/jnn.2012.5399

[18] Cao, L.M., Y.S. Chen, C.L. Yang, Y.Q. Song, J. Yang, and J.P. Jia. 2014. "Selective Fabrication of Carbon Nanowires, Carbon Nanotubes, and Graphene by Catalytic Chemical Liquid Deposition." *Materials Research Bulletin* 55, pp. 229–36. doi: http://dx.doi.org/10.1016/j.materresbull.2014.04.039

[19] Zhao, H., L. Dai, M. Zhao, Y. Xu, and X.L. Chen. 2006. "A New Catalyzed Process to Prepare Large-Scale Carbon Nanowires Based on CVD Method." *Journal of Alloys and Compounds* 416, no. 1–2, pp. 315–18. doi: http://dx.doi.org/10.1016/j.jallcom.2005.09.003

[20] Su, Y., H. Wei, Z. Yang, and Y. Zhang. 2011. "Highly Compressible Carbon Nanowires Synthesized by Coating Single-Walled Carbon Nanotubes." *Carbon* 49, no. 11, pp. 3579–84. doi: http://dx.doi.org/10.1016/j.carbon.2011.04.060

[21] Kim, P., M. Kim, I. Kwon, and G. Lim. 2007. "Low Temperature Carbon Nanowires Growth at the Microgap by Corona Discharge Assisted Thermal CVD." In *Microprocesses and Nanotechnology, 2007 Digest of papers*, pp. 164–165. IEEE. http://ieeexplore.ieee.org/stamp/stamp.jsp?tp=&arnumber=4456155

[22] Schueller, O.J., S.T. Brittain, and G.M. Whitesides. 1997. "Fabrication of Glassy Carbon Microstructures by Pyrolysis of Microfabricated Polymeric Precursors." *Advanced Materials* 9, no. 6, pp. 477–80. doi: http://dx.doi.org/10.1002/adma.19970090604

[23] Ma, K-S., G. Jia, Q. Xu, H. Zhou, C. Wang, J. Zoval, and M. Madou. 2005. *NSTI-Nanotech*. 2, pp. 151–54. http://www.nsti.org/publications/Nanotech/2005/pdf/493.pdf

[24] Sharma, C.S., H. Katepalli, A. Sharma, and M. Madou. 2011. "Fabrication and Electrical Conductivity of Suspended Carbon Nanofiber Arrays." *Carbon* 49, no. 5, 1727–32. doi: http://dx.doi.org/10.1016/j.carbon.2010.12.058

[25] Mortazavi, S.H., S. Pilehvar, M. Ghoranneviss, M.T. Hosseinnejad, S. Zargham, A.A. Mirarefi, and A.Y. Mirarefi. 2013. "Plasma Oxidation and Stabilization of Electrospun Polyacrylonitrile Nanofiber for Carbon Nanofiber Formation." *Applied Physics A* 113, no. 3, pp. 703–12. doi: http://dx.doi.org/10.1007/s00339-013-7707-2

[26] Heo, J.-I., Y. Lim, M. Madou, and H. Shin. 2012. "Scalable Suspended Carbon Nanowire Meshes as Ultrasensitive Electrochemical Sensing Platforms." In *IEEE 2012 IEEE 25th International Conference on Micro Electro Mechanical Systems (MEMS)*, pp. 878–81. Paris, France: IEEE.

[27] Lim, Y., J. Heo, M.J. Madou, and H. Shin. June 16–20, 2013. "Development of Suspended 2D Carbon Nanostructures: Nanowires to Nanomeshes." *The 17th International Conference on Solid-State Sensors, Actuators and Microsystems (Transducers 2013)*. Barcelona, Spain.

[28] Heo, J., Y. Lim, and H. Shin. June 16–20, 2013. "A Stacked Electrode Set Including Suspended Carbon Nanomeshes and Planar Carbon Pads for Electrochemical/Bio Sensor Applications." *The 17th International Conference on Solid-State Sensors, Actuators and Microsystems (Transducers 2013)*. Barcelona, Spain.

[29] Sharma, S., A. Sharma, Y.-K. Cho, and M. Madou. 2012. "Increased Graphitization in Electrospun Single Suspended Carbon Nanowires Integrated with Carbon-MEMS and Carbon-NEMS Platforms." *Applied Materials and Interfaces* 4, no. 1, pp. 34–39. doi: http://dx.doi.org/10.1021/am2014376

[30] Park, B.Y., L. Taherabadi, C. Wang, J. Zoval, and M.J. Madou. 2005. "Electrical Properties and Shrinkage of Carbonized Photoresist Films and the Implications for Carbon Microelectromechanical Systems Devices in Conductive Media." *Journals of Electrochemical Society* 152, no. 12, pp. J136–43. doi: http://dx.doi.org/10.1149/1.2116707

[31] Singh, A., J. Jayaram, M. Madou, and S. Akbar. 2002. "Pyrolysis of Negative Photoresists to Fabricate Carbon Structures for Microelectromechanical Systems and Electrochemical Applications." *Journal of Electrochemical Society* 149, no. 3, pp. E78–83. doi: http://dx.doi.org/10.1149/1.1436085

[32] Jenkins, G.M., and K. Kawamura.1971. "Structure of Glassy Carbon." *Nature* 231, no. 5299, pp. 175−76. doi: http://dx.doi.org/10.1038/231175a0

[33] Harris, P.J.F. 2004. "Fullerene-Related Structure of Commercial Glassy Carbons." *Philosophical Magazine* 84, no. 29, pp. 3159−67. doi: http://dx.doi.org/10.1080/14786430410001720363

[34] Franklin, R.E. 1951. "Crystallite Growth in Graphitizing and Non-Graphitizing Carbons." In *Proceeding of the Royal Society of London Series A* 209, no. 1097, pp. 196−218. doi: http://dx.doi.org/10.1098/rspa.1951.0197

[35] Ji, Y., C. Li, G. Wang, J. Koo, S. Ge, B. Li, J. Jiang, B. Herzberg, T. Klein, and S. Chen. 2008. "Confinement-Induced Super Strong PS/MWNT Composite Nanofibers." *EPL* 84, no. 5, p. 56002. doi: http://dx.doi.org/10.1209/0295-5075/84/56002

[36] Ehrenstein, G.W., and R.P. Theriault. *Polymeric Materials: Structure, Properties, Applications*, 67. Munich, Germany: Carl Hanser Verlag.

[37] Ko, F., Y. Gogotsi, A. Ali, N. Naguib, H. Ye, C. Li, and P. Willis. 2003. "Electrospinning of Continuous Carbon Nanotube-Filled Nanofiber Yarns." *Advanced Materials* 15, no. 14, pp. 1161−65. doi: http://dx.doi.org/10.1002/adma.200304955

[38] Kim, J.M., T. Ohtani, J.Y. Park, S.M. Chang, and H. Muramatsu. 2002. "DC Electric-Field-Induced DNA Stretching for AFM and SNOM Studies." *Ultramicroscopy* 91, no. 1−4, pp. 139−49. doi: http://dx.doi.org/10.1016/s0304-3991(02)00093-1

[39] Oya, A., and H.J. Marsh. 1982. "Phenomena of Catalytic Graphitization." *Journal of Material Science* 17, no. 2, pp. 309−22. doi: http://dx.doi.org/10.1007/bf00591464

[40] Du, R., S. Ssenyange, M. Aktary, and M.T. McDermott. 2009. "Fabrication and Characterization of Graphitic Carbon Nanostructures with Controllable Size, Shape, and Position." *Small* 5, no. 10, pp. 1162−68. doi: http://dx.doi.org/10.1002/smll.200801357

[41] Sevilla, M., and A.B. Fuertes. 2006. "Catalytic Graphitization of Templated Mesoporous Carbons." *Carbon* 44, no. 3, pp. 468−74. doi: http://dx.doi.org/10.1016/j.carbon.2005.08.019

[42] Serway, R.A., and J.S. Faughn. 2003. *College Physics*. 6th ed. Belmont, CA: Thomson.

[43] Tien, L.C., H.T. Wang, B.S. Kang, F. Ren, P.W. Sadik, D.P. Norton, S.J. Pearton, and J. Linc. 2005. "Room-Temperature Hydrogen-Selective Sensing Using Single Pt-Coated ZnO Nanowires at Microwatt Power Levels." *Electrochemical and Solid-State Letters* 8, no. 9, pp. G230–32. doi: http://dx.doi.org/10.1149/1.1979450

[44] Lee, S.W., J.A. Lee, and S.S. Lee. 2008."Vertically Aligned Carbon Nanowires (CNWs): Top-Down Approach Using Photolithography and Pyrolysis." *NSTI-Nanotech* 1, pp. 604–07. http://hdl.handle.net/10203/153622

[45] Wang, Y.G., Q.H. Li, T.H. Wang, X.W. Lin, V.P. Dravid, and S.X. Zhou. 2005. "In Situ Growth of Nanowire on the Tip of a Carbon Nanotube Under Strong Electric Field." *Applied Physics Letters* 86, no. 13, p. 133103. doi: http://dx.doi.org/10.1063/1.1879090

[46] Ji, M., C. Wang, Y. Bai, M. Yu, and Y. Wang. 2007. "Structural Evolution of Polyacrylonitrile Precursor Fibers During Preoxidation and Carbonization." *Polymer Bulletin* 59, no. 4, pp. 527–36. doi: http://dx.doi.org/10.1007/s00289-007-0796-3

[47] Al-Muhtaseb, S.A., and J.A. Ritter. 2003. "Preparation and Properties of Resorcinol-Formaldehyde Organic and Carbon Gels." *Advance Materials* 15, no. 2, pp. 101–14. doi: http://dx.doi.org/10.1002/adma.200390020

[48] Lozano, K., and K. Sarkar. 2009. "Methods and Apparatuses for Making Superfine Fibers." U.S. Patent 2009/0280325 A1.

CHAPTER 5

CARBON NANOWIRE FABRICATION: C-MEMS

Bidhan Pramanick[1], Fatimah Ibrahim[2], and Aung Thiha[2]

[1]Tecnologico de Monterrey, Mexico and UC Irvine, CA, USA,
[2]University of Malaya, Malaysia

5.1 OBJECTIVE

Nanotechnology has gained huge interest in research and industry because of the unique and fascinating properties of nanomaterials or nanostructures. In the past 15 years, the carbon microelectromechanical systems process (C-MEMS) has become useful and essential for various polymer-based microstructures because of its ease and inexpensive fabrication steps. The common manufacturing methodology for C-MEMS fabrication starts with photolithography of a photosensitive polymer precursor of high carbon content and it is followed by a carbonization process for the patterned polymer. Therefore, one photolithography step for polymer patterning and one step for pyrolysis to carbonize the patterned polymer may define the C-MEMS process. Various high aspect ratio 3D structures have been successfully fabricated using this process for diverse applications such as microbatteries and gas sensors [1, 2]. We are interested in reporting the fabrication of nanoscale functional components, namely, carbon nanowires (CNWs), using C-MEMS or better yet: carbon nanoelectromechanical system (C-NEMS). So for CNW-based devices, basically, CNWs are connected with MEMS electrodes that may be fabricated through a different process than traditional photolithography and this is also true for the fabrication of CNWs. Many fabrication techniques for nanowires (NWs) and CNWs used by various research groups were reported in Chapter 4,

and in this chapter, we discuss the CNWs in more detail with emphasis on the electrospinning technique. Electrospinning has emerged as a simple and low-cost approach to fabricate 1D structures and is based on an electrostatic force that acts on a conducting polymer solution to form a fiber jet. In general, polymer solutions do not respond to electric fields, as these are insulator materials by nature. In electrospinning, it is thus required to make the polymer solution (also ink) conductive by adding salts. For example, tetrabutyl ammonium tetrafluoride is a typical salt added to SU8, before using it as a source material for electrospinning. This way, we will learn how to fabricate long-continuous nanofibers with tunable diameters and controllable compositions with this technique.

The major challenges for CNW-based devices are the positioning and integration of the CNWs with the underlying platforms. So the main objective of this chapter is to discuss the most unique and suitable techniques for the fabrication, positioning, and integration of single CNWs with the underlying platforms (electrodes). We briefly discuss the basics of the photolithography and pyrolysis in the next section for the fabrication of supporting structures and then report on the NW fabrication using electrospinning. The fundamentals and various types of electrospinning are also discussed in this chapter.

5.2 FABRICATION OF SUPPORTING STRUCTURES FOR CNWs

In the late 1990s, Schueller, Brittain, and Whitesides first introduced carbon microstructures made using pyrolysis of a micromolded precursor polymer, and they used these microstructures as components in microreactors [3]. In 2002, Singh et al. fabricated C-MEMS structures using negative photoresist, SU8, on silicon wafers for the first time [4]. Since then, various complex high aspect ratio C-MEMS structures such as posts, self-organized bunched posts and carbon beams supporting wires, and interdigitated electrodes have been fabricated [5–7]. We discuss the fabrication of the supporting structures (electrodes) for suspended CNWs in this section.

Glassy carbon (GC) is a widely used electrode material in electrochemistry and also in high-temperature applications. GC is a nongraphitizing carbon that combines glassy and ceramic properties with high conductivity. The microstructure of GC is composed of both crystalline and amorphous regions. In the first chapter of this book, it was made clear that GC is not to be confused with amorphous carbon. GC has good resistance to

high temperatures, low density, low electrical resistance, and relatively high hardness and high resistance to chemical attack. It is the combination of all these properties that have made GC special for biological, chemical, and many other applications. A most interesting thing is that GC can be made from polymer carbon precursors (such as SU8) by pyrolyzing it at a temperature between 800°C and 3,000°C. We will see in the following that CNWs can be made from the same carbon precursor, SU8; this is a very advantageous process characteristic because the integration of CNWs with the supporting structure is rather simple. SU8 is a negative tone photoresist and has the flexibility to fabricate almost any desired design through conventional photolithography and this is followed by pyrolysis. We briefly address photolithography and pyrolysis in the next two subsections.

5.2.1 PHOTOLITHOGRAPHY

In a photolithography process, a 2D layout of a desired structure is transferred to the surface of a flat photosensitive-coated substrate. This process consists mainly of substrate preparation, photoresist spin coating, soft bake, exposure, postexposure bake, and development steps. In the case of C-MEMS, usually, silicon, silicon dioxide, silicon nitride, quartz, and more recently, sapphire are used as substrates. The substrate is first cleaned and coated with a photosensitive polymer (photoresist). The photoresist is then soft baked to improve its adhesion to the substrate. Subsequently, the photoresist is exposed to UV light through a mask (2D layout pattern of desired structures). Finally, the film is developed and the resist is hard baked, enhancing the resistance of the resist features against the additive and subtractive processes that follow. The resulting structure, ideally, has the exact same shape of the designed pattern with the resist vertical walls maintained throughout the thickness of the resist. In very few cases, the patterned photoresist is the final goal of the fabrication process, that is, the photoresist is a functional part of the intended design, but more typically, the binary pattern is needed as a mask or as a sacrificial layer only. In C-MEMS, the polymer pattern is the precursor of the intended carbon device. The photolithography processing steps including the final pyrolysis step are summarized in Figure 5.1. In Figure 5.2, we show a schematic illustration of the photolithography process used for producing a pair of 3D polymer walls that will be used as the CNW support structures.

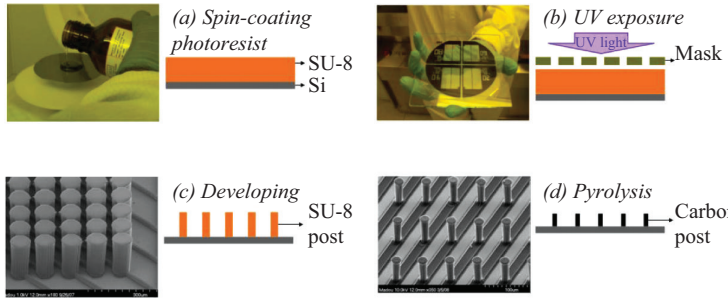

Figure 5.1. Typical C-MEMS fabrication process steps [8]: (a) spin-coating photoresist, (b) UV exposure, (c) developing, and (d) pyrolysis.

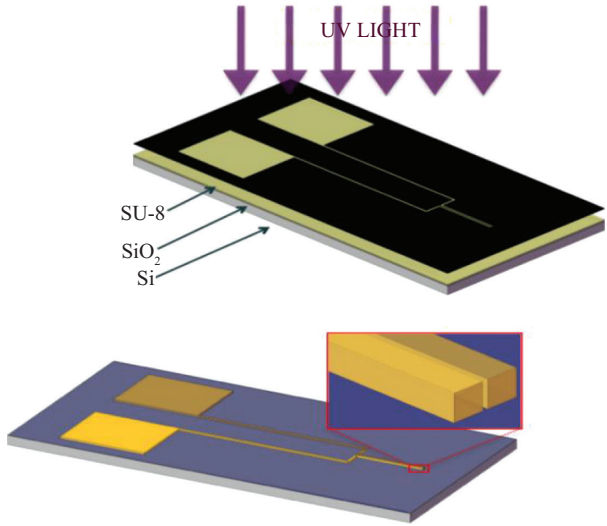

Figure 5.2. MEMS structures before and after UV exposure [8].

5.2.2 PYROLYSIS

The final step used in the C-MEMS process is the pyrolysis of the developed photoresist structure. In pyrolysis, a carbon precursor material (such as SU8 photoresist) is converted into carbon. This is accomplished by heating the precursor material in an inert atmosphere (e.g., nitrogen, argon, vacuum) at temperatures above 800°C and up to 3,000°C. The final temperature and also the temperature ramp rate of the process define various properties of the resulting carbon structure such as porosity, microstructure, electrical conductivity, and mechanical properties.

In general, samples are first introduced in a quartz tube furnace where an inert gas is flown for at least 10 minutes to ensure the required inert environment for pyrolysis. The furnace is then heated from room temperature to 300°C at a ramp rate of 5°C/min and kept at this temperature for an hour. Inert gas flow (flow rate = 2,000 sccm) is constant throughout the process. Then the oven temperature is ramped up at 10°C/min to a final temperature of 900°C, with a dwell time of one hour at this temperature. The heater is then turned off allowing the furnace to cool down to room temperature. During the pyrolysis, the precursor materials shrink considerably because of the loss of noncarbon atoms. In the case of parallel SU8 walls, the upper portion of the structures shrinks considerably more than the lower portion, which remains firmly attached to the substrate [8].

5.3 ELECTROSPINNING

Electrospinning is a straightforward and cost-effective method to produce CNWs with diameters ranging from less than 3 nm to more than 1 mm [8], and the electrospinning experiments can be performed by using simple experimental setups that do not require a vacuum. The first U.S. patent on electrospinning was issued to Formhals in 1934 [9]. This technique is actually only complicated in terms of a detailed theoretical understanding of the physics of the phenomenon and in adapting the technique to the types of NWs that are required for a given application. Electrospinning can be applied to the fabrication of NWs made from materials as diverse as synthetic and natural polymers, polymer alloys, and polymer composites, as well as metals and ceramics [10]. Some of the current electrospinning applications include filtrations [11], advanced fabrics (e.g., for wound dressing [12]), scaffolds [13, 14], medical implants [15], fabrication of micro- or nanodevices such as field effect transistors [16, 17], and gas sensors [2, 18].

5.3.1 ELECTROSPINNING SETUP DESCRIPTION

A conventional electrospinning setup with vertical feeding direction is shown in Figure 5.3. It consists of four key components: a high-voltage power supply (working range between 10 and 30 kV), a polymer precursor reservoir, a conductive dispensing needle, and a conductive substrate. The polymer precursor reservoir maintains a constant polymer solution flow rate through a syringe or dispensing needle, which may be connected to either

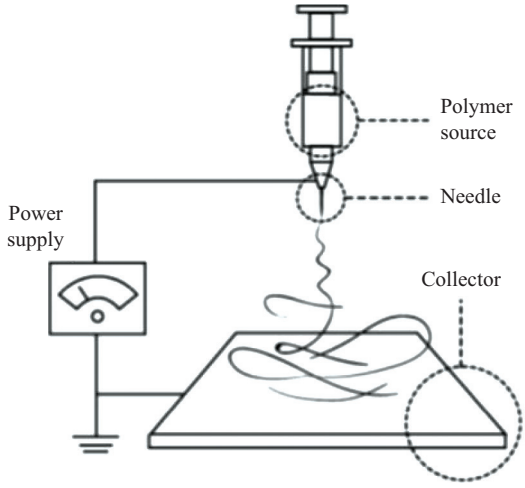

Figure 5.3. Schematic of traditional electrospinning setup [8].

a mechanical or a pneumatic syringe pump. The conductive dispensing needle is the polymer source, which is connected to a high-voltage power supply. The needle is also sometimes called tip, nozzle, or spinneret, and its internal diameter is often in the range of hundreds of micrometers. The conductive substrate is normally grounded and serves as a collector for the electrospun NWs.

When a high voltage (higher than 10 kV) is applied to the needle, the polymer solution at the needle tip becomes unstable and a jet is formed. Initially, the jet flows away from the needle following a nearly straight line and then it bends into a complex path during which electrical forces stretch and thin it to the nanometer scale. The initial straight section of the jet is known as *near-field* regime. The area where the electrical instabilities dominate creating a whipping motion of the jet is called the *far-field* regime. In Figure 5.4, we show the schematic of the path of the fiber (NW) jet.

The key stages of the polymer jet formation in the electrospinning process are (1) droplet formation, (2) Taylor cone formation, (3) launching of the jet, (4) elongation of straight segment, (5) whipping instability, and (6) solidification into NW [19]. These stages are described in detail next.

5.3.1.1 Droplet Formation

Droplet formation is the first step toward nanofiber formation in the electrospinning process. When the SU8 solution is pumped into the

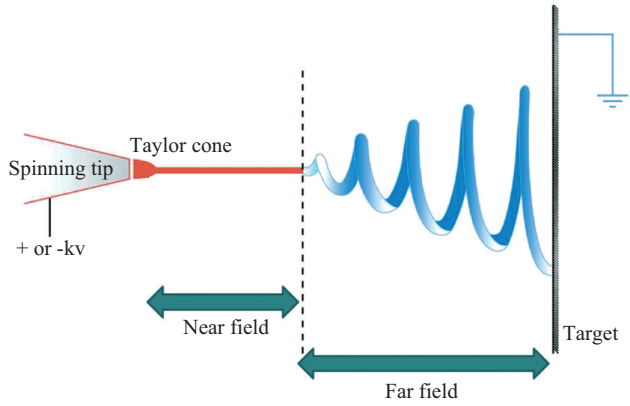

Figure 5.4. Schematic of the path of the fiber jet.

Courtesy: Wikipedia.

needle at a low flowrate, a droplet is formed at the tip of the needle. In the absence of an electric field, only two forces are acting on the droplet: the gravitational force (F_G) upon the polymer and the surface tension of the droplet (γ). For a solution with low viscosity, the surface tension is not high enough to hold the droplet and it drops off under the influence of gravity. Also, at a higher flowrate, droplets merge resulting in a continuous polymer flow through the needle. However, at a very low flowrate and at equilibrium of gravitational and surface tension forces, the droplet formed at the needle tip is assumed to be spherical with radius r_0 given as [19]

$$r_0 = \left(3R\gamma/2\rho g\right)^{1/3} \tag{5.1}$$

where R is the inner radius of the needle tip, ρ is the density of the solution, and g is the gravitational constant.

When a voltage is applied to the needle, an electric field develops between the needle and the collector. The electric force (F_E) and F_G now act together against the droplet surface tension. The electric field polarizes the ionic polymer solution, causing the positive and negative ions to move in opposite directions. For a positively charged needle, positive electric charges move to the droplet surface and negative charges move toward its bulk so that the presence of those opposite electric charges in the droplet act against the surface tension. For the droplet to remain in a stable state, the inward surface tension must exceed the outward electrostatic repulsion

forces between the charges [19]. This force balance equation is expressed as

$$F_E \leq g\rho\left[\left(\frac{r^2}{\beta}\right)-V\right] \tag{5.2}$$

where β is a shape factor of the droplet and V is its volume. The electric force, F_E, in the system is expressed as [19–21]

$$F_E = \left(4\pi\varepsilon V^2\right)\Big/\left[\ln\left(\frac{4L}{R}\right)^2\right] \tag{5.3}$$

where ε is the permittivity of the medium, which in most cases is air, and L is the needle to collector distance.

As the applied voltage increases, the magnitude of the electric force acting on the droplet starts to deform it. For a polymer solution with low molecular weight, this causes electrospraying in which the droplet degenerates into smaller droplets. However, for a polymer solution with sufficient molecular weight and viscosity, polymer chain entanglement prevents breaking up of the droplet and instead the droplet stretches into a polymer jet.

5.3.1.2 Taylor Cone Formation

Electrostatic repulsion between surface charges causes the polymer droplet to deform and elongate in order to increase its surface area. This results in a characteristic conical shape called the Taylor cone, and the steps of polymer jet formation are illustrated in Figure 5.5. At a critical voltage, V_C, a polymer jet is generated from the Taylor cone as electric forces overcome the droplet surface tension [22, 23]. The expression for V_C is given by

$$V_c^2 = \left(\frac{2L}{h}\right)^2 \left(\ln\left(\frac{2h}{R}\right)-1.5\right)(0.117\pi RT) \tag{5.4}$$

where h is the length of the needle.

5.3.1.3 Launching of the Jet

As the electric field, generated between the needle and the collector, and the electrostatic interaction between surface charges stretch the droplet,

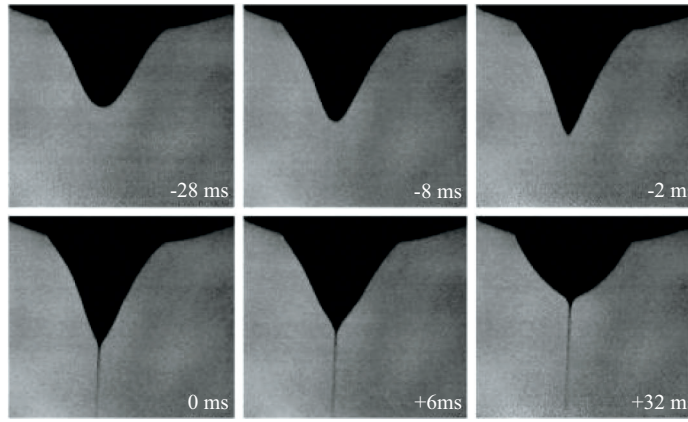

Figure 5.5. Taylor cone formation and polymer jet discharge during electrospinning process [24].

the polymer chain entanglement in a concentrated polymer solution prevents the droplet from breaking up and an NWs results. The mass and charge in the system is conserved as the polymer jet leaves the droplet [19, 25]. As we saw earlier and will detail later, the jet can be launched toward a substrate that is as far as 10 to 15 cm (far field) or as close as 100 μm to 2 mm (near field). The launching of a jet in near field is considerably different from that in far field and is not really well understood yet.

5.3.1.4 Elongation of the Straight Wire Segment

As the jet leaves the droplet, the external electric field and the electrostatic repulsion of the charges within the droplet make the jet at first to elongate in a straight line toward the collector [24]. The electrical forces are counteracted by the viscoelastic forces within the polymer solution, and the diameter of the jet decreases owing to its elongation as well as through the evaporation of the polymer solvent. Several groups have performed analytical and computational studies of the polymer jet elongation during electrospinning [26–28]. In the model developed by Reneker, and Yarin, a polymer jet emerging from the needle is divided into segments, and for computational reasons, each segment is considered as a charged bead [24]. Beads are connected to each like the viscoelastic dumbbell shown in Figure 5.6 [8, 24].

With Equation 5.5, one describes the momentum balance of the bead B (Figure 5.6) stretched by the external electric field and

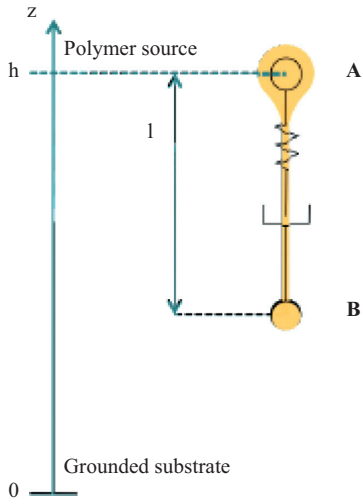

Figure 5.6. Model of a rectilinear segment of the electrospinning jet represented as a viscoelastic dumbbell [8].

the coulombic force of repulsion and with the viscoelastic forces counteracting them:

$$m\frac{dv}{dt} = \frac{e}{l^2} - \frac{eV_0}{h} + \pi a^2 \sigma \tag{5.5}$$

where m is the mass of the bead, e is the electrical charge, V_0 is the applied voltage, l is distance between beads, h is the distance between bead A to ground (Figure 5.6), and a is the bead radius.

5.3.1.5 Whipping Instability

Initially, the polymer jet moves toward the grounded collector following a straight trajectory. Then, after traversing a certain distance, electrostatic instabilities produce a whipping motion in the polymer jet. Several studies have attempted modeling of the polymer jet whipping motion in the electrospinning processes [25, 26, 28, 29]. The forces involved in the whipping motion of the jet and their effects are summarized as follows [19, 30]: (a) F_G, which is dependent on the density of the solution, acts vertically downwards toward the collector; (b) F_E, which is produced by

the applied electric field, stretches the polymer jet toward the collector; (c) columbic force of repulsion F_C on the surface of the jet, which introduces bending instability and whipping motion and depends on the electrical characteristics of the polymer and its solvents; (d) viscoelastic force F_{ve}, which acts against the stretching of the jet and is dependent on the polymer molecular weight, the solvent, and the type of polymer; (e) surface tension forces, which also act against the stretching of the jet and depend on the composition of the polymer solution, solvent type, and any additives such as surfactants; and (f) frictional forces between the surface of the jet and the surrounding medium.

The whipping motion in electrospinning is the interplay between all these forces and, hence, consideration of these parameters is important. Although the existing models only consider some of the parameters affecting the process, their predictions have been found to be in close agreement with experimental observations [19].

5.3.1.6 Solidification into Nanowires

During the polymer jet flight and while undergoing whipping, evaporation of solvent leads to the solidification into nanofibers. The volatile solvents may evaporate before thinning (during whipping motion) and evaporation rate is an important parameter in this process [19]. The solidified nanofibers are deposited randomly on the collector electrode, and under optimized conditions, these fibers are circular, continuous, and bead free.

5.3.2 DIMENSIONS OF THE NANOWIRES

The dimensions of the polymer fibers depends on the following parameters: (a) polymer precursor material, (b) polymer solution concentration, (c) needle-to-collector distance, (d) flow rate of the precursor, (e) applied voltage (f), and mechanical stretching (see more details on this parameter further ahead).

The morphology and dimensions of the fabricated polymer fibers depend on the composition of the electrospun polymer and the solution concentration. The latter parameter has the dominant influence on the thickness of NW with the more diluted solutions generating the thinner fibers and the concentrated solutions producing the thicker fibers. There is an important caveat here: When the polymer concentration is too low, beads are formed instead of fibers, and with the very high concentrations, electrospinning might not be possible. Needle-to-collector distance

and the polymer flow rate influence the distribution, density, thickness, and homogeneity of the fibers. A typical electrode-to-collector distance varies from 8 to 30 cm. The applied voltage mainly influences the thickness of the fibers: thinner fibers are produced at higher applied voltages. In Figure 5.7, we show a photograph of the UCI BioMEMS lab far-field electrospinning setup.

5.3.3 CHALLENGES: ALIGNMENT IN FAR-FIELD ELECTROSPINNING

NWs are randomly deposited on the collector electrode during an electrospinning experiment using a conventional far-field setup. However, for many applications (e.g., electronic devices, photonic devices, and structures for cell cultures, among others), highly aligned nanofibers are required. Hence, the alignment of electrospun nanofibers is one of the most important challenges encountered in the electrospinning field.

In [31], Kim and Reneker used a rotating drum as collector electrode, aligning the collected fibers in the direction of the drum rotation and producing relatively uniform mats of oriented fibers. The use of a rotating drum electrode is the most used commercial technique for collecting aligned polymer nanofibers. In Figure 5.8, we show a schematic drawing of an electrospinning setup with a rotating drum collector and a picture of a commercially available electrospinning system.

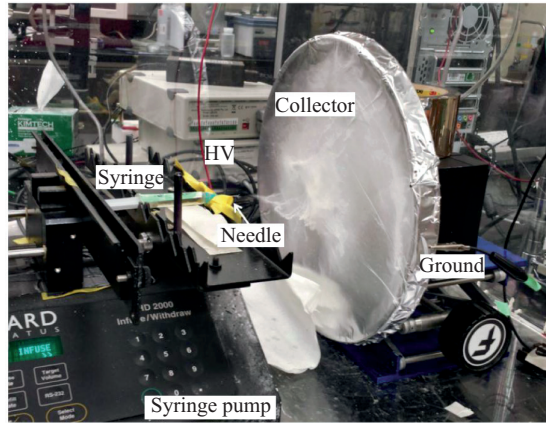

Figure 5.7. Photographs of UCI BioMEMS lab electrospinning setup [8].

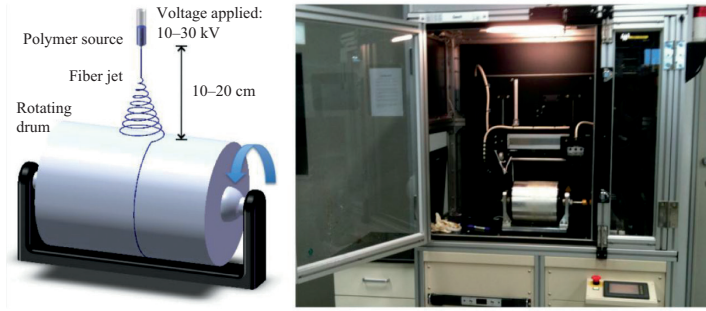

Figure 5.8. Schematic of an FFES system with rotating drum and commercially available electrospinning setup [8].

5.4 ELECTRO-MECHANICAL SPINNING

Electrospinning has emerged as a successful method for the fabrication of various types of long and continuous nanofiber mats, not only in research and niche market environments but also for industrial mass production markets [32–34]. The nanofiber mats can be produced by a standard far-field electrospinning (FFES) method. However, electric instabilities inherent in FFES make this process inappropriate for a wide range of applications that require isolated NWs to be deposited in a controlled pattern or to be deposited only in predetermined locations. Near-field electrospinning (NFES) technology was developed to fill the demand for production of micro- and nanofibers with increased positioning precision [35–37]. The main difference between FFES and NFES is the distance between the fiber source and the collector, which is significantly reduced for NFES. This reduction in distance between the needle and substrate allow for depositing the fibers on the substrate before the onset of the whipping motion because of electrical instabilities. But the application of an electric field alone does not provide a force strong enough to stretch out the fiber jet diameter to the nanometer scale. Using the NFES process, only micrometer-sized fibers can be reproduced. Electromechanical spinning (EMS) developed by Madou et al. [38] improves upon NFES by offering thinner fibers with an exceptional nanofiber deposition control. The fundamental principle behind EMS is the use of viscoelastic polymer inks in conjunction with a low deposition voltage and a mechanical pull on the polymer fibers.

5.4.1 SETUP DESCRIPTION

The distance between the needle and the collector electrode in EMS is smaller than that required for FFES. In EMS, this distance is in the range of 500 μm to 1.5 mm, and thus EMS operates in the stable liquid jet region. The polymer solution is contained, for example, in a 3-ml syringe bore fitted with a 25 to 33 stainless steel needle gauge (ID from 250 to 100 μm). The syringe is mounted on a syringe pump (either mechanical or pneumatic) to dispense the polymer solution at a controlled flow rate.

Generally, the syringe in the EMS setup is mounted using a syringe holder. This holder can be manually or automatically positioned in the *x*–*y*–*z* directions and is connected to a pneumatic syringe pump. The target substrate is mounted on an automated X-Y microstage that can be programmed to move in any desired pattern at different speeds and accelerations. In Figure 5.9, we show a schematic of the electrode configuration in an EMS setup.

A power supply, shown in Figure 5.10, is connected to the needle to provide the high-voltage signal and the substrate is grounded. The polymer solution flows through the needle to form a full-sized droplet at the needle tip. The voltage is then turned on to initiate the polymer jet. Importantly, the jet does not self-initiate in a near-field setup, because the electrostatic force is not strong enough to overcome the surface tension at the droplet–air interface. This can be observed from a video of the EMS process in

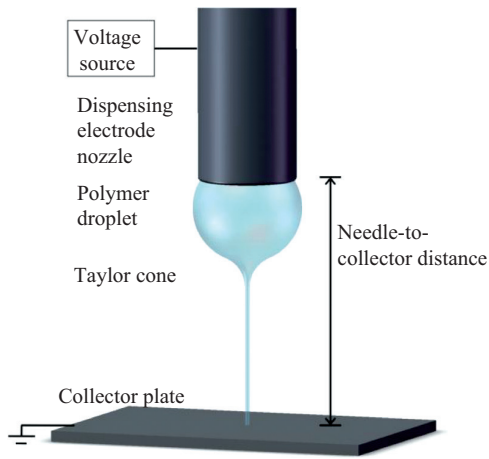

Figure 5.9. Schematic of EMS setup [8].

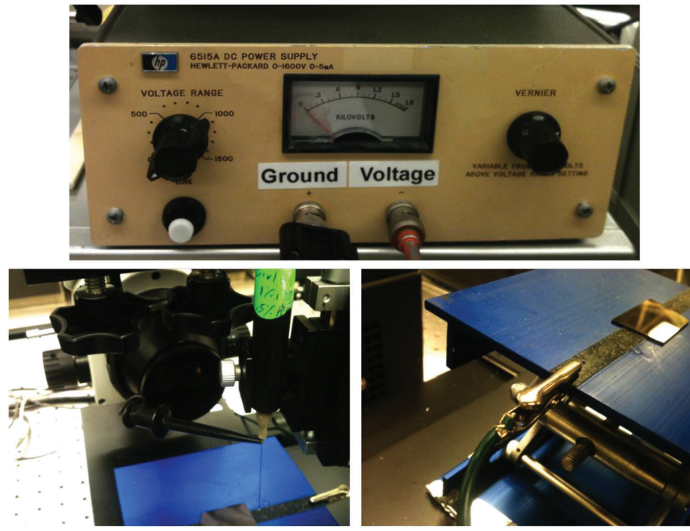

Figure 5.10. Photographs of voltage supply, syringe, and grounded substrate of EMS setup [8].

which the droplet shape is seen to only slightly be deformed by the electric field and still be approximated as having a spherical geometry. To initiate the jet in EMS, it is necessary to introduce an artificial instability at the droplet–air interface that results in a very high local electric field. If this local electrical field is sufficient to overcome the interfacial surface tension, then a jet initiates. This artificial instability can be induced, for example, by poking the droplet with a glass microprobe tip (1 to 3 μm tip diameter). Once the jet is initiated, the system reaches a new equilibrium with a jet that continues to flow as long as the electric field is applied and new polymer solution is available.

5.4.2 MATERIALS AND METHODS

A special EMS polymer formulation is required to be able to produce stretched fibers without breaking. Highly viscoelastic polymer solutions contain long entangled polymer chains that promotes stretchability and defines the continuity of the electrospun jets and the thinning to the nanometer scale of the fiber. Also, the continuous electrospinning of the polymer jet into patterned nanofibers is ensured this way. In an experiment, different concentrations of high-molecular-weight poly

(ethylene oxide) (PEO; MW = 4,000,000) from Dow Inc. (WSR-301) were used, giving rise to the first successfully tested EMS polymer solutions [8].

5.4.3 VOLTAGE EFFECTS

In far-field electrospinning, the fiber diameter decreases with higher applied voltages because of an increase in bending instabilities that stretches the nanofibers further. However, an opposite trend is observed in EMS. In EMS, the voltage can be manipulated to directly control the thickness of the nanofibers. Low-voltage operation results in the reduction of the jet diameter, leading to thinner nanofibers. This is because of the lower electrostatic forces, which reduce the feed rate of the polymer, reducing jet thickness. Another advantage of using lower operation voltage is that it increases the deposition control of the fibers, avoiding NW jittering.

5.4.4 CONTROL OF MECHANICAL STRETCHING

A low average velocity of the stage leads to fiber thickening and thinner fibers are obtained with higher average stage velocities. This is a result of the mechanical stretching of the nanofibers between the point of contact with the substrate and the droplet. To obtain wires of uniform thickness, EMS must only be run in the constant velocity regime. It is also feasible to use the stage motion to create a smooth continuous transition between nanofibers of different thickness.

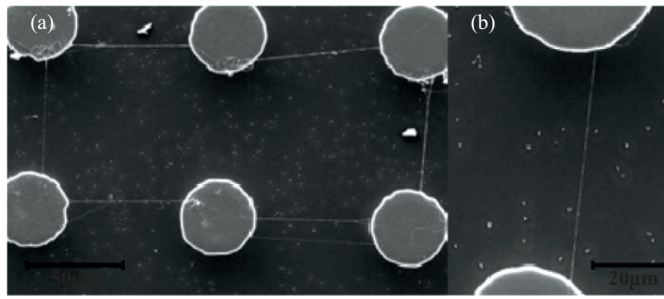

Figure 5.11. SEM images of suspended nanowires on carbon posts (a) six carbon post connected to each other by nanowires, (b) and individual nanowire [8].

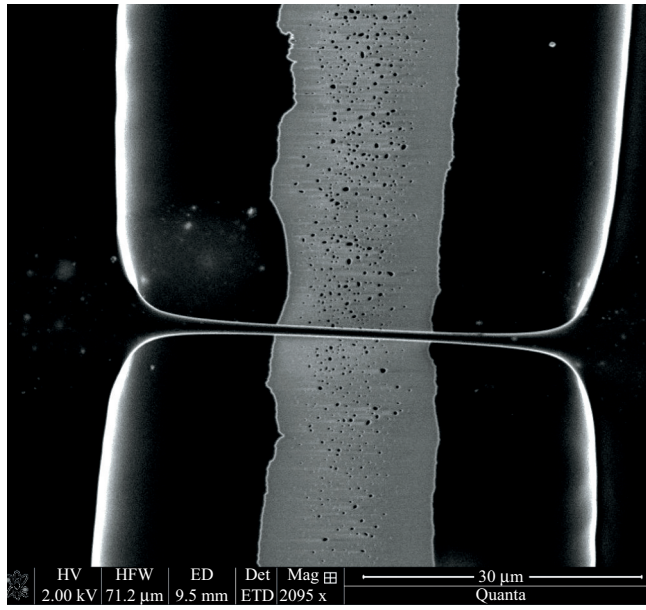

Figure 5.12. SEM image of a single suspended CNW between two carbon electrodes.

In Figure 5.11, we show a scanning electron microscope (SEM) image of suspended NWs on carbon posts. An SEM image of a single suspended CNW between two carbon electrodes is shown in Figure 5.12.

5.5 CONCLUSIONS

The main focus of this chapter was to discuss the process details used to fabricate suspended CNWs that are precisely aligned on supporting structures, establish a good ohmic contact with those supporting structures, and can be produced in a batch mode. C-MEMS has started to provide solutions for the aforementioned requirements. The biggest advantage of the C-MEMS process is that it starts with a polymer carbon precursor that is the same for NW and supporting electrodes and that the conversion of both into carbon during the pyrolysis step automatically results in a good ohmic contact. No extra, high temperature, postprocessing are necessary. Details of electrospinning for NW deposition have also been discussed in this chapter. Research on C-MEMS is still in its infancy and many discoveries are to be expected.

REFERENCES

[1] Wang, C., L. Taherabadi, G. Jia, M. Madou, T. Yeh, and B. Dunn. 2004. "C-MEMS for the Manufacture of 3D Microbatteries." *Electrochemical and Solid-State Letters* 7, no. 11, pp. A435–38. doi: http://dx.doi.org/10.1149/1.1798151

[2] Sharma, S., and M. Madou. 2012. "A New Approach to Gas Sensing with Nanotechnology." *Philosophical Transactions of the Royal Society A: Mathematical, Physical and Engineering Sciences* 370, no. 1967, pp. 2448–73. doi: http://dx.doi.org/10.1098/rsta.2011.0506

[3] Schueller, O.J., S.T. Brittain, and G.M. Whitesides. 1997. "Fabrication of Glassy Carbon Microstructures by Pyrolysis of Microfabricated Polymeric Precursors." *Advanced Materials* 9, no. 6, pp. 477–80. doi: http://dx.doi.org/10.1002/adma.19970090604

[4] Singh, A., J. Jayaram, M. Madou, and S. Akbar. 2002. "Pyrolysis of Negative Photoresists to Fabricate Carbon Structures for Microelectromechanical Systems and Electrochemical Applications." *Journal of the Electrochemical Society* 149, no. 3, pp. E78–83. doi: http://dx.doi.org/10.1149/1.1436085

[5] Wang, C., and M. Madou. 2005. "From MEMS to NEMS with Carbon." *Biosensors and Bioelectronics* 20, no. 10, pp. 2181–87. doi: http://dx.doi.org/10.1016/j.bios.2004.09.034

[6] Park, B.Y., R. Zaouk, C. Wang, and M.J. Madou. 2007. "A Case for Fractal Electrodes in Electrochemical Applications." *Journal of the Electrochemical Society* 154, no. 2, pp. 1–5. doi: http://dx.doi.org/10.1149/1.2400607

[7] Heo, J.-I., Y. Lim, M. Madou, and H. Shin. 2012. "Scalable Suspended Carbon Nanowire Meshes as Ultrasensitive Electrochemical Sensing Platforms." *IEEE 25th International Conference on Micro Electro Mechanical Systems (MEMS)*, pp. 878–81. doi: http://dx.doi.org/10.1109/memsys.2012.6170326

[8] Canton, G. 2014. *Development of Electro-Mechanical Spinning for Controlled Deposition of Carbon Nanofibers* [PhD Thesis]. UCI.

[9] Formhals, A. 1934. Process and Apparatus for Preparing Artificial Threads. US Patent 1975504, filed December 5, 1930, and issued October 2, 1934.

[10] Greiner, A., and J.H. Wendor. 2007. "Electrospinning: A Fascinating Method for the Preparation of Ultrathin Fibers." *Angewandte Chemie International Edition* 46, no. 30, pp. 5670–03. doi: http://dx.doi.org/10.1002/anie.200604646

[11] Gibson, P., H. Schreuder-Gibson, and D. Rivin. 1999. "Electrospun Fiber Mats: Transport Properties." *AIChE Journal* 45, no. 1, pp. 190–95. doi: http://dx.doi.org/10.1002/aic.690450116

[12] Jin, H.-J., S.V. Fridrikh, G.C. Rutledge, and D.L. Kaplan. 2002. "Electrospinning Bombyx Mori Silk with Poly(ethylene oxide)." *Biomacromolecules* 3, no. 6, pp. 1233–39. doi: http://dx.doi.org/10.1021/bm025581u

[13] Pham, Q.P., U. Sharma, and A.G. Mikos. 2006. "Electrospinning of Polymeric Nanofibers for Tissue Engineering Applications: A Review." *Tissue Engineering* 12, no. 5, pp. 1197–11. doi: http://dx.doi.org/10.1089/ten.2006.12.1197

[14] Murugan, R., and S. Ramakrishna. 2006. "Nano-Featured Scaffolds for Tissue Engineering: A Review of Spinning Methodologies." *Tissue Engineering* 12, no. 3, pp. 435–47. doi: http://dx.doi.org/10.1089/ten.2006.12.435

[15] Agarwal, S., J.H. Wendor, and A. Greiner. 2008. "Use of Electrospinning Technique for Biomedical Applications." *Polymer* 49, no. 26, pp. 5603–21. doi: http://dx.doi.org/10.1016/j.polymer.2008.09.014

[16] Babel, A., D. Li, Y. Xia, and S.A. Jenekhe. 2005. "Electrospun Nanofibers of Blends of Conjugated Polymers: Morphology, Optical Properties, and Field-Effect Transistors." *Macromolecules* 38, no. 11, pp. 4705–11. doi: http://dx.doi.org/10.1021/ma047529r

[17] Pinto, N., A. Johnson, A. MacDiarmid, C. Mueller, N. Theofylaktos, D. Robinson, and F. Miranda. 2003. "Electrospun Polyaniline/Polyethylene Oxide Nanofiber Field-Effect Transistor." *Applied Physics Letters* 83, no. 20, pp. 4244–46. doi: http://dx.doi.org/10.1063/1.1627484

[18] Liu, H., J. Kameoka, D.A. Czaplewski, and H. Craighead. 2004. "Polymeric Nanowire Chemical Sensor." *Nano Letters* 4, no. 4, pp. 671–75. doi: http://dx.doi.org/10.1021/nl049826f

[19] Andrady, A.L. 2008. *Science and Technology of Polymer Nanofibers*. New York, NY: John Wiley & Sons.

[20] Bugarski, B., B. Amsden, M. Goosen, R. Neufeld, and D. Poncelet. 1994. "Effect of Electrode Geometry and Charge on the Production of Polymer Microbeads by Electrostatics." *The Canadian Journal of Chemical Engineering* 72, no. 3, pp. 517–21. doi: http://dx.doi.org/10.1002/cjce.5450720318

[21] DeShon, W.E., and R.S. Carson. 1968. "Electric Field Investigations and a Model for Electrical Liquid Spraying." *Journal of Colloid and Interface Science* 28, no. 1, pp. 161–66. doi: http://dx.doi.org/10.1016/0021-9797(68)90218-x

[22] Taylor, G. 1969. "Electrically Driven Jets." In *Proceedings of the Royal Society of London. A. Mathematical and Physical Sciences* 313, no. 1515, pp. 453–75. doi: http://dx.doi.org/10.1098/rspa.1969.0205

[23] Taylor, G. 1964. *Proceedings of the Royal Society of London A: Mathematical, Physical and Engineering Sciences,* pp. 383–97. The Royal Society.

[24] Reneker, D.H., and A.L. Yarin. 2008. "Electrospinning Jets and Polymer Nanofibers." *Polymer* 49, no. 10, pp. 2387–25. doi: http://dx.doi.org/10.1016/j.polymer.2008.02.002

[25] Hohman, M.M., M. Shin, G. Rutledge, and M.P. Brenner. 2001. "Electrospinning and Electrically Forced Jets. I. Stability Theory." *Physics of Fluids (1994-present)* 13, no. 8, pp. 2201–20. doi: http://dx.doi.org/10.1063/1.1383791

[26] Feng, J. 2002. "The Stretching of an Electrified non-Newtonian Jet: A Model for Electrospinning." *Physics of Fluids (1994-present)* 14, no. 11, pp. 3912–26. doi: http://dx.doi.org/10.1063/1.1510664

[27] Feng, J. 2003. "Stretching of a Straight Electrically Charged Viscoelastic Jet." *Journal of Non-Newtonian Fluid Mechanics* 116, no. 1, pp. 55–70. doi: http://dx.doi.org/10.1016/s0377-0257(03)00173-3

[28] Reneker, D.H., A.L. Yarin, H. Fong, and S. Koombhongse. 2000. "Bending Instability of Electrically Charged Liquid Jets of Polymer Solutions in Electrospinning." *Journal of Applied Physics* 87, no. 9, pp. 4531–47. doi: http://dx.doi.org/10.1063/1.373532

[29] Ramakrishna, S., K. Fujihara, W.-E. Teo, T.-C. Lim, and Z. Ma. 2005. *An Introduction to Electrospinning and Nanofibers*. Singapore, Singapore: World Scientific.

[30] Wannatong, L., A. Sirivat, and P. Supaphol. 2004. "Effects of Solvents on Electrospun Polymeric Fibers: Preliminary Study on Polystyrene." *Polymer International* 53, no. 11, pp. 1851–59. doi: http://dx.doi.org/10.1002/pi.1599

[31] Kim, J.-S., and D.H. Reneker. 1999. "Polybenzimidazole Nanofiber Produced by Electrospinning." *Polymer Engineering & Science* 39, no. 5, pp. 849–54. doi: http://dx.doi.org/10.1002/pen.11473

[32] Persano, L., A. Camposeo, C. Tekmen, and D. Pisignano. 2013. *Macromolecular Materials and Engineering*.

[33] Mitchell, G.R., K.-H. Ahn, and F.J. Davis. 2011. "The Potential of Electrospinning in Rapid Manufacturing Processes." *Virtual and Physical Prototyping* 6, no. 2, pp. 63–77. doi: http://dx.doi.org/10.1080/17452759.2011.590387

[34] Reneker, D., A. Yarin, V. Zussman, and H. Xu. 2007. "Electrospinning of Nanofibers from Polymer Solutions and Melts." *Advances in Applied Mechanics* 41, pp. 43–346. doi: http://dx.doi.org/10.1016/s0065-2156(07)41002-x

[35] Sun, D., C. Chang, S. Li, and L. Lin. 2006. "Near-Field Electrospinning." *Nano Letters* 6, no. 4, pp. 839–42. doi: http://dx.doi.org/10.1021/nl0602701

[36] Zheng, G., W. Li, X. Wang, D. Wu, D. Sun, and L. Lin. 2010. "Precision Deposition of a Nanofibre by Near-Field Electrospinning." *Journal of Physics D: Applied Physics* 43, no. 41, p.415501. doi: http://dx.doi.org/10.1088/0022-3727/43/41/415501

[37] Chang, C., K. Limkrailassiri, and L. Lin. 2008. "Continuous Near-Field Electrospinning for Large Area Deposition of Orderly Nanofiber Patterns." *Applied Physics Letters* 93, no. 12, pp. 123111–11. doi: http://dx.doi.org/10.1063/1.2975834

[38] Sharma, C.S., H. Katepalli, A. Sharma, and M. Madou. 2011. "Fabrication and Electrical Conductivity of Suspended Carbon Nanofiber Arrays." *Carbon* 49, no. 5, pp. 1727–32. doi: http://dx.doi.org/10.1016/j.carbon.2010.12.058

CHAPTER 6

ORGANIC XEROGEL-BASED C-MEMS

Chandra S. Sharma and Manohar Kakunuri

Indian Institute of Technology, Hyderabad

6.1 INTRODUCTION TO ORGANIC AND CARBON XEROGEL

The sol–gel process is a chemical route to the synthesis of an interconnected network of solid particles (gel) from a starting colloidal solution (sol) of monomers. Silica gel was the first inorganic gel synthesized by Ebelmen in 1846 [1]. A number of inorganic precursors such as metallic salts and alkoxides were used for the synthesis of those silica gels [1]. However, the synthesis of organic gels using organic precursors was only reported first as recently as 1989 by Pekala [2]. He introduced the fabrication of resorcinol–formaldehyde (RF)-based organic aerogels through the polycondensation of resorcinol with formaldehyde in alkaline conditions. Although a number of other organic gels such as phenol–formaldehyde, phenolic–furfural, melamine–formaldehyde, and resorcinol–furfural were prepared using the sol–gel method after these, RF-based, organic gels have been studied and used most extensively [3–8].

For the preparation of an RF organic gel, resorcinol is first added to formaldehyde in a given molar ratio followed by stirring to obtain a homogeneous solution. In another beaker, an aqueous alkaline solution of the catalyst (e.g., sodium carbonate or potassium carbonate) is separately prepared and then added to the RF homogeneous solution [4, 9]. After continuous stirring for 15 to 30 minutes, a brown color homogenous solution (RF sol) is obtained. The alkaline catalyst initiates the resorcinol anion

formation and these anions react with formaldehyde to form hydroxymethyl derivatives. These hydroxymethyl derivatives then participate in condensation polymerization reactions to form cross-linked clusters of size 7 to 10 nm. These clusters (colloid particles) start forming a stiff and interconnected network in the aqueous solution to ultimately yield an RF organic gel [10]. A schematic explaining the mechanism of formation of RF organic gel is shown in Figure 6.1 [10]. There are also a few reports on using acidic catalysts in organic solvents for the preparation of RF organic gels [10–12].

The physicochemical properties of RF organic gels largely depend on the method used for drying them among several other parameters including initial molar ratios of resorcinol to formaldehyde, amount of catalyst, and diluent (generally water) [10]. Depending on the nature of the drying process, the final dry RF organic gel is classified as follows:

a. Aerogel (supercritical drying)
b. Cryogel (freeze drying)
c. Xerogel (subcritical drying)

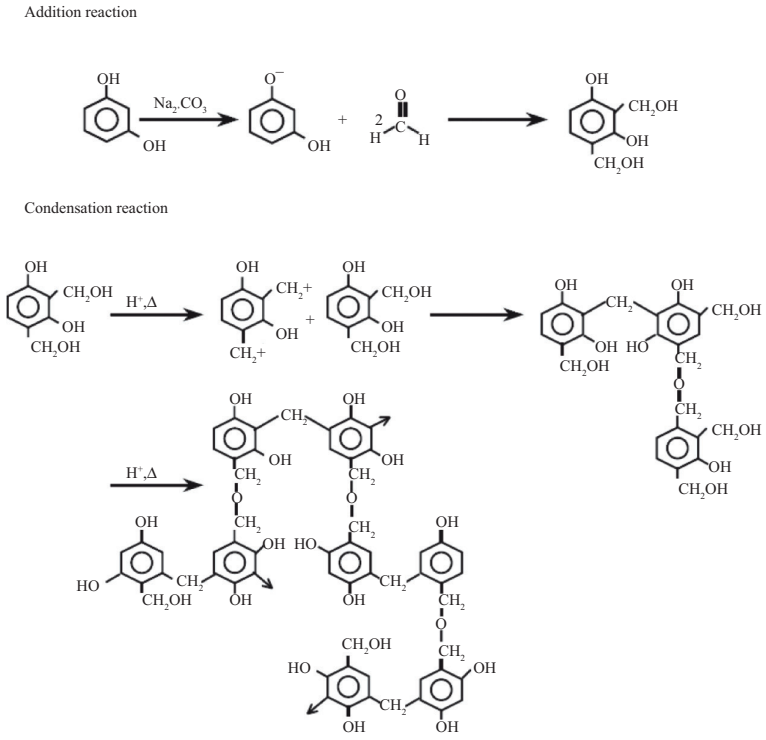

Figure 6.1. Schematic illustrating the mechanism of polymerization of resorcinol and formaldehyde [10].

Supercritical drying: In this method, water is evaporated from the pores inside the wet gel using CO_2 in supercritical conditions, so as to retain the skeleton structure formed during the gelation process. Before supercritical drying, the removal of aqueous solvent that is used as reaction medium through repetitive washing with organic solvent is important because of the insolubility of CO_2 in water. Supercritical drying takes place inside an autoclave, where the aqueous solvent that is present inside the pores of the gel is interchanged with the supercritical state liquid CO_2 with its much lower surface tension. This supercritical drying generally takes place for more than four hours, and gels dried by this method are called aerogels. Aerogels possess large surface area and pore volume and are very lightweighted [6, 10, 13].

Freeze drying: Freeze drying is another method to prepare porous gels with large surface area and is less expensive compared to supercritical drying. In this method, the frozen solvent is removed by sublimation to avoid formation of a vapor–liquid interface. Similar to aerogels, before freeze drying, these gels must have the solvent exchanged with an alternative liquid. The liquid is selected in such a way that it does not considerably change in density on freezing (e.g., tert-butanol). The advantage is that this prevents the destruction of the inner gel structure because of the expansion of the solution. After solvent exchange, the organic gels are frozen for 1 h at 243 K followed by drying for 1 day at 263 and 273 K to obtain an RF cryogel [14].

Subcritical drying: This method of drying is quite inexpensive, and it does not involve any solvent exchange as in the case of supercritical drying or freeze drying. Evaporation of solvent at atmospheric pressure by simple oven drying may cause drastic changes in surface tension of the solvent, thus inducing large capillary forces at the liquid–vapor interfaces. This effect subsequently causes pores to shrink and collapse, thus resulting in more dense polymeric structures known as xerogels [15]. Although there are few recent reports on porous RF xerogels (RFX) formation, RFX remain quite dense and almost nonporous when compared to aerogels and cryogels.

RF organic gels when heated at elevated temperature in inert atmosphere (pyrolysis) yield carbon gels. RF-derived carbon aerogels were the first conductive gels synthesized [13]. RF-derived carbon aerogels and cryogels because of their unique physical and chemical properties such as large surface area, chemical stability, low density, homogeneity, and conductivity received wide attention in the literature and have been studied for various applications such as electrodes for energy storage devices, adsorbents, and catalyst support materials [16–23].

6.2 IMPORTANCE OF CARBON XEROGELS

As discussed earlier, carbon xerogels can be synthesized through the pyrolysis of organic RFX via simple oven drying at atmospheric pressure. However, until recently, carbon xerogels did not get much attention largely because of their relatively nonporous nature. However, there has been a tremendous effort in the literature over the past decade to modify the properties of RF-derived carbon xerogels in terms of their porosity, surface area, and conductivity by simply tuning the synthesis conditions. Nonporous dense carbon xerogels of low surface area are transformed to high-surface-area porous carbon xerogels by changing the pH of the RF aqueous solution or by physical and chemical activation after carbonization or by addition of metal salts in the precursor solution [17, 24–26]. Job observed an increase in surface area from less than 40 to 635 m^2/g simply by changing the pH from 7.35 to 5.45 [25]. These high-surface-area porous carbon xerogels were then suggested for potential applications in catalysis and as adsorbents [18, 19].

However, for electrochemical applications, where large surface area and low density may not be that important a benchmark because of the high irreversible capacity losses associated with solid electrolyte interface (SEI) formation in lithium-ion batteries (e.g., irreversible capacity losses as high as 83 percent were reported for activated carbon aerogels when tested for lithium-ion insertion performance [27]), carbon xerogels are rather better contenders for those battery electrodes. This led to a major focus in recent times on the tailoring of the surface morphology of RF-derived carbon xerogels with tunable porosity. A wide variety of morphologies including microspheres, microspheres with nanofeatures, hollow particles, and fractal-like have been synthesized in aerogels, cryogels, and xerogels using inverse emulsification in which the RF gel is mixed with some organic solvent in the presence of surfactants and is continuously stirred [10, 28–37]. By varying the various process conditions such as stirring time and the amount of surfactant, RF-derived carbon xerogels have been synthesized with moderate surface area and porosity [30, 36]. Further activation in an oxygen or a carbon dioxide environment and addition of melamine for nitrogen doping provide the required characteristics for a carbon xerogel with much more active sites and more surface defects for potential application as high-capacity anode materials in lithium-ion batteries [24, 27, 38].

In this chapter, we present an overview of some of the methods to synthesize a wide variety of exotic morphologies in RF-derived carbon xerogels. These RF-derived carbon xerogel structures range in size from

a few micrometers to tens of nanometers with spherical to multiscale three-dimensional fractal-like hybrid architectures. To enable their use as potential electrodes in microelectromechanical systems, we then demonstrate the possibility of reversible lithium-ion intercalation in these RF-derived carbon xerogels.

6.3 SYNTHESIS OF VARIOUS MORPHOLOGIES IN CARBON XEROGELS

6.3.1 INVERSE EMULSIFICATION METHOD

As mentioned earlier, carbon xerogels today are candidates for a number of applications including adsorbents, catalysts, and electrodes for energy storage devices. With such very diverse applications in mind, the surface morphology of these carbon xerogels plays an important role for exploiting their full potential in each of those applications. Inverse emulsification has been considered as one of the most viable techniques to produce a variety of morphologies in RF-based xerogels. As shown in the schematic in Figure 6.2, during inverse emulsification, a hydrophilic monomer in aqueous solution (RF sol) is emulsified in a continuous oil phase (e.g., cyclohexane) containing an emulsifier (e.g., span-80).

The emulsifier minimizes the interfacial surface tension at the boundary of two immiscible fluids to form the spherical RF droplets, which are then dried and pyrolyzed in an inert atmosphere to yield carbon xerogel particles. As the inverse emulsification of an RF sol involves a number of synthesis parameters such as sol concentration and its pH, amount of catalyst while preparing the sol, stirring time, shear conditions, and amount and type of surfactants, it has been used as a potential way to produce a large spectrum of morphologies in RF-derived carbon xerogels [30–36].

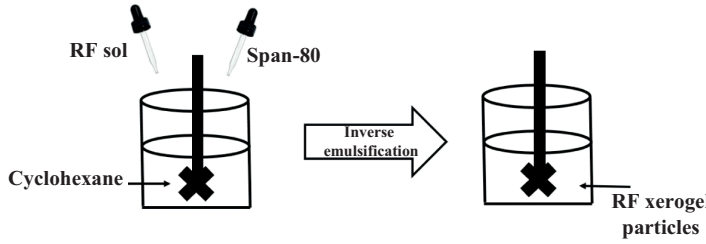

Figure 6.2. Schematic showing inverse emulsification of RF sol in organic phase (cyclohexane) to form RFX particles.

While preparing the RF sol, dilution ratio (ratio of resorcinol to diluent, R/W), pH, and amount of catalyst play an important role in deciding the final size distribution of the RF droplets [10, 30]. It has been shown that by varying the dilution ratio to three orders of magnitude from 0.0037 to 3.7, not only the average size of RF-derived carbon xerogel particles is decreased over more than one order of magnitude (from about 28 to almost 1 μm) but the shape was also distorted from spherical (see Figure 6.3 and Table 6.1) [30]. This phenomenon may be due mostly to a delay in gelation time, which permitted more time for the particles to grow and at the same time to deform the particles to elongated nonspherical shapes.

Other than the dilution ratio, the amount of catalyst and, therefore, the pH of the RF sol play a significant role in determining the final morphology of carbon xerogels. Job et al. reported the significant increase in total pore volume with a change in initial pH of the RF sol from 6.25 to 5.45 [25].

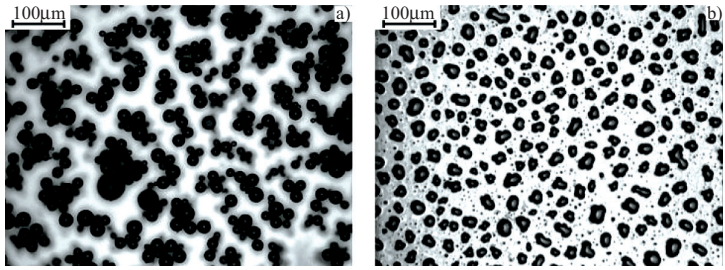

Figure 6.3. Optical micrographs showing the transition to nonspherical shapes of RF-derived carbon xerogel microparticles with a change in dilution ratio: (a) R/W = 0.037; (b) R/W = 0.0037. Other conditions for both cases are R/C = 25, surfactant concentration = 1% (v/v), and stirring time = 5 h.

Source: Reproduced with permission from Sharma et al. [36].

Table 6.1. Characteristic sizes of RF-derived carbon xerogel particles synthesized at different R/W ratios with 5 h of stirring time and 1% (v/v) span-80 concentration

R/W ratio	Mean particle diameter, d_{av} (μm)	Standard deviation (μm)
0.0037	27.9	11.3
0.037	17.2	4.9
0.37	11.8	4.5
3.7	1.4	0.6

Source: Reproduced with permission from Sharma, Upadhyay, and Sharma [30].

We varied the amount of catalyst (R/C from 0.2 to 500) and found that at very low R/C ratio, that is, higher amount of catalyst, submicrometer-sized spherical carbon particles were obtained. However, upon increasing the R/C ratio to 100 (a low catalyst concentration), carbon particles as large as 58 μm were obtained with elongated shapes. This effect may be understood from the fact that with a lesser amount of catalyst, the number of nucleation sites is effectively reduced and this results in the size of individual RF sol droplets to become larger. On further reducing the amount of catalyst (R/C = 500), carbon started agglomerating and formed layered fractal-like structures [36] (see Figure 6.4 and Table 6.2).

Stirring conditions also affect the size of the RF droplets and, therefore, the resulting carbon xerogel particles. Upon increasing the stirring time from 2 to 7 h, the RF-derived carbon xerogel particles grew in size almost an order of magnitude from 5 to 46 μm. Further ultrasonication provided better control of the carbon xerogel particles uniformity as compared to magnetic stirring (also shown in Figure 6.5). Moreover, ultrasonication reduced the mean diameter of the particles.

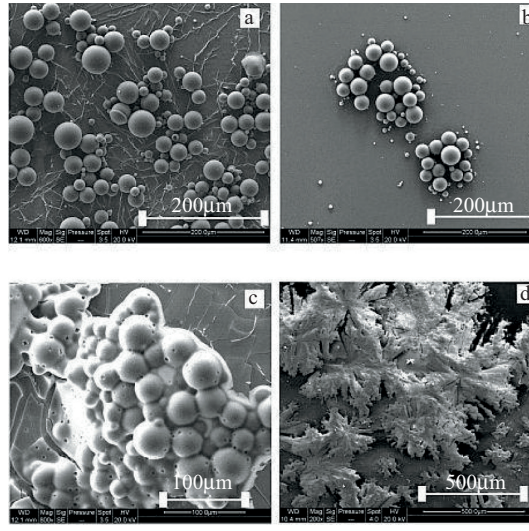

Figure 6.4. Field emission scanning electron microscopy (FESEM) images showing aggregation and coalescence of RF-based carbon microspheres at a span-80 concentration of 1% (v/v) (a) R/C = 10, stirring time = 5 h; (b) R/C = 10, stirring time = 24 h; (c) R/C = 25, stirring time = 24 h; (d) R/C = 500, stirring time = 24 h.

Source: Reproduced with permission from Sharma et al. [36].

Table 6.2. Characteristic sizes of RF-derived carbon xerogel particles synthesized at different R/C ratios with 5 h of stirring time and 1% (v/v) span-80 concentration

R/C ratio	Mean particle diameter (μm)	Standard deviation
0.2	0.90	0.1
1	3.8	1.1
25	18.1	6.8
100	57.9	19.7

Source: Reproduced with permission from Sharma et al. [36].

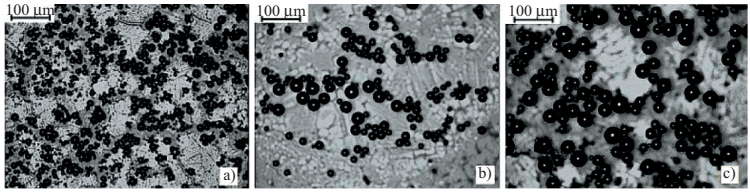

Figure 6.5. Optical micrographs of the RF-based carbon microspheres obtained at R/C = 25, 1% (v/v) span-80 concentration with different stirring times: (a) 2 h; (b) 5 h; (c) 7 h.

Source: Reproduced with permission from Sharma et al. [36].

One of the major factors that determines the size, as well as the morphology, of RF-derived carbon xerogel particles in the inverse emulsification process is the type and amount of surfactant [30]. Nonionic surfactants with different hydrophilic–lipophilic balance (HLB) values were used to examine their effect on emulsion stability and, therefore, on particle morphology. HLB value for a surfactant molecule is defined as the ratio of molecular mass of hydrophilic to lipophilic groups and is an indicator of the degree to which the surfactant is hydrophilic. It was observed from these experiments that the presence of bulky oleic groups (higher HLB value) created steric hindrance to the drop coalescence leading to a reduction in droplet size. More specifically, surfactant with HLB value 8.6 (span-20) resulted in the reduction of average diameter of RF-derived carbon xerogel particles to 4 μm from 10 μm as in the case of the surfactant with HLB value 4.3 (span-80). More interestingly, it is the amount of surfactant that controls the morphology and forms structures ranging from spheres to branched and folded fractal-like carbon microstructures. Varying the surfactant concentration basically modulates the interfacial tension and the composition of the continuous phase in the inverse emulsification. Earlier with a change in catalyst and diluent

concentration, it was found that the dispersed phase composition was the controlling factor for the final size and shape of the carbon particles. With an initial increase in surfactant concentration from 1 to 4 percent, the average size of the particles was reduced and the density was increased as shown in Figure 6.6a and b, respectively.

Upon increasing the surfactant concentration further from 16 to 33 percent and then up to 50 percent, the viscoelasticity of the dispersion increases, and with a reduced interfacial tension, this leads to shear deformation under continuous stirring. This distorts the spherical droplets first into elongated shapes followed by sharp needle-like branched carbon structures that are fractal like. Some of these carbon xerogel structures are shown in Figure 6.7. More details on the exact conditions to form these highly branched, fractal-like, high-external-surface-area carbon xerogel structures can be found in one of our previous publications [36].

In all the earlier cases, the RF-derived carbon xerogel structures were in the micrometer size range. However, in one of our more recent studies, we have obtained RF-derived carbon xerogel nanoparticles by adding a sedimentation step after the inverse emulsification and by repeating the process for a couple of cycles [39]. A schematic of this process is shown in Figure 6.8.

Sedimentation facilitates the settling of micrometer-sized RF sol droplets, which were then again mixed with the oil phase and further stirred. This allowed for the further breaking up of the RF sol droplets, which ultimately narrowed down the size of the RF-derived carbon xerogel particles to a few hundred of nanometers. At the same time, the increased coalescence between the resulting particles finally yielded an interconnected network of RF-derived carbon xerogel nanoparticles as shown in Figure 6.9.

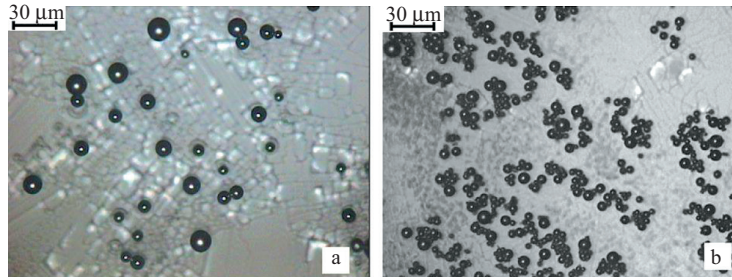

Figure 6.6. Optical micrographs showing the effect of surfactant concentration on particle size at R/C = 25, stirring time of 5 h in *low surfactant concentration* region (a) 1% (v/v) span-80; (b) 4% (v/v) span-80.

Source: Reproduced with permission from Sharma et al. [36].

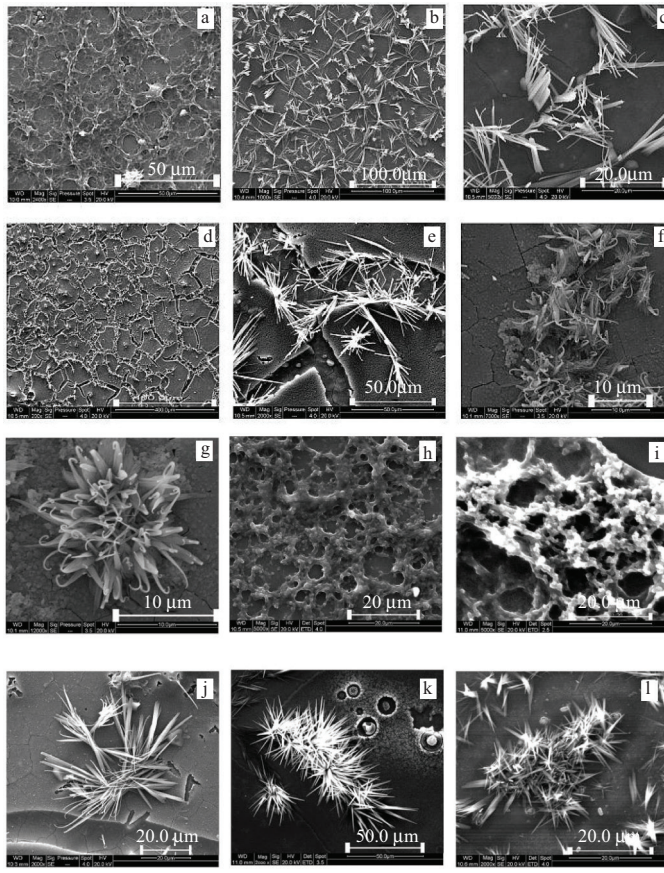

Figure 6.7. FESEM images of carbon *bushes* and *flowers* type fractal-like structures obtained at high surfactant concentrations: (a) 16 percent span-80, 2 h stirring; (b) 16 percent span-80, 5 h stirring; (c) 33 percent span-80, 1 h stirring; (d) 33 percent span-80, 2 h stirring; (e) high magnification image of (d); (f) 50 percent span-80, 1 h stirring; (g) 50 percent span-80, 2 h stirring. Images (a)–(g) are obtained using the surfactant from Loba Chemie at R/C = 25. Images (h) and (j) are obtained using the surfactant from Sigma Aldrich at R/C = 10, 2 h stirring with 33 and 50 percent span-80, respectively. Images (i), (k), and (l) are obtained using the surfactant from SD Fine Chemicals with other conditions such as 33 percent span-80, 2 h stirring with R/C = 10 and 25, respectively, for image (i) and (k) and 50 percent span-80, 2 h stirring, R/C = 25 for image (l).

Source: Reproduced with permission from Sharma et al. [36].

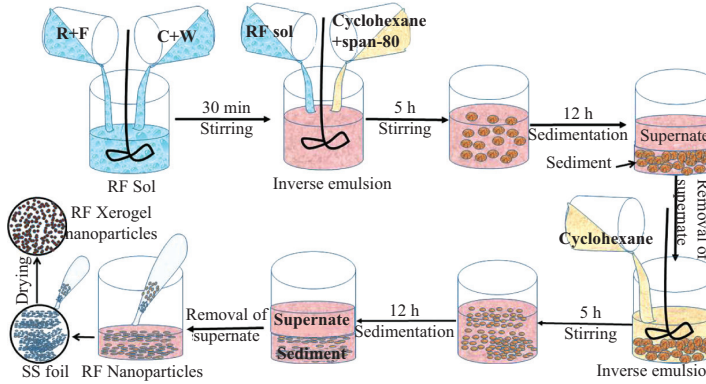

Figure 6.8. Schematic showing the various steps of synthesis of RF-derived carbon xerogel nanoparticles using repetitive inverse emulsification.

Source: Reproduced with permission from Kakunuri, Vennamalla, and Sharma [39].

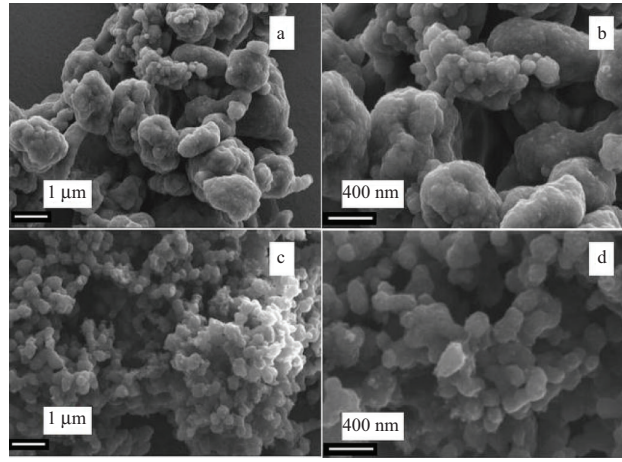

Figure 6.9. Low- and high-magnification FESEM images of carbon xerogel nanoparticles network: (a–b) sample collected from sediment after 12 h sedimentation of first cycle; (c–d) sample collected after 12 h sedimentation of second cycle.

Source: Reproduced with permission from Kakunuri, Vennamalla, and Sharma [39].

6.3.2 ELECTROSPRAYING

In another recent work, we have shown that the RF sol–gel process in combination with electrospraying followed by pyrolysis is able to produce discrete carbon xerogel nanoparticles [11]. Electrospraying uses a high-voltage source connected to a syringe filled with a polymer solution (the RF sol in this case). Upon applying a high voltage of the order of tens of kilovolts, electrostatic forces overcome the surface tension and viscoelastic forces and initiate a charged jet of RF sol, which finally erupts into nanometer-sized droplets before being deposited on the collector as shown in Figure 6.10a. By controlling the various process parameters such as needle diameter, flow rate, and applied voltage, we were able to synthesize spherical and monodispersed carbon xerogel nanoparticles with an average diameter of nearly 30 nm as shown in Figure 6.10b and c.

As far as the internal structure of these RF-derived carbon xerogels is concerned, to a very large extent, it depends on the method of preparation and temperature of pyrolysis. However, RF-derived carbon xerogel largely falls into the category of hard carbons [39]. Hard carbons have smaller crystallites than graphite, which are arranged randomly and, therefore, are amorphous in nature. As these hard carbon cannot be graphitized even at elevated temperatures, these are also known as nongraphitizable carbons. A typical X-ray diffraction (XRD) and Raman spectrum for RF-derived carbon xerogel nanoparticles is shown in Figure 6.11a and b. A broad peak at $\theta = 24°$ in the XRD pattern that corresponds to (0 0 2) reflections of graphite gives interlayer spacing (d_{002}) of 3.71 Å as calculated from Bragg's law. This indicates the amorphous nature of RF-derived carbon xerogels. Further, we observe two broad peaks of characteristic D and G band at 1,331 and 1,592 cm^{-1}, respectively, in the Raman spectrum. D band signifies the presence of dangling bonds and defects in the carbon structure, while G band corresponds to in-plane vibrations of carbon atom in graphene layers. A strong presence of the D band and the intensity ratio (I_D/I_G), which was calculated to be 1.01, indicates the higher fraction of disordered carbon [40, 41] in RF-derived carbon xerogels. The transmission electron microscopy image shown in Figure 6.11c also confirms the lack of long-range order of graphitic crystallites in these RF-derived carbon xerogels.

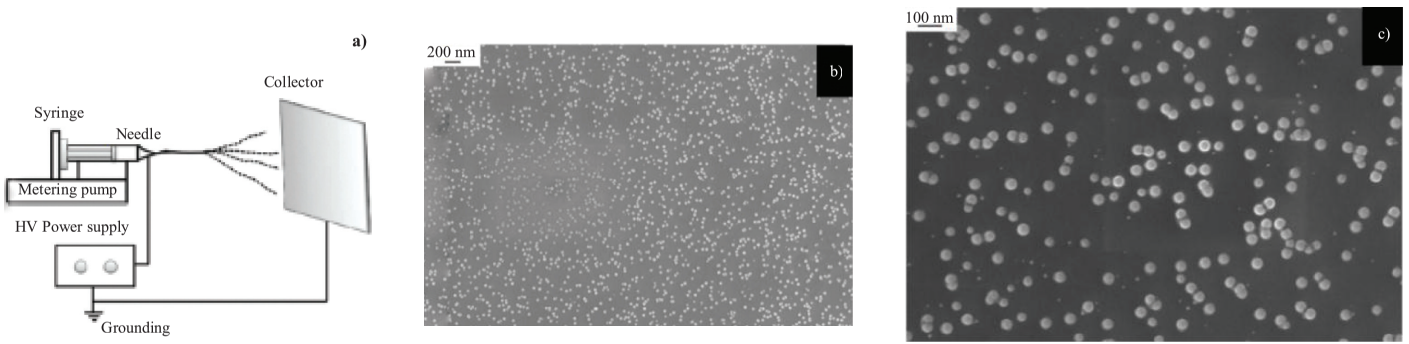

Figure 6.10. (a) Schematic of electrospraying setup; (b) scanning electron microscope image of carbon nanoparticles; (c) magnified image of (b). *Source*: Reproduced with permission from Sharma et al. [11].

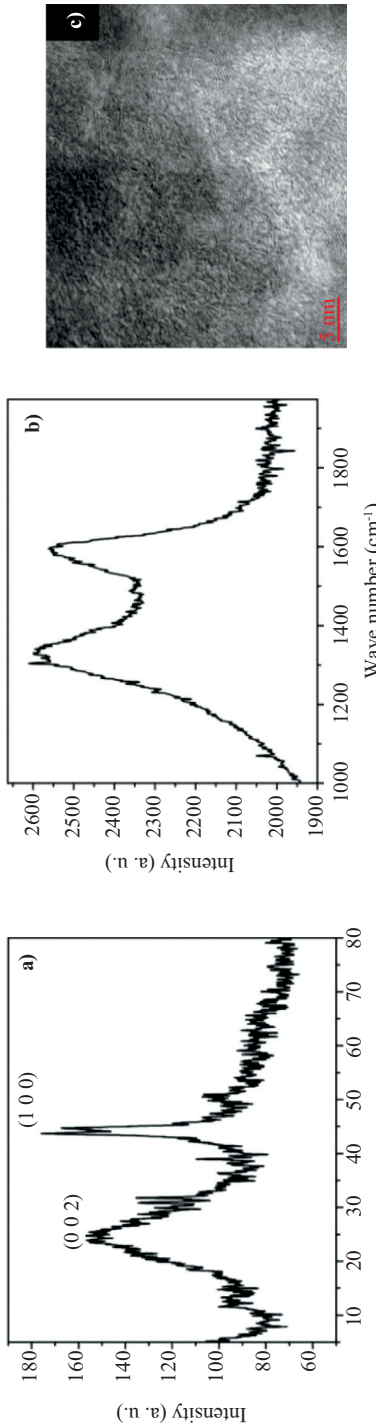

Figure 6.11. (a) X-ray diffraction pattern; (b) Raman spectra; (c) high-resolution transmission electron microscopy image of RF-derived carbon xerogel nanoparticles.

Source: Reproduced with permission from Kakunuri, Vennamalla, and Sharma [39].

6.4 FABRICATION OF THREE-DIMENSIONAL C-MEMS STRUCTURES USING RF-DERIVED CARBON XEROGEL

For improved energy as well as power density of lithium-ion batteries, three-dimensional electrode architecture is proposed because of the reduced ohmic losses and the accommodation of more active electrode material. One of the most promising way to fabricate 3D carbon electrodes is patterning of SU-8 negative photoresist using photolithography followed by pyrolysis. RF-derived carbon xerogels also find increased acceptance as anode materials because of their easily tunable physical and chemical properties. However, to fabricate three-dimensional carbon electrodes from RFX, we need to find alternative fabrication approaches other than photolithography that is limited to photoresist materials.

We have fabricated three-dimensional carbon microelectromechanical systems (C-MEMS) structures from RF-derived carbon xerogels using replica molding, a method that can be categorized as soft lithography, followed by controlled pyrolysis [42]. In the replica molding technique, a master pattern to be replicated is made first. As illustrated in Figure 6.12, we patterned a three-dimensional microarray in SU-8 using photolithography (Figure 6.12a). A prepolymer solution of polydimethylsiloxane (PDMS) elastomer was then poured over this master pattern (Figure 6.12b). Once the PDMS was cured at 80°C, the

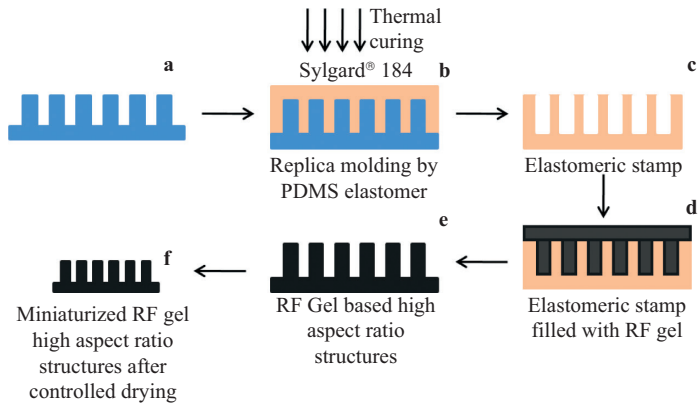

Figure 6.12. Schematic diagram of replica molding to fabricate three-dimensional microposts arrays in RFX.

Source: Reproduced with permission from Sharma et al. [12].

mold with PDMS was put into a chloroform solution to swell the PDMS so as to peel it off easily from the master to fabricate negative replicas in PDMS (Figure 6.12c). This process, known as replica molding, is continued but now by using the PDMS replica as a master. The RF sol is poured onto the PDMS stamp (Figure 6.12d) and allowed to dry to form the xerogel. Curing and peeling off the PDMS replica yields the patterned RFX (Figure 6.12e), which were further shrinked isotropically [42] under controlled drying conditions to yield three-dimensional array of RFX microposts (Figure 6.12f).

After controlled drying and pyrolysis, the patterned RF gels are converted into three-dimensional carbon xerogel structures. Drying of the patterned RFX is a crucial step, and it has to be optimized very carefully to prevent distortion, buckling, and cracks. Pyrolysis of the RFX patterns yielded 3D carbon patterns that importantly retained the same aspect ratio as the master pattern because of their isotropic shrinkage. Up to 60 percent shrinkage can be obtained in one cycle of drying and pyrolysis of RFX. RF sol composition, drying, and pyrolysis conditions are some of the important parameters that need fine tuning to yield crack- and distortion-free 3D carbon xerogel structures. Further miniaturization of these patterns can be achieved by replicating the fabricated 3D carbon xerogel pattern for subsequent cycles of replica molding. This way we reduced the dimensions of the original patterns by an order of magnitude in four successive cycles of replica molding, drying, and pyrolysis. In Figure 6.13, we show, as an example, three-dimensional microposts arrays of SU-8, which were then transferred using replica molding into RFX and pyrolyzed into carbon. This simple fabrication method of arrays of three-dimensional microposts in carbon xerogels as shown in Figure 6.12 opens up new possibilities for their use in electrochemical applications. The replica molding technique is not limited to replicating micrometer-sized features but can also be used for replicating hierarchical structures (such as fractals) with features in the micrometer and nanometer range [43].

Recently, Park et al. demonstrated that a fractal 3D electrode design is the most appropriate electrode shape for batteries, fuel cells, and sensors because of the minimized transport losses and maximized surface area [44]. Taking this into consideration, we have suggested the combination of a top-down approach (soft lithography) with a bottom-up technique such as electrospraying to make such three-dimensional fractal-like hierarchical C-MEMS structures using RFX [12]. A schematic demonstrating this principle is shown in Figure 6.14.

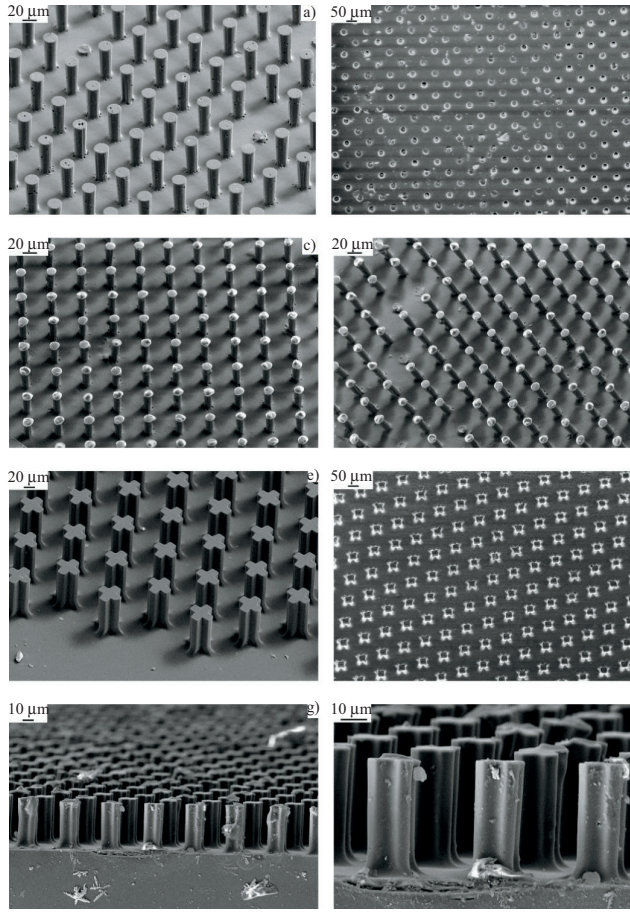

Figure 6.13. (a) High aspect ratio (HAR) 3D cylindrical posts in SU-8 used as master pattern; (b) PDMS replica showing holes; (c) RFX-based cylindrical posts; (d) RFX-derived cylindrical nonporous carbon posts; (e) HAR 3D posts with cross-shaped design in SU-8; (f) PDMS replica showing holes; (g)–(h) RFX-derived 3D cross-shaped nonporous carbon posts.

Source: Reproduced with permission from Sharma et al. [12].

As illustrated here, SU-8 2002 photoresist was electrosprayed to deposit submicrometer-sized beads, while RF sol was separately electrosprayed in the form of nanometer-sized droplets on to these three-dimensional HAR carbon micropost arrays, which were used as a collector. In the latter case, the RF sol is electrosprayed in the form of

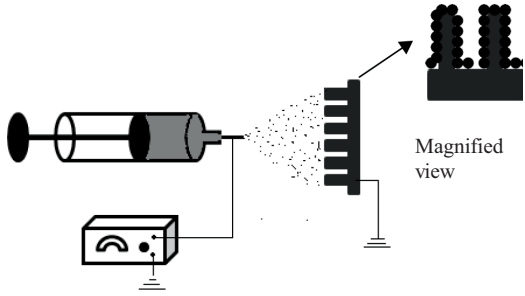

Figure 6.14. Schematic for fabricating hierarchical C-MEMS structures by combining electrospraying with lithographically fabricated master stamp.

Source: Reproduced with permission from Sharma et al. [14].

nanoparticles with an average diameter of 72 ± 21 nm, while in the former case, the SU-8 photoresist is electrosprayed as submicrometer-sized particles (average diameter of 275 ± 83 nm). These integrated hierarchical structures were then subjected to pyrolysis in the inert atmosphere to yield three-dimensional HAR C-MEMS structures. As observed at different magnifications in Figure 6.15, there was an efficient conformal coverage with the RF-derived carbon xerogel nanoparticles or the SU-8-derived submicrometer-sized particles on an array of three-dimensional carbon microposts of different shapes.

6.5 ELECTROCHEMICAL PERFORMANCE OF RF-DERIVED CARBON XEROGELS

In order to demonstrate the utility of RF-derived carbon xerogels as anodes in lithium-ion batteries, we have demonstrated that RF-derived carbon xerogels in different formats such as thin films or nanoparticles can be reversibly intercalated with lithium ions [12, 39]. In Figure 6.16, we show the cyclic voltammograms of RF-derived carbon xerogel nanoparticles. The broad cathodic current peaks between 0.5 and 1 V are attributed to the formation of a SEI layer, a typical characteristic of carbon materials. A peak near 0 V confirms the insertion of lithium ions in these carbon xerogels, while the anodic peak at 1.2 V may be attributed to the deintercalation of lithium ions.

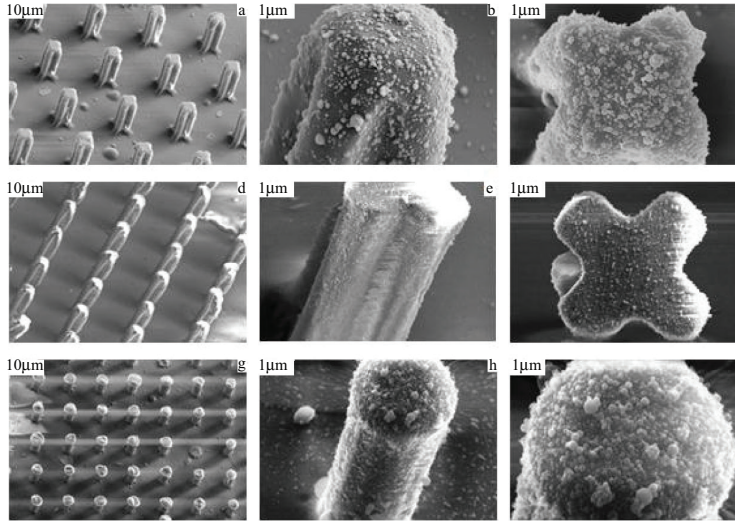

Figure 6.15. (a) An array of RFX-derived cross-shaped carbon posts integrated by electrosprayed SU-8-derived submicrometer-sized carbon spheres; (b) magnified side view of a post; (c) magnified top view of one of the posts showing a conformal deposition of submicrometer-sized carbon spheres; (d) an array of RFX-derived cross-shaped carbon posts integrated by electrosprayed RFX-derived carbon nanospheres; (e) magnified side view of a post; (f) magnified top view of one of the posts showing a conformal deposition of carbon nanospheres; (g) an array of RFX-derived cylindrical carbon posts integrated by electrosprayed SU-8-derived submicrometer-sized carbon spheres; (h) magnified side view of such a hierarchical post; (i) magnified top view of one of the cylindrical posts showing a dense conformal deposition of submicrometer-sized carbon spheres.

Source: Reproduced with permission from Sharma et al. [14].

Galvanostatic charge or discharge experiments were also performed on RF-derived carbon xerogel thin films and nanoparticles. For RF-derived carbon xerogel thin films, a reversible capacity of nearly 200 mAh/g was established with more than 90 percent coulombic efficiency in second and subsequent cycles as illustrated in Figure 6.17a. Irreversible capacity losses at different current densities as shown in Figure 6.17b and c were found to be significantly lower than what has been reported for SU-8-photoresist-derived carbon films. This confirms that RF-derived carbon xerogels can be reversibly intercalated with lithium ions; however, the reversible capacity remains lower than that of graphite (200 to 300 mAh/g). However, as observed in Figure 6.18, RF-derived carbon

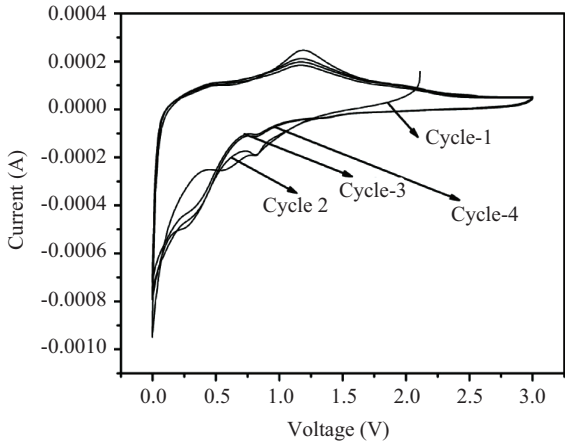

Figure 6.16. Cyclic voltammogram of RF-derived carbon xerogel nanoparticles at a scan rate of 0.1 mV/s.

Source: Reproduced with permission from Kakunuri, Vennamalla, and Sharma [39].

xerogel nanoparticles exhibited significant improvement in their reversible capacity. Initial discharge capacity was found to be 1,127 mAh/g with coulombic efficiency of 44 percent. After initial five cycles, coulombic efficiency reached up to 95 percent. Moreover, after 30 cycles of continuous charge or discharge at 0.1 C rate, reversible capacity was stabilized at ~400 mAh/g, which is even larger than that of graphite.

In order to more clearly understand the importance of RF-derived carbon xerogels and to bring more clarity on their electrochemical performance, we provide a quick summary of the electrochemical performance of various other organic-gel-derived carbon morphologies as anode materials for lithium-ion batteries in Table 6.3. We observed that the nanostructuring of RF-derived carbon xerogels facilitates the insertion and deinsertion of lithium ions that results in a lower irreversible capacity and higher specific reversible capacity even after 100 cycles. The initial coulombic efficiency for RF-derived carbon xerogel was significantly higher than that of RF-derived carbon aerogels and cryogels irrespective of their morphology. Nitrogen doping using melamine and activation of RF-derived carbon xerogels surface to generate porosity further helped in obtaining a significantly higher capacity of 640 mAh/g, a value nearly double to that of graphite, one of the most commonly used anode material for commercial lithium-ion batteries. The excellent electrochemical behavior of carbon xerogels as reported here opens up many new possibilities for energy storage devices.

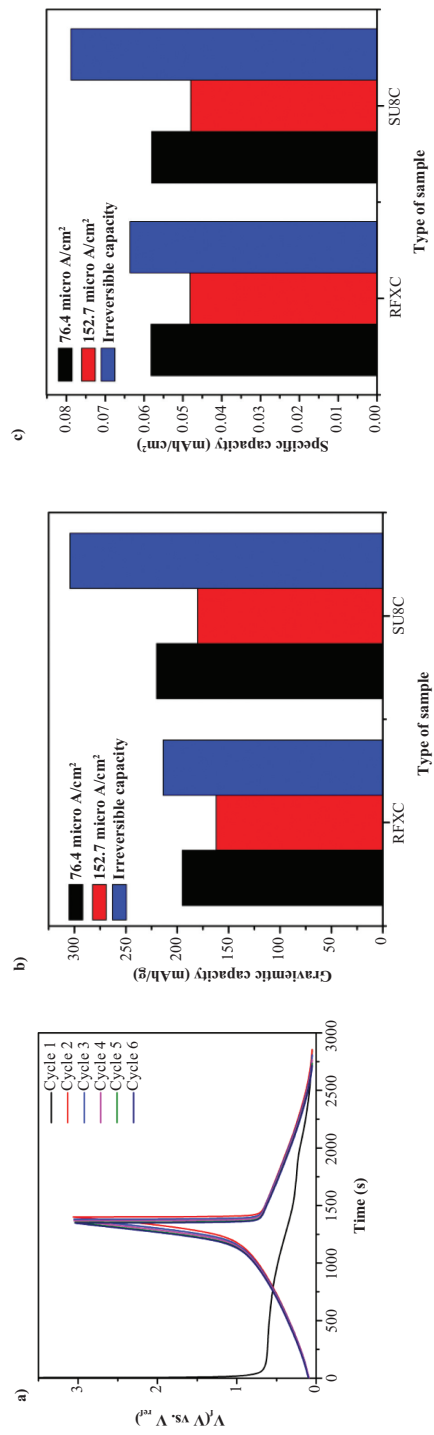

Figure 6.17. (a) Galvanostatic charge or discharge cycle behavior of RF-gel-derived carbon film for first six cycles; (b) comparison of gravimetric capacity of RFX-derived carbon with SU-8-derived carbon; (c) comparison of specific capacity of RFX-derived carbon with SU-8-derived carbon. The reported values for capacities in (b) and (c) are after 20 cycles.

Source: Reproduced with permission from Sharma et al. [14].

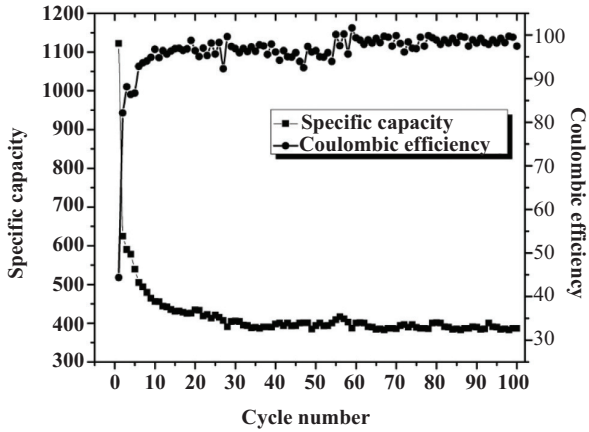

Figure 6.18. Cycling performance of carbon xerogel nanoparticles.

Source: Reproduced with permission from Kakunuri, Vennamalla, and Sharma [39].

6.6 SUMMARY

Carbon xerogels have received quite some attention in recent years because of their tunable unique physical, chemical, and electrochemical properties. In this chapter, we briefly reviewed the various strategies to modulate the size, morphology, and internal structure of RF-derived carbon xerogels. Furthermore, we demonstrated that RF-derived carbon xerogels can successfully be reversibly intercalated with lithium ions and thus find their potential application as anode materials for lithium-ion batteries. The microstructural characterization, as discussed in this chapter, reveals that RF-derived carbon xerogels are hard carbons. Random stacking of smaller graphite crystallites in hard carbons thus allow more lithium-ion insertion, which explains the large lithium-ion intercalation capacity observed for these carbon xerogels. Moreover, to achieve excellent cyclic stability and capacity retention, in these carbon xerogels, some of the efforts such as nanostructuring, doping with foreign molecules, and activation of RF carbon xerogels (which have been tried successfully in recent literature) were also discussed in this chapter. For C-MEMS applications, we later outlined various approaches to fabricate RF-xerogel-derived three-dimensional HAR multiscale carbon structures over large areas. It would be interesting to study the electrochemical performance of some

Table 6.3. Summary of electrochemical performance of previously reported carbon gel materials and a comparison with present work [39]

Sample or ref. no	First cycle reversible capacity (mAh/g)/ coulombic efficiency (%)	Number of cycles reported (n)	Specific capacity after "n" cycles (mAh/g)/current density
Carbon xerogel (powder) [45]	171/43	30	145/100 mA/g
Carbon cryogel hollow microspheres [46]	164/33	5	155/0.15 mA/cm^2
Carbon cryogel microcapsules [46]	360/34	5	340/0.15 mA/cm^2
Carbon cryogel microspheres [46]	140/32	5	130/0.15 mA/cm^2
Carbon aerogel [27]	312/20	50	242/50 mA/g
Activated carbon aerogel [27]	658/17	50	333/50 mA/g
Nitrogen-doped carbon xerogel [38]	275/43	50	212/37.2 mA/g
Nitrogen-doped porous carbon xerogel (activated) [38]	800/45	50	640/37.2 mA/g
Carbon xerogel nanoparticles [39]	497/44	100	385/37.2 mA/g
Carbon xerogel thin films [12]	195/47	20	190/76.4 μA/cm^2

of these three-dimensional electrodes integrated with RF-derived carbon xerogel nanostructures as already fabricated. The hybrid approach for the fabrication of multiscale carbon structures may open new possibilities not only in energy storage devices but also in sensing devices and catalytic applications.

REFERENCES

[1] Pierre, A.C., and G.M. Pajonk. 2002. "Chemistry of Aerogels and Their Applications." *Chemical Reviews* 102, no. 11, pp. 4243–65. doi: http://dx.doi.org/10.1021/cr0101306

[2] Pekala, R.W. 1989. "Organic Aerogels from the Polycondensation of Resorcinol with Formaldehyde." *Journal of Materials Science* 24, no. 9, pp. 3221–27. doi: http://dx.doi.org/10.1007/bf01139044

[3] Pekala, R.W., C.T. Alviso, X. Lu, J. Gross, and J. Fricke. 1995. "New Organic Aerogels Based Upon a Phenolic-Furfural Reaction." *Journal of Non-Crystalline Solids* 188, no. 1–2, pp. 34–40. doi: http://dx.doi.org/10.1016/0022-3093(95)00027-5

[4] Tamon, H., H. Ishizaka, M. Mikami, and M. Okazaki. 1997. "Porous Structure of Organic and Carbon Aerogels Synthesized by sol-gel Polycondensation of Resorcinol with Formaldehyde." *Carbon* 35, no. 6, pp. 791–96. doi: http://dx.doi.org/10.1016/s0008-6223(97)00024-9

[5] Zhu, Y., X. Xiang, E. Liu, Y. Wu, H. Xie, Z. Wu, and Y. Tian. 2012. "An Activated Microporous Carbon Prepared from Phenol-Melamine-Formaldehyde Resin for Lithium Ion Battery Anode." *Materials Research Bulletin* 47, no. 8, pp. 2045–50. doi: http://dx.doi.org/10.1016/j.materresbull.2012.04.003

[6] Wu, D., R. Fu, Z. Sun, and Z. Yu. 2005. "Low-Density Organic and Carbon Aerogels from the sol–gel Polymerization of Phenol with Formaldehyde." *Journal of Non-Crystalline Solids* 351, no. 10–11, pp. 915–21. doi: http://dx.doi.org/10.1016/j.jnoncrysol.2005.02.008

[7] Wu, D., R. Fu, S. Zhang, M.S. Dresselhaus, and G. Dresselhaus. 2004. "The Preparation of Carbon Aerogels Based Upon the Gelation of Resorcinol–Furfural in Isopropanol with Organic Base Catalyst." *Journal of Non-Crystalline Solids* 336, no. 1, pp. 26–31. doi: http://dx.doi.org/10.1016/j.jnoncrysol.2003.12.051

[8] Wu, D., R. Fu, and Z. Yu. 2005. "Organic and Carbon Aerogels from the NaOH-Catalyzed Polycondensation of Resorcinol-Furfural and Supercritical Drying in Ethanol." *Journal of Applied Polymer Science* 96, no. 4, pp. 1495–35. doi: http://dx.doi.org/10.1002/app.21582

[9] Zhu, Y., H. Hu, W. Li, and X. Zhang. 2007. "Resorcinol-Formaldehyde Based Porous Carbon as an Electrode Material for Supercapacitors." *Carbon* 45, no. 1, pp. 160–65. doi: http://dx.doi.org/10.1016/j.carbon.2006.07.010

[10] Al-muhtaseb, S.A., and J.A. Ritter. 2003. "Preparation and Properties of Resorcinol-Formaldehyde Organic and Carbon Gels." *Advanced Materials* 15, no. 2, pp. 101–14. doi: http://dx.doi.org/10.1002/adma.200390020

[11] Sharma, C.S., S. Patil, S. Saurabh, A. Sharma, and R. Venkataraghavan. 2009. "Resorcinol-Formaldehyde Based Carbon Nanospheres by Electrospraying." *Bulletin of Materials Science* 32, no. 3, pp. 239–46. doi: http://dx.doi.org/10.1007/s12034-009-0036-6

[12] Sharma, C.S., H. Katepalli, A. Sharma, G.T. Teixidor, and M. Madou. 2014. "Fabrication of Resorcinol-Formaldehyde Xerogel Based High Aspect Ratio 3-D Hierarchical C-MEMS Structures." *Electrochemical Society Transactions* 61, no. 7, pp. 45–54. doi: http://dx.doi.org/10.1149/06107.0045ecst

[13] Li, W., A. Lu, and S. Guo. 2001. "Characterization of the Microstructures of Organic and Carbon Aerogels Based Upon Mixed Cresol–Formaldehyde." *Carbon* 39, no. 13, pp. 1989–94. doi: http://dx.doi.org/10.1016/s0008-6223(01)00029-x

[14] Tamon, H., H. Ishizaka, T. Yamamoto, and T. Suzuki. 1999. "Preparation of Mesoporous Carbon by Freeze Drying." *Carbon* 37, no. 12, pp. 2049–55. doi: http://dx.doi.org/10.1016/s0008-6223(99)00089-5

[15] Job, N., R. Pirard, B. Verturyen, J.-F. Colomer, J. Marien, and J.-P. Pirard. 2007. "Synthesis of Transition Metal-Doped Carbon Xerogels by Cogelation." *Journal of Non-Crystalline Solids* 353, no. 24–25, pp. 2333–45. doi: http://dx.doi.org/10.1016/j.jnoncrysol.2007.04.001

[16] Alcantara, R., P. Lavela, G.F. Ortiz, and J.L. Tirado. 2005. "Carbon Microspheres Obtained from Resorcinol-Formaldehyde as High-Capacity Electrodes for Sodium-Ion Batteries." *Electrochemical and Solid-State Letters* 8, no. 4, pp. A222–25. doi: http://dx.doi.org/10.1149/1.1870612

[17] Calvo, E.G., F. Lufrano, P. Staiti, A. Brigandi, A. Arenillas, and J.A. Menendez. 2013. "Optimizing the Electrochemical Performance of Aqueous Symmetric Supercapacitors Based on an Activated Carbon Xerogel." *Journal of Power Sources* 241, pp. 776–82. doi: http://dx.doi.org/10.1016/j.jpowsour.2013.03.065

[18] Girgis, B.S., I.Y. El-sherif, A.A. Attia, and N.A. Fathy. 2012. "Textural and Adsorption Characteristics of Carbon Xerogel Adsorbents for Removal of Cu (II) Ions from Aqueous Solution." *Journal of Non-Crystalline Solids* 358, no. 4, pp. 741–47. doi: http://dx.doi.org/10.1016/j.jnoncrysol.2011.12.004

[19] Liu, B., and S. Creager. 2010. "Carbon Xerogels as Pt Catalyst Supports for Polymer Electrolyte Membrane Fuel-Cell Applications." *Journal of Power Sources* 195, no. 7, pp. 1812–20. doi: http://dx.doi.org/10.1016/j.jpowsour.2009.10.033

[20] Mezzavilla, S., C. Zanella, P.R. Aravind, C.D. Volpe, and G.D. Soraru. 2012. "Carbon Xerogels as Electrodes for Supercapacitors. The Influence of the Catalyst Concentration on the Microstructure and on the Electrochemical Properties." *Journal of Materials Science* 47, no. 20, pp. 7175–80. doi: http://dx.doi.org/10.1007/s10853-012-6662-1

[21] Smirnova, A., X. Dong, H. Hara, A. Vasiliev, and N. Sammes. 2005. "Novel Carbon Aerogel-Supported Catalysts for PEM Fuel Cell Application." *International Journal of Hydrogen Energy* 30, no. 2, pp. 149–58. doi: http://dx.doi.org/10.1016/j.ijhydene.2004.04.014

[22] Zhang, L., H. Liu, M. Wang, and L. Chen. 2007. "Structure and Electrochemical Properties of Resorcinol–Formaldehyde Polymer-Based Carbon for Electric Double-Layer Capacitors." *Carbon* 45, no. 7, pp. 1439–45. doi: http://dx.doi.org/10.1016/j.carbon.2007.03.030

[23] Zhou, G., H. Tian, H. Sun, S. Wang, and C.E. Buckley. 2011. "Synthesis of Carbon Xerogels at Varying sol–gel pHs, Dye Adsorption and Chemical Regeneration." *Chemical Engineering Journal* 171, no. 3, pp. 1399–405. doi: http://dx.doi.org/10.1016/j.cej.2011.05.054

[24] Samant, P.V., F. Goncalves, M.M.A. Freitas, M.F.R. Pereira, and J.L. Figueiredo. 2004. "Surface Activation of a Polymer Based Carbon." *Carbon* 42, no. 7, pp. 1321–25. doi: http://dx.doi.org/10.1016/j.carbon.2004.01.034

[25] Job, N., R. Pirard, J. Marien, and J.P. Pirard. 2004. "Porous Carbon Xerogels with Texture Tailored by pH Control During sol–gel Process." *Carbon* 42, no. 3, pp. 619–28. doi: http://dx.doi.org/10.1016/j.carbon.2003.12.072

[26] Job, N., R. Pirard, J. Marien, and J.P. Pirard. 2004. "Synthesis of Transition Metal-Doped Carbon Xerogels by Solubilization of Metal Salts in Resorcinol–Formaldehyde Aqueous Solution." *Carbon* 42, no. 15, pp. 3217–27. doi: http://dx.doi.org/10.1016/j.carbon.2004.08.013

[27] Nian-Ping, L., S. Jun, G. Da-yung, L. Dong, Z. Xiao-Wei, and L. Ya-Jie. 2013. "Effect of Carbon Aerogel Activation on Electrode Lithium Insertion Performance." *Acta Physico-Chimica Sinica* 29, pp. 966–72. doi: 10.3866/PKU.WHXB201302281

[28] Soottitantawat, A., T. Yamamoto, A. Endo, T. Ohmori, and M. Nakaiwa. 2007. "Synthesis of Ultrafine Carbon Cryogel Microspheres Using a Homogenizer." *AIChE Journal* 53, no. 1, pp. 228–36. doi: http://dx.doi.org/10.1002/aic.11053

[29] Yamamoto, T., A. Endo, T. Ohmori, and M. Nakaiwa. 2005. "The Effects of Different Synthetic Conditions on the Porous Properties of Carbon Cryogel Microspheres." *Carbon* 43, no. 6, pp. 1231–38. doi: http://dx.doi.org/10.1016/j.carbon.2004.12.016

[30] Sharma, C.S., D.K. Upadhyay, and A. Sharma. 2009. "Controlling the Morphology of Resorcinol−Formaldehyde-Based Carbon Xerogels by Sol Concentration, Shearing, and Surfactants." *Industrial & Engineering Chemistry Research* 48, no. 17, pp. 8030–36. doi: http://dx.doi.org/10.1021/ie900359w

[31] Kim, S., T. Yamamoto, A. Endo, T. Ohmori, and M. Nakaiwa. 2006. "Influence of Nonionic Surfactant Concentration on Physical Characteristics of Resorcinol-Formaldehyde Carbon Cryogel Microspheres." *Journal of Industrial Engineering Chemistry* 12, pp. 484–88.

[32] Wang, X., X. Wang, L. Liu, L. Bai, H. An, L. Zheng, and L. Yi. 2011. "Preparation and Characterization of Carbon Aerogel Microspheres by an

Inverse Emulsion Polymerization." *Journal of Non-Crystalline Solids* 357, no. 3, pp. 793–97. doi: http://dx.doi.org/10.1016/j.jnoncrysol.2010.11.015

[33] Alviso, C.T., R.W. Pekala, J. Gross, X. Lu, R. Caps, and J. Fricke. 1996. "Resorcinol-Formaldehyde and Carbon Aerogel Microspheres." *Materials Research Society Symposium Proceedings* 431, pp. 521–25. doi: http://dx.doi.org/10.1557/proc-431-521

[34] Horikawa, T., J. Hayashi, and K. Muroyama. 2004. "Size Control and Characterization of Spherical Carbon Aerogel Particles from Resorcinol–Formaldehyde Resin." *Carbon* 42, no. 1, pp. 169–75. doi: http://dx.doi.org/10.1016/j.carbon.2003.10.007

[35] Zhang, H., F. Ye, H. Xu, L. Liu, and H. Guo. 2010. "Synthesis of Carbon Hollow Particles by a Simple Inverse-Emulsion Method." *Materials Letters* 64, no. 13, pp. 1473–75. doi: http://dx.doi.org/10.1016/j.matlet.2010.03.065

[36] Sharma, C.S., M.M. Kulkarni, A. Sharma, and M. Madou. 2009. "Synthesis of Carbon Xerogel Particles and Fractal-Like Structures." *Chemical Engineering Science* 64, no. 7, pp. 1536–43. doi: http://dx.doi.org/10.1016/j.ces.2008.12.013

[37] Yamamoto, T., A. Endo, T. Ohmori, and M. Nakaiwa. 2004. "Porous Properties of Carbon Gel Microspheres as Adsorbents for Gas Separation." *Carbon* 42, no. 8–9, pp. 1671–76. doi: http://dx.doi.org/10.1016/j.carbon.2004.02.021

[38] Liu, X., S. Li, J. Mei, W. Lau, R. Mi, Y. Li, H. Liu, and L. Liu. 2014. "From Melamine–Resorcinol–Formaldehyde to Nitrogen-Doped Carbon Xerogels with Micro-and Meso-Pores for Lithium Batteries." *Journal of Materials Chemistry A* 2, no. 35, pp. 14429–38. doi: http://dx.doi.org/10.1039/c4ta02928c

[39] Kakunuri, M., S. Vennamalla, and C.S. Sharma. 2015. "Synthesis of Carbon Xerogel Nanoparticles by Inverse Emulsion Polymerization of Resorcinol–Formaldehyde and Their Use as Anode Materials for Lithium-Ion Battery." *RSC Advances* 5, no. 7, pp. 4747–53. doi: http://dx.doi.org/10.1039/c4ra15171b

[40] Maldonado-Hodar, F.J., C. Moreno-Castilla, J. Rivera-Utrilla, Y. Hanzawa, and Y. Yamada. 2000. "Catalytic Graphitization of Carbon Aerogels by Transition Metals." *Langmuir* 16, no. 9, pp. 4367–73. doi: http://dx.doi.org/10.1021/la991080r

[41] Schwan, J., S. Ulrich, V. Batori, H. Ehrhardt, and S.R.P. Silva. 1996. "Raman Spectroscopy on Amorphous Carbon Films." *Journal of Applied Physics* 80, no. 1, pp. 440–47. doi: http://dx.doi.org/10.1063/1.362745

[42] Sharma, C.S., A. Verma, M.M. Kulkarni, D.K. Upadhyay, and A. Sharma. 2010. "Microfabrication of Carbon Structures by Pattern Miniaturization in Resorcinol-Formaldehyde Gel." *ACS Applied Materials & Interfaces* 2, no. 8, pp. 2193–97. doi: http://dx.doi.org/10.1021/am100512c

[43] Mattaparthi, S., and C.S. Sharma. 2013. "Biomimicked High-Aspect-Ratio Hierarchical Superhydrophobic Polymer Surfaces." *Bioinspired, Biomimetic Nanobiomaterials* 3, no. 1, pp. 4–9. doi: http://dx.doi.org/10.1680/bbn.13.00015

[44] Park, B.Y., R. Zaouk, C. Wang, and M. Madou. 2006. "A Case for Fractal Electrodes in Electrochemical Applications." *Journal of Electrochemical Society* 154, no. 2, pp. P1–P5. doi: http://dx.doi.org/10.1149/1.2400607

[45] Yuan, X., Y. Chao, Z. Ma, and X. Ding. 2007. "Preparation and Characterization of Carbon Xerogel (CX) and CX–SiO Composite as Anode Material for Lithium-Ion Battery." *Electrochemistry Communications* 9, no. 10, pp. 2591–95. doi: http://dx.doi.org/10.1016/j.elecom.2007.08.004

[46] Zhang, H., H. Xu, and C. Zhao. 2012. "Synthesis of Morphology-Controlled Carbon Hollow Particles by Carbonization of Resorcinol–Formaldehyde Precursor Microspheres and Applications in Lithium-Ion Batteries." *Materials Chemistry and Physics* 133, no. 1, pp. 429–36. doi: http://dx.doi.org/10.1016/j.matchemphys.2012.01.055

CHAPTER 7

SURFACE MODIFICATION OF CARBON MATERIALS

Salvador Borrós, Victor Ramos, Guillermo Reyes, Núria Tricás, Anna Cifuentes-Rius

Institut Químic de Sarrià, Universitat Ramon Llull, Spain

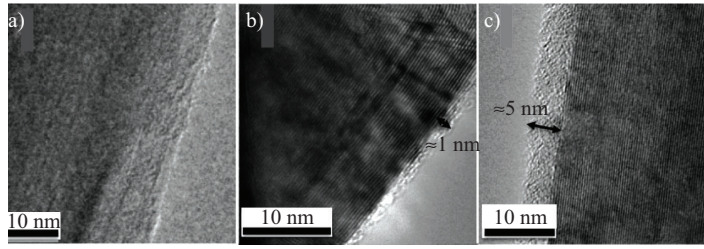

Plasma polymerization of an acrylic monomer on carbon nanotubes (CNTs) surfaces: (a) bare CNT, (b) 5-minute polymerization, (c) 15-minute polymerization [1].

7.1 PURPOSE OF CHAPTER 7

The purpose of this chapter is to describe the importance of carbon surface control and modification in terms of chemical composition and microstructure for carbon microelectromechanical system (C-MEMS) and carbon nanoelectromechanical system (C-NEMS) applications. The chapter points out that the performance of carbon materials is determined to a large extent by their surface and interfacial properties. It describes methods to tailor the surface activity of different carbon structures, how to characterize them, and the potential applications derived from the modifications achieved. Carbon black (CB) and carbon nanotubes (CNTs) are chosen as reference carbon materials for describing in detail the surface modifications.

7.2 SURFACE MODIFICATION OF CARBON MATERIALS: AN INTRODUCTION

Native carbon surfaces present highly hydrophobic surfaces, which result in poor aqueous media interaction, making them unsuitable for some key applications, especially in biology. The improvement of the hydrophilicity of such materials can be achieved through surface modification or functionalization [2, 3]. Modification of carbonaceous materials may be performed by covalent and noncovalent methods [4–6]. Covalent functionalization exploits the chemical reactivity of carbon surfaces to form bonds between the carbon surface and a hydrophilic moiety. For instance, covalent bonding of modified moieties having hydrophilic groups in their structure results in increased water solubility of modified CNTs. In contrast, noncovalent modification techniques are based on hydrophobic interactions between the CNT surface and the hydrophobic region of an amphiphilic moiety. CNT wrapping with multiple amphiphilic moieties having surfactant-like activity again results in solubilization of CNTs in aqueous media [7–11]. Both the techniques provide efficient carbonaceous material modification strategies for different applications, resulting in increased biocompatibility and reduced toxicity.

However, covalent functionalization is typically more attractive because of the more controlled nature of the procedure, allowing the formation of surfaces with a higher degree of specificity and greater tunability of properties [12, 13]. Among the approaches to covalently modify carbonaceous surfaces described in the literature, most involve multistep reactions and rather harsh conditions to achieve the desired functional groups. An alternative that will be extensively commented on this chapter is the use of plasma treatment for surface activation and modification. Plasma polymerization, which is a dry method, has been demonstrated to be a relatively simple and fast approach for the modification of different surfaces without affecting the mechanical properties of the bulk material [14–15]. Plasma polymerization is basically used to control the surface chemistry of a desired material. The technique was originally developed to modify polymers surfaces, providing homogeneous reactive coatings with a high degree of specificity for the immobilization of molecules [16–18]. In recent years, because of the many advantages that this technique offers, it has also been used for the chemical modification of materials such as hydroxyapatite powder, metal nanoparticles, carbon nanofibers, and also CNTs [19, 20]. As will be seen in this chapter, by using this method, carbon surfaces can be tuned in order to improve wettability, dispersibility, stability, and biocompatibility, while retaining structural integrity.

Plasma treatment can be used to activate the surface before the polymerization is carried out, or directly by the effect of the same resorcinol–formaldehyde (RF) glow-discharge used to polymerize the desired monomer present in the reactor chamber. Over the past decade, plenty of studies on plasma polymerization on carbon materials have been carried out. These studies are mainly focused on applications involving electrochemical sensors in which this technique is used to increase the interaction of the sensor surface with the analytes [21, 22].

In Section 7.3, a short overview of plasma technologies for surface modification is presented. In Section 7.4, examples of modifications of different carbon materials are described.

7.3 PLASMA MODIFICATION

It seems clear from the preceding that the surface of carbonaceous materials requires modification by different chemical synthetic methods to generate appropriate functionalities, enabling covalent attachment of suitable solubilizing, bioactive, or biocompatible moieties. However, this modification depends on the structure and composition of the carbonaceous material. For instance, researchers have differentiated CNTs into two reaction zones in terms of their reactivity, that is, sidewalls and tips [23–25]. It has been shown that tips are more prone to modification than sidewalls and both may be dramatically altered, changing the entire CNT morphology. Overall, plasma techniques have been demonstrated as a surface modification approach that is able to homogeneously modify a wide variety of surfaces without affecting their bulk properties [18, 26–27].

In recent years, plasma polymerization approaches have also been used as initial surface treatments to achieve functionalized surfaces, because of their capacity to modify all kinds of materials, even inert ones, and their ability to do so for all types of geometries.

Although some phenomena related to plasmas had already been described, Cookes first defined a plasma in 1879 as electrically charged gas molecules (however, it was Langmuir in 1923 who gave the name plasma to the fourth state of matter that occurs when a gas at low pressure is submitted to an electric field). Since then, many efforts have been undertaken in order to understand the plasma state better and also in order to use plasma as a surface processing tool. The microelectronics industry was the first driving force to develop plasma processes in the early 1960s for processing of surfaces, but nowadays, many other fields such

as biomedical, automotive, textile, and many others that deal with surface modification have adopted this technology [28].

Although a plasma is generally defined as a partially ionized gas very rich in charged and reactive species, different types of plasma may be obtained as a function of temperature and pressure. One of the most used classifications of plasmas is based on equilibrium versus nonequilibrium. Here the word *equilibrium* refers to thermal equilibrium among the species present in the plasma state. Nonequilibrium plasmas are commonly known as cold plasmas, while equilibrium plasmas are also known as thermal plasmas.

Equilibrium plasmas, known as thermal plasmas, are those in which the temperature is the same for all the species present in the plasma. The energy to ionize and activate the gas in this case comes from thermal heating, which can reach well above 10,000°C. A well-known example of equilibrium plasma in nature is the solar corona. These types of plasmas are mainly used in plasma spray, plasma torches, waste destruction, and welding applications. In nonequilibrium plasmas, also known as cold plasmas, electrons have a much higher temperature (around 30,000°C) than ions and neutrals, which allows those electrons to activate other species and produce ionization, excitation, and dissociation of molecules [29]. Because ions, atoms, and molecules cannot exchange heat with electrons, because of the fast movement of the latter, the former species remain almost at room temperature. As a consequence, this plasma features temperatures similar to room temperature, sometimes slightly higher but generally lower than 100°C. For this type of cold plasmas, the generation of an electric field at low pressures is usually required to activate the plasma. Before the electric field is applied, there are not many free electrons (10^{-11} to 10^{-12} e^- cm^{-3}), but their number increases once a voltage is applied to the system. The electrons are accelerated and produce excited species and molecular fragments, including new electrons (10^{-5} to 10^{-7} e^- cm^{-3}). If the pressure is too high, there are too many collisions and ion and excited species cannot be formed (or their lifetime is too short) to generate a stable plasma. Therefore, it can be said that plasma is a steady state because of the production of ionized and excited species and the recombination of these activated species. A natural cold plasma can be observed in the gorgeous *aurora borealis* or *northern lights*.

In recent developments, researchers have been successful in achieving glow discharges at atmospheric pressures under certain conditions [30]. Although the plasma temperature in this case is higher than that in the just introduced cold plasmas, they are far away from the thousands of degrees Celsius typical for thermal plasmas. Despite the restrictions inherent to

these atmospheric systems as we will present later, they constitute one of the main breakthroughs from the industrial point of view [31]. The main advantage of using nonequilibrium plasmas is clear: they allow for the treatment of materials that have a low thermal resistance and that would be damaged by other modification techniques such as a thermal plasma.

Being a gas, plasma enables the treatment of materials in different shapes and complex geometries including webs, tubes, and powders [32–34]. A plasma also introduces very high reactivity and unique chemistries that allow one to obtain final surface properties that could not be achieved by any other process. Moreover, the absence of solvents and the use of very low amounts of chemicals make plasma processes one of the most preferred treatments as far as environmental aspects are concerned. Because of the reasons presented here, plasmas have found a wider and wider use over the past years.

What kind of surface modifications are possible using plasma modification? Mainly, three different groups can be distinguished.

1. Etching or ablation, that is, removing of the substrate material itself. This can be used to obtain specific physical patterns and is exploiting the effect of positive ions in the plasma bombarding the substrate placed on the cathode in a plasma reactor [35].
2. Plasma deposition, also known as plasma-enhanced chemical vapor deposition (PECVD), occurs when the plasma contains reactive species that are able to react with each other (polymerize) and form thin films on the top of the substrate [29].
3. Plasma functionalization: In this case, the plasma species do not react among themselves but only with the substrate surface at specific positions only. It allows for functionalization while retaining the initial surface structure [36].

It is rather easy to treat flat surfaces with a nonequilibrium plasma [37, 32]. However, so much work has not been done yet on nonflat surfaces or powder materials. As most of the C-MEMS and C-NEMS structures correspond to the latter kind of complex surfaces, the next pages focus on the application of plasmas to the surface modification of powderlike materials.

7.3.1 LOW-PRESSURE PLASMA

As for other types of cold plasma reactors, reactors designed to treat powders have a number of internal parameters that define the composition

and activity of plasma. These internal parameters are listed in Table 7.1 and are determined by the external parameters imposed to the plasma reactor (presented in the same table). It is important to remember that in order to obtain reproducibility in different systems, external parameters have to be selected in order to obtain the same internal parameters.

Gas feed composition, gas flow rate, power density, and substrate position are the most frequently studied external parameters for a given reactor system that effect internal parameters such as gas species fragmentation degree, residence time of the species, and substrate ion bombardment, among others. In order to create an electric field that is able to generate plasma, an AC generator is needed. Most plasma sources use an AC generator at a radiofrequency of 13.56 or 27 MHz. Another AC source that is commonly used is a microwave generator at 2.53 GHz. Microwaves allow for working at higher pressures, thus enabling higher plasma densities.

Concerning the electrodes used to apply the electric field in a plasma reactor, different configurations can be found. Electrodes can be positioned either on the inside of the reactor, as is the case for all metallic reactors, or on the outside of the reactor, as is mostly the case for Pyrex and quartz reactors. In the case of powder treatment, the outer position is preferred as it avoids the powder from getting in direct contact with the

Table 7.1. Internal and external parameters for cold plasma characterization

Internal parameters	External parameters
- Fragmentation degree of the gas	- Pressure
- Density of neutrals	- Feed composition, flow rate, leaks
- Density of electrons and electron energy	- Field frequency
- Ionization degree	- Power density
- Residence time of the species	- Reactor configuration, materials, electrode geometry
- Process homogeneity	- Substrate position
- Positive ion bombardment, sputtering	- Duty cycle %, time on, time off in pulsed plasmas
- Deposition, etching, treatment rate	- Substrate temperature
- Contaminations	- Substrate bias potential

electrodes. Another useful configuration when dealing with powders is the use of a copper coil inductively coupled to the generator. With that, the powders are not in contact with the electrodes, preventing the damage of the plasma generator. In all cases, an impedance matching box is needed in order to effectively generate the plasma inside the reactor and minimize the reflected power.

It is also worth remembering here that an electron space charge sheet (giving rise to a negative bias) covers any surface immersed in a plasma. This effect causes the plasma bulk potential to be always higher than that of the surfaces in the reactor. Therefore, electrons are not accelerated to the surfaces but positive ions are. These accelerated ions may produce etching and surface ablation. In order to minimize this effect, the substrates and other surfaces may be grounded or connected to another radio frequency (RF) generator, avoiding this potential difference and minimizing the ion impact effect [38]. This bombardment avoidance is not possible when powders are being modified and, therefore, the etching and ablation effect of positive ions may be an important effect to be taken into account when working with powders.

As a consequence of the afore-explained effect, sample position is another important factor to take into account. The sample can be placed in the zone where the plasma is being generated, in which case the plasma effect on the substrate is characterized by a high ion bombardment and high fragmentation. But the sample can also be placed remote from the plasma generation region, in which case the bombarding effect is very low. The latter plasma treatments are less severe and, when using monomers, the substrate structure retention is much higher [39].

As already mentioned, cold plasma reactors are mainly designed to treat flat surfaces. However, some types of reactors have also been designed and adapted to treat powder materials. The first type of powders that researchers attempted to modify by plasma techniques was pigments in order to improve their dispersion [40–41]. Many other types of powder materials have been treated by low-pressure plasma (LPP). Both plasma deposition and plasma functionalization treatments have been introduced. It is worth to point out that the main powder characteristics that have to be taken into account in order to achieve a successful modification are particle size, geometry, density, agglomeration, and reactor capacity.

With the plasma principles introduced here, the surface modification of different carbonaceous materials are described in the following section. Special attention will be given to carbonaceous powders such as activated carbon, CB, carbon nanofibers, and CNTs.

7.4 SURFACE MODIFICATION OF CARBONACEOUS MATERIALS

Modification of carbonaceous materials, especially CB has been used for a long time in order to improve the final properties and behavior of this carbon powder material (see also Section 7.2). For instance, for CB reinforcing rubber applications, surface modifications have been used to maximize the interaction between the filler and the polymer chain in order to increase the final mechanical properties. But it is not only for rubber reinforcing that carbon surface modifications can play an important role, as will be described in this section, other applications, such as the use of carbon materials in inks and pigments and the use of this material as a catalyst support in electrochemical reactions, have also used this approach in order to improve performance.

In this section, we summarize some of the carbon surface treatments described in the literature. Wet and gas chemistries, as well as plasma techniques will be considered. Two main treatment groups can be distinguished: one is based on the grafting of polymer chains and polymer deposition on the surface (I) and the other is based on the functionalization of the surface (II), which involves elements such as oxygen, nitrogen, fluorine, and chlorine, among others.

7.4.1 GRAFTING AND POLYMER DEPOSITION ON CARBON MATERIALS

Several research groups have studied grafting on carbon materials using wet techniques. The group of Tsubokawa et al., for example, have reported on several wet techniques that can be used in order to graft polymer chains on the surface of CB. In most cases, the reactions sites are the carboxylic groups present at the surface. Graft processes are based in radical or ionic addition polymerization [42–43].

Some authors studied the effect of grafting hydrocarbon chains on carbonaceous materials, such as CB, with increasing C atom number (C_1 to C_{16}) in the chain. The final aim of the study was to evaluate the reinforcing properties of the CB on different types of rubber polymers. Although rheological experiments show a better dispersion of the modified filler because of a decrease in the thixotropic phenomena, the final mechanical properties of the CB-reinforced polymer were not improved. The effect is explained by the coverage of the most energetic sites of the carbon with the grafted chains, which prevented the chains from the polymeric matrix to interact with the filler [44, 45].

In the rubber reinforcement field, the idea to graft silane molecules to the surface of CB has also been studied. Silanes are used successfully to diminish the interaction between silica particles and, in some cases, link them covalently to the rubber polymer matrix. This process dramatically improves the performance of the final rubber goods [46]. However, this does not seem to be the case when CB is used as filler. Results reported by Wang et al. show that although some of the silane was chemisorbed on the surface of CB, most of it was only physisorbed and only on the most energetic zones of CB, probably because of the lack of functional groups that react with silane [47]. Yoon et al., who modified CB with amino-propyltrimethoxysilane and trimethoxy-*n*-propylsilane, presented similar results [48]. Changes in the dispersion were also observed in this case, but once again, improvements in the mechanical properties were not noticeable. In all the cases, the blocking of the most reactive sites on CB owing to the grafting process prevented good interaction with the polymer matrix.

Carbonaceous material grafting has also been applied in other fields. Cabot Corporation, for example, has proposed the modification of different carbon black in order to improve their behavior in water and organic-based inks. The modification consists in linking an ionic group to the surface of carbon black particles by means of an organic spacer. By changing the ionic group as well as the length of the organic spacer, the surface of CB can be tuned to obtain an optimal dispersion and suspension in all types of coating formulations [49]. Bergemann et al. reported CB surface modification by the reaction with maleic acid derivatives (at 180°C for 4 to 5 h) [50]. The final hydrophilicity of the carbonaceous material could be tuned as a function of the specific derivative that was used, and therefore, the interaction with several solvents could be adjusted.

It has to be pointed out, however, that the carbon surface modifications presented so far are often time consuming (from 5 to 10 hours) and they also need a washing step of the unreacted reagents as well as a drying step before the thus modified filler can be used in final applications.

Concerning plasma modification techniques, some grafting and polymerization deposition treatments on the surface of carbon materials have been reported. The group of Donnet et al. used a plasma reactor to modify CB with several reactive plasma gases. After the treatment, both the surface energy and surface topology were studied by scanning tunneling microscopy (STM) [51–52]. The amount of modified material was 0.2 g per batch. Schukin et al. were able to modify 0.1 g of several active carbons coming from eight different precursors in a rotating reactor with oxygen plasma in order to study the influence of the active carbon origin [53].

Three different types of CB were treated using the plasma method described earlier to obtain a fluorinated surface; the amount of treated

sample, however, was not reported [54], but they found the fluorination to be dependent on the CB surface structure. A study worth mentioning is the one performed by Favia et al. [55], who modified CB pellets in order to tune the surface acidity or basicity. In this case, up to 500 g of CB were modified in a batch in an oxygen and ammonia RF plasma. The size of carbon granules was in a range between 0.1 and 2 mm.

Brüsser et al. have also modified fibers such as carbon nanofibers with nitrogen and oxygen plasma treatments with the aim of improving their wettability. The treatments were performed on 1 g of carbon nanofibers of 100 to 300 nm in diameter and 10 to 100 μm in length [56].

Some attempts have been made by our own research group to modify carbon powder surfaces by plasma polymerization with acrylic acid (AA) as the reactive monomer [57]. CB was modified in a Bell-Jar reactor type at 40 W for 60 minutes and 0.2 mbar (pressure inside the reactor). The pH of a water dispersion of CB decreased from 7.5 to 4 after the deposition of AA. Moreover, the structure of CB remained unchanged as measured by Raman spectroscopy (this can be observed from Figure 7.1 where the main Raman peaks corresponding to the CB crystallites show no differences between treated and untreated samples). When the surface energy was evaluated by means of inverse gas chromatography (IGC), both dispersive (hydrophobic) as well as specific components (polar) were diminished as can be seen in Table 7.2.

The modified CBs were mixed with different rubber polymers. The dynamic mechanical analysis results obtained from filled compounds

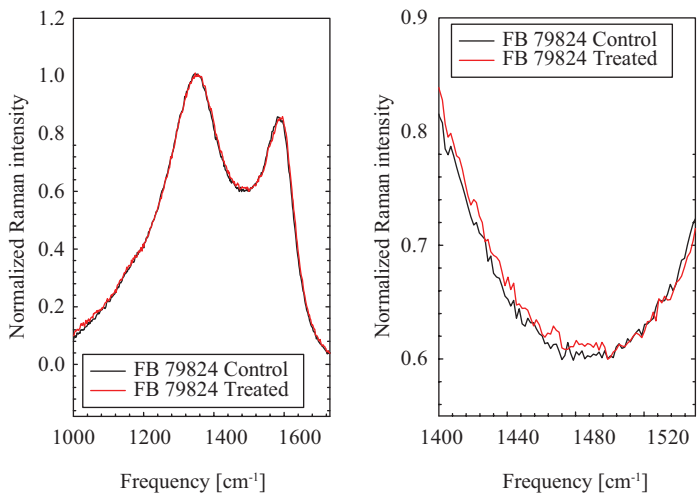

Figure 7.1. Raman spectra of unmodified CB and after AA deposition by cold plasma.

Table 7.2. Surface energy for unmodified CB and after AA deposition

	Total surface energy (mJ/m^2)	**Dispersive component γ_s^d (mJ/m^2)**	**Specific component γ_s^{sp} (mJ/m^2)**
Unmodified CB	778	608	170
AA-CB	333	250	83

showed that the AA polymer deposition decreased the power of CB reinforcement. This effect was attributed, as it was in the previous cases, to the coverage of the CB surface active sites, which were no longer able to interact with the rubber. The deposited AA polymer did not have enough long chains to cause entanglements with the polymer matrix to increase the filler–polymeric matrix interaction.

The effect of CB coverage to the detriment of CB reinforcement ability was also observed by Akovali et al. after modifying CB with styrene and butadiene vapor plasma [58]. Shyoama et al. used plasma polymer deposition using C_2F_6 as plasma reactive monomer in order to cover carbon material at 40 W for 60 mins. at 0.8 mbar of pressure inside the reactor and an RF frequency of 13.56 MHz. CB was used thereafter as platinum catalyst support for the oxygen reduction reaction in the anode of a polymer membrane fuel cell. Improvements in the reaction rate as well as in the lifetime of platinum as a catalyst were observed; the hydrophobicity as well as the affected electronic state of the Pt particles are thought to be the consequence of the CF_3 groups introduced on the CB surface [59].

As a conclusion, one can say that both carbon material grafting and polymer deposition can be very useful in surface modification applications, where these processes help to improve the carbon particle dispersion in different media and to change the final surface activity of the carbon-based material. However, these carbon modifications do not seem to be useful for reinforcing applications. This result is a consequence of the coverage of the high-energetic carbon sites, which play a very important role in the filler–polymer interaction. Therefore, other approaches such as trying to functionalize CB surface without annihilating the high-energy sites could be interesting in order to improve CB behavior in this application.

7.4.2 FUNCTIONALIZATION ON THE SURFACE OF CARBONLIKE MATERIALS

This section deals with functionalization of carbon materials. Some of the surface modifications studied in the literature have been carried out in

order to gain fundamental insights into the surface and interior of carbon structures, while others were implemented to achieve a performance improvement. The functionalization treatments have been divided here into four main groups: (1) oxidation, (2) nitration, (3) other functionalization treatments and (4) CNT functionalization.

7.4.2.1 Carbon Surface Oxidation

Oxidation of carbon materials has been widely studied in order to not only change their hydrophilicity but also, as mentioned earlier, elucidate their structure by means of studying the reaction of oxygen with the carbonaceous material. The latter was the case of one of the earliest works on this topic, where CB was progressively oxidized in hot air [60]. It was observed that CB particles oxidation took place preferably in the bulk, meaning that the bulk portion was more susceptible to burning than the surface. As a consequence, it was assumed that the inner part of the particle was formed by a less-ordered carbon structure than that found at its surface. This hypothesis was confirmed by small angle neutron scattering experiments [61].

From that time on, many oxidation treatments of carbon materials have been described using several types of oxidizing agents with acids such as HNO_3, ozone, KOH, and hydrogen peroxide, among others [62–64]. Although all these treatments successfully increased the level of oxygen on the surface of carbon, they also produced changes in the surface microstructure and morphology. Often, the use of the same oxidation reagent led to contradictory results about the changes produced in specific surface area, measured by the Brunauer–Emmett–Teller method, and the microporosity. For example, Krishanankutty et al. reported that CB presented a lower specific surface area and lower microporosity after being modified with HNO_3 (15.8N during 6 h at 100°C) [65]. Park et al. also reported a drastic decrease in specific surface area after H_3PO_4 modification [66]. However, other groups have found that the specific surface area remained at a constant value after HNO_3 (0.3M at 95ºC for 6 h) modification or even increased because of microporosity formation [67].

It was also reported that oxidation in hot air led to an increase in the oxygen content on the carbonaceous surface. Similar results on specific surface as the ones obtained for HNO_3 (15.8N during 6 h at 100°C) oxidation [68–69] were obtained, but in some occasions, a decrease in the total oxygen content on the CB surface was described [67]. Chen et al. studied the difference between ozone and molecular oxygen carbon oxidation; while

molecular oxygen is believed to attack only selective positions such as crystallite edges, ozone seems to attack the whole surface. The same study showed that while molecular oxygen produced an increase in the specific surface area, because of microporosity formation, it remained unchanged after the ozone treatment [69]. Other ozone modification studies showed that specific surface area decreased for treatments below 150°C but increased for higher temperatures [70].

Given the many contradictory results, a clear mechanism for the oxidation of carbon has not been presented yet and the influence of the reaction parameters such as acid concentration, reaction duration, CB grade, and temperature, among others, seem to be crucial to obtain reproducibility and avoid changes in CB structure and morphology.

Oxidized CB has been tested for many different applications. As early as 1969, Cotten used ozone or air and HNO_3 (at 120°C) oxidized CB in order to observe changes in the vulcanization reaction because of the presence of the oxidized groups on CB surface. [71]. Later on, during the 1990s, several research groups studied the effect of oxidized CB in different polymer matrixes. Belmont et al. introduced oxygen functionalities on the CB surface by reacting it with phosphines and phosphates; it is thought that peroxide groups are introduced on the surface of CB during these reactions. However, because phosphine solutions are air sensitive, experiments must be carried out under inert atmosphere [72]. In several works, researchers studied the interaction of CB in polymer matrixes containing oxygen groups such as epoxydated natural rubber and carboxylated nitrile rubber [73–74]. In some cases, the use of a silane coupling agent was also evaluated for the same application [75]. Improvements were found when the CB loading was higher than 80 parts per 100 parts of the polymer (phr) and an optimal silane content was 4 phr, as higher amounts initiated plasticizing effects. In 1998, it was demonstrated that oxygen on the CB surface decreases the cross-linking level when butyl rubber was vulcanized in a peroxide system, probably because of the interaction of the peroxide compound with the oxygen groups on the surface of the CB [76].

Contrary to the grafting process, carbonaceous material functionalization seems to have a positive effect in reinforcing applications. This reinforcing effect depends on the polarity of the polymer matrix and the interaction of the carbonaceous materials with other ingredients of the compound formulation.

Carbon oxidation seems also a good way to improve electrochemical properties of the material. For instance, Sosa et al. oxidized CB with several reagents such as H_2O_2, HNO_3 hot air, and humid ozone. The

first two methods increased the surface oxygen content and the surface negative charge. As a consequence, catalysts such as adsorbed catalase and iron porphyrins preserve a higher planarity and, therefore, a higher activity for H_2O_2 decomposition. Treatment of the carbonaceous material with hot air did not produce an increase in surface oxygen, while when using humid ozone, the oxygen concentration increased for short periods and subsequently decreased [67]. CB and carbon filaments have also been modified with hot air and acid medium (HCl and HNO_3 differently) in order to improve the electrochemical catalytic effect of these materials [77]. From the two processes, the hot air treatment gave the best performance enhancement in terms of surface-oxidation-induced reversibility of the $Fe(CN)_6^{3-/4-}$ redox reaction. Wang et al. used ozone to improve the activity of Pt catalyst supported on CB for oxygen reduction in a direct methanol fuel cell (DMFC). Ozone modification studies were performed in a temperature range from 60°C to 180°C [71]. An optimal treatment to increase the platinum activity was found to be 6 mins. at 140°C.

An interesting industrial application of wet oxidation of CB, a process used by many companies (Cabot Corporation, Degussa, Columbian Carbon among others), is the improvement of its dispersion in water for inks, as described in several patents [78–80].

It seems that in all the studies, we were able to find that wet oxidation treatments produced oxidation at preferential positions on the carbon surface only, including amorphous structures and crystalline edges, while basal graphitic planes only reacted in more aggressive conditions that provoked severe changes in the carbon particles. In contrast, the use of ozone in the gaseous state induces a more homogeneous oxidation with lower structural changes.

The use of oxygen plasma to modify CB surfaces has also been studied. However, it is still not clear in this case whether the oxidation of CB in an oxygen plasma attacks preferential sites such as crystallite edges or if the oxidation is nonpreferential as in the case of ozone.

The oxidation process of CBs in a microwave plasma reactor has also been investigated. Although the reactor was not adapted to treat powders and only very small amounts of CB were processed, some very interesting results were found. CB was treated at 2.45 GHz, with a power setting of 150 W for 35 mins. A comparative study using oxygen plasma and molecular oxygen on several carbon types showed that the resulting reactivity is different in those two media; while molecular oxygen oxidizes preferably activated carbon, showing a higher reactivity for noncrystalline structures, plasma oxidation was very reactive with the crystalline phase of CB. This could give a hint that oxygen plasma could modify the graphitic

structures. The latter hypothesis was confirmed by the successful modification of graphitized CB using oxygen plasma in a microwave setting [81–82]. In another study, using STM and atomic force microscopy, it was shown that CB, after such an oxygen plasma treatment, was oxidized homogeneously all over the particle [51, 83].

Takada et al. used an RF reactor at 13.56 MHZ and a 50 W power setting with different treatment durations (from 5 to 480 mins.) to study high-specific-surface CB oxidation. It was shown that surface oxygen content was enhanced for the first 120 mins. of this treatment, thereby increasing the total weight of the carbon; however, subsequently, the oxygen content is decreased and carbon gasification took place. The main functionalities found were C=O, O–C–O, and O–C=O [84].

The use of plasma-oxidized carbon material has been tested in several applications. Li et al., for example, showed that the electrochemical properties of carbon powder were improved after plasma oxidation as tested by H_2O_2 decomposition capability. This group used an RF (13.56 MHz) Bell-Jar reactor where CB was deposited in a vibrating tray. Reaction took place at 15 W for 10 mins. [85].

Summarizing, oxygen plasma treatment is a good way to introduce oxygen species on carbon surfaces without producing other important structural changes. However, it has to be pointed out that no continuous or atmospheric plasma reactor treatments have been described yet and this is a needed step if production is to be scaled up to an industrial level.

7.4.2.2 Carbon Surface Nitrogen Enrichment

Surface nitration and amination is quite a common topic for polymer surfaces where these processes are used to enhance polymer adhesion [86] biocompatibility and cell adhesion [87]. In Figure 7.2, a picture with the main surface modification using nitrogen plasma and oxygen plasma on a polymeric surface can be seen. Nitrogen surface modification has not been deeply studied on carbon materials. Few works we found on this topic are summarized next.

Cataldo used N_2O_3, NO, and N_2O_4 to introduce nitro and nitrous groups on the surface of carbon. He found that the carbon structure remained unaffected as revealed by Raman spectroscopy [88].

Some early works from Loh, report about the use of an ammonia plasma, nitrogen, and nitrogen–hydrogen mixtures on CB. Modification with ammonia plasma was carried out with a power setting of 100 W for 30 mins. using 0.1 g of CB at 1 mbar of internal pressure. A mixture of

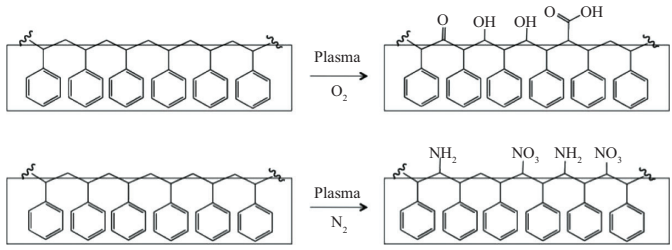

Figure 7.2. Scheme of the main groups formed on a polymeric surface (polystyrene) after nitrogen and oxygen plasma treatments.

N_2:H_2 was also used (1:2) under the same operational conditions; however, the nitrogen content on the final surface was in this case lower than when using the ammonia plasma [89].

Park et al. also used nitrogen plasma in order to modify the surface of different carbonaceous materials. In this case, an RF (13.56 MHz) reactor at 30 W from 0 to 30 mins. at 1 mbar of internal pressure. Structural changes in the crystallinity of the surface and energetic changes were observed but no applications were evaluated in this work [90]. Kima et al. used a nitrogen plasma to modify CB for support of a platinum catalyst in DMFC. CB was modified in an RF (13.56 MHz) reactor at a power setting of 300 W. It was found that a treatment of 30 secs. was optimal to increase the platinum activity toward methanol oxidation. New functional groups on the CB surface were found to be C–N, C=N, $–NH_3^+$, –NH, and =NH [91].

Ammonia plasmas have been used to modify other carbon powders such as CNT and carbon nanofibers. The group of Felten et al. modified CNTs in an RF (13.56 MHz) LPP reactor at 30 W and 0.1 mbar of internal pressure for 30 mins. Imine, amine, nitrile, and amide groups were found on the CNT surface after this modification procedure [92]. Brüser et al. modified carbon nanofibers in a plasma reactor at 0.01 mbar using NH_3. No dependence of surface composition on the nanofibers surface on the plasma power was found between 50 and 80 W, while the nitrogen content decreased when the internal pressure of the reactor was lower than 0.01 mbar [56].

7.4.2.3 Other Carbon Functionalization Treatments

In this section, we discuss the functionalization of carbon surfaces with species different from O and N. Attempts at introducing sulfurated species

on the surface of different carbon species is the first case in point. In this case, the presence of sulfur at the carbon surface was expected to take part in the cross-linking by sulfur vulcanization. Some first results in this respect were presented by Papier et al. who studied the introduction of sulfur at the surface of CB by oxidation of CB using $ClSO_3H$ and C_4H_9SH [93]. The increase in the sulfur concentration on the surface was around 0.15 percent. Later, studies by Gajewski et al. demonstrated a higher cross-link density and better tear properties when the sulfur content on the CB surface is higher. In this case, the CB was modified by means of S_8, CS_2, SO_2, and H_2S, and it was found that the most reactive species was SO_2 and the less reactive was H_2S [94].

Introduction of other heteroatoms on the surface of carbon has also been studied. The group of Tressaud et al. studied the fluorination of different carbon surfaces in detail. Reaction conditions for fluorination were analyzed as a percentage of F_2 gas and as a function of the pretreatment of the carbon material with O_2. The latter increases the F content on the surface. Similar studies were performed by the same group in a CF_4 plasma using an RF (13.56 MHz) reactor with a power range from 40 to 100 W and a treatment duration between 10 and 30 minutes. Under these conditions, fluorination was found to be dependent on the carbon structure: with a more crystalline structure favoring the formation of fluorine graphite while more disordered structures promoted the formation of CF_x groups [95–98].

Cl and Br have been also introduced on the surface of carbons. Br atoms, for example, were introduced by using liquid reagents (Br_2 dissolved in CCl_4) and bromine vapors at 120°C. A similar method was used to introduce Cl on carbon surfaces; Cl_2 was bubbled through CCl_4, and thereafter, this mixture was carried over the carbonaceous material at 450°C [97]. In both the cases, the specific surface energy component was increased (measured with IGC): 6.7 percent of bromine and 6.9 percent of chlorine on the carbon surface.

7.4.2.4 Specific Surface Treatments for CNTs

CNTs are one of the more extensively studied carbon allotropes. Existing strategies for proper dispersion of CNTs in aqueous media include covalent modification by various grafting reactions and noncovalent adsorption or wrapping with functional molecules with surfactant nature [97–98]. Covalent modification treatments have been shown to induce a large number of defects into the graphene structure, which may lead

to alteration of its properties. In contrast, noncovalently modified CNTs may suffer ligand- or surfactant-exchange reactions with proteins and other components of biological media, leading to the formation of large aggregates [99]. Furthermore, the density of the modifying groups on the surface of CNTs is often inadequate. The latter limits the packing of therapeutically active molecules, such as nucleic acids, and the presentation and display of biological ligands, which is a key factor in assay and sensor applications where a high biological specificity is required. Therefore, the development of new coating strategies of CNTs requires more investigation.

In general, two main modification strategies have been developed for the covalent functionalization of CNTs: (i) amidation and esterification of oxidized CNTs and (ii) addition reactions.

The treatment of CNTs under strong acidic and oxidizing conditions is a common method for the generation of oxygen-containing functional groups. Typically, prolonged heating or sonication of CNTs using strong acids, such as concentrated sulfuric or nitric acid or mixtures of sulfuric and nitric acid or sulfuric acid and hydrogen peroxide, results in the formation of hydroxyl, carbonyl, and especially carboxyl groups on the sidewalls and, predominantly, on the tips of CNTs [2, 100]. Carboxylic acids generated by oxidative methods on CNTs can be further modified to produce ester or amide derivatives via reaction with alcohols and amines, respectively. Amidation and esterification reactions can be performed using standard methods, such as activation of carboxylic acids via acid halides or carbodiimide-mediated coupling. Several strategies leading to solubilization of CNTs in organic solvents have been reported, mainly through esterification or amidation reactions between oxidized CNTs and long-chain alcohols or amides, respectively [48]. The resulting alkyl chains present on the CNTs surface act as solubilizing agents and the derivatized nanotube becomes soluble in most organic solvents. However, most biological applications require the conjugation of rather hydrophilic ligands that promote dispersion of functionalized CNTs in biological media or aqueous solutions. To increase water dispersion, oxidized CNTs have been modified via activation of their carboxylic acids using thionyl chloride or oxalyl chloride with a wide range of hydrophilic moieties, such as small molecules, hydrophilic polymers, proteins, and nucleic acids [101–103]. Macromolecules, such as proteins and nucleic acids, have also been explored as modifying moieties for the solubilization of CNTs in aqueous solutions or biological media [104–105]. The same procedure was also used for the covalent conjugation of DNA strands bearing a nucleophilic primary amine at the 5′ and 3′ ends [106–107]. Additionally, biopolymers, such as chitosan, have

been covalently grafted to acid-functionalized single- and multiwalled CNTs via the reaction of their acyl chloride derivatives with suitable amines present on this kind of biopolymers [108–109]. In addition to biopolymers, covalent grafting of hydrophilic polymers is a popular strategy for increasing the water dispersion of CNTs. Pegylation, which consists of the covalent attachment of poly (ethylene glycol) polymer chains to proteins and nanoparticles, is a common strategy used to improve the biocompatibility of such nanostructures [110–112]. Similarly, other works have reported CNT grafting of other highly water-soluble polymers, such as poly(vinyl alcohol), poly(*m*-aminobenzene sulfonic acid), or poly (propionylethylenimine-*co*-ethylenimine), to improve compatibility in biological media [113–115].

In contrast to postmodification of carboxylic groups generated on CNTs by oxidative processes, which take place mainly at the CNT ends and sidewall defects, functionalization of the sidewalls of CNTs is more difficult to accomplish. The different reactivity toward covalent chemical modification of defect-free CNT sidewalls requires the use of more reactive species. Research on fullerenes has revealed that it is the curvature of the fullerene molecule that drives the reactivity of addition reactions. Increased curvature of the carbon network results in an enhanced or increased pyramidalization of the sp^2-hybridized C atoms, which makes addition reactions on carbon–carbon double bonds more favorable. However, CNTs consist of graphitic sidewalls that do not present strongly curved regions in comparison to fullerenes. Therefore, functionalization of the sidewalls via addition reactions is less favorable, and it is only possible or achieved by more reactive species, such as nitrenes, carbenes, and radicals. In reality, CNTs always contain defects though, so it is likely that even in this case, addition reactions take place preferentially at defect sites [116–117]. Functionalization of both single- and multiwalled CNTs via addition reactions to render them water soluble has been achieved in both native and premodified CNTs. The [2 + 1] cycloaddition of nitrenes is a popular route for derivatizing CNTs in order to improve their solubility and making them more amenable for biological applications. A variety of hydrophilic functional groups, such as crown ethers and poly(ethylene glycol), and different types of sugars (glucose, galactose and mannose) have been successfully attached onto CNTs resulting in water-soluble conjugates [118–119].

A simple method for obtaining water-soluble CNTs was developed by Prato and colleagues [120]. Their method is based on 1,3-dipolar cycloaddition reactions of azomethine ylides generated in situ by thermal condensation of α-aminoacids and aldehydes (see Figure 7.3).

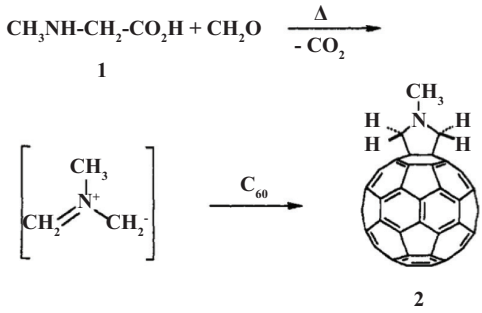

Figure 7.3. Reaction of azomethine ylides on C60 fullerenes as suggested in reference [120].

1,3-Cycloaddition on CNTs produces substituted pyrrolidine fused rings on the surface of CNTs, which are amenable for further functionalization. The use of hydrophilic a-aminoacids, such as pegylated α-aminoacids, is an interesting approach for obtaining water-soluble CNTs [121]. Functionalized oligoethylene glycol chains have shown to be particularly suitable for the covalent immobilization of biomolecules such as aminoacids on CNTs [122–124].

Another attractive way of functionalizing CNTs is by free-radical addition, which is a widely used one-step method for the derivatization of CNT sidewalls. In general, carbon radicals generated by various methods, such as photochemically, thermally, or via oxidation–reduction reactions, react covalently with CNTs to form conjugates [125–129].

Alternatively, PECVD appears to be an interesting technique in which polymer chains can be grown directly onto the surface of CNTs. This approach provides superior surface coverage and involves the covalent attachment of moieties that can initiate a polymerization reaction such as monomers or initiators. As described in previous sections, over the past couple of decades, plasma polymerization approaches have been optimized as a surface treatment to achieve covalently functionalized surfaces with a high degree of specificity, density of active groups, and versatility. It allows for the modification of all kinds of materials and geometries without affecting their intrinsic properties (see Section 7.3) [18, 26, 27]. Besides its versatility, this technique is a dry process and thus avoids the use of wet chemistry limiting the generation of chemical residues. As a result, with PECVD, one is able to modulate the modification of CNTs and any other surface in a tailored and controlled way.

However, there are still some drawbacks that need to be addressed. In some studies performed by Vohrer et al., the hydrophilization of

CNT sheets (called buckypapers) by plasma treatment with different nonpolymerizable monomer gases, including their possible postreactions, was studied [22]. These authors achieved a gentle surface modification of CNTs by treating them with N_2 gas in a cold plasma reactor followed by an oxidation posttreatment. Their treated CNTs showed a high increase in solubility, reducing the 150° water contact angle of the unmodified buckypapers to 10° for oxidized ones. With this treatment, no alteration of CNT morphology was observed. Nonetheless, X-ray photoelectron spectroscopy results revealed a constant decrease in the oxidation degree of the CNTs over time, eventually losing the functionality achieved. This phenomenon may have a negative effect when these nanoparticles have to be used in biomedical applications. Chen et al. used the polymerization of two types of monomers, acetaldehyde and ethylenediamine, in order to permanently immobilize different types of polysaccharides and thus provide highly hydrated coatings on the CNT surface [14]. Although this approach allows the formation of highly hydrophilic and soluble CNTs without significant changes in the nanotube's structure integrity, it involved complicated and costly multistep reactions before the desired properties of the CNTs were achieved. Nonetheless, this study showed how plasma polymerization results in a promising technique to homogeneously modify CNT surfaces. This statement was confirmed in the work by Ávila-Orta et al., where thin PPEG (plasma polyetylene glycol) layers (1 to 3 nm thick) were deposited on CNTs [130]. They used sensitive techniques such as high-resolution transmission electron microscopy and Fourier-transform infrared spectroscopy to study the structure and morphology of their polymer films. Moreover, they proved that this plasma coating provided the needed hydrophilicity in order to disperse the modified nanotubes in water, methanol, and ethylene glycol, maintaining a dispersion stability over time. Therefore, the deposition of a polymer coating that can provide chemical reactive sites for the specific anchoring of active molecules may become highly promising, as was stated earlier.

7.5 CONCLUDING REMARKS

In this chapter, different methods to modify the surface of carbonaceous materials have been presented. It seems clear that the technologies (both wet chemistry and plasma based) presented here can be used to tailor the properties of a wide range of carbon allotropes. Most of these methods, because of their versatility, can then also be applied to a wide variety of

C-MEMS and C-NEMS applications. However, there is still a lack of carbon surface modification methods that are scalable to an industrial level using economic and environmental sustainable processes.

REFERENCES

[1] Cifuentes-Rius, A., A. de Pablo, V. Ramos-Pérez, and S. Borrós. 2014. "Tailoring Carbon Nanotubes Surface for Gene Delivery Applications." *Plasma Processes and Polymers* 11, no. 7, pp. 704–13. doi: http://dx.doi.org/10.1002/ppap.201300167

[2] Chen, J., Q. Chen, and Q. Ma. 2012. "Influence of Surface Functionalization via Chemical Oxidation on the Properties of Carbon Nanotubes." *Journal of Colloid and Interface Science* 370, no. 1, pp. 32–38. doi: http://dx.doi.org/10.1016/j.jcis.2011.12.073

[3] Chen, R.J., Y. Zhang, D. Wang, and H. Dai. 2001. "Noncovalent Sidewall Functionalization of Single-Walled Carbon Nanotubes for Protein Immobilization." *Journal of the American Chemical Society* 123, no. 16, pp. 3838–39.

[4] Bianco, A., R. Saiz, S. Li, H. Dumortier, L. Lacerda, K. Kostarelos, S. Giordani, and M. Prato. 2008. *Medicinal Chemistry and Pharmacological Potential of Fullerenes and Carbon Nanotubes* Vol. 1, eds. F. Cataldo and T. Ros, 23–50. Netherlands: Springer.

[5] Balasubramanian, K., and M. Burghard. 2005. "Chemically Functionalized Carbon Nanotubes." *Small* 1, no. 2, pp. 180–92. doi: http://dx.doi.org/10.1002/smll.200400118

[6] Hirsch, A. 2002. "Functionalization of Single-Walled Carbon Nanotubes." *Angewandte Chemie International Edition* 41, no. 11, p. 1853. doi: http://dx.doi.org/10.1002/1521-3773(20020603)41:11%3C1853::aid-anie1853%3E3.0.co;2-n

[7] Liu, Y., C. Chipot, X. Shao, and W. Cai. 2010. "Solubilizing Carbon Nanotubes Through Noncovalent Functionalization. Insight from the Reversible Wrapping of Alginic Acid Around a Single-Walled Carbon Nanotube." *The Journal of Physical Chemistry B* 114, no. 17, pp. 5783–89. doi: http://dx.doi.org/10.1021/jp9110772

[8] Ntim, S.A., O. Sae-Khow, F.A. Witzmann, and S. Mitra. 2011. "Effects of Polymer Wrapping and Covalent Functionalization on the Stability of MWCNT in Aqueous Dispersions." *Journal of Colloid and Interface Science* 355, no. 2, pp. 383–88. doi: http://dx.doi.org/10.1016/j.jcis.2010.12.052

[9] Petrov, P., F. Stassin, C. Pagnoulle, and R. Jerome. 2003. "Noncovalent Functionalization of Multi-Walled Carbon Nanotubes by Pyrene Containing Polymers." *Chemical Communications*, no. 23, p. 2904. doi: http://dx.doi.org/10.1039/b307751a

[10] Sun, Y.-P., K. Fu, Y. Lin, and W. Huang. 2002. "Functionalized Carbon Nanotubes: Properties and Applications." *Accounts of Chemical Research* 35, no. 12, pp. 1096–104. doi: http://dx.doi.org/10.1021/ar010160v

[11] Vaisman, L., H.D. Wagner, and G. Marom. 2006. "The Role of Surfactants in Dispersion of Carbon Nanotubes." *Advances in Colloid and Interface Science* 128–130, pp. 37–46. doi: http://dx.doi.org/10.1016/j.cis.2006.11.007

[12] Bahr, J.L., and J.M. Tour. 2002. "Covalent Chemistry of Single-Wall Carbon Nanotubes." *Journal of Materials Chemistry* 12, no. 7, pp. 1952–58. doi: http://dx.doi.org/10.1039/b201013p

[13] Dyke, C.A., and J.M. Tour. 2004. "Covalent Functionalization of Single-Walled Carbon Nanotubes for Materials Applications." *The Journal of Physical Chemistry A* 108, no. 51, pp. 11151–59. doi: http://dx.doi.org/10.1021/jp046274g

[14] Chen, C., A. Ogino, X. Wang, and M. Nagatsu. 2010. "Plasma Treatment of Multiwall Carbon Nanotubes for Dispersion Improvement in Water." *Applied Physics Letters* 96, no. 13, p. 131504. doi: http://dx.doi.org/10.1063/1.3377007

[15] Chen, Q., L. Dai, M. Gao, S. Huang, and A. Mau. 2001. "Plasma Activation of Carbon Nanotubes for Chemical Modification." *The Journal of Physical Chemistry B* 105, no. 3, pp. 618–22. doi: http://dx.doi.org/10.1021/jp003385g

[16] Duque, L., B. Menges, S. Borros, and R. Förch. 2010. "Immobilization of Biomolecules to Plasma Polymerized Pentafluorophenyl Methacrylate." *Biomacromolecules* 11, no. 10, pp. 2818–23. doi: http://dx.doi.org/10.1021/bm100910q

[17] Francesch, L., S. Borros, W. Knoll, and R. Förch. 2007. "Surface Reactivity of Pulsed-Plasma Polymerized Pentafluorophenyl Methacrylate (PFM) toward Amines and Proteins in Solution." *Langmuir* 23, no. 7, pp. 3927–31. doi: http://dx.doi.org/10.1021/la062422d

[18] Francesch, L., E. Garreta, M. Balcells, E.R. Edelman, and S. Borrós. 2005. "Fabrication of Bioactive Surfaces by Plasma Polymerization Techniques Using a Novel Acrylate-Derived Monomer." *Plasma Processes and Polymers* 2, no. 8, pp. 605–11. doi: http://dx.doi.org/10.1002/ppap.200500042

[19] Khare, B.N., P. Wilhite, R.C. Quinn, B. Chen, R.H. Schingler, B. Tran, H. Imanaka, C.R. So, C.W. Bauschlicher, and M. Meyyappan. 2004. "Functionalization of Carbon Nanotubes by Ammonia Glow-Discharge: Experiments and Modeling." *The Journal of Physical Chemistry B* 108, no. 24, pp. 8166–72. doi: http://dx.doi.org/10.1021/jp049359q

[20] Garreta, E., N. Tricás, L. Quintana, C.E. Semino, and S. Borrós. 2006. "Plasma Polymerization on Hydroxyapatite Powders to Increase Water Dispersability for Biomedical Applications." *Plasma Processes and Polymers* 3, no. 6–7, pp. 553–61. doi: http://dx.doi.org/10.1002/ppap.200600036

[21] Tseng, C.H., C.C. Wang, and C.Y. Chen. 2006. "Modification of Multi-Walled Carbon Nanotubes by Plasma Treatment and Further Use as Templates for Growth of CdS Nanocrystals." *Nanotechnology* 17, no. 22, pp. 5602–12. doi: http://dx.doi.org/10.1088/0957-4484/17/22/013

[22] Vohrer, U., N.P. Zschoerper, Y. Koehne, S. Langowski, and C. Oehr. 2007. "Plasma Modification of Carbon Nanotubes and Bucky Papers." *Plasma Processes and Polymers* 4, no. S1, pp. S871–77. doi: http://dx.doi.org/10.1002/ppap.200732102

[23] Dai, H. 2002. "Carbon Nanotubes: Synthesis, Integration, and Properties." *Accounts Chemical Research* 35, no. 12, pp. 1035–44. doi: http://dx.doi.org/10.1021/ar0101640

[24] Balasubramanian, K., and M. Burghard. 2005. "Chemically Functionalized Carbon Nanotubes." *Small* 1, no. 2, pp. 180–92. doi: http://dx.doi.org/10.1002/smll.200400118

[25] Tasis, D., N. Tagmatarchis, A. Bianco, and M. Prato. 2006. "Chemistry of Carbon Nanotubes." *Chemical Reviews* 106, no. 3, pp. 1105–36. doi: http://dx.doi.org/10.1021/cr050569o

[26] Chu, P.K., J.Y. Chen, L.P. Wang, and N. Huang. 2002. "Plasma-surface Modification of Biomaterials." *Materials Science and Engineering: R: Reports* 36, no. 5–6, pp. 143–206. doi: http://dx.doi.org/10.1016/s0927-796x(02)00004-9

[27] Förch, R., Z. Zhang, and W. Knoll. 2005. "Soft Plasma Treated Surfaces: Tailoring of Structure and Properties for Biomaterial Applications." *Plasma Processes and Polymers* 2, no. 5, pp. 351–72. doi: http://dx.doi.org/10.1002/ppap.200400083

[28] BMBF, German Federal Ministry of Education and Research. 2001. *Plasma Technology: Process Diversity and Sustainability.* Bonn: BMBF.

[29] Yasuda, H. 1985. *Plasma Polymerization*. Orlando, FL: Academic Press.

[30] S. Kanazawa, M. Kogoma, T. Moriwaki, and S. Okazaki. 1988. "Stable Glow Plasma at Atmospheric Pressure." *Journal of Physics D: Applied Physics* 21, no. 5, 838–45. doi: http://dx.doi.org/10.1088/0022-3727/21/5/028

[31] VDI Technologiezentrum GmbH. 2004. *Evaluierung Plasmatechnik.* Düsseldorf.

[32] Hudec, I., and M. Jaso. November 2006. "Influence of Plasma Polymerization on Adhesion of Polyester Cords to Rubber Matrix." Presented at the KHK, Hannover, Germany.

[33] Bretagnol, F., M. Tatoulian, F. Arefi-Khonsari, G. Lorang, and J. Amouroux. 2004. "Surface Modification of Polyethylene Powder by Nitrogen and Ammonia Low Pressure Plasma in a Fluidized Bed Reactor." *Reactive and Functional Polymers* 61, no. 2, pp. 221–29. doi: http://dx.doi.org/10.1016/j.reactfunctpolym.2004.06.003

[34] Pappas, D., A. Bujanda, J.D. Demaree, J.K. Hirvonen, W. Kosik, J. Jensen, and S. McKnight. 2006. "Surface Modification of Polyamide Fibers and Films Using Atmospheric Plasmas." *Surface and Coatings Technology* 201, no. 7, pp. 4384–88. doi: http://dx.doi.org/10.1016/j.surfcoat.2006.08.068

[35] Norton, D.P., and S. Pearton. 2005. "Dry Etching of Electronic Oxides, Polymers, and Semiconductors." *Plasma Processes Polymers* 2, no. 1, pp. 16–37. doi: http://dx.doi.org/10.1002/ppap.200400035

[36] Meyer-Plath, A.A., K. Schröder, B. Finke, and A. Ohl. 2003. "Current Trends in Biomaterial Surface Functionalization—Nitrogen-Containing Plasma Assisted Processes with Enhanced Selectivity." *Vacuum* 7, no. 3, pp. 391–406. doi: http://dx.doi.org/10.1016/s0042-207x(02)00766-2

[37] Gupta, B., J. Hilborn, C. Hollenstein, C.J.G. Plummer, R. Houriet, and N. Xanthopoulos. 2000. "Surface Modification of Polyester Films by RF Plasma." *Journal of Applied Polymer Science* 78, no. 5, pp. 1083–91. doi: http://dx.doi.org/10.1002/1097-4628(20001031)78:5%3C1083::aid-app170%3E3.0.co;2-5

[38] Fracassi, F. 2005. "Lecture at International Symposium on Plasma Chemistry (ISPC 17)." Low Pressure Plasma Summer School, Toronto, August.

[39] Borros, S., L. Picazo, N. Ferrer-Anglada, Y. Takhtoukh, and J. Esteve. 1999. "Plasma Polymer Thin Films Obtained by Plasma Polymerization of Pyrrole." *Journal de Physique IV* 9, no. PR8, pp. 461–69. doi: http://dx.doi.org/10.1051/jp4:1999858

[40] Tsusui, K., K. Nishizawa, and S. Ikeeda. 1988. "Plasma Surface Treatment of an Organic Pigment." *Journal Coatings of Technology* 69, no. 765, pp. 107–12.

[41] Ihara, T., S. Ito, and M. Kiboku. 1986. "Low Temperature Plasma Oxidation Treatment of Several Organic Pigments." *Chemistry Letters* 5, pp. 675–78. doi: http://dx.doi.org/10.1246/cl.1986.675

[42] Tsubokawa, N. 1985. "Theory and Practice of Filler Reinforcement. II. Grafting onto Carbon Black." *International Polymer Science and Technology* 12, p. 31.

[43] Hayashi, S., A. Naitoh, S. Machida, M.Okazaki, K. Maruyama, and N. Tsubokawa. 1998. "Grafting of Polymers onto a Carbon Black Surface by the Trapping of Polymer Radicals." *Applied Organometallic Chemistry* 12, no. 10–11, pp. 743–48. doi: http://dx.doi.org/10.1002/(sici)1099-0739(199810/11)12:10/11%3C743::aid-aoc781%3E3.0.co;2-n

[44] Papirer, E., and D.Y. Wu. 1990. "Study of the Behavior and Conformation of Linear Hydrocarbon Chains Grafted on the Surface of Carbon Black." *Carbon* 28, no. 2–3, pp. 393–99. doi: http://dx.doi.org/10.1016/0008-6223(90)90013-o

[45] Vidal, A., S. Zhi Hao, and J.B. Donnet. 1991. "Modification of Carbon Black Surfaces—Effects on Elastomer Reinforcement." *Kautschuk Gummi Kunststoffe* 44, p. 419.

[46] Wang, M.J. 1999. "Effect of Polymer-Filler and Filler-Filler Interaction on Dynamic Properties of Filled Vulcanizates." *Rubber Chemistry and Technology* 71, no. 3, pp. 520–89. doi: http://dx.doi.org/10.5254/1.3538492

[47] Wang, W.D., A. Vidal, G. Nanse, and J.B. Donnet. 1994. "Study of Surface Activity of Carbon Black by Inverse Gas Chromatography. Part V: Modification of Carbon Black Surface by Silane." *Kautschuk Gummi Kunststoffe* 47, p. 493.

[48] Yoon, H.G., K.W. Kwon. K. Nagata, and K. Takahashi. 2004. "Changing the Percolation Threshold of Carbon Black by a Coupling Treatment of the Black." *Carbon* 42, no. 8–9, pp. 1877–79. doi: http://dx.doi.org/10.1016/j.carbon.2004.02.036

[49] Belmont, J., and C. Adams. 1997. CABOT CORP (CA19972258188) Modified Carbon Products For Inks And Coatings.

[50] Bergemann, K., E. Fanghänel, B. Kmackfuss, T. Lüthge, and G. Schukat. 2004. "Modification of Carbon Black Properties by Reaction with Maleic Acid Derivatives." *Carbon* 42, no. 11, pp. 2338–40. doi: http://dx.doi.org/10.1016/j.carbon.2004.03.041

[51] Donnet, J.B., W.D. Wang, and A. Vidal. 1994. "Observation of Plasma Treated Carbon Black Surfaces by Scanning Tunnelling Microscopy." *Carbon* 32, no. 2, pp. 199–206. doi: http://dx.doi.org/10.1016/0008-6223(94)90183-x

[52] Wang, W., A. Vidal, J.B. Donnet, and M.-J. Wang. 1993. "Study of Surface Activity of Carbon Black by Inverse Gas Chromatography, Part III. Superficial Plasma Treatment of Carbon Black and Its Surface Activity." *Kautschuk Gummi Kunststoffe* 46, p. 933.

[53] Schukin, L.I., M.V. Kornievich, R.S. Vartapetjan, and S.I. Beznisko. 2002. "Low-Temperature Plasma Oxidation of Activated Carbons." *Carbon* 40, no. 11, pp. 2028–30. doi: http://dx.doi.org/10.1016/s0008-6223(02)00153-7

[54] Tressaud, A., T. Shirasaki, G. Nanse, and E. Papirer. 2002. "Fluorinated Carbon Blacks: Influence of the Morphology of the Starting Material on the Fluorination Mechanism." *Carbon* 40, no. 2, pp. 217–20. doi: http://dx.doi.org/10.1016/s0008-6223(01)00177-4

[55] Favia, P., N. De Vietro, R. Di Mundo, F. Fracassi, and R. d'Agostino. 2006. "Tuning the Acid/Base Surface Character of Carbonaceous Materials by Means of Cold Plasma Treatments." *Plasma Processes and Polymers* 3, no. 1, pp. 66–74. doi: http://dx.doi.org/10.1002/ppap.200500073

[56] Bruser, V., M. Heintze, W. Brandl, G. Marginean, and H. Bubert. 2004. "Surface Modification of Carbon Nanofibres in Low Temperature Plasmas." *Diamond and Related Materials* 13, no. 4–8, pp. 1177–81. doi: http://dx.doi.org/10.1016/j.diamond.2003.10.061

[57] Tricás, N. 2006. Tesis Doctoral. Universitat Ramon llull.

[58] Akovali, G., and I. Ulkem. 1999. "Some Performance Characteristics of Plasma Surface Modified Carbon Black in the (SBR) Matrix." *Polymer* 40, no. 26, pp. 7417–22. doi: http://dx.doi.org/10.1016/s0032-3861(99)00094-4

[59] Shioyama, H., K. Honjo, M. Kiuchi, Y. Yamada, A. Ueda, N. Kuriyama, and T. Kobayashi. 2006. "C_2F_6 Plasma Treatment of a Carbon Support for a PEM Fuel Cell Electrocatalyst." *Journal of Power Sources* 161, no. 2, pp. 836–38. doi: http://dx.doi.org/10.1016/j.jpowsour.2006.05.046

[60] Melore, P.J., and F.J. Eckert. 1966. Columbian Carbon (US3245820) Preparation of Long-Flow Carbon Black, filed February 7, 1963, and issued April 12, 1966.

[61] Hjelm, R.P., W. Wampler, and M. Gerspacher. 2000. "The Structure of Carbon Black and Its Associations in Elastomer Composites: A Study Using Neutron Scattering." *Kautschuk Gummi Kunststoffe* 53, p. 592.

[62] Donnet, J.B., P. Ehrburger, and A. Voet. 1972. "Mechanism of the Oxidation of Carbon Black by Ozone in Aqueous Solution." *Carbon* 10, p. 737.

[63] Otake, Y., and R. Jenkins. 1993. "Characterization of Oxygen-containing Surface Complexes Created on Microporous Carbon by Air and Nitric Acid Treatment." *Carbon* 31, no. 1, pp. 109–21. doi: http://dx.doi.org/10.1016/0008-6223(93)90163-5

[64] Park, S.J., and J.S. Kim. 2001. "Influence of Plasma Treatment on Microstructures and Acid-Base Surface Energetics of Nanostructured Carbon Blacks: N_2 Plasma Environment." *Journal of Colloid and Interface Science* 244, no. 2, pp. 336–41. doi: http://dx.doi.org/10.1006/jcis.2001.7920

[65] Krishnankutty, N., and M.A. Vannice. 1995. "Effect of Pre-Treatment on Surface Area, Porosity and Adsorption Properties of Carbon Black." *Chemistry of Materials* 7, no. 4, pp. 754–63. doi: http://dx.doi.org/10.1021/cm00052a022

[66] Park, S.J., and J.S. Kim. 2001. "Surface Energy Characterization of Modified Carbon Blacks and Its Relationship to Composites Tearing Properties." *Journal of Adhesion Science and Technology* 15, no. 12, pp. 1443–52. doi: http://dx.doi.org/10.1163/156856101753213295

[67] Sosa, R.C., R.F. Parton, P.E. Neys, O. Lardinois, P.A. Jacobs, and P.G. Rouxhet. 1996. "Surface Modification of CB by Oxidation and Its Influence on the Activity of Immobilized Catalase and Iron Phtalocyanines." *Journal of Molecular Catalysus A: Cheminal* 110, no. 2, pp. 141–51. doi: http://dx.doi.org/10.1016/1381-1169(96)00197-5

[68] Fanning, P.F., and M.A. Vannice. 1993. "A Drifts, Study of the Formation of Surface Groups on Carbon Black by Oxidation." *Carbon* 31, no. 5, pp. 721–30. doi: http://dx.doi.org/10.1016/0008-6223(93)90009-y

[69] Chen, X., M. Farber, Y. Gao, I. Kulaots, E.M. Suuberg, and R.H. Hurt. 2003. "Mechanisms of Surfactant Adsorption on Non-polar, Air-oxidizes and Ozone Treated Carbon Surfaces." *Carbon* 41, no. 8, pp. 1498–500. doi: http://dx.doi.org/10.1016/s0008-6223(03)00053-8

[70] Wang, Z.B., G.P. Yin, and P.-F. Shi. 2006. "Effects of Ozone Treatment of Carbon Support on Pt–Ru/C Catalysts Performance for Direct Methanol Fuel Cell." *Carbon* 44, no. 1, pp. 133–40. doi: http://dx.doi.org/10.1016/j.carbon.2005.06.043

[71] Cotton, G.R., B.B. Boonstra, D. Rivin, and F.R. Williams. 1969. "Effect if Chemical Modification of Carbon Black on Its Behaviour in Rubber." *Kautschuk Gummi und Kunststoffe* 9, p. 477.

[72] Belmont, J.A., and J.M. Funt. 1991. "Carbon Black Surface Activity and Rubber Properties." *Kautschuk Gummi Kunstoffe* 44, p. 1135.

[73] Roychoudhury, A., and P.P. De. 1993. "Reinforcement of Epoxidized Natural Rubber by Carbon Black: Effect in Surface Oxidation of Carbon Black Particles." *Journal of Applied Polymer Science* 50, no. 1, pp. 181–86. doi: http://dx.doi.org/10.1002/app.1993.070500120

[74] Manna, A.K., P.P. De, D.K. Tripathy, S.K. De, and M.K. ChatterJee. 1997. "Chemical Interaction Between Surface Oxidized Carbon Black and Epoxidized Natural Rubber." *Rubber Chemistry and Technology* 70, no. 4, pp. 624–33. doi: http://dx.doi.org/10.5254/1.3538448

[75] Manna, A.K., P.P. De, D.K. Tripathy, S.K. De, and M.K. ChatterJee. 1999. "Effect of Surface Oxidation of Carbon Blacks on Its Bonding with Epoxidized Natural Rubber in the Presence of Silane Coupling Agent." *Rubber Chemistry and Technology* 72, no. 2, pp. 398–409. doi: http://dx.doi.org/10.5254/1.3538810

[76] Bellander, M., B. Stenberg, and S. Persson. 1998. "Influence of Oxidized Carbon Black on the Degree of Cure in Polybutadiene Crosslinked by High Pressure Vulcanization." *Kautschuk Gummi Kunstoffe* 51, no. 7, pp. 512–17.

[77] Frysz, A., and D.D.L. Chung. 1997. "Improving the Electrochemical Behavior of Carbon Black and Carbon Filaments by Oxidation." *Carbon* 35, no. 8, pp. 1111–27. doi: http://dx.doi.org/10.1016/s0008-6223(97)00083-3

[78] Masayuki, M., and k. Miharu. 2004. Seiko Epson Corp Chemical Ind., (EP1479732) Modified Carbon Black, Carbon Black Dispersion Liquid and Water Base Ink, filed December 26, 2003, and issued June 13, 2007.

[79] Kalbitz, W., and A. Karl. 2001. Degussa, (EP1099735) Aqueous Carbon Black Dispersion and Its Production Method and Use, filed November 04, 2000, and issued January 28, 2004.

[80] Suetsugu, K., and E. Maruyama. 1976. Mitsubishi Chem Ind., (US3992218) Black Coloring Agent, filed May 2, 1975, and issued November 16, 1976.

[81] De Torre, L.E.C., E.J. Bottani, A. Martinez-Alonso, A. Cuesta, A.B. Garcia, and J.M.D. Tascon. 1998. "Effects of Oxygen Plasma Treatment on the Surface of Graphitized Carbon Black." *Carbon* 36, no. 3, pp. 277–82. doi: http://dx.doi.org/10.1016/s0008-6223(97)00180-2

[82] Cuesta, A., A. Martinez-Alonso, and J.M.D. Tascon. 2001. "Carbon Reactivity in an Oxygen Plasma: A Comparison with Reactivity in Molecular Oxygen." *Carbon* 39, no. 8, pp. 1135–46. doi: http://dx.doi.org/10.1016/s0008-6223(00)00235-9

[83] Paredes, J.I., M. Gracia, A. Martinez-Alonso, and J.M.D. Tascon. 2005. "Nanoscale Investigation of the Structural and Chemical Changes Induced by Oxidation on Carbon Black Surfaces: A Scanning Probe Microscopy Approach." *Journal of Colloid and Interface Science* 288, no. 1, pp. 190–99. doi: http://dx.doi.org/10.1016/j.jcis.2005.02.081

[84] Takada, T., M. Nakahara, H. Kumagai, and Y. Sanada. 1996. "Surface Modification and Characterization of Carbon Black with Oxygen Plasma." *Carbon* 34, no. 9, pp. 1087–91. doi: http://dx.doi.org/10.1016/0008-6223(96)00054-1

[85] Li, X., and K. Horita. 2000. "Electrochemical Characterization of Carbon Black Subjected to RF Oxygen Plasma." *Carbon* 38, no. 1, pp. 133–38. doi: http://dx.doi.org/10.1016/s0008-6223(99)00108-6

[86] Creatore, M., P. Favia, G. Tenuto, A. Valentini, and R. D'Agostino. 2001. "NH_3 Plasma Treatments of PET for Enhancing Aluminum Adhesion." *Plasmas and Polymers* 5, no. 3–4, pp. 201–18.

[87] Schroder, K., A. Meyer-Plath, D. Keller, W. Besch, G. Babucke, and A. Ohl. 2001. "Plasma-Induced Surface Functionalization of Polymeric Biomaterials in Ammonia Plasma." *Contributions to Plasma Physics* 41, no. 6, pp. 562–72. doi: http://dx.doi.org/10.1002/1521-3986(200111)41:6%3C562::aid-ctpp562%3E3.0.co;2-y

[88] Cataldo, F. 1999. "Carbon Nitration and Nitrosation and Its Application to Improve Mechanical Hysteresis of a Rubber Tread Compound." *Die Angewandte Makromolekulare Chemie* 270, no. 1, pp. 81–86. doi: http://dx.doi.org/10.1002/(sici)1522-9505(19990901)270:1%3C81::aid-apmc81%3E3.0.co;2-n

[89] Loh, I.H., R.E. Cohen, and R.F. Baddour. 1987. "Modification of Carbon Surface in Cold Plasmas." *Journal of Materials Science* 22, no. 8, pp. 2937–47. doi: http://dx.doi.org/10.1007/bf01086494

[90] Park, S.J., and J.S. Kim. 2001. "Influence of Plasma Treatment on Microstructures and Acid-Base Surface Energetics of Nanostructured Carbon Blacks: N_2 Plasma Environment." *Journal of Colloid and Interface Science* 244, no. 2, pp. 336–41. doi: http://dx.doi.org/10.1006/jcis.2001.7920

[91] Kima, S., M.H. Choa, J.R. Lee, and S.J. Park. 2006. "Influence of Plasma Treatment of Carbon Blacks on Electrochemical Activity of Pt/carbon Blacks Catalysts for DMFCs." *Journal of Power Sources* 159, no. 1, pp. 46–48. doi: http://dx.doi.org/10.1016/j.jpowsour.2006.04.039

[92] Felten, A., C. Bittencourt, J.J. Pireaux, G. Van Lier, and J.C. Charlier. 2005. "Radio-Frequency Plasma Functionalization of Carbon Nanotubes Surface O_2, NH_3, and CF_4 Treatments." *Journal of Applied Physics* 98, no. 7, pp. 4308/1. doi: http://dx.doi.org/10.1063/1.2071455

[93] Papier, E., V.T. Nguyen, and J.B. Donnet. 1978. "Introduction of Sulfur Groups onto the Surface of Carbon Blacks." *Carbon* 16, no. 2, pp. 141–44. doi: http://dx.doi.org/10.1016/0008-6223(78)90011-8

[94] Gajewski, M., and T. Prot. 1994. "Correlation Between Crosslink Density and Properties of Rubber Containing Chemically Modified Carbon Black." *Kautschuk Gummi Kunststoffe* 47, no. 8, pp. 574–77.

[95] Tressaud, A., T. Shirasaki, N. Ganse, and E. Papirer. 2002. "Fluorinated Carbon Blacks: Influence of the Morphology of the Starting Material on the Fluorination Mechanism." *Carbon* 40, no. 2, pp. 217–20. doi: http://dx.doi.org/10.1016/s0008-6223(01)00177-4

[96] Papier, E., R. Lacroix, and J.B. Donnet. 1996. "Chemical Modifications and Surface Properties of Carbon Blacks." *Carbon* 34, no. 12, pp. 1521–29. doi: http://dx.doi.org/10.1016/s0008-6223(96)00103-0

[97] Douroumis, D., D.G. Fatouros, N. Bouropoulos, K. Papagelis, and D. Tasis. 2007. "Colloidal Stability of Carbon Nanotubes in an Aqueous Dispersion of Phospholipid." *International Journal of Nanomedicine* 2, no. 4, pp. 761–66.

[98] Singh, P., S. Campidelli, S. Giordani, D. Bonifazi, A. Bianco, and M. Prato. 2009. "Organic Functionalisation and Characterisation of Single-walled Carbon Nanotubes." *Chemical Society Reviews* 38, no. 8, pp. 2214–30. doi: http://dx.doi.org/10.1039/b518111a

[99] Liu, Z., C. Davis, W. Cai, L. He, X. Chen, and H. Dai. 2008. "Circulation and Long-Term Fate of Functionalized, Biocompatible Single-Walled Carbon Nanotubes in Mice Probed by Raman Spectroscopy." *Proceedings of the National Academy of Sciences* 105, no. 5, pp. 1410–15. doi: http://dx.doi.org/10.1073/pnas.0707654105

[100] Liu, J., A.G. Rinzler, H. Dai, J.H. Hafner, R.K. Bradley, P.J. Boul, A. Lu, T. Iverson, K. Shelimov, C.B. Huffman, F. Rodriguez-Macias, Y.-S. Shon, T.R. Lee, D.T. Colbert, and R.E Smalley. 1998. "Fullerene Pipes." *Science* 280, no. 5367, pp. 1253–56. doi: http://dx.doi.org/10.1126/science.280.5367.1253

[101] Li, H.J., W.G. Lu, J.J. Li, X.D. Bai, and C.Z. Gu. 2005. "Multichannel Ballistic Transport in Multiwall Carbon Nanotubes." *Physical Review Letters* 95, no. 8, p. 086601. doi: http://dx.doi.org/10.1103/physrevlett.95.086601

[102] Matsuura, K., K. Hayashi, and N. Kimizuka. 2003. "Lectin-Mediated Supramolecular Junctions of Galactose-Derivatized Single-Walled Carbon Nanotubes." *Chemistry Letters* 32, no. 3, pp. 212–13. doi: http://dx.doi.org/10.1246/cl.2003.212

[103] Pompeo, F., and D.E. Resasco. 2002. "Water Solubilization of Single-Walled Carbon Nanotubes by Functionalization with Glucosamine." *Nano Letters* 2, no. 4, pp. 369–73. doi: http://dx.doi.org/10.1021/nl015680y

[104] Huang, W., S. Taylor, K. Fu, Y. Lin, D. Zhang, T.W. Hanks, A.M. Rao, and Y.P. Sun. 2002. "Attaching Proteins to Carbon Nanotubes via Diimide-Activated Amidation." *Nano Letters* 2, no. 4, pp. 311–14. doi: http://dx.doi.org/10.1021/nl010095i

[105] Jiang, K., L.S. Schadler, R.W. Siegel, X. Zhang, H. Zhang, and M. Terrones. 2004. "Protein Immobilization on Carbon Nanotubes via a Two-Step Process of Diimide-Activated Amidation." *Journal of Materials Chemistry* 14, no. 1, pp. 37–39. doi: http://dx.doi.org/10.1039/b310359e

[106] Weizmann, Y., D.M. Chenoweth, and T.M. Swager. 2010. "Addressable Terminally Linked DNA CNT Nanowires." *Journal of the American Chemical Society* 132, no. 40, pp. 14009–11. doi: http://dx.doi.org/10.1021/ja106352y

[107] Hazani, M., R. Naaman, F. Hennrich, and M.M. Kappes. 2003. "Confocal Fluorescence Imaging of DNA-Functionalized Carbon Nanotubes." *Nano Letters* 3, no. 2, pp. 153–55. doi: http://dx.doi.org/10.1021/nl025874t

[108] Carson, L., C. Kelly-Brown, M. Stewart, A. Oki, G. Regisford, Z. Luo, and V.I. Bakhmutov. 2009. "Synthesis and Characterization of Chitosan Carbon Nanotube Composites." *Materials Letters* 63, no. 6–7, pp. 617–20. doi: http://dx.doi.org/10.1016/j.matlet.2008.11.060

[109] Ke, G., W. Guan, C. Tang, W. Guan, D. Zeng, and F. Deng. 2007. "Covalent Functionalization of Multiwalled Carbon Nanotubes with a Low Molecular Weight Chitosan." *Biomacromolecules* 8, no. 2, pp. 322–26. doi: http://dx.doi.org/10.1021/bm0604146

[110] Harris, J.M., and R.B. Chess. 2003. "Effect of Pegylation on Pharmaceuticals." *Nature Reviews Drug Discovery* 2, no. 3, 214–21. doi: http://dx.doi.org/10.1038/nrd1033

[111] Sano, M., A. Kamino, J. Okamura, and S. Shinkai. 2001. "Self-Organization of PEO-Graft-Single-Walled Carbon Nanotubes in Solutions and Langmuir-Blodgett Films." *Langmuir* 17, no. 17, pp. 5125–28. doi: http://dx.doi.org/10.1021/la010126p

[112] Zhao, B., H. Hu, A. Yu, D. Perea, and R.C. Haddon. 2005. "Synthesis and Characterization of Water Soluble Single-Walled Carbon Nanotube Graft Copolymers." *Journal of the American Chemical Society* 127, no. 22, pp. 8197–203. doi: http://dx.doi.org/10.1021/ja042924i

[113] Riggs, J.E., Z. Guo, D.L. Carroll, and Y.-P. Sun. 2000. "Strong Luminescence of Solubilized Carbon Nanotubes." *Journal of the American Chemical Society* 122, no. 24, pp. 5879–80. doi: http://dx.doi.org/10.1021/ja9942282

[114] Sahoo, N.G., H. Bao, Y. Pan, M. Pal, M. Kakran, H.K.F. Cheng, L. Li, and L.P. Tan. 2011. "Functionalized Carbon Nanomaterials as Nanocarriers for Loading and Delivery of a Poorly Water-Soluble Anticancer Drug: A Comparative Study." *Chemical Communications* 47, no. 18, pp. 5235–37. doi: http://dx.doi.org/10.1039/c1cc00075f

[115] Aitchison, T.J., M. Ginic-Markovic, J.G. Matisons, G.P. Simon, and P.M. Fredericks. 2007. "Purification, Cutting, and Sidewall Functionalization of Multiwalled Carbon Nanotubes Using Potassium Permanganate Solutions." *The Journal of Physical Chemistry C* 111, no. 6, pp. 2440–46. doi: http://dx.doi.org/10.1021/jp066541d

[116] Ziegler, K.J., Z. Gu, H. Peng, E.L. Flor, R.H. Hauge, and R.E. Smalley. 2005. "Controlled Oxidative Cutting of Single-Walled Carbon Nanotubes." *Journal of the American Chemical Society* 127, no. 5, pp. 1541–47. doi: http://dx.doi.org/10.1021/ja044537e

[117] Holzinger, M., J. Abraham, P. Whelan, R. Graupner, L. Ley, F. Hennrich, M. Kappes, and A. Hirsch. 2003. "Functionalization of Single-Walled Carbon Nanotubes with (R-) Oxycarbonyl Nitrenes." *Journal of the American Chemical Society* 125, no. 28, pp. 8566–80. doi: http://dx.doi.org/10.1021/ja029931w

[118] Gao, C., H. He, L. Zhou, X. Zheng, and Y. Zhang. 2009. "Scalable Functional Group Engineering of Carbon Nanotubes by Improved One-Step Nitrene Chemistry." *Chemistry of Materials* 21, no. 2, pp. 360–70. doi: http://dx.doi.org/10.1021/cm802704c

[119] Moghaddam, M.J., S. Taylor, M. Gao, S. Huang, L. Dai, and M.J. McCall. 2004. "Highly Efficient Binding of DNA on the Sidewalls and Tips of Carbon Nanotubes Using Photochemistry." *Nano Letters* 4, no. 1, pp. 89–93. doi: http://dx.doi.org/10.1021/nl034915y

[120] Maggini, M., G. Scorrano, and M. Prato. 1993. "Addition of Azomethine Ylides to C60: Synthesis, Characterization, and Functionalization of Fullerene Pyrrolidines." *Journal of the American Chemical Society* 115, no. 21, pp. 9798–99. doi: http://dx.doi.org/10.1021/ja00074a056

[121] Georgakilas, V., K. Kordatos, M. Prato, D.M. Guldi, M. Holzinger, and A. Hirsch. 2002. "Organic Functionalization of Carbon Nanotubes." *Journal of the American Chemical Society* 124, no. 5, pp. 760–61. doi: http://dx.doi.org/10.1021/ja016954m

[122] Georgakilas, V., N. Tagmatarchis, D. Pantarotto, A. Bianco, J.P. Briand, and M. Prato. 2002. "Amino Acid Functionalisation of Water Soluble Carbon Nanotubes." *Chemical Communications*, no. 24, pp. 3050–51. doi: http://dx.doi.org/10.1039/b209843a

[123] Singh, R., D. Pantarotto, D. McCarthy, O. Chaloin, J. Hoebeke, C.D. Partidos, J.P. Briand, M. Prato, A. Bianco, and K. Kostarelos. 2005. "Binding and Condensation of Plasmid DNA onto Functionalized Carbon Nanotubes: Toward the Construction of Nanotube-Based Gene Delivery Vectors." *Journal of the American Chemical Society* 127, no. 12, pp. 4388–96. doi: http://dx.doi.org/10.1021/ja0441561

[124] Bahr, J.L., and J.M. Tour. 2001. "Highly Functionalized Carbon Nanotubes Using in Situ Generated Diazonium Compounds." *Chemistry of Materials* 13, no. 11, pp. 3823–24. doi: http://dx.doi.org/10.1021/cm0109903

[125] Karousis, N., H. Ali-Boucetta, K. Kostarelos, and N. Tagmatarchis. 2008. "Aryl-Derivatized, Water-Soluble Functionalized Carbon Nanotubes for Biomedical Applications." *Materials Science and Engineering: B* 152, no. 1–3, pp. 8–17. doi: http://dx.doi.org/10.1016/j.mseb.2008.06.002

[126] Ménard-Moyon, C., C. Fabbro, M. Prato, and A. Bianco. 2011. "One-Pot Triple Functionalization of Carbon Nanotubes." *Chemistryì A European Journal* 17, no. 11, pp. 3222–27. doi: http://dx.doi.org/10.1002/chem.201003050

[127] Peng, H., L.B. Alemany, J.L. Margrave, and V.N. Khabashesku. 2003. "Sidewall Carboxylic Acid Functionalization of Single-Walled Carbon Nanotubes." *Journal of the American Chemical Society* 125, no. 49, pp. 15174–82. doi: http://dx.doi.org/10.1021/ja037746s

[128] Stephenson, J.J., J.L. Hudson, A.D. Leonard, B.K. Price, and J.M. Tour. 2007. "Repetitive Functionalization of Water-Soluble Single-Walled Carbon Nanotubes. Addition of Acid-Sensitive Addends." *Chemistry of Materials* 19, no. 14, pp. 3491–98. doi: http://dx.doi.org/10.1021/cm070076v

[129] Yang, Y., S. Qiu, X. Xie, X. Wang, and R.K.Y. Li. 2010. "A Facile, Green, and Tunable Method to Functionalize Carbon Nanotubes with Water-Soluble Azo Initiators by One-step Free Radical Addition." *Applied Surface Science* 256, no. 10, pp. 3286–92. doi: http://dx.doi.org/10.1016/j.apsusc.2009.12.020

[130] Ávila-Orta, C.A., V.J. Cruz-Delgado, M.G. Neira-Velázquez, E. Hernández-Hernández, M.G. Méndez-Padilla, and F.J. Medellín-Rodríguez. 2009. "Surface Modification of Carbon Nanotubes with Ethylene Glycol Plasma." *Carbon* 47, no. 8, pp. 1916–21. doi: http://dx.doi.org/10.1016/j.carbon.2009.02.033

INDEX

Carbon: The Next Silicon?

Book 1 – Fundamentals

Marc J. Madou • Victor H. Perez-Gonzalez • Bidhan Pramanick

This book provides an introduction to the state-of-the art in C-MEMS/C-NEMS with an emphasis on lithographically patterned photo-polymers, carbonized in an inert atmosphere. We can expand our perspective considerably by learning from the traditional carbon manufacturing community where researchers deal with a much wider variety of carbon feed stocks such as coal, coconut shell, wood, agricultural wastes, and industrial wastes to make all types of useful carbons. The new concepts are introduced by discussing carbon nanomaterials synthesis aided with catalysts and chemistry and detailing the microstructure of the resulting nanocarbons.

Dr. Marc J. Madou is the chancellor's professor in mechanical and aerospace engineering (MEA) as the University of California Irvine. Dr. Madou is the author of several books, including *Fundamentals of Microfabrication*. Some of Dr. Madou's current research work involves a compact disc-based fluidic platform and carbon MEMS. Learn more about those recent research projects, visit www.biomems.net.

Dr. Victor H. Perez-Gonzalez, received the BS degree from *Universidad Autonoma de Nuevo Leon*, Mexico; and his MS and PhD from *Tecnologico de Monterrey*, Mexico, where he is now a research associate. He is a member of the National System of Researchers, Mexico. Dr. Perez-Gonzalez's research interests are focused in the field of miniaturization science, where he has published several papers.

Dr. Bidhan Pramanick received his PhD from Indian Institute of Technology Kharagpur, India. He was assistant professor in the Indian Institute of Space Science and Technology before joining Tec de Monterrey, Mexico (and UCI, CA) as postdoctoral research investigator. He has authored and co-authored several papers in international journals and conference proceedings and one book.

MOMENTUM PRESS
ENGINEERING

ISBN: 978-1-60650-723-0
90000
9 781606 507230